Experimental Analysis of Crankcase Oil Aerosol Generation and Control

By

Benjamin T. Johnson

MEng. (Hons) DIS

A Doctoral Thesis submitted in partial fulfilment of the requirements for the award of Doctor of Philosophy of Loughborough University

2012

Certificate of Originality

This is to certify that I am responsible for the work submitted in this thesis, that the original work is my own except as specified in acknowledgements or in footnotes, and that neither the thesis nor the original work therein has been submitted to this or any other institution for a degree

……………………………………………………… (Signed)

……………………………………………………… (Date)

ABSTRACT

Crankcase ventilation contributes significantly to diesel engine particulate emissions. Future regulations will not only limit the mass of particulate matter, but also the number of particles. Controlling the source of crankcase emissions is critical to meeting the perennial legislation. Deficiency in the understanding of crankcase emissions generation and the contribution of lubricating oil has been addressed in detail by the experimental study presented in this thesis.

A plethora of high speed laser optical diagnostics techniques have been employed to deduce the main mechanisms of crankcase oil aerosol generation. Novel images have captured oil atomisation and passive oil distribution around the crankcase of an optically accessed, motored, four cylinder, off-highway, heavy duty, diesel engine. Rayleigh type ligament breakup of oil films present on the surface of dynamic components, most notably the crankshaft, camshaft and valve rockers generated oil drops below 10 micrometers. Data illustrated not only crankcase oil aerosol generation at source, but it has provided valuable information on methods to control oil aerosol generation and improve oil circuit efficiency. The feasibility of utilising computational fluid dynamics to predict crankcase oil aerosol generation has been successfully assessed using the experimental data.

Particle sampling has characterised the crankcase emissions from both a fired and motored diesel engine crankcase. The evolution of submicron crankcase particles down to 5 nm has been recorded from both engines, including the isolated contribution of engine oil, at a wide range of engine test points. Results have provided constructive insight into the generation and control of this complex emission.

The main mechanism of crankcase oil aerosol generation was found to be crankshaft oil atomisation. This atomisation process has been analysed in detail, involving high speed imaging of primary and satellite drop generation and high speed digital particle image velocity of the crankshaft air flow. A promising mechanism of regulating and controlling crankcase oil aerosol emissions at source has been studied experimentally.

ACKNOWLEDGEMENTS

All of this would not have been possible without my family and friends. I am indebted to them, thank you Mum, Emily and Jessica for your love and support. Thank you also to all who sacrificed their time reading drafts of my thesis. I will always be grateful to my friends around the country, thank you for your patience and persistence despite the numerous events and bike rides that I did not attend the invitations never relinquished. I can now focus on the next exciting chapter of my life.

"*Only those who will risk going too far can possibly find out how far one can go*"

      T.S.Eliot

CONTENTS

NOMENCLATURE

a	-	Disc oil film thickness	[m]
a	-	Acceleration	[m.s^{-2}]
A_c	-	Camera chip area	[m^2]
A_I	-	Imaged area	[m^2]
a_L	-	Ligament radius	[m]
a_n	-	Normal / centripetal acceleration	[m.s^{-2}]
A_n	-	Nozzle cross sectional area	[m^2]
a_p	-	Seeding particle radius	[m]
a_t	-	Tangential acceleration	[m.s^{-2}]
Bo	-	Bond number	-
Bo_D	-	Rotating disc Bond number	-
c	-	Radial bearing clearance	[m]
C_D	-	Drop drag coefficient	-
D	-	Disc diameter	[m]
d^*	-	Kelvin drop diameter	[m]
D_{Aero}	-	Aerodynamic particle diameter	[m]
d_c	-	Supply hole diameter	[m]
d_{diff}	-	Diffraction limited spot size	[m]
d_g	-	Geometric mean diameter	[m]
d_i	-	Midpoint diameter of the ith group	[m]
D_j	-	Jet diameter	[m]
dN	-	Particle number concentration	-
d_p	-	Drop diameter	[m]
D_p	-	Midpoint particle diameter	[m]
$D_{p,l}$	-	Lower channel diameter	[m]
$D_{p,u}$	-	Upper channel diameter	[m]
Dt	-	PIV frame separation	[s]
$f^{\#}$	-	Aperture / f-number	-
F_{Aero}	-	Aerodynamic force	[N]
F_n	-	Normal or centripetal force	[N]
F_t	-	Tangential force	[N]

f_u	-	Seeding particle frequency response	[Hz]
F_W	-	Weight	[N]
F_σ	-	Surface tension force	[N]
G	-	Acceleration due to gravity	$[\text{m.s}^{-2}]$
g^*	-	Acceleration due to body force	$[\text{m.s}^{-2}]$
h_f	-	Oil film thickness at the supply hole	[m]
K	-	Empirical constant	-
K_F	-	Fluid number	-
K_R	-	Kelvin ratio	-
L	-	Hydrodynamic bearing transverse length	[m]
L_c	-	Characteristic length	[m]
l_{lig}	-	Distance between ligaments	[m]
L_α	-	Laplace number	-
M	-	Molecular weight	-
M	-	Lens magnification factor	-
m_o	-	Oil mass	[kg]
N	-	Speed	$[\text{rev.s}^{-1}]$
N	-	Total particle number	-
n_i	-	Number of particles in the ith group	-
Oh	-	Ohnesorge number	-
P	-	Partial pressure of a gas in a mixture of gases	[Pa]
p_0	-	Maximum pressure	[Pa]
p_A	-	External aerodynamic pressure	[Pa]
p_d	-	Partial pressure of vapour at drop surface	[Pa]
p_I	-	Internal pressure	[Pa]
p_s	-	Saturation vapour pressure	[Pa]
p_σ	-	Surface tension pressure	[Pa]
Q	-	Flow rate	$[\text{m}^3.\text{s}^{-1}]$
Q_a	-	Pump axial flow	$[\text{m}^3.\text{s}^{-1}]$
Q_a^*	-	Single hole axial flow factor	$[\text{m}^3.\text{s}^{-1}]$
Q_b	-	Crankcase / blow-by flow rate	$[\text{m}^3.\text{s}^{-1}]$
Q_p	-	Total side flow	$[\text{m}^3.\text{s}^{-1}]$

Q_s	-	Bearing side leakage flow rate over pressurised region	[m^3.s^{-1}]
$Q_s{}^*$	-	Side flow factor	[m^3.s^{-1}]
R	-	Radius	[m.s^{-1}]
R	-	Bearing radius	[m]
R	-	Gas constant	[J.mol^{-1}.K^{-1}]
Re	-	Reynolds number	-
S_R	-	Saturation ratio	-
T_A	-	Gas temperature	[K]
U_g	-	Gravitationally induced drop velocity	[m.s^{-1}]
U_R	-	Relative axial velocity	[m.s^{-1}]
$U_{R,Crit}$	-	Critical relative velocity	[m.s^{-1}]
V	-	Tangential velocity	[m.s^{-1}]
V_d	-	Drop velocity	[m.s^{-1}]
$\dot{V}^*$	-	Dimensionless volume flow rate number	-
$\dot{V}$	-	Volume flow rate	[m^3.s]
We	-	Weber number	-
We_{Aero}	-	Aerodynamic Weber number	-
$We_{Aero,Crit,}$	-	Critical aerodynamic Weber number	-

E	-	Eccentricity ratio	-
H	-	Dynamic viscosity	[kg.s^{-1}.m^{-1}]
η_a	-	Air dynamic viscosity	[kg.s^{-1}.m^{-1}]
η_l	-	Liquid dynamic viscosity	[kg.s^{-1}.m^{-1}]
θ_c	-	Oil contact angle	[rad]
Λ	-	Pinch off wavelength	[m]
ν	-	Kinematic viscosity	[m^2.s^{-1}]
ρ	-	Density	[kg.m^{-3}]
ρ_0	-	Standard density	[kg.m^{-3}]
ρ_a	-	Gas density	[kg.m^{-3}]
ρ_l	-	Liquid density	[kg.m^{-3}]

σ	-	Surface tension	$[kg.s^{-2}]$
σ_g	-	Geometric standard deviation	-
ϕ	-	Bearing polar coordinate angle	$[rad]$
ω	-	Angular velocity	$[rad.s^{-1}]$

ABBREVIATIONS

ACGIH	-	American Conference of Governmental Industrial Hygienists
ACU	-	Automotive Council UK
APS	-	Aerodynamic Particle Sizer
BDC	-	Bottom Dead Centre
CA	-	Crank Angle
CAE	-	Computer Aided Engineering
CCV	-	Closed Crankcase Ventilation
CEAS	-	Crankcase Emissions Abatement System
CFD	-	Computational Fluid Dynamics
CO	-	Carbon Monoxide
CPC	-	Condensation Particle Counter
DISI	-	Direct Injection Spark Ignition
DMA	-	Differential Mobility Analyser
DMS	-	Differential Mobility Spectrometer/ Sizer
DPF	-	Diesel Particulate Filter
DSLR	-	Digital Single-lens Reflex Camera
EC	-	European Commission
EHO	-	Environmental Health Organisation
ELPI	-	Electrical Low Pressure Impactor
EPA	-	Environmental Protection Agency
EU	-	European Union
HC	-	Hydrocarbons
HSDPIV	-	High Speed Digital Particle Image Velocimetry
imep	-	Indicated Mean Effective Pressure
IPSD	-	Industrial Power Systems Division is the enterprise division of Caterpillar that manufactures engines and promotes these under the

		Cat and Perkins brands
LDV	-	Laser Dopper-Velocimetry
MMD	-	Mass Median Diameter
NA	-	Naturally Aspirated
NMOS	-	N-type Metal Oxide Sensor
NO_x	-	Oxides of Nitrogen
OCV	-	Open Crankcase Ventilation
OSHA	-	Occupational Safety and Health Administration
PASS	-	Photo-Acoustic Soot Sensor
PDA	-	Phase Doppler Anemometry
PM	-	Particulate Matter
PN	-	Particle Number
RGB	-	Red Green Blue image colour scale
SI	-	Spark Ignition
SMD	-	Sauter Mean Diameter
SOF	-	Soluble Organic Fraction
STEL	-	Short Term Exposure Limit
TC	-	Turbo charged
TDC	-	Top Dead Centre
TTL	-	Transistor-transistor Logic
TWA	-	Time Weighted Average
UHC	-	Unburned Hydrocarbons
USA	-	United States of America

CHAPTER 1

INTRODUCTION

1.1   Background

The internal combustion engine is a formidable and ubiquitous source of mechanical power. Over 2 million engines are manufactured in the United Kingdom alone per year (ACU, 2010). Global popularity of the internal combustion engine has resulted in engine emissions becoming a major contributor to air pollution. Substantial investment in research and development is necessary to meet the consumer and government demands for high performance, high efficiency and low emissions.

In order to limit any detrimental effects on air quality, IC engine emissions are heavily regulated, with the limits becoming more stringent at each revision of the legislation. The main source of IC engine emissions are the products of combustion, which consist mainly of unburned hydrocarbons (UHC), carbon monoxide (CO), Oxides of Nitrogen (NO_x), and particulate matter (PM). PM comprises an aerosol of liquid drops and solid particles. Aerosols emitted by engines are regulated, as they have a detrimental impact on the environment and health, with long term exposure being linked to cardiovascular and respiratory diseases (Kim *et al.,* 2006). Diesel particle emissions are now classified as carcinogenic (IARC, 2012).

Within an internal combustion engine there is an undesirable leakage of gas past the piston rings into the crankcase, which is known as 'blow-by' (Heywood, 1988). The subsequent increase in crankcase pressure can be relieved in two ways: i) into the atmosphere, which is known as open crankcase ventilation (OCV), ii) re-distribution into the inlet mixture, which is known as closed crankcase ventilation (CCV). Since 2007 the US Environmental Protection Agency (EPA) and more recently European legislation (EU), have ruled if CCV is not used, crankcase emissions must be added to tailpipe emissions, giving a total emissions measurement. This was a significant step in emissions regulation, it emphasised the need for better emissions control and management as the contribution of crankcase emissions to total engine emissions is substantial.

Crankcase emissions are a complex mixture of combustion products, water vapour, un-burnt fuel and most significantly, particulate matter (PM). PM is the most complex diesel engine emission and it is classified by the EPA as an aerosol of solid

particles and liquid drops. Several studies have shown that crankcase emissions from heavy duty diesel engines can contribute up to 120% of the total allowable PM emissions (Heckel, Steffen and Fedorowicz, 2006; Pardue 2004). Clark *et al.* (2006b) found that the engine lubricant oil contributed to approximately 50% of the PM emissions from the crankcase, whilst the other 50% was associated with combustion emissions, wear and other sources. After-treatment devices reduce the combustion PM emissions, however, they do not resolve the issue since additional crankcase PM emissions increase filter loading and reduce filter performance (Givens *et al.*, 2003). Crankcase emissions exacerbate the existing emissions levels and create a range of new technical challenges. If OCV is employed, the engine out emissions will increase directly. If CCV is used any oil carried into the intake system will foul intake components and increase combustion emissions. For both crankcase ventilation strategies the engine oil consumption will increase significantly if the oil is not returned back to the crankcase.

Crankcase PM from lubricant oil is an aerosol of oil drops and can be characterised by its particle number (PN) and particle size distribution. Studies have found crankcase oil aerosols containing particles ranging from 50 nm to 10 µm in particle diameter (d_p) (Jaroszczyk *et al.*, 2006; Dollmeyer *et al.*, 2007; Tatli and Clark, 2008). Large particles, $d_p = 10$ - 20 µm, can be removed from the crankcase emissions using impaction separators where the blow-by is forced through a rapid change in geometry. Suspended oil drops cannot follow the flow path and are impacted onto a surface then drained away (Long *et al.*, 2009). To remove smaller drops more restrictive geometry is required, this increases the back pressure on the crankcase and impaction becomes substantially more complicated to control. To achieve the desired filtration performance, dynamic and consumable components can be employed, but these systems reduce the engine efficiency and increase engine costs (Kissner and Ruppel, 2009).

Lubricant oil is actively supplied to critical engine components, however, the passive movement of the oil as it drains back to the sump can generate an aerosol. Crankcase oil aerosol contributes to the engine emissions and can limit performance, but it is critical to lubrication of the piston ring pack and cylinder liner. Despite this reliance

there is little understanding of crankcase oil aerosol generation, with limited research or literature explaining the mechanisms of oil atomisation within an engine crankcase. Research has focussed on reducing the oil aerosol at the crankcase breather with no attempts to understand the sources of oil atomisation. The impact of crankcase emissions is summarised well by Maricq (2007, p1103) "With Diesel Particulate Filters (DPF) drastically reducing soot emissions, condensed crankcase vapours may dominate the overall PM emissions. What this means in terms of PM composition remains largely unknown". Understanding of the physical processes generating crankcase oil aerosols is essential to the future of high performance, low emissions engines.

1.2   Research Overview

It is clear that crankcase emissions are a prominent problem for engine manufacturers. Modern engines, specifically off-highway diesel engines, are required to operate over large duty cycles at high loads and in harsh environments, as a result engine design has become extremely complicated. To meet emissions targets components have been added to the engine package, increasing engine cost and size, and reducing efficiency. This study focuses on the sources of crankcase oil aerosol emissions and provides novel information on the generation of aerosols within the main body of the engine crankcase. The generation of crankcase oil aerosols is not actively designed into engine lubricating circuits, but it is vital to engine operation. A critical review of engine lubrication, associated research identifying factors influencing aerosol generation and the requirement for experimental investigation is described in the following sections in this chapter and in Chapter 2.

1.3   Emissions Legislation

The research presented within this thesis is driven by off-highway legislation, therefore it is important to introduce and define the limits and restriction. Legislation for off-highway diesel engines was introduced within the United States of America (USA) in 1994 and the EU in 1997. Emissions of carbon monoxide (CO), hydrocarbons (HC), oxides of nitrogen (NO_x) and particulate matter (PM) from non-road diesel engines are controlled. Engines are categorised by their power and

application, legislation limits the total emission of each species to a single value, commonly g.kWh^{-1}, measured over a prescribed transient test cycle. Figure 1.1 illustrates how the European legislation for PM and NO$_x$ has become increasingly stringent, forcing engine manufactures to develop innovative and complex solutions to reduce engine emissions.
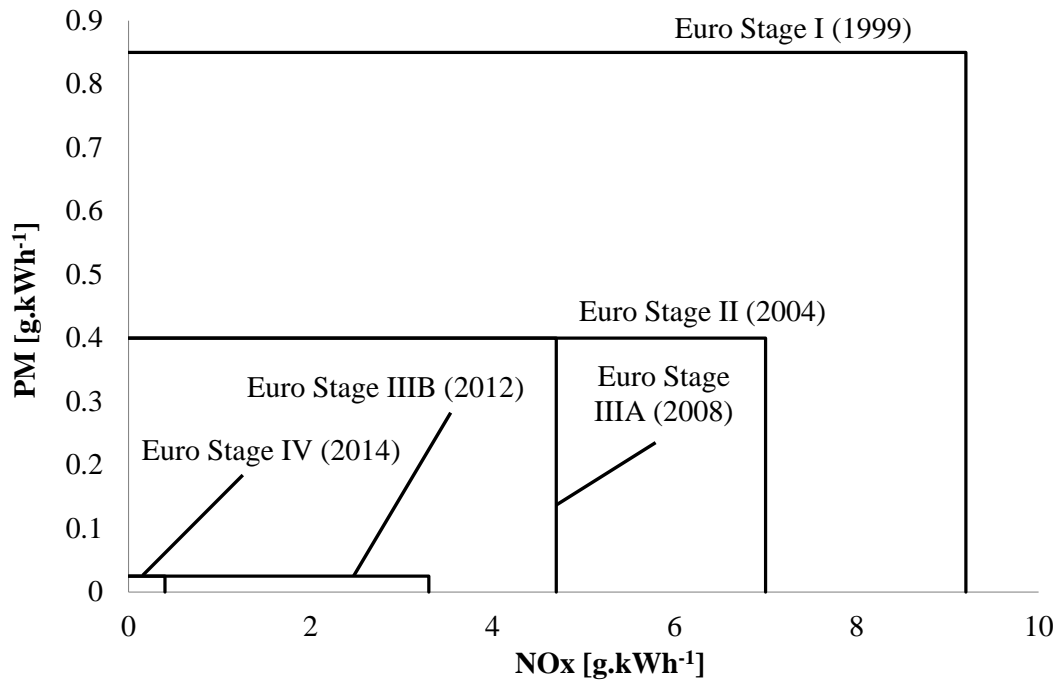
Figure 1.1 Evolution of EU PM and NO$_x$ emissions legislation for a 65 kW off-highway diesel engine. Data for Euro Stage I and Stage II from Dir 97/68/EC, amended by Dir 2002/88/EC. Data for Euro Stage III and Stage IV Dir from 97/68/EC amended by Dir 2004/26/EC, Dir 2006/105/EC and Dir 2010/26/EU

Within Europe PM and NO$_x$ emissions must be 96% lower in 2014 compared to acceptable levels for 1999. It is a huge engineering challenge to reach these targets with simultaneous improvements in fuel efficiency, performance and engine durability. To ease the global emissions challenge Tier 3/4 USA and Stage III/IV EU off-highway diesel regulations are aligned. Engine research motivated by meeting emissions legislation advances the understanding of both emissions generation and measurement.

PM is the most complex engine emission, consequently it is the only pollutant regulated by the EPA that is not chemically defined (Maricq, 2007). PM is classified as an aerosol of solid particles and liquid drops, it is separated into two categories:

coarse particles that are $2.5\,\mu m \geq d_p \leq 10\,\mu m$ and fine particles $d_p \leq 2.5\,\mu m$. Kittleson (1998) showed that the typical exhaust particle composition for a heavy-duty diesel engine is 41% carbon, 25% unburnt oil, 14% sulfate and water, 13% ash and 7% unburnt fuel. It was also shown that the levels of Soluble Organic Fractions (SOF) present in PM emissions originate from lubricant oil and are highest during light engine loads when the exhaust gas temperatures are low.

PM is currently legislated by mass per engine energy output (g.kW.hr^{-1}), the PM emissions are sampled from the engine via a precisely described test procedure (GPO, 2012). The emissions sample is diluted with air, condensed and collected on a filter medium that will remove 99.7% of particles $d_p \geq 0.3\,\mu m$, the change in filter mass during the test duration quantifies the PM emissions.

Coarse and particularly fine particles have detrimental health effects as their smaller diameter means that they are easily carried into the human respiratory tract, causing significant adverse health effects (Pope *et al.*, 1995). Although legislation has driven down PM emissions, studies have found that some low emissions diesel engines emit much higher number concentrations of nanoparticles than older designs (Bagley *et al.*, 1996; Hunter, 1997). The high number concentration of nanoparticles present in modern low emission engines may be caused by two mechanisms; formation of new particles by nucleation, and absorption onto the surface of existing particles. These processes will occur during cooling and dilution, transferring some of the SOF from the gas phase to the particle phase (Kittelson, 1998).

The majority of the nanoparticle mass emitted from engines is in the particle size range $50\,nm < d_p < 1\,\mu m$, but the majority of the particle number is in the particle size range $d_p < 50\,nm$ (Kittelson, 1998). It is extremely difficult to measure nanoparticles. Careful consideration must be given to sample extraction, transport and instrument dilution as small changes can have a noticeable effect on the results. The additional information gained from measuring the particles directly is invaluable, for this reason substantial effort has been focused on measuring PM in more detail (Maricq, 2007; Okada *et al.*, 2003). A further challenge exists in overcoming the difficulties of particle measurement with a standardised test across all possible engine variants (Kittelson *et al.*, 2002). Despite these factors on-highway

legislation currently regulates both PM mass and Particle Number (PN) (Glechaskel *et al.,* 2009). The legislating bodies recognise the importance of particle number as a means of characterising particulate emissions. Particle count legislation is provisionally set to be introduced to off-highway engines by the EPA in 2018.

1.4 Crankcase Emissions

Crankcase emissions contribute significantly to the mass and number of particulate matter emitted from an engine (Tatli and Clark, 2008; Zielinska *et al.*, 2008). Crankcase emissions are a mixture of combustion products, water vapour, fuel vapour, oil and soot. Considering the 2007 EPA off-highway heavy duty engine emission legislation, crankcase gases can contribute up to 120% of the total allowable PM emissions (Heckel *et al.*, 2006; Pardue, 2004).
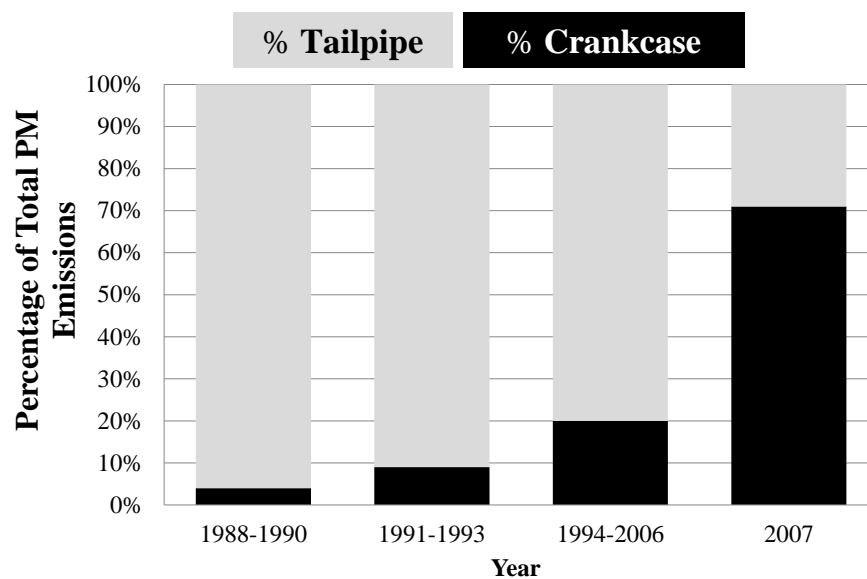
Figure 1.2 Crankcase emissions levels in diesel engines. Adapted from Donaldson (2008)

The influence of crankcase emissions on the total PM emission is shown in Figure 1.2. As legislated levels of PM have forced a reduction in tailpipe PM, the crankcase emissions contribute a greater percentage to the total PM emissions. Clark *et al.* (2006b) found that the engine lubricant oil contributed to approximately 50% of the PM emissions from the crankcase, the remaining 50% was associated with combustion emissions, wear and other sources. Zielinska *et al*. (2008) conducted a thorough chemical analysis of crankcase and tailpipe PM, they observed

higher emissions of engine oil from the crankcase than the tailpipe. This result highlights the additional affect that crankcase derived oil emissions have on the total PM emissions, and the requirement for better of understanding of their generation.

Crankcase particulate emissions can be characterised by particle size, to provide substantial information on behaviour and generation mechanisms. Studies have found particles ranging from 50 nm to 10 μm in diameter, (Jaroszczyk, 2006; Dollmeyer, 2007). When sampling crankcase emissions from a transient heavy duty diesel engine, Clark *et al.* (2006b) found a total particle number concentration in the order of 1×10^7 particles per m^3 with a mean particle diameter of approximately 70 nm.
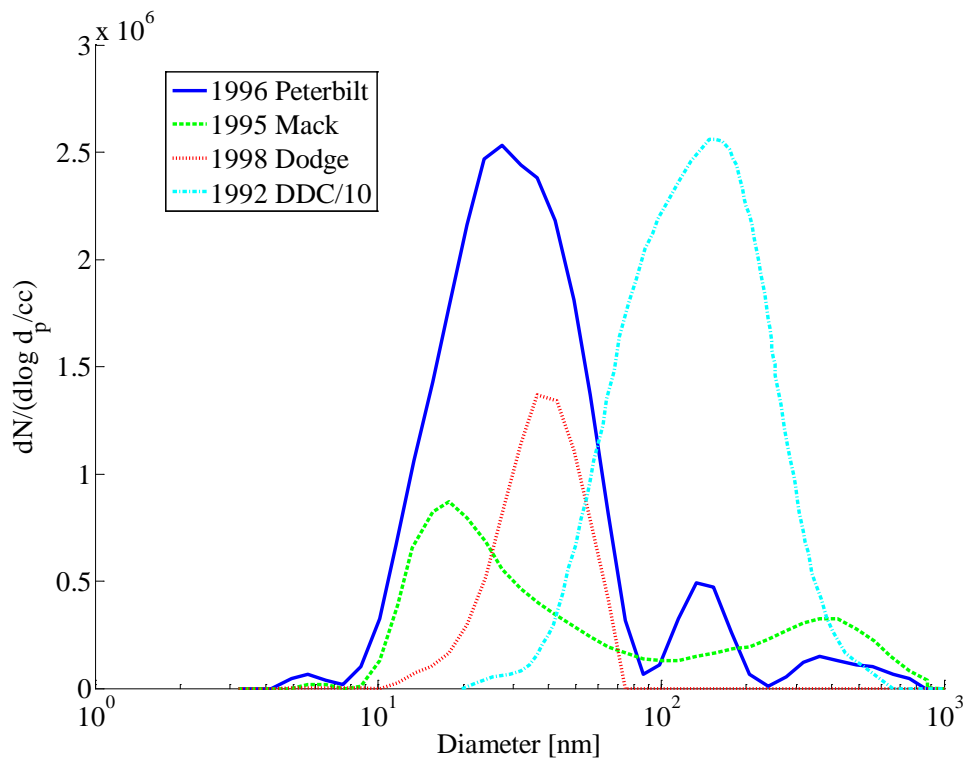
Figure 1.3 Hot idle particle size distributions from crankcase vents for four heavy duty diesel engines (Note the factor of 10 for the DDC engine). Adapted from Tatli and Clark (2008)

A study by Tatli and Clark (2008) measured the crankcase emissions from four heavy duty diesel engines as displayed in Figure 1.3. This work showed that when the engine temperature increased the bimodal number concentration of the aerosol decreased. Their study also highlighted that crankcase particulate size distribution and number concentration differ greatly between engines. The difference in their

results was attributed to the variation in crankcase ventilation designs and the sensitivity of aerosol formation. Particular mention was given to thermal effects, as temperature variations between the engines may have influenced drop formation substantially, altering the balance of drop evaporation and condensation. Kittelson (1998) concluded that the formation of nanoparticles is highly dependent on the amount of condensable species and the particle/drop surface for condensation and absorption.

The particle diameter in Figure 1.3 is shown against normalised number concentration, $dN/d\log D_p$, and for a given aerosol this enables the comparison of aerosol size distributions between different aerosol sizing instruments. Aerosol sizing instruments have a finite number of size bins, each size bin has a lower and upper particle diameter. The greater the number of size bins and the smaller the bin width, the better the instrument resolution. The normalised number concentration is simply dN the total number of particles, divided by $d\log D_p$, the change in the log of the particle size bin width. The parameter $d\log D_p$ is calculated by subtracting the log of the lower bin boundary ($d\log D_{p,l}$) from the log of the upper boundary ($d\log D_{p,u}$) for each bin. The full equation for particle number concentration is shown in Equation (1.1) (TSI, 2012).

$$\text{Particle Number Concentration} \quad dN/d\log D_p = \frac{dN}{d\log D_{p,u} - d\log D_{p,l}} \quad (1.1)$$

A range of studies have quantified crankcase PM emissions (RTI 2003; Farmer 2004; RTI 2005; Clark 2006b; RTI 2007; Schmeichel 2007; Tatli and Clark, 2008). However, as expected, there were contradictions across the range of engines tested illustrating the difficultly of accurate sampling measurement, the sensitivity to testing procedures and most importantly the requirement for better understanding of crankcase aerosol generation.

1.5   Crankcase Flow

Within an internal combustion engine there is a pressure difference between the combustion chamber and the crankcase. As the piston rings do not generate a complete seal, a gas flow known as blow-by is induced. Typically high cylinder pressure drives gas into the crankcase. However, there is the potential for reverse blow-by where crankcase gas is drawn into the combustion chamber. Both these effects are undesirable, hence substantial engineering resource is focussed on optimising piston ring design and minimising blow-by.
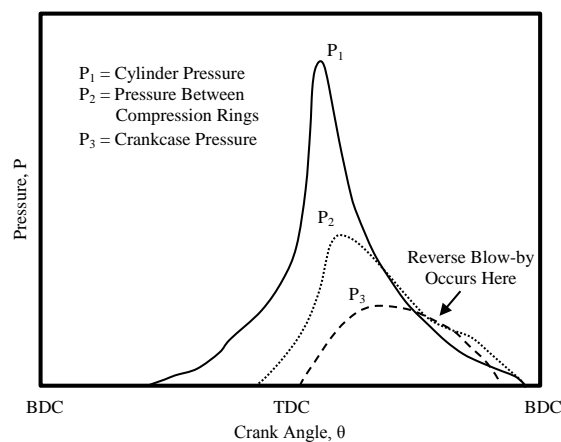
Figure 1.4 Pressure acting on a piston during compression and expansion. Adapted from Pulkrabek (2001)

Figure 1.4 illustrates the variation of cylinder and crankcase pressure for a four stroke cycle during compression and expansion. For the majority of the trace the crankcase pressure is lower than the cylinder pressure. Despite the piston ring pack pressure also being lower than the cylinder pressure, the piston rings must provide a sufficient seal to regulate the blow-by. The crankcase pressure peaks just after peak cylinder pressure, during the expansion stroke. Towards the end of the expansion stroke the exhaust valve opens and the cylinder pressure falls below the crankcase pressure generating the conditions for reverse blow-by. Blow-by generally increases with load as the cylinder pressure increases.
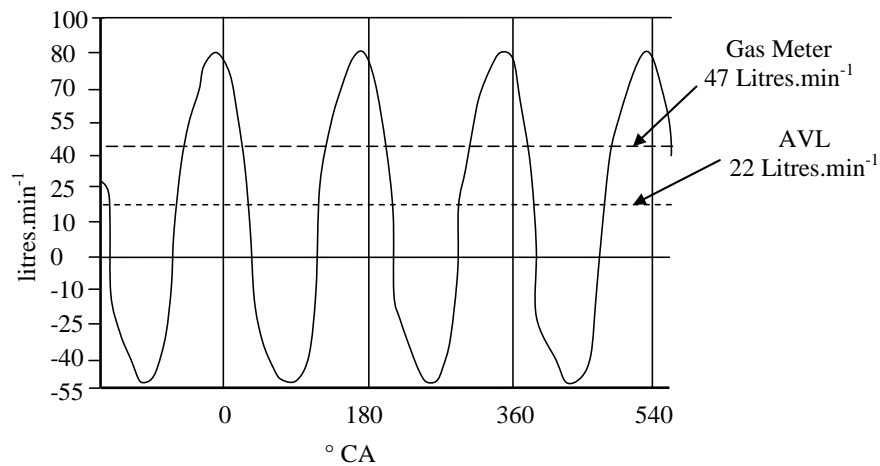
Figure 1.5 AVL blow-by meter trace for a 1.3 litre 4 Cyl SI engine. Adapted from Ebner and Jaschek (1998)

An oscillating blow-by flow is created by the pressure changes between the cylinder and the crankcase, an example blow-by trace is shown in Figure 1.5. The magnitude of reverse blow-by is lower than the main blow-by event and the mean volumetric blow-by flow rate is positive. The results from two different blow-by measurement instruments are shown by the dashed horizontal lines in Figure 1.5. The difference between the two mean flow rates illustrates the large levels of variability between different measurement techniques.
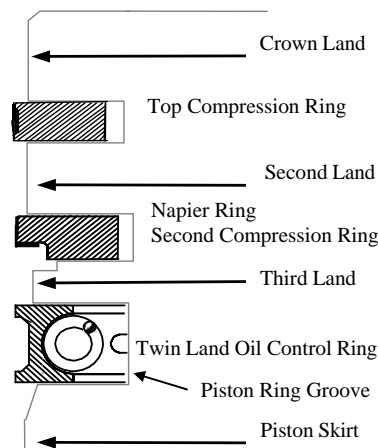
Figure 1.6 Piston Ring Pack Schematic. Adapted from Vokac and Tian (2004)

The piston ring pack commonly contains two compression rings and an oil control ring, as shown in Figure 1.6. The purpose of these rings is threefold: (i) to seal the gap between the piston and cylinder, retaining gas pressure and therefore improving indicated mean effective pressure (imep) (ii) to deliver lubricant to the cylinder liner

to reduce friction, under sustained high gas loads and high pistons speeds (iii) regulating piston temperatures by transferring heat to the cylinder liner. The most obvious blow-by leakage path is through the piston ring gap, which is present to enable installation of the piston rings. Gas will travel past both sides of the piston rings (Ebner and Jaschek, 1998).

Blow-by levels are a direct indicator of engine wear, they are used to measure engine quality and can provide a reliable indication of imminent engine damage. For a new engine there is an initial "run-in" period where blow-by rates are high. After the piston rings and cylinder liner are "worn-in", the blow-by rate stabilises for the majority of the engine life. Towards the end of an engine's life the blow-by rate increases again due to excessive wear between components (Gangopadhyay, 2000). Engineers strive to reduce the "run-in" period and maximise the stable engine life. Blow-by flow rates are not readily available in the public domain, however, generally the larger the engine volume the greater the blow-by flow rate. Manufacturers provide estimates of blow-by rates based on engine power ratings, (Caterpillar, 2000), but these vary between manufacturers and only provide an approximate measure of blow-by flow rate. Yilmaz, Tian, Wong and Heywood (2004) noted for a 4 cylinder SI engine that the volumetric blow-by rate decreased for increasing engine speed, they attributed this to the reduction in the time available for the gases to flow through the piston ring pack for one cycle. They found the greatest increase in blow-by rate between 0% and 100% load at 2000 rpm.

Blow-by, friction, component wear and oil consumption are directly influenced by the dynamic nature of the piston ring pack. A substantial body of research was conducted by Tian (2002) to model and experimentally validate the complex dynamic behaviour of the piston rings. A piston ring may lose radial and axial stability by two mechanisms, thus introducing new blow-by flow paths. Firstly under the influence of inertial force when there is insufficient gas pressure to hold the ring into the piston groove, the ring may flutter, altering the relative angle between the ring and groove. The second mechanism is known as radial ring collapse, where the ring is forced inwards by elevated pressure on the running surface of the ring and gas flows directly past the piston ring and cylinder liner. The effect of second

compression ring groove normalised axial clearance on overall blow-by, as modelled for a heavy duty diesel engine, is shown in Figure 1.7. These results serve to illustrate the strong and complex relationship between ring dynamics and blow-by (Tian, 2002).
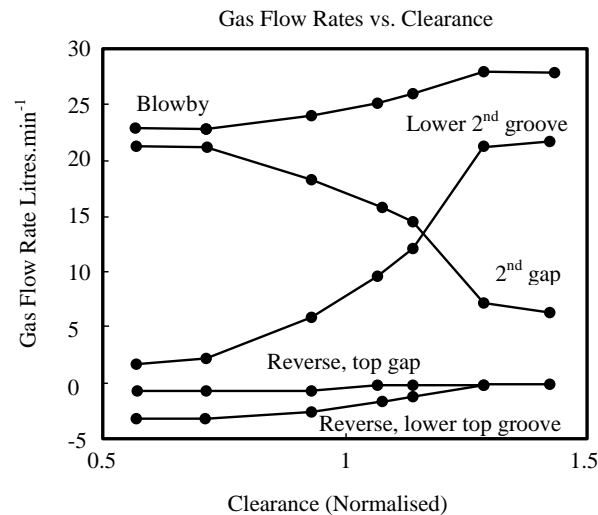
Figure 1.7 Effect of ring clearance on blow-by at 1200 rpm full load. Adapted from Tian (2002)

Usui, Murayama, Oogake and Yoshida (2008) confirmed the importance of piston ring side surface sealing on blow-by and oil consumption using an optically accessed cylinder liner. They improved the sealing ability of the piston ring pack and consequently reduced the blow-by rate by modifying the piston ring design.

Approximately 60% of the crankcase blow-by originates from the combustion process, the remaining 40% is generated by other sources (Avergard and Lindstorm, 2003). High cylinder pressures can generate gas flow past the valve stem seals. To minimise leakage, valve stem seals are carefully designed to meter oil flow, allowing some lubrication of the valve stem whilst restricting the gas flow into the combustion chamber. If valve stem seal blow-by is significant, ideal conditions exist for the generation of a two phase flow, as high velocity and high temperature gas will interact with the lubricated valve stem atomising the oil. Little information exists to validate and quantify this hypothesis as modern valve stem seals are extremely efficient. Typical oil leakage into the cylinder ranges from 0.0001 to 0.001 $g.h^{-1}$ per valve stem (SKF, 2006).

Leakage past turbocharger seals into oil galleries is recognised as a source of blow-by and a significant contributor to oil consumption. The primary function of turbocharger oil seals, is to prevent the egress of oil into the turbine or compressor. During operation there is a substantial pressure difference between the intake and exhaust system, and the turbocharger centre housing which is normally at crankcase pressure. The turbo charger oil seals are least effective at low rotational speeds when there is a high vacuum on the compressor inlet and low pressure at the turbocharger outlet. In this situation gas leaks past the oil seal into the oil circuit, increasing the blow-by and oil consumption (Payri, Galindo, Climent and Guardiola, 2005). The oil viscosity and feed pressure dramatically affect the oil consumption within the turbocharger, therefore these parameters need to be selected carefully to suit the specific engine requirements.
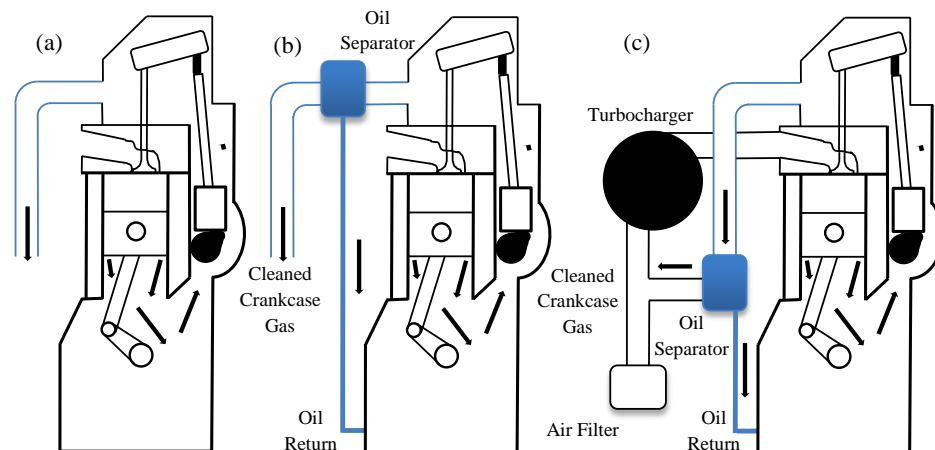
Figure 1.8 Crankcase ventilation systems (a) open unfiltered crankcase (b) open crankcase filtration system (c) closed crankcase ventilation. Adapted from Dieselnet (2010)

The increase in crankcase pressure generated by blow-by must be relieved, normally via a breather positioned in the rocker cover. There are two main approaches to crankcase ventilation as highlighted in Figure 1.8. Firstly, open crankcase ventilation (OCV), Figure 1.8 (a), where the crankcase is simply vented to atmosphere. OCV increases the total engine emissions and oil consumption. The alternative is closed crankcase ventilation, crankcase gases are re-circulated back into the engine intake. CCV is common on naturally aspirated (NA) spark ignited (SI) engines, however, on turbo charged (TC) engines there are significant fouling problems. Due to the high boost pressure on TC engines crankcase gases have to be introduced upstream of the

turbocharger compressor. Oil vapour and particulates from the crankcase foul intake components such as the compressor wheel and turbocharger back plate, reducing the engine efficiency (Gray, Irving and Locke, 2004). Furthermore for CCV systems, high PM from the crankcase present in the combustion emissions can poison exhaust catalysts.

For both crankcase ventilation strategies, filters and separators can be used to reduce emissions, fouling and oil consumption. A range of crankcase ventilation and filtration systems are displayed in Figure 1.8 (b) and (c). Dollmeyer *et al.* (2007) state that for a heavy duty diesel engine to meet EPA 2007 emissions regulation, a CCV system must be coupled with a > 98% efficient PM filtration system to protect turbocharger components, however, only > 90% filtration efficiency is required for OCV. Clearly the whole crankcase ventilation system needs to be carefully managed to suit the specific engine and its application.

1.6   Engine Lubrication

The main objectives of engine lubricating oil are to reduce friction, improve fuel economy and transfer heat. Additives are added to the oil to optimise its performance throughout the whole engine system. The additives are designed to reduce oil foaming and aeration, manage soot contamination and minimise poisoning of exhaust after treatment devices (Taylor *et al.*, 2005).

Engine oil is commonly lifted from a sump in the bottom of the engine, using a pump driven by the crankshaft, the oil is then cooled and filtered. Galleries in the engine block deliver oil to components, typically journal bearings in the crankshaft, camshaft and connecting rods, but also the rocker shaft, piston cooling jets and when appropriate the turbocharger shaft. A schematic of the lubrication circuit on a heavy duty diesel engine is shown in Appendix A Figure A-1.1. When the oil passes through cross drilling in the crankshaft the oil pressure must be sufficient to overcome the centripetal forces present and maintain a sufficient oil supply at the bearing (Maassen *et al.*, 1998). The timing gears and cylinder liner are commonly splash lubricated by the oil in the crankcase, (Mian, 1997). Reference is often made to splash lubrication of components by an oil mist or aerosol, however, there is little

information describing its generation. Furthermore, no information specifies how much oil aerosol lubrication is required. As previously highlighted, emission of the oil aerosol from the crankcase is problematic as it will increase the PM emission in an OCV system and cause fouling problems in a CCV system (Gray *et al.*, 2004). Reducing crankcase oil aerosol generation at source will dramatically reduce engine emissions, but the impact of this on the engine lubrication needs to be fully understood, there is it limited published research in both these areas.

Research has been conducted to measure the success of active vapour lubrication. Groeneweg *et al.* (1992), noted a 52% and 72% reduction in piston ring and cylinder liner wear coefficients when using vapour phase lubrication, compared to normal splash lubrication on a single cylinder diesel test engine. The oil vapour was introduced beneath the upper piston ring via the gap between the upper and lower piston rings. The oil vapour mixed with the blow-by gas and was carried out of the opposite side of the engine block, but high blow-by events resulted in intermittent lubricant delivery. Tests were not conclusive as the run-in wear coefficients on the vapour lubricated engine were two orders of magnitude greater than typical production diesel engine run-in wear coefficients. Lubricant delivery to the piston rings is complex, the full effects of any changes to the ring pack lubrication strategy must be tested thoroughly.

In high performance applications, where lateral forces are high and engine power is critical, dry sumps are used. Two oil pumps are required, the first pump scavenges from the small volume of oil stored in the bottom of the crankcase and pumps to a tall cylinder stored at the side of the engine. The second oil pump then draws from the cylinder and supplies the engine oil circuit. Dry sump oil systems prevent starvation of oil to the engine, but are more complex and expensive when compared to a simple wet sump system. Additionally, the scavenge pump has to transport both the oil and oil aerosol if there is no oil in the bottom of the engine. Two-phase pumping of the oil and the crankcase gas phases is extremely difficult, consequently phase separation including drop filtration is required.

1.6.1   Oil Cavitation

When a flow is subjected to pressures below the vapour pressure of the liquid, a two-phase mixture is formed by a process is known as cavitation. Work by Maassen *et al.* (1998) identified the problem of two phase aeration cavitation in journal bearings and oil galleries, where dissolved air is released in the oil due to the pressure decrease caused by centripetal forces. The sudden loss of pressure causes a change in the saturation state of the unsaturated oil. The oversaturated oil contains molecularly dissolved gas, which separates from the oil as small bubbles. Experimental work by Maassen *et al.* (1998) identified a minimum oil pressure, below which molecularly dissolved gas in the oil separated in the rotating big-end bearing bore and impeded the oil supply, generating a so called 'aeration-cavitation limit'. Clearly the oil film generation and collapse in journal bearings is very complex. Due to the durability demands placed on journal bearings, lubrication systems are designed to ensure there is always sufficient oil pressure at critical locations. Increasing the oil pump supply pressure increases the side flow out of the journal bearing, and as a result of this more oil is distributed over rotating components such as the crankshaft and thicker oil films are generated around the crankcase.

Stucke *et al.* (2009) also investigated the generation of two phase flows by cavitation within a journal bearing. They mathematically modelled the bearing to predict the onset of cavitation, the generation of vapour bubbles and formation of two-phase flow. Cavitation can lead to significant bearing wear as the bubbles collapse in the vicinity of the bearing wall. Damage is commonly found close to feed holes and other changes in geometry around the bearing where modelling assumption do not hold. A three-dimensional Computational Fluid Dynamics (CFD) model of the fluid film between a simple hydrodynamic rotating cylinder within a fixed outer cylinder was validated using Laser Dopper Velocimetry (LDV). Complex three-dimensional vortices were witnessed in experimental results but full computational modelling of the cavitation theory was not achieved.

1.6.2 Cylinder Liner Oil Films

The thickness of the oil film present on the cylinder liner is critical in reducing engine friction. Vaporisation of this oil film, due to high local gas and surface temperatures, reduces the film thickness and contributes to oil consumption and emissions. Phen *et al.* (1993) used laser induced fluorescence to experimentally measure the oil film thickness between the piston rings and cylinder liner on a single cylinder version of a Cummins L-10 diesel engine. They concluded that the oil film thickness increased with engine speed and an increased liner temperature resulted in a lower oil film thickness. Complex mathematical models have been developed to predict the oil film thickness around the piston ring pack, Audette and Wong (1999) developed a model to predict the oil vaporisation rate from the cylinder liner. They found that oil vaporisation is highly dependent on cylinder liner temperature, with a noticeable difference in steady state oil consumption over the length of the cylinder liner. Yilmaz, Tian, Wong and Heywood (2002) also found a linear relationship between oil consumption and coolant outlet temperature due to oil evaporation from the cylinder liner. Their experimental investigation was conducted under steady state speed and load for a 4 cylinder SI engine. They also found that reducing the oil volatility improved oil economy, notably at high engine loads.

1.6.3 Oil Consumption

Research by Yilmaz, Tian, Wong and Heywood (2004) identified that there are numerous contributors to oil consumption and there is a lack of oil consumption studies that connect comprehensive experiments with theoretical analysis. Their work identified five mechanisms of oil consumption, these were; oil thrown off the piston up into the combustion chamber, transport of oil suspended in the reverse blow-by flow up into the combustion chamber, oil entrainment into the crankcase blow-by, oil evaporation and valve guide leakage. Considering the oil entrainment into the crankcase, they initially reported that entrainment of oil occurs around the piston ring pack where gas velocities are very high, potentially reaching sonic values (Edelbauer, 2007). Oil entrainment through the blow-by leakage paths in the piston ring pack, as discussed in Section 1.5, is believed to be in the liquid and vapour form (Tian, 2002; Tian, Wong and Heywood, 1998; Tian, 1997). Assuming that ring

stability is maintained for most operating conditions, the ring gap gas flow is the main blow-by leakage path. It is believed that oil on the piston lands is dragged towards the ring gap, where it is atomised due to the high local velocity (Thirouard, 2001; Vokac and Tian 2004). Thirouard (2001) found that oil entrainment from the piston ring pack was affected by the oil distribution on the piston lands and the volumetric blow-by gas flow rate.

Yilmaz, Tian, Wong and Heywood (2004) indicate additional oil entrainment by oil splashing from moving parts and oil leakage from bearings and piston cooling jets. The significant gas velocities experienced within the crankcase may cause drop breakup, drop impingement onto dynamic surfaces could also cause further breakup. Condensation of oil vapour in cooler sections of the crankcase and associated ventilation systems will further increase the oil drop number concentration. Yilmaz, Tian, Wong and Heywood (2004) emphasised the complexity of drop generation in the crankcase, as oil entrainment in the crankcase gas varied with engine speed and load. Experimental studies conducted by Hill and Sytsma (1999) and Froelund (2000) provide further evidence that crankcase oil emissions contribute significantly to the total oil consumption.

Crankcase oil aerosol generation is an acknowledged contributor to engine emissions and oil consumption, but little information exists on the precise details of its generation. Mechanisms of oil drop generation and entrainment in blow-by gas are speculative. There is a distinct lack of robust experimental data on crankcase oil aerosol generation, information pertaining to the design of modern low emissions engines.

1.7   Research Overview

Recent advances in emissions legislation have forced engine manufacturers to quickly adopt complex and expensive crankcase filtration systems to remove suspended oil drops. There has been little experimental investigation focussed on explaining how these oil drops are generated. The work documented in this thesis describes a novel fundamental investigation into crankcase oil aerosol generation,

providing valuable data on drop generation mechanisms from a motored and fired compression ignition engine. The specific objectives of this research were:

(i)   To locate and evaluate sources of oil aerosol particles.

(ii)   To understand processes driving oil aerosol generation.

(iii)   To provide solutions to reduce oil aerosol generation.

(iv)   To provide solutions to control oil aerosol particles 5 nm – 20 μm in diameter.

(v)   In coordination with Industrial Power Systems Division (IPSD), the enterprise division of Caterpillar that manufactures engines and promotes these under the Caterpillar and Perkins brands, to investigate the feasibility of using Computational Fluid Dynamics (CFD) to predict crankcase oil aerosol generation.

1.8   Thesis Overview

Chapter 1 of this thesis introduces the requirement for a reduction in crankcase emissions from modern internal combustion engines. Understanding and controlling the generation of crankcase oil emissions is highlighted as a vital factor to aid the design of new engines that adhere to pertinent emissions legislation. The fundamental process of crankcase breathing on internal combustion engines is introduced and research on lubricating oil system performance is acknowledged.

Chapter 2 provides a summary of aerosol behaviour and experimental measurement techniques. The fundamentals of liquid atomisation and modelling, relevant to an engine crankcase are introduced. Published work on the characterisation and control of crankcase emissions is reviewed. Existing work emphasises areas lacking in understanding and demonstrates the requirement for experimental investigation.

Chapter 3 describes the design and implementation of a motored engine with a novel optically accessed crankcase. All major regions around the crankcase were studied experimentally using a range of optical diagnostics techniques. The imaging and illumination techniques are introduced within this chapter. The setup of a detailed particle sampling investigation on the motored and a fired engine is covered.

Chapter 4 presents the results from the optical investigation of the motored engine described in Chapter 3. The major mechanisms of oil atomisation within the crankcase are captured. Processing tools were developed to analyse optical data and provide novel qualitative and quantitative information on the oil distribution. The feasibility of using computational fluid dynamics to model and predict crankcase oil aerosol generation is investigated.

Chapter 5 documents a sampling investigation that measured particles 5 nm – 20 μm in the crankcase of a fired and motored compression ignition engine. Tests were completed at a range of engine test points. Analysis of the results provides novel insight and understanding into how crankcase vapours and nanoparticles are generated.

Chapter 6 focuses on the main mechanism of crankcase oil aerosol generation, oil atomisation from the crankshaft. The oil breakup and crankcase flow structure are examined around a rotating crankshaft within an optically accessed motored engine. This chapter describes the experimental setup and optical techniques including High Speed Digital Particle Image Velocimetry (HSDPIV). The results of a single phase Computational Fluid Dynamics (CFD) model are also presented. Finally the performance of a control strategy to regulate crankshaft oil atomisation is assessed experimentally.

Chapter 7 defines the main conclusions from this research. A review of strategies to regulate and control crankcase emissions within an engine is presented. Potential areas of further work are identified.

1.9   Contribution to Knowledge

The experimental and theoretical work documented in this thesis has made novel advances in the understanding and modelling of physical phenomenon, specifically aerosol generation and behaviour.

The crankcase of a motored compression ignition engine has been optically accessed for non-intrusive measurement of crankcase oil distribution, drop generation and atomisation. This experimental investigation has produced quantitative high

resolution images of the oil atomisation within an internal combustion engine crankcase, facilitating superior engine design for improved efficiency and lower emissions. The wealth of experimental data collected has been successfully employed to qualitatively assess the feasibility of using CFD to predict crankcase oil atomisation.

The crankcase particulate matter emissions from a fired and motored compression ignition engine have been quantified in the particle size range 5 nm – 20 μm, from 360 – 2200 rpm and 0 - 100% rated load. The evolution of the PM species has been assessed by measuring at a range of crankcase locations. This study has added to the limited information on crankcase PM emissions, by providing specific information on the lubricant oil contribution to crankcase emissions and given further insight into mechanisms generating submicron crankcase particulate matter emissions.

High speed imaging and High Speed Digital Particle Image Velocimetry (HSDPIV) of the oil breakup and air flow from an internal combustion engine crankshaft within an optically accessed production crankcase. The phenomenon of oil droplet generation from ligament breakup and transport has been captured, providing fundamental information on methods to improve engine emissions by design.

1.10 Publications Arising From This Work

JOHNSON, B.T., HARGRAVE, G.K., REID, B.A. AND PAGE. V.J. 2011 Crankcase Sampling of PM from a Fired and Motored Compression Ignition Engine SAE Conference Paper 2011-24-0209, *10th International Conference on Engines and Vehicles, Naples Italy 2011.*

JOHNSON, B.T., HARGRAVE, G.K., REID, B.A., PAGE. V.J. AND WAGSTAFF, S. 2012 Optical Analysis and Measurement of Crankcase Lubricant Oil Atomisation SAE Conference Paper 2011-24-0209, *10th SAE World Congress, Detroit USA 2012.*

CHAPTER 2

LITERATURE REVIEW

2.1 Introduction

This chapter provides a thorough explanation of the fundamental processes relevant to crankcase oil aerosol generation and behaviour. Particulate measurement and sampling techniques are reviewed and the range of oil aerosol filtration strategies adopted in industry have been evaluated in detail. The purpose of this literature review is to identify any deficiency in understanding and indicate areas that require experimental investigation.

2.2 Aerosols Fundamentals

Understanding the fundamentals of aerosol science provides valuable insight into the control of engine emissions. The simplest definition of an aerosol is the suspension of solid or liquid particles in a gas, for this reason aerosols are often referred to as suspended particulate matter. For theoretical analysis, particles are assumed to be spherical. For non-spherical particles, commonly solid particles, an equivalent diameter is used. A significant concentration of aerosol is present within the atmosphere, in some locations concentrations of 1×10^{14} particles per m^3 (Seinfeld, 2006). These suspended particles originate from natural sources such as volcanic ash and from anthropogenic activities, most noticeably combustion (Hinds, 1999).

Aerosols are grouped by their generation mechanism. Primary aerosols are introduced directly into the atmosphere, secondary aerosols contain particles chemically formed in the atmosphere. Further to this, aerosols are classified as; homogenous if they are composed of chemically identical particles, monodisperse, if they are composed of identical size particles, or as is most often the case, polydisperse, when they contain a range of particle sizes (Hinds, 1999). A microscopic analysis of individual particles, considering motion and impaction, facilitates a thorough understanding of aerosol behaviour. Particle diameter, d_p, is the single most important factor used to characterise aerosol behaviour, the most common unit is the micrometre (μm). Particle diameters can range from a few nanometres (nm) to 1000 μm. Aerosol generation from the combustion of organic fuels covers the majority of the aerosol particle size range.

There are numerous mechanisms that cause aerosol particles to change size and composition, these can be summarised as; evaporation, condensation of vapour species, coagulation with other particles and chemical reactions. Condensation of vapour onto particles, or evaporation from the aerosol to the gas phase, alters the particles diameter and the size distribution of the aerosol. Condensation and evaporation is discussed further in Section 2.7. Coagulation is when particles in an aerosol collide and due to the relative motion between them, adhere to each other forming a large particle (Hinds, 1999).

Generally particles $d_p \leq 1$ µm have atmospheric concentrations ranging from 0.01 to 1 particles per mm^3, particles over 1 µm in diameter are found in concentrations less than 0.001 particles per mm^3 (Seinfeld, 2006). Figure 2.1 illustrates the size range for a selection of aerosol groups, most importantly fine and coarse particles as there are significant differences in their generation, transformation and atmospheric removal.
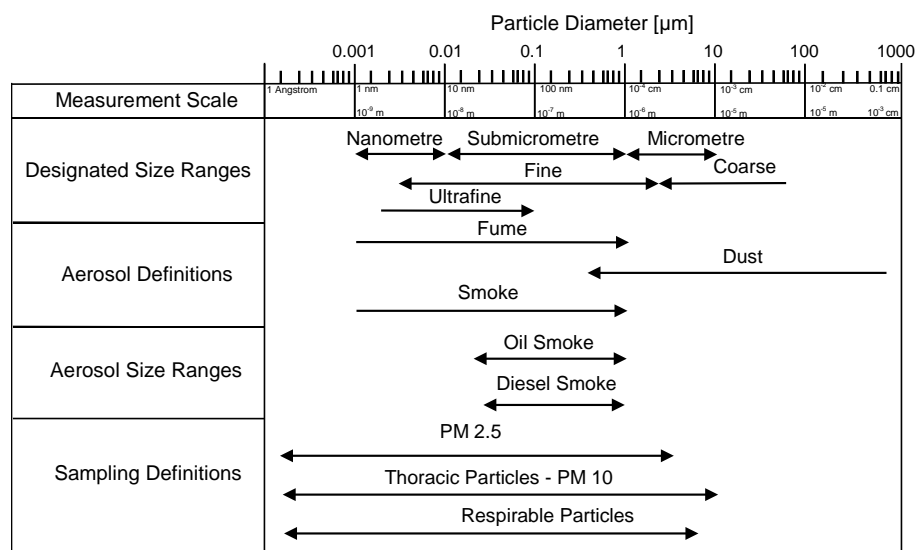
Figure 2.1 Aerosol particle size ranges and definitions. Adapted from Hinds (1999)

Aerosols can be further divided into different modes depending on the particle diameters. The nucleation mode (nuclei) $d_p = 5 - 100$ nm, primarily contains particles formed during combustion. For diesel combustion particulates the nucleation mode contains 0.1 - 10% of the particle mass and up to 90% of the particle number (Kittelson, Watts and Johnson, 2002). Condensation of hot vapours, as discussed further in Section 2.7, will generate nuclei. Due to their extremely small

size, the majority of the nuclei will coagulate with each other to form larger particles in the accumulation mode. The Aitken nuclei mode (Aitken, 1897) comprises of particles $10\,\text{nm} < d_p < 100\,\text{nm}$. The small particles in these first two modes have relatively short lifetimes and contribute only a few percent to the total airborne particle mass.

The majority of atmospheric aerosol surface area and mass lies in the accumulation mode $0.1\,\mu\text{m} < d_p < 2.5\,\mu\text{m}$. Particles in the accumulation mode are formed by coagulation of particles in the nuclei mode and condensation of vapour onto particles. The accumulation mode is where particle removal is most difficult, hence particles are said to accumulate in this mode. The nucleation and accumulation modes comprise the entire fine particle size range. Coarse particles $2.5\,\mu\text{m} < d_p < 10\,\mu\text{m}$, are usually formed by anthropogenic mechanical processes or natural dust, Due to their large particle diameter and associated sedimentation velocities, coarse particles settle in the atmosphere quickly (Seinfeld, 2006). Figure 2.2 illustrates an idealised distribution of atmospheric aerosol over the range of particle modes and the associated transformation mechanisms.

Figure 2.2 Schematic of the distribution of an atmospheric aerosol. Adapted from Whitby (1976)

The following properties provide further quantification and understanding of aerosol behaviour (Hinds, 1999). The aerodynamic diameter is the diameter of a water drop having the same aerodynamic properties a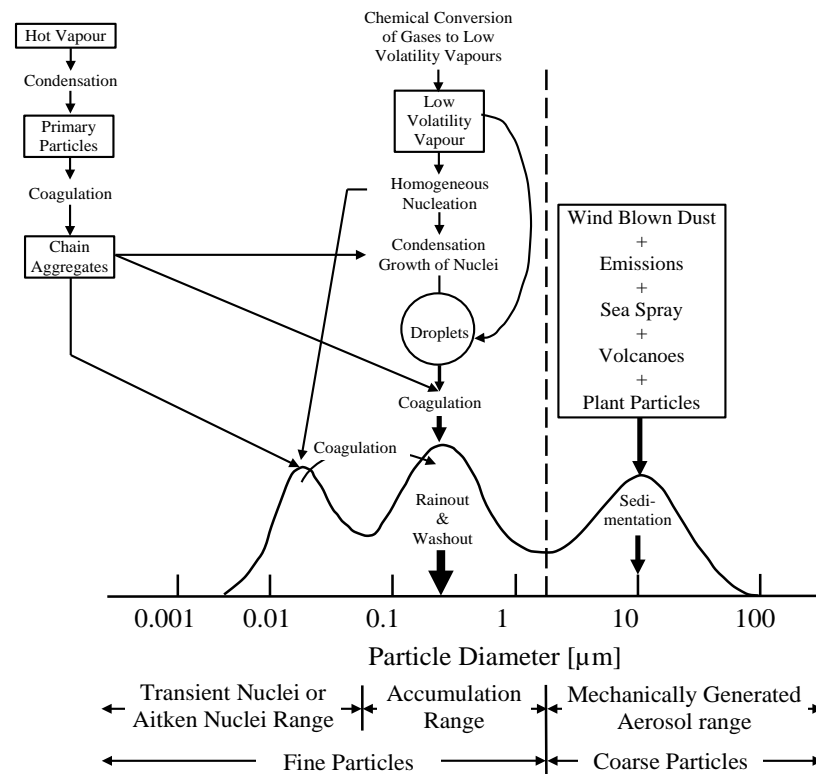s the measured particle, therefore aerodynamic diameter standardises for particle shape and density. The Sauter mean diameter (SMD) is the diameter of a drop whose surface-to-volume ratio is equal to that of all the drops in a particular aerosol or spray (Lefebvre, 1989). The mass median diameter is the diameter of a particle representing the median point of the total particle mass (Lefebvre, 1989). A particle that is released in a gas stream will quickly reach its terminal settling velocity, where the drag acting on the particle is equal and opposite to the force of gravity. For particles $d_p < 1.0\,\mu\text{m}$ a slip correction factor must be used to calculate the terminal settling velocity, as slip at the surface of the particles means that the particles settle faster than Stokes's Law predicts.

2.3   Lubrication Fundamentals

Oil is present in an engine primarily to reduce the friction between surfaces in relative motion. The two common lubrication schemes found in internal combustion engines are; hydrodynamic journal bearings, found in the crankshaft and camshaft and slider bearings, between the cylinder liner and piston rings. Oil is supplied to journal bearings to completely separate the bearing surfaces and reduce the friction between them. The bearing coefficient of friction is a measure of the tangential force acting on the bearing, it is related to the lubricant and metal surface properties. Journal bearings are designed to maintain a minimum oil film thickness of approximately $2\,\mu\text{m}$, to enable the bearing to sustain high loads without excessive friction or wear (Heywood, 1988). The total flow in a hydrodynamic bearing is caused by two components; one due to the velocity of the dynamic bearing surface, the Couette flow and one caused by the change in pressure distribution, the Poiseuille flow (Gohar and Rahnejat, 2008).

A narrow or finite length journal bearing is constantly supplied with oil as the supplied oil is lost out of the sides of the bearing. Oil must be delivered to the journal bearing at a sufficient pressure to maintain an oil film. Gohar and Rahnejat (2008) provide a detailed description of the side flow from hydrodynamic action in a journal bearing. The side leakage has two components; firstly the Poiseuille flow pressure

gradient and secondly the pressure from the oil supply. The Poiseuille flow is the difference in hydrodynamic flow at the start and finish of the pressure curve, across the bearing diameter, points A to F on Figure 2.3. Oil is supplied to the bearing at point A and is lost along the length of the bearing (L). Narrow bearing theory neglects the Poiseuille flow caused by the pressure gradient in the $\emptyset$ direction, when compared to the Couette term. Calculating the narrow bearing side leakage flow rate Q_s, over the pressurised region AF yields Equation (2.1), where R is the bearing radius, N is the rotational bearing speed, c is the radial bearing clearance and ε is the eccentricity ratio.
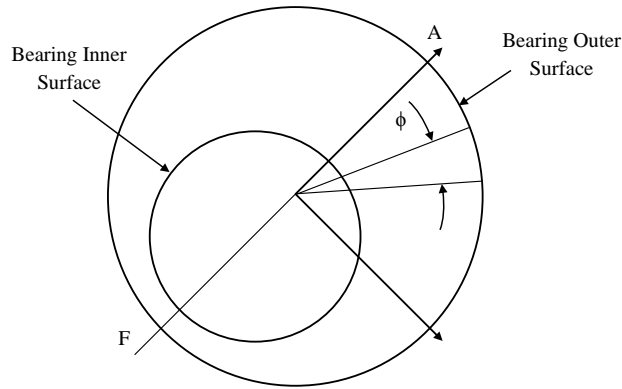
Figure 2.3 Forces on a journal bearings. Adapted from Gohar and Rahnejat (2008)

Narrow Bearing Side Leakage	$Q_s = (\pi RNLc)2\epsilon$	(2.1)
Side Flow Factor	$Q_s^* = Q_s(\pi RNLc)2\epsilon$	(2.2)
Narrow Bearing Side Flow Factor	$Q_s^* = 2\epsilon$	(2.3)

For finite length journal bearings, the term Q_s^* represents the side flow factor as used in Equation (2.2), which must be determined numerically. For a narrow bearing the side flow factor is simply calculated using Equation (2.3). In a 360° finite length bearing there is an approximately linear variation of Q_s^* with ε, but for 180° finite and narrow length bearings Q_s^* peaks near ε = 0.8 before reducing (Cameron, 1964).

The second component of side leakage is generated solely by the oil supply pressure. For a 360° journal bearing with a circular feed hole at the top of the bearing d_c is the diameter of the feed hole, h_f is the thickness of the oil film at the feed hole, p_0 is the maximum pressure and η_l is the oil dynamic viscosity. Assuming linear pressure loss across the bearing and that the leakage component in the y-direction occurs only at the supply hole, the total pump axial flow Q_a , can be calculated using Equation (2.4). Where Q_a^* is the side flow axial flow factor for a single feed hole and can be approximated using Equation (2.5) for a narrow bearing (Cameron, 1964).

Total Pump Axial Flow

$$Q_a = \left(\frac{d_c h_f^3 p_0}{12 \eta_l L}\right) Q_a^* \tag{2.4}$$

Side Flow Axial Flow Factor

$$Q_a^* \approx 1.2 + 11 \frac{d_c}{L} \tag{2.5}$$

The total flow the oil pump must deliver to the journal bearing (Q_P), or the total side flow out of the bearing, is the sum of the two flow components shown in Equations (2.1) and (2.4). For a fixed bearing geometry and supply hole diameter, an appropriate viscosity oil must be chosen to suit the bearing operating temperature and maximum pressure.

To tolerate vertical loads in both directions, journal bearings are often composed of two finite length 180° bearing shells joined at $\phi = \pi/2$ and $\phi = 3\pi/2$. Commonly there is also an oil feed at each bearing shell join, where the oil supply is divided equally between the two feed holes. The performance of this 180° bearing is very similar to that of a 360° bearing, however, its arrangement forces the majority of the pressure to occur in the bottom half of the bearing.

2.4   Atomisation and Aerosol Generation

Atomisation is the mechanism of generating small drops from a bulk liquid, it occurs when there is sufficient internal or external force to disrupt the liquid surface tension. Lefebvre (1989) gives an excellent description of drop atomisation, discussing the relevant research that has been conducted for over a century. To facilitate thorough experimental analysis and computational modelling of aerosol generation, it is important to understand the fundamentals of drop generation.

Liquid surface tension and viscosity are physical properties critical to atomisation. Without any disruptions, surface tension acts to form a sphere of minimum surface energy and viscosity provides stability opposing any changes to geometry. These physical properties are temperature dependent. The surface tension of SAE 15W-40 engine lubricant oil at 25°C is 0.035 N.m^{-1}, increasing the temperature reduces the oil surface tension. An approximation for the effect of temperature on the surface tension of SAE 15W-40 oil was calculated with reference to work by Ross (1950), the results are displayed in Appendix B Figure B-1.1. Viscosity has an even stronger thermal dependency, for the same temperature range the viscosity of SAE 15W40 oil reduces by 92%, further oil properties can be found in Appendix B Table B-1.1. The viscosity of a Newtonian fluid is specified either as dynamic or kinematic. Dynamic viscosity (η_l), is expressed in SI units of N.s.m^{-2}, kinematic viscosity v, is expressed in SI units of m^2.s^{-1}. The dynamic viscosity of a liquid in one-dimensional flow is the ratio of the shear stress acting on the liquid, to the velocity gradient acting across the liquid thickness, the shear strain rate. Kinematic viscosity is simply the ratio of dynamic viscosity and density (Gohar and Rahnejat, 2008).

For small drops 1 μm < d_p < 300 μm gravitational forces are negligible, however, aerodynamic forces are extremely significant. As aerodynamic pressure is applied to a drop deformation will occur modifying the pressure distribution around the drop. Equilibrium is only reached when the internal pressure (p_I) at any point over the whole drop surface is constant, this occurs when the aerodynamic pressure (p_A) is balanced against the surface tension pressure (p_σ), as shown in Equation (2.6). At a given temperature, surface tension and viscosity are constant, however, the surface

tension pressure is dependent not only on the surface tension (σ), but also on the drop diameter (d_p), see Equation (2.7).

Internal Pressure $\qquad\qquad p_I = p_A + p_\sigma = \text{constant}$ $\qquad$ (2.6)

Surface Tension
Pressure $\qquad\qquad\qquad p_\sigma = \dfrac{4\sigma}{d_p}$ $\qquad\qquad$ (2.7)

Atomisation occurs when the aerodynamic pressure is large enough, compared to the surface tension pressure, to deform the drop into a shape where the surface tension is too small to sustain the drop. The smaller the drop the higher the surface tension pressure, therefore for constant aerodynamic pressure, drop breakup occurs until the surface tension is sufficient to sustain the aerodynamic pressure acting at all points on the drop surface. Large drops formed during primary atomisation often breakup into smaller drops during secondary atomisation. The breakup time has been shown to increase for decreasing drop size, until a critical drop size with infinite breakup time is reached. The liquid viscosity acts to increase the breakup time when the aerodynamic force is sufficient to induce breakup. If the force declines before the breakup time has elapsed then breakup may not occur.

When the liquid viscosity is low, drop deformation is the ratio of aerodynamic forces and surface tension forces. The aerodynamic forces are related to the multiple of the gas density (ρ_A) and the square of the relative axial velocity between the gas and the drop (U_R), as shown fully in Equation (2.8). The surface tension force is controlled by the ratio of the drop surface tension (σ) and diameter (d_p). Combining these two forces forms the dimensionless aerodynamic Weber number, which is the ratio of aerodynamic forces to surface tension forces, as shown in Equation (2.9).

Aerodynamic Forces $\qquad\qquad\qquad 0.5\rho_A U_R^2$ $\qquad\qquad$ (2.8)

Aerodynamic Weber Number $\qquad\qquad We_{Aero} = \rho_A U_R^2 d_p / \sigma$ $\qquad$ (2.9)

A high Weber number indicates that the external aerodynamic forces are high compared to the surface tension forces, thus drop breakup is likely. For a given liquid there is a critical Weber number for drop breakup, when the aerodynamic drag equals the surface tension force, Equation (2.10). Rearranging Equation (2.10) shows that the critical aerodynamic Weber number ($We_{Aero,Crit}$), is the inverse of the drop drag coefficient (C_D), Equation (2.11). At the critical condition, Equation (2.11) can be rearranged to yield the maximum drop size and the critical relative velocity for drop breakup.

Condition of Breakup
$$C_D \frac{\pi d_p^2}{4} 0.5 \rho_a U_R^2 = \pi d_p \sigma \tag{2.10}$$

Critical Aerodynamic
Weber Number for
Low Re
$$We_{Aero,Crit} = \frac{8}{C_D} \tag{2.11}$$

Importantly, Hinze (1955) and Lane (1951) showed experimentally and theoretically that the mode of drop disintegration depends on its acceleration, either the drop is steadily accelerated, or rapidly accelerated in a high velocity stream. The drop acceleration controls the critical relative velocity ($U_{R,Crit}$), as a steadily accelerated drop has a higher critical Weber number than a rapidly accelerated drop. When investigating droplet distortion, Bond (1927) and Bond and Newton (1927) derived the dimensionless Bond Number. The Bond number, as shown in Equation (2.12), balances the surface tension force with a body force, the term g^* represents the acceleration due to body-force and ρ_l is the liquid density. In their experiments of drops falling under their own weight, g^* was the acceleration due to gravity, however, the relationship holds for higher values of g^*.

Bond Number
$$Bo = \frac{\rho_l g^* d_p^2/4}{\sigma} \tag{2.12}$$

Another important dimensionless fluid dynamic parameter is the Reynolds number, which is the ratio of inertial forces to viscous forces, as shown in Equation (2.13), where η is the dynamic viscosity. For a low Reynolds number flow around a drop, Stokes' law in Equation (2.14), can be used to define the drop drag coefficient as shown in Equation (2.15). For higher Reynolds numbers, viscous forces are significant, due to the formation of vortices and boundary layers. There have been numerous correction factors added to Stokes' law derived from the analysis of experimental data to calculate C_D, a list of approximations are given in Appendix C Table C-1.1. As highlighted previously, the drop viscosity will influence breakup. The Ohnesorge number (oh), Equation (2.16), gives a dimensionless ratio of internal viscosity force to interfacial surface tension force, accounting for the influence of liquid viscosity on breakup.

$$Reynolds\ Number \qquad Re = \frac{\rho U_R d_p}{\eta} \qquad (2.13)$$

$$Stokes'\ Law \qquad F_{Aero} = 3\pi d_p \eta_a U_R \qquad (2.14)$$

$$
\begin{array}{c}
Drag\ Coefficient \\
Re < 0.1
\end{array}
\qquad C_D = \frac{24}{Re} \qquad (2.15)
$$

$$Ohnesorge\ Number \qquad oh = \frac{\sqrt{We}}{Re} \qquad (2.16)$$

2.5   Jet and Ligament Breakup

A cylindrical body of liquid with minimal external forces acting on it will contain oscillations and perturbations, generated by the cohesive surface tension forces in the liquid opposing any disruptive forces. Ideally the oscillations are amplified to a magnitude sufficient to break the liquid body into drops and as discussed in Section 2.4, either the surface tension is sufficient to sustain the drop, or secondary breakup into smaller drops occurs. Rayleigh (1878) calculated that a nonviscous

liquid jet only affected by surface tension forces, will become unstable when the wavelength of any axisymmetrical disturbance is greater than the product of the jet diameter and π.

Lefebvre (1989) documents that studies of liquid jets have shown for a constant jet velocity, the jet length is directly proportional to its diameter. Similarly a cylinder of liquid is unstable if its length exceeds its perimeter. In this case two drops would be formed with a surface area less than that of the original cylinder, (Lefebvre, 1989).
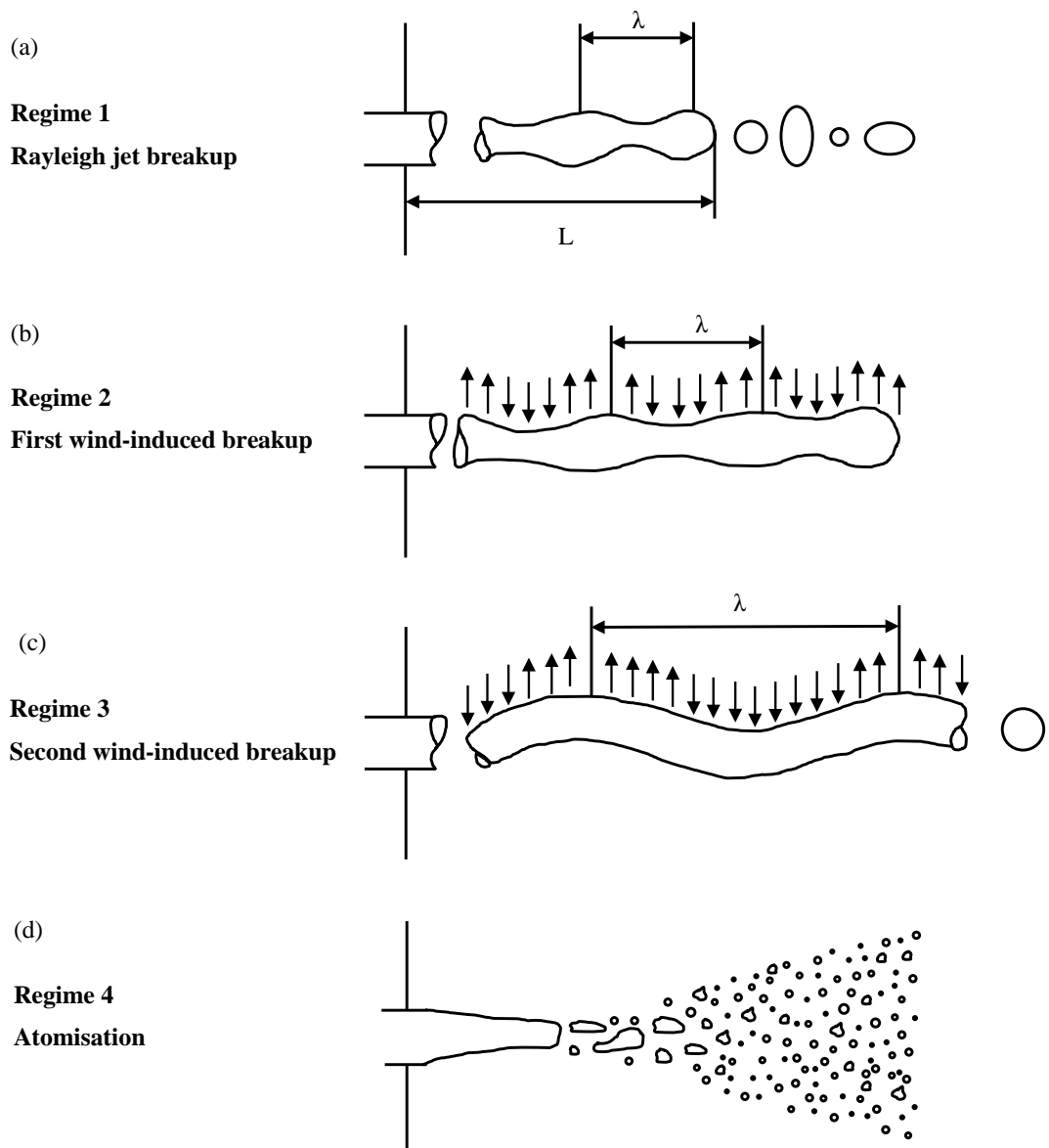
Figure 2.4 Mechanisms of jet breakup and drop formation. Adapted from Lefebvre (1989)

Sterling (1969) captured the fundamental steps of low velocity jet breakup and droplet generation using high speed photography. Images recorded the formation and growth of axisymmetrical disturbances, then the thinning and pinching of the liquid cylinder and finally breakup as a drop separated from the main liquid cylinder. Further breakup of the liquid occurs by the same mechanism, generating large drops surrounded by small "satellite" drops. Weber (1931) continued Rayleigh's work, investigating viscous fluids, he noted that the minimum wavelength of oscillations to cause jet breakup is the same for viscous and nonviscous liquids, but the optimum wavelength for drop formation is greater for viscous liquids. As discussed in Section 2.4, additional disturbing forces increase breakup and reduce the optimum wavelength for breakup. Aerodynamic forces above a threshold can directly induce waves on the liquid cylinder and reduce the distance to jet breakup. Increasing the jet velocity and therefore aerodynamic forces, causes the jet length to exhibit a wave profile. Any further increase in the jet velocity results in extremely complex jet atomisation. These four fundamental regimes of jet breakup are shown in Figure 2.4. The dimensionless Reynolds and Ohnesorge numbers introduced in Section 2.4, can be used to delineate between the four breakup regimes, using the Ohnesorge's chart shown in Figure 2.5. It is important to note that Figure 2.5 predicts jet breakup, therefore in Equations (2.9) and (2.13) the liquid oil density ρ_l, dynamic viscosity η_l and jet D_j or nozzle orifice diameter must be used.
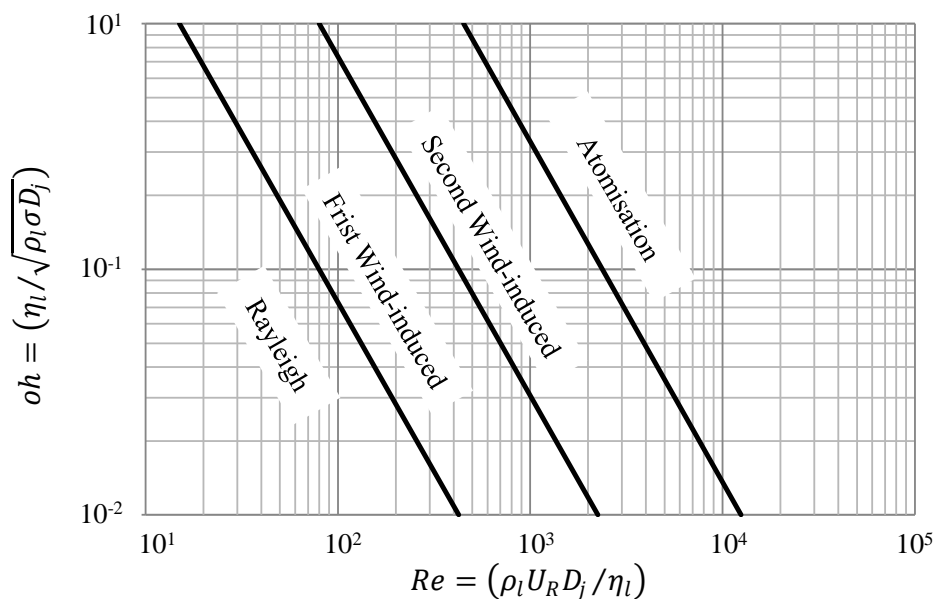

Figure 2.5 Ohnesorge's chart of modes of jet breakup. Adapted from Baumgarten (2006)

For a fixed nozzle and liquid, Ohnesorge's number is constant, therefore increasing the jet velocity will increase the Reynolds number, following a horizontal line through all the breakup regimes across Figure 2.5. Regime 1 contains Rayleigh jet breakup, axisymmetric oscillations in the jet are induced by surface tension in the liquid and the drops generated are larger than the jet diameter. In Regime 2, first wind-induced breakup, aerodynamic forces accelerate jet breakup, there is a static pressure distribution over the jet length. Drop diameters are approximately equal to the jet diameter and as with Regime 1 breakup occurs many jet diameters downstream of the nozzle. Second wind-induced breakup is associated with Regime 3, larger aerodynamic forces accelerate jet breakup by inducing short wavelength waves in the liquid jet. Final drop diameters are smaller than the jet diameter. Finally Regime 4 is full atomisation of the jet close to the nozzle exit, generating drop diameters significantly smaller than the jet diameter.

Despite numerous investigations, the mechanisms of liquid atomisation are still not fully understood, (Lin, 2003). This is attributed to the difficulty of experimentally capturing atomisation with high temporal and spatial resolution. Generating and validating computational atomisation models is extremely valuable, in the context of the automotive industry it provides critical information on spray development and drop generation enabling the enhancement of fuel and emissions systems.

Shinjo and Umemura (2010) successfully modelled the ligament and droplet formation from a liquid jet. For a liquid Re = 1470 and We = 14100 this required 6 billion grid points and a mesh resolution of 0.35 μm, to be resolved using a 13500 core supercomputer. Clearly computational investment on this scale is prohibitive, however, this study very successfully captures the fundamental dynamics of ligament and droplet formation at submicron resolution, reflecting the macroscopic behaviour of an entire jet. Ligament production and direction was strongly correlated with the local gas velocity and the presence of vortices. As expected the ligament or drop scale decreased for increasing Weber number. Interestingly the ligament breakup process for a high velocity jet was analogous to low velocity pinch-off jet breakup, as short capillary waves driven from the ligament tip dominated the jet breakup.

The computational mesh size was carefully controlled to achieve a compromise between spatial resolution and computational time, whilst managing the undesirable contribution of artificial drops. As an approximate rule the mesh sizes was at least one fifth of the expected drop diameter. Remembering fundamental theory, Shinjo and Umemura (2010) recognised that their computational results could be very quickly evaluated by inspecting for waves and oscillations over the ligament and drop surfaces, indicating the presence of local surface tension effects within the liquid.

It is important to remember, with reference to Figure 2.6, that surface tension generates capillary waves. Surface tension in the generating line of the ligament i.e along its length, acts to increase the neck radius and recover the ligament. The surface tension also works in the circumferential direction to reduce the neck radius and generate a drop. Initially surface tension causes the liquid tip to contract, pushing the centre of the ligament along the generating line and increasing the tip bulb pressure. Compression waves emanate and the neck length grows. The tip bulb absorbs liquid from the contraction and grows. The larger tip bulb has a lower internal pressure and therefore absorbs more liquid from the neck. The rarefaction wave process continues reducing the neck size until the circumferential surface tension is sufficient to break the neck.
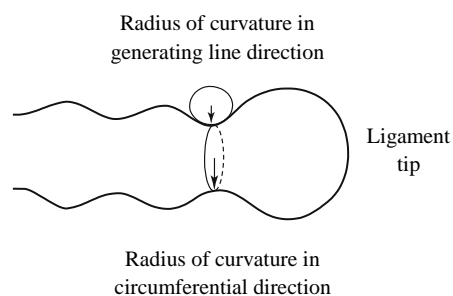
Figure 2.6 Liquid ligament. Adapted from Shinjo (2010)

Earlier work highlighted the crucial influence of propagating capillary waves on ligament breakup, (Umemura and Wakashima, 2002; Umemura, 2007a,b,c; Shinjo et al., 2009). This work identified two pinch-off modes, short wave and the previously discussed long-wave Rayleigh mode. The relevant mode is dependent on Weber number and Ohnesorge number. The short wave mode has also been referred to in

literature as end-pinching for Stokes Flows (Stone et al., 1986, Stone and Leal, 1989a,b; Stone, 1994). Umemura (2007a) showed that the pinch-off wavelength (λ) is close to the steady propagation wavelength, as shown in Equation (2.17) where a_L is the ligament radius.

Ligament Pinch-off
Wavelength

$$\lambda = \left(2\pi/\sqrt{3}\right)a_L \qquad (2.17)$$

The long-wave Rayleigh pinch-off mode is driven by short and fast capillary waves generated at the nozzle tip. Steady waves can also be naturally generated, resulting in destabilisation and pinch-off without the requirement for an injection nozzle. Both modes are shown computationally in Figure 2.7, they are very similar to the breakup regimes displayed in Figure 2.4. The computational modelling highlighted that the short-waves evolve slowly, with final pinch-off occurring at the ligament tip. Comparatively, when the ligament length is high long-waves are generated.
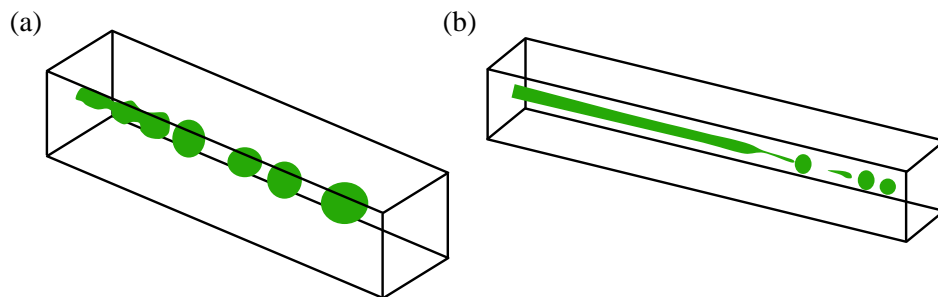
Figure 2.7 Ligament pinch-off modes We = 1.4 Oh = 0.076 (a) short-wave (b) long-wave. Adapted from Shinjo et al. (2009)

2.6 Rotary Atomisation

Liquid film flow over a rotating disc has a wide range of useful industrial applications, including uniform fine film coating and monodisperse drop generation. The rotating crankshaft and camshaft in an internal combustion engine behave in a manner analogous to a rotating disc, atomising the oil film present on their surface. Despite numerous uses, comprehensive and thorough understanding of the complex fluid mechanics of rotary atomisation is rare.

Hege (1964), Grave (1967) and Mehrhardt (1978) experimentally examined rotary oil atomisation, their work was referenced by Edelbauer, Kratochwill, Brenn and Tatschl (2009) and their discussion is summarised below. Hege (1964) evaluated the thickness of the oil film (*a*) on a rotating disc diameter D, by balancing the surface tension and centripetal forces, as shown in Equation (2.18), where ω is the disc angular velocity. Hege (1964) observed that the ligament regime was the most regular breakup regime and produced a very narrow size spectrum of drops. Hege (1964) also conducted a linear stability analysis of a liquid ring and derived an expression for the distance between ligaments l_{lig}, Equation (2.19), where η_l is the dynamic viscosity of the liquid.

Oil Film Thickness
$$a = \left(\frac{4\sigma}{D\rho_l\omega^2}\right)^{\frac{1}{2}}$$
(2.18)

Ligament Separation
$$l_{lig} = a\pi\left(2 + \frac{6\eta_l}{\sqrt{\sigma\rho_l a}}\right)^{\frac{1}{2}}$$
(2.19)

Grave (1967) and Mehrhardt (1978) compared different rotating atomiser disintegration regimes for varying disc diameters and oil volume flow rates. They recognised that drop formation could be categorised by the disc angular velocity ω and diameter *D*, the liquid volume flow rate $\dot{V}$, gravitational acceleration g and the liquid properties. From these parameters four dimensionless quantities can be defined: (i) disc Weber number, Equation (2.20), where the velocity and geometry are related to the rotating disc (ii) Ohnesorge Number, Equation (2.16) (iii) Volume Flow Rate Number $\dot{V}^*$, Equation (2.21) (iv) Fluid Number K_F, Equation (2.22). Dimensionless plots were divided into regions of drop, ligament, sheet and atomisation breakup regimes using data from the two investigations by Grave (1967) and Mehrhardt (1978), their results showed good agreement for defining the different breakup regimes.

Weber Number for a Rotating Disc	$$We = \frac{\omega^2 D^3 \rho_l}{\sigma}$$	(2.20)
Volume Flow Rate Number	$$\dot{V}^* = \frac{\dot{V}^2 \rho_l}{D^3 \sigma}$$	(2.21)
Fluid Number	$$K_F = \frac{\rho_l \sigma^3}{g^* \eta_l^4}$$	(2.22)

Sisoev, Matar and Lawrence (2003) and Matar, Sisoev and Lawrence (2008) have mathematically modelled the complex flow patterns present on the film of a rotating disc. During rotation the liquid film is subjected to centripetal forces which generate large amplitude non-linear waves on the liquid surface. The wave profile is controlled by the liquid flow rate and rotation speed. Inertia was found to be most significant near the liquid inlet whilst viscous forces are most important at the disc edge (Burns, Ramshaw and Jachuck, 2003).

Simpkins (1997) showed that the Bond number can be defined in terms of the disc diameter (D), where g^* is the acceleration due to centripetal force at an angular velocity (ω), Equation (2.23) and Equation (2.24) respectively. Simpkins (1997) compared a range of experimental studies analysing monodisperse drop generation and showed that for a range of liquid properties and aerosol generators, the Bond number as defined by Equation (2.23), was approximately constant. He illustrated that the dimensionless droplet diameter (d_p/D), can be represented by a simple universal law as shown in Equation (2.25). The surface tension and dynamic viscosity of the liquids examined ranged from 0.0315 - 465 N.m^{-1} and 1.0x10^{-3} - 1.5 kg.m^{-1}.s^{-1} respectively. For low temperatures, the physical properties of automotive lubricant oil would fall between these tested values. The drop diameter can be defined in terms of disc angular velocity directly, as shown in Equation (2.26). An empirical constant K is used in Equation (2.26), it ranged from 2.67 to 6.55. The constant K can also be defined in terms of Bond Number Equation (2.27).

Rotating Disk Bond Number	$$Bo_D = \frac{\rho_l g^* D^2}{4\sigma}$$	(2.23)
Acceleration due to Centripetal Force	$$g^* = \frac{1}{2}\omega^2 D$$	(2.24)
Universal Law of Dimensionless Droplet Diameter	$$(d_p/D) = 1.28 Bo_D^{-1/2}$$	(2.25)
Drop Diameter	$$d_p = \frac{K}{\omega}\left(\frac{\sigma}{\rho_l D}\right)^{\frac{1}{2}}$$	(2.26)
Drop Diameter Empirical Constant	$$K^2 = 8Bo$$	(2.27)

Sternowsky, Schulte, Guardani and Nascimento (2002) recognised the complexity of ligament breakup and drop generation from a rotary atomiser. They conducted an experimental parameter study of a simple rotating cylinder atomiser, their results were used to validate a Neural Network model to predict drop sizes. Images captured the ligament growth from the periphery of the disk, "instability waves" were seen to grow in the ligament before final disintegration. They witnessed that as the ligament moved away from the disk edge its diameter reduced, resulting in smaller drops at the point of breakup. For higher viscosity liquids they observed an increase in the breakup length, therefore a reduction in ligament diameter and final droplet diameter. Similarly for higher rotational velocities they noted more stretching of the ligaments, due to higher tangential and radial velocity components.

Begg, Sercey, Miche and Heikal (2010) experimentally recorded the oil drops thrown from an internal combustion engine crankshaft at rotational speeds up to 6000 rpm using non-intrusive laser optical diagnotics. They observed the formation of liquid

filaments and particles from the periphery of the crankshaft web. The trajectories of the atomised drops were very repeatable, three speed dependent breakup regimes were witnessed. The low speed regime, 1800 – 4200 rpm, contained long twisted ligaments ejected along involute-shaped paths. Between 4200 – 6000 rpm discrete particles were formed from the thinning and necking of the oil ligaments, subsequently at the highest speeds a fine aerosol of drops was seen. The rotational speed, crank angle and location affected the drop diameter, Phase Doppler Anemometry (PDA) captured drop diameters from 2 – 130 μm with a maximum velocity of 25 m.s^{-1}. In a similar manner to Simpkins (1997) they compared the dimensionless droplet diameter to the disk Bond Number. They found an approximate Bond Number of 2.21 and the empirical constant K ranging from 1.82 - 2.39, Equation (2.26). Importantly they noted the presence of two drop types that cannot be differentiated directly from their PDA results. Drops were generated by primary atomisation directly from the crankshaft edge, secondary breakup then generated smaller drops.

2.7   Oil Evaporation and Condensation

The high temperatures and large temperature variations present in an internal combustion engine crankcase provide ideal conditions for oil evaporation and vapour condensation. Hinds (1999) acknowledges the importance of condensation as the main mechanism of aerosol generation in nature and he gives a thorough description of particle generation by condensation. Initially it is important to define some useful quantities. The dew-point temperature, is the temperature at which condensation begins when a vapour is cooled at constant pressure (Cengel and Boles, 2002). The partial pressure (p) of a gas in a mixture of gases, denotes the volume fraction of that particular gas. The saturation vapour pressure (p_s) is the pressure, at a specified temperature, required to maintain mass equilibrium between a vapour and its condensate, either a liquid or solid. The ratio of these two pressures yields the saturation ratio, Equation (2.28). For a saturation ratio of unity the mixture is saturated, there is mass equilibrium at the liquid surface, when evaporation from the liquid equals condensation at its surface. When the saturation ratio is greater than

unity, the mixture is supersaturated. For a saturation ratio less than unity, the mixture is unsaturated.

Saturation Ratio $$S_R = \frac{p}{p_s}$$ (2.28)

The saturation vapour pressure is defined for a flat liquid surface, if the liquid is in a drop and has a curved surface, the partial pressure required to maintain mass equilibrium is much greater. Evaporation from a drop surface is much easier than for a flat liquid of the same surface area. The Kelvin ratio K_R, Equation (2.29), yields the saturation ratio required for drop equilibrium of a pure liquid, where p_d is the partial pressure of the vapour at the drop surface. For a prescribed saturation ratio, particles are stable only if their diameter is equal to the Kelvin drop diameter (d^*), given by Equation (2.30), where σ is the liquid surface tension, M is the molecular weight of the liquid, ρ_l is the liquid density, R is the gas constant and T_A is the gas temperature. If the drop saturation ratio is greater than the Kelvin ratio then the drop will grow by condensation. If the drop saturation ratio is smaller than the Kelvin ratio then the drop will evaporate. Similarly for a given saturation ratio, particles smaller than the Kelvin diameter will evaporate and larger particles will grow by condensation.

Kelvin Ratio $$K_R = \frac{p_d}{p_s}$$ (2.29)

Thomson-Gibbs Equation $$K_R = \exp\left(\frac{4\sigma M}{\rho_l R T_A d^*}\right)$$ (2.30)

There are several methods of particle condensation. Homogeneous nucleation is self-nucleation and it occurs without the aid of nuclei acting as sites for condensation. Particles are formed from a supersaturated vapour, when molecular clusters are generated by inter-molecular van der Waals forces. For a supersaturated vapour there are sufficient molecular clusters for them to collide and agglomerate to form particles bigger than d^*, at this point the particles becomes stable and will grow

by condensation. For a given temperature, condensation will occur on any particle that exceeds d^*, the rate of condensation is controlled by the saturation ratio, the particle size and the time between particle collisions.

Particles can also be formed by heterogeneous nucleation or nucleated condensation, as the name suggests nuclei or ions act as sites for vapour condensation. For this reason, heterogeneous nucleation occurs at much lower saturation ratios around 0.02, compared to homogenous nucleation which occurs at saturation ratios of 2 - 10. At a specified supersaturation level an insoluble nucleus with a wettable surface will absorb vapour molecules onto its surface. Again once the nucleus diameter is greater than d^* it will behave like a drop and grow by condensation.

Bulk liquid evaporation and drop evaporation are of concern when considering crankcase emissions. Drop evaporation occurs when conduction and convection transfer sufficient heat from the surrounding gas to the drop surface. The resulting vapour is convected and diffused back into the gas stream (Lefebvre, 1989). The vapour generated at the drop surface impedes heat transfer to the drop, making drop evaporation very difficult to model. The physical parameters critical to drop evaporation are temperature, liquid volatility, drop diameter and relative drop velocity. As the surface of a drop evaporates the drop losses mass by vapourisation and diffusion to the surrounding air. Throughout this process the drop diameter and velocity will change, altering the drop Reynolds number and consequently adjusting the rates of heat and mass transfer around the drop. Larger drops take longer to evaporate and follow a different path to smaller drops since aerodynamic drag is more influential. Drop evaporation is extremely complex, particularly for multi-component liquids such as oil that contain a variety of different volatility components.

2.8   Oil Aeration

The aeration of lubricant oil within an internal combustion engine can severely impact the performance of the lubrication system. Nemoto *et al*. (1997) investigated the effect of entrained air on engine reliability. They saw foaming on the sump oil surface, but only at low engine speeds. At high engine speeds and high oil

temperatures they found more entrained air bubbles. Nemoto *et al.* (1997) noted the influence of oil formulation on aeration and concluded that bearing reliability could be improved by controlling the oil formulation. Lubricant oil manufactures have taken significant steps to reduce oil aeration by using anti-foaming additives.

High speed imaging in the sump of a SI V6 engine captured oil drops flung from the crankshaft counterweight, impacting on the surface of oil in the sump (Manz, Cowart and Cheng, 2004). Above a specific engine speed, foam was generated on the surface of the sump oil. Foam formation only occurred when the sump windage trays were in place. When the Windage tray was not used, additional oil drops thrown from the crankshaft were able to pierce the air bubbles rising to the surface of the sump oil. This result supports the work by Nemoto *et al.* (1997) and suggests a complex balance between air bubble formation and destruction.

Baran and Cheng (2007) also acknowledge the generation of oil drops from a rotating crankshaft. Their experimental investigation concluded that the interaction of oil drops spun from the crankshaft and crankcase gas, were not major contributors to aeration at the oil pump inlet.

Oil aeration continues to be a significant problem, for this reason Takahashi *et al.* (2008) developed a model for predicting aeration rate, by evaluating bubble number and size from a series of windows positioned in the oil circuit of a SI V6 engine. Viewing windows were installed to examine the oil aeration around the timing gear, crankshaft, pistons and the valve train. Their results provided experimental evidence that the aeration rate varies with engine speed, but did not capture the aeration process itself.

2.9   Modelling Crankcase Flow

The pressure differentials generated by the crankcase flow, covered in Section 1.4, can have a negative impact on both emissions and engine pumping. A significant body of novel computational work has been conducted by Edelbauer (2007), Edelbauer, Kratochwill, Brenn and Tatschl (2009), Edelbauer, Diemath, Kratochwill and Brenn (2010), who numerically simulated lubricant oil and air flows in an internal combustion engine crankcase. Edelbauer (2007) commented that oil

disintegration at the crankshaft and oil atomisation around the piston rings, are the major sources of oil drops. He acknowledged the contribution of oil vapour condensation to drop formation, but over the model time scale of a few engine cycles, it was considered negligible.

The blow-by gas flow and oil disintegration at the crankshaft were modelled separately. The blow-by flow was simulated with just dynamic pistons and no crankshaft or connecting rods, enclosed by a simple crankcase geometry. The oil disintegration was simulated with a piston and crankshaft. The AVL (2006) computational fluid dynamics code FIRE$^{\text{TM}}$ was used to model the two-phase flow with a Euler-Eulerian framework, to minimise the computational demand compared to a Euler-Lagrangian Discrete Droplet Method. Additional transport equations were combined to evaluate the moments of the drop size spectrum and enable simulation of a drop laden flow. The oil film thickness and breakup regimes were based on a series of criteria, including dimensionless numbers, determined from previous experimental studies of rotary atomisers as discussed in Section 2.6. The simulations show that blow-by generates small diameter drops 1 - 3 μm, whilst the crankshaft generated larger drops.

In later work Edelbauer, Diemath, Kratochwill and Brenn (2010) generated a single phase model of the ventilation losses around a rotating crankshaft web and a linear piston motion for one engine cycle. The blow-by flow was modelled using a separate labyrinth model. They coupled the crankshaft and piston motion to resolve the motion of the connecting rod, within an enclosed simple crankcase geometry. Their mesh and simulations were completed using AVL List GmbH (2008a; 2008b) computational fluid dynamics code FIRE$^{\text{TM}}$. Their results were not experimentally validated but showed that at high engine speeds the windage losses within the crankcase can consume considerable power. Although their work was complex Edelbauer, Diemath, Kratochwill and Brenn (2010) concluded the requirement for extending their work to simulate two-phase flows and full crankcase breather systems over several engine cycles. Adding this level of complexity to the computational model would increase the computational demand dramatically.

2.10 Aerosol Measurement

Particles and drops are present in an aerosol with a range of diameters, speeds and number concentrations, making aerosol measurement extremely difficult. Prior knowledge of the aerosol characteristics is beneficial for aerosol measurement, as valuable results are reliant on selecting appropriate equipment, with an associated appreciation of the measurement limits. Aerosol measurement is an evolving science where critical appraisal of techniques and results are actively encouraged. There are three categories of aerosol particle size measurement, mechanical, electrical and optical (Lefebvre, 1989). Errors in all methods of drop size measurement can be caused by incorrect sample size, drop saturation, drop evaporation, drop coalescence and sampling location. Drop evaporation and condensation can significantly affect drop measurement, however, it is difficult to control these phenomena. For a mono-disperse spray, evaporation always reduces the mean drop size, but evaporation of a spray containing a wide range of drop sizes may increase the mass median diameter (MMD) (Lefebvre, 1989). Drop coalescence, as the result of a collision between drops, can also alter drop size and concentration. Lefebvre (1989) identifies the following factors to consider when measuring aerosol particle size:

1. The drop/particle generation process should not be disturbed by the measurement. When intrusive measurements are taken, size bias can occur, small drops commonly follow streamlines whereas large drops migrate across streamlines.
2. The sampling location is critical to aerosol measurement, depending on the generation mechanism, the drop diameter may change across the aerosol area.
3. Have a suitable dynamic size range for the application, as a minimum, 10 times the expected nominal drop diameter.
4. Measure both temporal and spatial resolutions. Spatial sampling measures a sample volume over a small period of time, where the contents of the volume can be assumed constant. Temporal sampling measures the drops that pass through a fixed volume over a period of time

5. Have the ability to provide a large sample, containing at least 5000 drops. The larger the sample the more confidence in the measurement (Bowen and Davies 1951).

6. Avoid drop saturation, if the sample is too large this will cause significant error due to overlapping drops.

7. Sufficient tolerance to variations in aerosol properties, both the gas and suspended particles.

8. Have a rapid means of sampling and counting, to measure every drop passing through the measurement volume. Data acquisition and processing should display promptly a drop size distribution histogram, mean diameters and standard deviations.

A range of aerosol measurement equipment is used in the automotive industry to measure and characterise engine emissions. The Cambustion DMS500 or Differential Mobility Spectrometer (DMS) is commonly used for automotive PM measurement (Reavell *et al.*, 2002a; Reavell *et al.*, 2002b; Collings *et al.*, 2003). Price *et al.* (2006) measured the exhaust PM emissions from a Direct Injection Spark Ignition (DISI) engine tailpipe using a DMS500, Dekati Electrical Low Pressure Impactor (ELPI), TSI Condensation Particle Counter (CPC) and AVL Photo-Acoustic Soot Sensor (PASS) and compared the results. Qualitative agreement was generally found across all measurement types, with less variation in PM mass measurement than for PN. The measurements principals of a range of aerosol measurement instruments, including sample dilution, are discussed in detail below.

TSI^{TM} Model 3321 Aerodynamic Particle Sizer$^{®}$ (APS)

The APS has an actual measurement range 0.5 µm–20 µm**,** it uses a time of particle flight measurement to indicate aerodynamic particle size, (TSI, 2010). The aerosol flow is accelerated through a converging nozzle, two focussed beams from a collimated 30 mW diode laser are positioned at the nozzle exit, a known distance apart. The particles passing through the laser beams produce two pulses of scattered light which is collected by a photo multiplier. The average velocity of the particle can then be evaluated. Larger particles are accelerated slower in the nozzle and lag behind the accelerating air flow. With calibration the aerodynamic diameter is

interpreted from the particle lag. Smaller particles, $d_p < 0.5\,\mu m$, are not measured as they do not lag the accelerating nozzle flow and therefore there is no second pulse of scattered light. There is a maximum interval between the two scattered light pulses, larger particles that substantially lag the accelerating nozzle flow are not recorded. The APS also detects the scattered light intensity for reference, although this is not used in the calculation of aerodynamic diameter.

The APS sample is diluted using a closed system aerosol diluter in increments of 20:1 or 100:1. A small sample of the aerosol is diluted with filtered air from the original sample to maintain the sample elemental composition, temperature and relative humidity, no power or compressed air is required. The sample flow rate is evaluated by measuring the pressure drop across a laminar-flow capillary tube. The sample used for dilution is forced through a 90° bend and two HEPA filters to remove particles. The clean gas is reunited with the sample flow through a multi-hole mixing cone. The range of hole diameters in the mixing cone generate turbulence to improve the mixing and ensures the flow is fully mixed before it enters the APS. Pressure gauges are used to monitor the aerosol path and total path flow rates. A valve on the filter side of the diluter can be used to adjust the pressure drop to match calibrated values.

Cambustion DMS500 MkII Fast Particulate Spectrometer (DMS500)

The DMS500 has an actual measurement range 5 nm - 1 µm, it has an integrated two-stage dilution system. Primary dilution occurs at the sampling point in a heated line at 90°C, where compressed air is passed through a HEPA filter and then used to dilute the sample. Secondary dilution is applied using a rotating disc diluter. Both dilution strategies are shown in the schematic in Figure 2.8.

The aerosol of particles enters a cyclone which removes particles above the maximum measureable size, the remaining particles are electrically charged by collisions with air ions, this is known as diffusion charging. The charged particles enter a classification column and are subjected to a radial electrical field, the particles will be repelled off according to their electrical charge. A series of electrometer rings along the column measure the electrical current from the arrival of

charged particles and therefore their mobility. Electrical mobility is a measure of the ease with which a charged particle is deflected by an electrical field and is a function of both the charge on the particle and its aerodynamic drag. Both of these parameters are a function of the particle diameter, therefore the particles electrical mobility enables calculation of the particle diameter. The DMS500 is capable of resolving PM size distribution and number concentration with a time response of 200 ms.
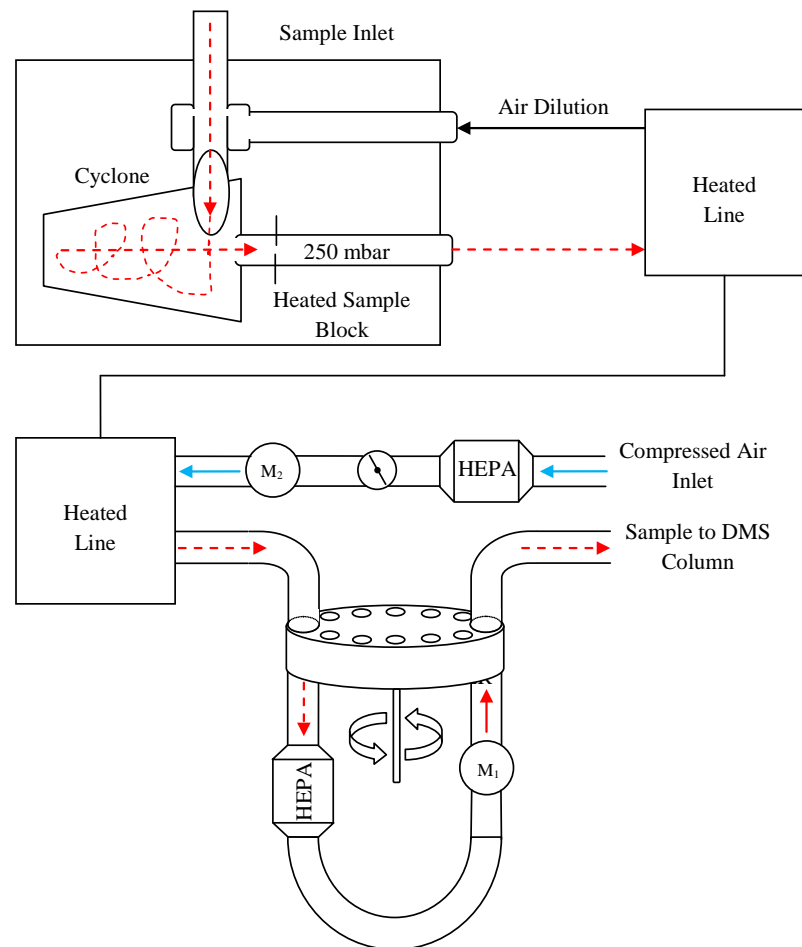

Figure 2.8 DMS500 sample dilution. Adapted from (Cambustion, 2010)

TSI^{TM} Scanning Mobility Particle Sizer^{TM} (SMPS)

The SMPS has an actual measurement range 15 nm – 660 nm, it works in a similar manner to the DMS500. Aerodynamic particles are charged by a bipolar ion neutralizer, they then enter a Differential Mobility Analyzer (DMA) which separates the particles according to their electrical mobility (TSI, 2005). The SMPS takes around 30 seconds to evaluate each particle size bin, the voltage of the DMA

electrodes are adjusted over the measurable particle size range for each size bin. For each size bin, only particles within a narrow range of electrical mobility can pass out of the DMA where they are then counted by a Condensation Particle Counter (CPC) to classify the particle concentration.

AVL Photo-Acoustic Soot Sensor (PASS)

Black carbon mass is measured by irradiating soot in a dilute sample with near infra-red light, the resulting resonance amplified standing acoustic wave is detected with a microphone, (Schindler *et al,*. 2004) (Haisch and Niessner, 2002).

Condensation Particle Counter (CPC)

Particle number concentration in a dilute sample is measured by optical detection, once the particles have been grown to a sufficient size. All particles serve as nucleation sites for condensation of super-saturated 1-butanol vapour and are grown and counted regardless of their composition (Price *et al.*, 2006).

Dekati Electrical Low Pressure Impactor (ELPI)

The ELPI measures particle size 6 nm – 10 μm and number concentration. Different size particles are classified according to their inertia within a cascade impactor. In a similar manner to the DMS500, particle number concentration is determined by the current flowing through the electrometers, (Dekati, 2010).

Phase Doppler Anemometry (PDA)

PDA is a reliable optical technique and with two or more detectors is capable of measuring three components of particle velocity, particle size 1 μm – 5 mm, mass flux and particle number concentration. However, spherical particles within a homogenous medium are required. The particles within the flow are directed into a control volume where two laser beams intersect generating a uniform interference fringe pattern. Particles passing through the fringe pattern scatter the incident laser light that is moderated at a frequency proportional to the particle velocity. Two off-axis detectors receive the signal, the phase difference between the two detector signals is proportional to the particle diameter.

2.11 Aerosol Filtration

Aerosol filtration can be traced back to 1850 when Stokes' law was first defined (Spurny, 1997). The current crankcase emissions legislation demands highly efficient filtration of suspended oil particles. Coupled with the filtration demand is the requirement to reduce oil consumption, therefore filtered oil must be returned back to the crankcase. Off highway crankcase filtration systems should have long service intervals, typically 1000 hours or ideally last the life of the engine. It is difficult to quantify the filtration requirement as this depends on the crankcase ventilation system. Dollmeyer *et al.* (2007) stated for a heavy duty diesel engine to meet EPA 2007 emissions regulation, a CCV system must be coupled with a $> 98\%$ efficient PM filtration system to protect turbocharger components, however, only a $> 90\%$ filtration efficiency is required for OCV.

Impaction/baffle separators are widely used to remove oil drops. In an impaction separator the aerosol is directed through a rapid change in geometry, the inertia of the oil drops prevents them from following the flow, therefore they impact onto a surface and are separated from the flow. The oil drops agglomerate on a catch plate and are drained to the engine sump. The flow can be accelerated using careful nozzle design to improve the removal of oil drops, however, this increases the back pressure on the crankcase. Long *et al.* (2009) thoroughly describe the experimental optimisation of an oil impactor. Care must to taken with impaction separators, although drop removal can be effective, the filter can also function as an atomiser if the liquid is not drained away correctly.

Until the 1990s, baffle separators were used to filter flows, in the early 21st century when the emissions standards were more demanding, cyclone separation became increasingly common. Cyclones utilise a nozzle to accelerate the flow around a cylindrical separator body, the centripetal force on the flow causes the heavy drops in the flow to be forced outwards and impact on the walls of the separator. The oil then drains out of the separator whilst the filtered gas exits through the centre of the separator. Multiple cyclones can be designed in parallel to improve the filter efficiency. Cyclone separators have a low flow restriction but are not effective

throughout the whole particle size range present in crankcase emissions, particularly for drops $d_p < 0.4$ µm which are not filtered.

Candy and Guerbe (2009) investigated the performance of a coalescing separator for crankcase emissions control, as they highlighted that cyclone separators were not efficient enough. Coalescing separators are becoming popular due to their ability to remove small drops. Commonly a fibrous medium captures impacted oil drops, which then agglomerate and drain off the medium by the action of gravity. These systems have high filtration efficiency, however, they increase the back pressure on the crankcase. An example coalescing separator is shown in Figure 2.9.
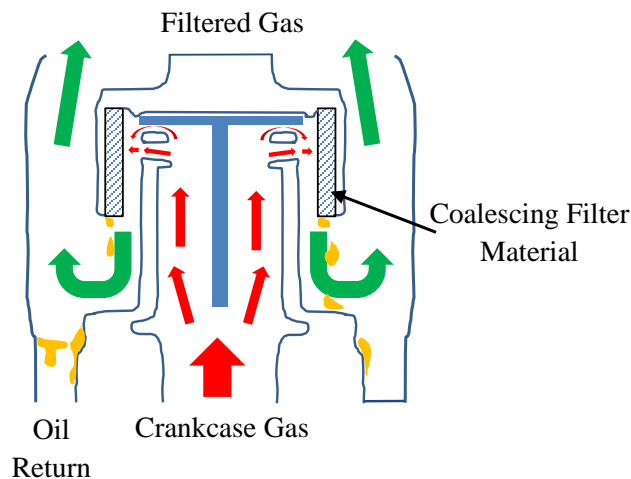
Figure 2.9 Coalescing impactor. Adapted from Kissner and Ruppel (2009)

Other systems include cone stack separators, which use dynamic components to accelerate the flow and provide sufficient centripetal force to remove the oil drops. The two filtration strategies can be balanced, as the rotating components increase parasitic losses and coalescing filters increase the flow restriction. More complex electrostatic separators deflect the oil drop in an electrical field, this is an extremely effective way of removing small drops and has minimal flow restriction, but does require additional power.

Clark *et al.* (2006a) evaluated the performance of a new condensator Crankcase Emissions Abatement System (CEAS) on a heavy duty on highway diesel engine, but precise details of the filter mechanism are limited. The crankcase emissions were sampled using a Cambustion DMS500. The CEAS removed 37 mg of PM, 16 mg of

HC and 0.225×10^{12} particles from the crankcase emission per mile of operation. They concluded that the CEAS removed 100% of the crankcase emissions over 13,400 miles of on-road operation, with an associated improvement in fuel economy with a 1% increase in NO_x tail pipe emissions.

Diesel Particulate filters have also been identified as a method of removing oil particles from crankcase emissions. Under California's retrofit program Partial filters are verified to provide 50 - 84% PM reduction, although beneficial this is not sufficient filtration for the current demand placed on crankcase emissions. Donaldson (2008) claim 95% crankcase emissions filtration using a static impaction Donaldson OCV design and Synteq^{TM} filter media.

Schellhase *et al.* (2007) utilised the centripetal forces generated by the rotation of the camshaft to remove oil drops from the crankcase emission, without additional parasitic losses. Although this separator method requires complex integration into the cylinder head, initial testing has shown promising results (Schellhase *et al.*, 2007). Improvement of filtration design requires a comprehensive experimental and computational investigation. Satoh *et al.* (2000) have developed a computational model of an impaction separator showing a maximum of 10% variation between computational and experimental visualisation and sampling results.

Clearly the filtration demand placed on an engine crankcase is extremely high, a plethora of studies have evaluated the performance of crankcase filtration system, to develop optimal solutions. Typical filtration performance available is very high, but the systems increase parasitic losses and increase engine service costs, with component fouling being a prevalent issue. Crankcase ventilation systems must be managed carefully utilising filtration strategies and pressure control valves to suit the specific engine and its operation.

2.12 Literature Summary

A vast body of work had been conducted in the field of aerosol science, particularly concerning the impact of anthropogenic activities on the environment. Engine lubricant systems have evolved to improve engine performance and durability, research has shown that crankcase oil aerosols are generated by these systems. Oil

aerosols are critical to the operation of some engine components, but they also contribute to engine emissions and reduce engine performance. Liquid atomisation and drop generation has been a topic of substantial research, mainly in the field of fuel injection. The complex fluid mechanics associated with atomisation and drop generation continues to be at the forefront of research. Engineers and scientist are interested in how to generate reliable computational models that can accurately predict atomisation and drop generation. Recent crankcase emissions legislation has forced engine manufactures to address the problem of crankcase oil aerosols. For this reason a selection of innovative and complex filtration strategies have been developed. Research has focussed on characterising crankcase emissions to quantify required filtration performance. Results have revealed the complexity of aerosol measurement and the requirement for better understanding of the factors controlling crankcase aerosol generation and behaviour. There are many topics relevant to crankcase oil aerosol generation that have been covered in isolation, the knowledge from these separate topics must be consolidated in a specific experimental investigation, directly addressing the problem of crankcase oil aerosol generation.

2.13 Concluding Remarks

Oil atomisation is utilised as a critical engine lubrication mechanism, however, oil aerosols increase crankcase emissions and increase parasitic losses. A comprehensive literature review has shown that there is little understanding of crankcase oil aerosol generation. Knowledge of crankcase oil atomisation processes is extremely valuable, it will help engine designers and developers regulate the atomisation process and drop transport within the crankcase. Reducing and controlling crankcase oil aerosol generation at source will reduce engine emissions and crankcase filtration requirements, whilst improving engine lubrication and oil consumption. The next chapter presents a robust experimental procedure addressing this lack of fundamental knowledge and understanding.

CHAPTER 3

EXPERIMENTAL METHOD AND EQUIPMENT

3.1 Introduction

The lubricant circuit is an integral part of an internal combustion engine, oil is actively supplied to specific locations to reduce friction and transfer heat. Once supplied to these critical locations, the oil is left to drain down to the bottom of the crankcase where it is then scavenged and pumped back into the oil circuit. A crankcase is designed to ensure sufficient oil return for different engine orientations and engine loads, whilst maximising structural integrity and minimising the packaging space.

The literature survey in the previous chapter highlighted the significant contribution of lubricant oil to crankcase PM emissions. There is little understanding of crankcase oil aerosol generation, particularly how the oil is atomised and an aerosol produced. This chapter describes the development and implementation of two comprehensive experimental studies: (i) an optical investigation of crankcase oil distribution and aerosol generation (ii) a particle sampling study capturing drops 5 nm $< d_p > 20$ μm. The experimental work was sponsored by IPSD and completed at Loughborough University.

A motored test engine was installed at Loughborough University to isolate the contribution of lubricant oil to crankcase emissions. The motored test engine replicated the crankcase architecture, oil temperatures, gas flow rates and engine speeds present on a firing engine. Full optical access to the crankcase facilitated a thorough analysis and quantification of the oil distribution and atomisation. A detailed particle sampling study was conducted around the motored engine crankcase to provide valuable novel information on crankcase aerosol generation. A comparative particle sampling study was completed on a fired engine with identical crankcase architecture.

3.2   Engine Specification

The objective of this experimental investigation was to identify the main sources of oil aerosol and understand the parameters controlling aerosol generation. An IPSD 1104C-44 engine was chosen as a representation of a typical heavy duty off-highway diesel engine, the full engine specification is shown in Appendix A Table A-1.1. The engine used a wet sump and a gear driven gerotor oil pump to lift oil from the sump and deliver it around the engine, the total oil volume in the engine was 6.5 litres. The complete oil circuit on the 1104C-44 engine is shown in Figure 3.1. The manufacturer's specification of the oil circuit is detailed in Appendix A Section A-2.
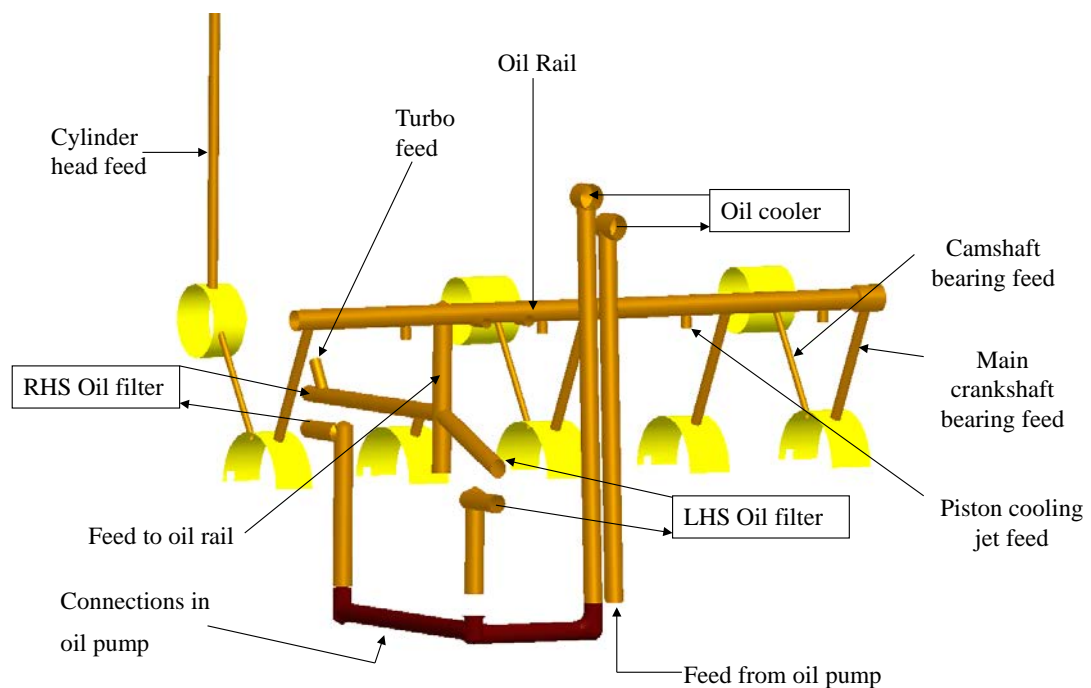
Figure 3.1 IPSD 1104C-44 lubrication system. (IPSD, 2008a)

Oil is lifted from the bottom of the sump via a strainer pipe. The pressure differential between the inner and outer lobes of the oil pump creates suction or positive pressure depending on the relative motion between the lobes. Hot oil is pumped through a plate oil cooler, and then sent to a filter and cleaned.

The clean cool oil is supplied to the oil rail along the engine block that feeds the five crankshaft main hydrodynamic journal bearings, and the four piston cooling jets positioned at the bottom of each cylinder liner. Crossing drillings in the crankshaft

feed the big end bearings at the end of each of the four connecting rods. Three of the five main bearing shells have an output, supplying oil to the three camshaft journal bearings. The front camshaft journal bearing has an output feeding the cylinder head in the top of the engine. Oil fills the static rocker shaft and intermittently moves through the rockers to lubricate the valves, valve springs, and the pushrods. The oil supply is intermittent, as the actuation of the rocker temporarily blocks off the oil feed hole in the rocker shaft. The idler gear bearing on the front of the engine is lubricated from the oil rail. When a turbocharger is used, the bearing oil supply is taken just before the oil rail.

The oil flows from the side of the crankshaft bearings onto the crankshaft and is either flung off or drains onto the walls of the engine block and into the sump. Oil drains from the camshaft bearings in a similar manner. The oil supplied to the underside of the piston is left to drain down past the crankshaft into the bottom of the engine. Oil supplied to the cylinder head drains down the pushrod gallery for each pair of valves and onto the tappets above the camshaft. The oil film lubricating the tappets eventually drains down two channels past the camshaft and crankshaft into the sump. The hot dirty oil form the turbocharger is returned to the side of the engine block, above the surface of the sump oil.

Although this is a 2004 EC and USA emissions compliant engine, the lubricant circuit remains fundamentally the same as an equivalent 2012 engine. During this 8 year gap the requirement for higher power density has forced engine manufacturers to increase imep by using higher boost pressures and complex turbocharging strategies. These changes have increased thermal loading and blow-by rates, therefore the oil circuit must transfer more heat and oil films must be maintained with higher levels of vapourisation and increased potential for atomisation. To combat these changes, engine manufacturers have increased the oil pump size to provide a higher oil pressure at critical bearings and the piston cooling jets. The service manual for the 1104C-44 states that the piston, cylinder liner, valves, valve springs and timing gears are all lubricated by splashed oil and an oil aerosol. This is an important statement as it indicates the reliance of engine lubrication on an oil aerosol. However, the dependence of piston ring pack lubrication on crankcase oil

aerosols is not understood or quantified. It was not until 2007, when the crankcase regulations were enforced, that there has been any significant concern about crankcase emissions and the effect the lubrication system has on crankcase emissions. The pressure of crankcase emission regulations and the drive for improved engine efficiency forces engine manufacturers to understand the generation of oil aerosols.

3.3 Experimental Method

Assuming that the main source of blow-by on this NA 1104C-44 engine was ring pack blow-by, the crankcase can be divided into three distinct regions. The blow-by can be traced through each crankcase region, before being vented from the rocker cover on the top of the engine. These regions are; the cylinder liners, sump and pushrod galleries. Within each region potential mechanisms of oil atomisation and aerosol generation were identified, these mechanisms are described below and indicated in Figure 3.2:

Cylinder Liners – Potential Aerosol Generation Mechanisms
  (i)   Piston rings and cylinder liner - Atomisation of oil films due to high velocity gas from combustion.
  (ii) Piston cooling jets - Atomisation directly from the piston cooling jets.
  (iii) Piston and cylinder liners - Atomisation/vapour generation when oil from the piston cooling jets impacts on the high temperature surfaces with a high relative velocity.

Sump - Potential Aerosol Generation Mechanisms
  (i)   Sump oil volume - Atomisation when trapped bubbles of gases rise to the surface of the oil and burst. The bubbles are generated in oil galleries and regions of high pressure drop, due to sharp changes in geometry.
  (ii) Crankshaft and camshaft - Atomisation at the side of journal bearings.
  (iii) Crankshaft and camshaft - Atomisation of oil films due to rotational forces.
  (iv) Engine block - Atomisation of oil films by high velocity blow-by gas.
  (v)   Sump - Impaction and breakup of oil drops on static or dynamic surfaces.

(vi)   Journal bearings, oil pump vanes, oil cooler, oil filter - Cavitation and aeration within galleries and components.

Cylinder Head and Pushrod Galleries - Potential Aerosol Generation Mechanisms

 (i)   Pushrod galleries and cylinder head oil drainage path ways - Atomisation of oil films by high velocity blow-by gas.

 (ii)   Cylinder head and pushrod galleries - Impaction and breakup of oil drops on static or dynamic surfaces.

(iii)   Valves, valve springs, rockers and pushrods - Atomisation of oil by the motion of the valve gear.

(iv)   Valve guides - Atomisation of oil by the blow-by.
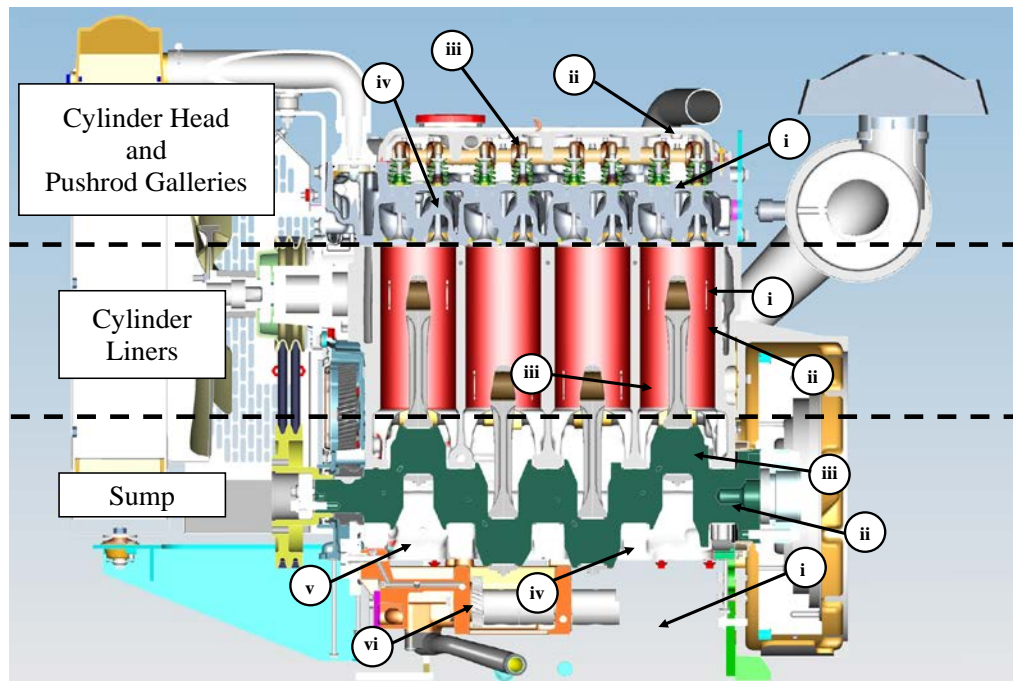
Figure 3.2 Potential sources of oil aerosol from the 1104C-44

There is a distinct lack of information on atomisation from dynamic components and the breakup of the oil films that coat the majority of the internal crankcase surfaces. The contribution of these processes to crankcase oil aerosol generation has been investigated experimentally to advance fundamental understanding. In this study a motored engine has been used to isolate the contribution of oil to crankcase emissions, whilst optical access to this engine has enabled a quantitative high speed

laser diagnostics study of oil aerosol generation. This experimental study has focussed on the main crankcase volume as this is the region lacking in experimental investigation. Optical accessed was gained in the sump, around the crankshaft, in the pushrod galleries and in the rocker cover. A further particle sampling study has quantified the crankcase particle emissions from both the motored engine and an identical fired engine.

3.4 Motored Engine

The motored engine installation was designed, manufactured and installed at Loughborough University specifically for the analysis of crankcase oil aerosol generation. The motored engine installation at Loughborough University is shown in Figure 3.3, the specific details of the setup follows.
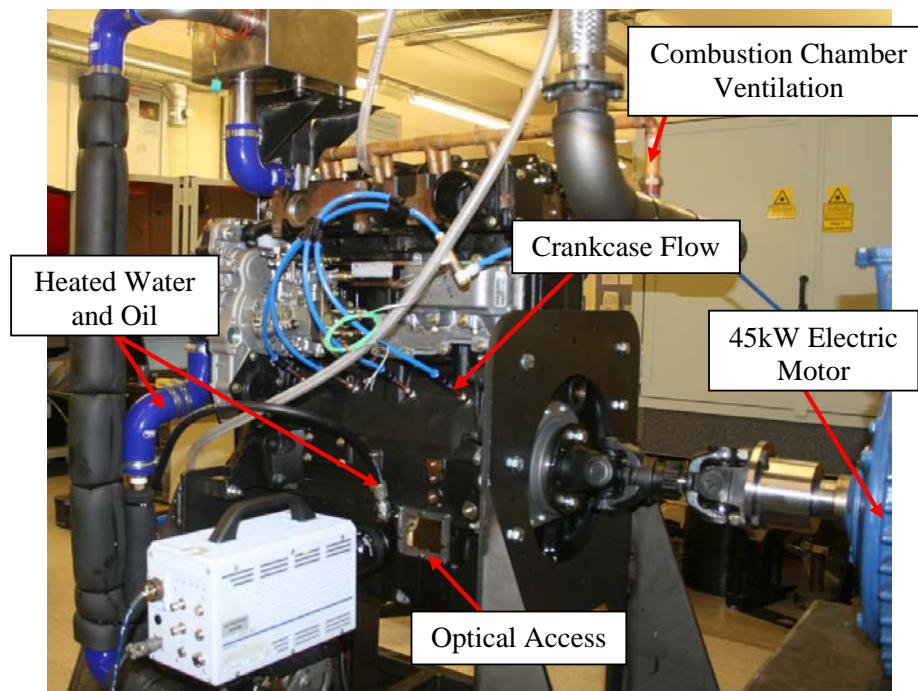
Figure 3.3 Motored engine installation at Loughborough University

The 1104C-44 engine was elevated 500 mm from the floor to achieve optical access and substantial exterior space for imaging and sampling equipment. The engine was held between two 16 mm laser cut steel plates and a steel box section frame secured the plates. The entire assembly was supported on four anti-vibration rubber feet. A Computer Aided Design (CAD) model of the engine rig is displayed in Figure 3.4.
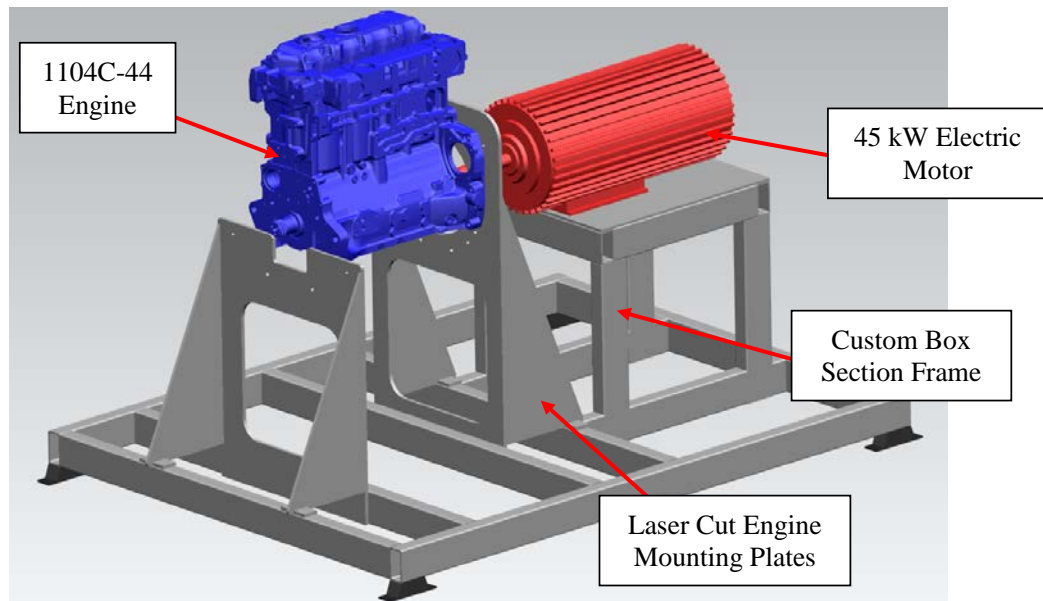
Figure 3.4 Motored engine CAD assembly

The engine was directly coupled to an inverter driven 3-phase 30 kW electric motor via a universal joint using open loop frequency control to set the engine speed. A light sensor was positioned on the end of the crankshaft to measure the engine speed and provide a trigger for imaging equipment. The cylinder head was removed to set the trigger point to TDC using a dial gauge. The light sensor signal was monitored and recorded using a data logger. To reach higher engine speeds the motored engine assembly was modified, components were removed to reduce the work required to turn the engine over. Depending on the region under analysis, different components were removed, a summary of the engine configurations that were used is shown in Table 3.1.

Table 3.1 Motored Engine Configurations

	Imaging Location		
Components	**Sump**	**Pushrod gallery**	**Rocker Cover**
Pistons and connecting rods	Yes	Yes	No
Injectors and glow plugs	No	No	Yes
Valves	Yes	Yes	Yes
Pushrods	Yes	Yes	Yes

When imaging in the sump, only the injectors and glow plugs were removed as this reduced the pumping work, but maintained the aerosol generation from the rotation of the crankshaft, connecting rods and pistons. For the pushrod gallery imaging the same engine configuration was used, therefore not only was primary atomisation captured, but also the transportation of any aerosol generated in the sump. For analysis of the oil distribution in the rocker cover, the pistons and connecting rods were removed, the big end journal bearing shells were clamped to the crankshaft. These modifications did not alter the primary atomisation processes occurring in the rocker cover.

3.4.1   Motored Engine Coolant Circuit

The engine coolant system was used to maintain a stable temperature of 90°C in the cylinder head and block. A mixture of water and anti-freeze was continually circulated around the engine from an external tank using a separate central heating pump. The gear driving the engine water pump and the thermostat were removed for all tests. The engine coolant temperature was measured in the external water tank and used to regulate the heaters in a closed loop system. A header tank above the cylinder head was used to bleed the system and provide an additional point to measure the coolant temperature.

3.4.2   Motored Oil Circuit

As identified in Chapter 2, oil density, viscosity and surface tension effect the force required to atomise the oil. However, these physical properties change with temperature. For this reason a heated oil circuit was used to replicate the oil temperatures found within a firing engine, the full oil circuit is shown in Figure 3.5. The oil was heated in an external closed loop system using an immersion heater and continuously mixed during the heating process in an 8 litre tank. Once the prescribed oil temperature was reached, the oil was pumped into the engine sump. A ball valve and flow meter were used to regulate and monitor the oil supply. Once the oil was supplied to the sump it was lifted into the engine oil circuit using the production engine oil pump. A second ancillary pump returned the cold oil from the sump back to the heater unit. K-type thermocouple readings were taken in the external heater

tank, the sump and the engine oil rail to ensure that a constant oil rail temperature was maintained.
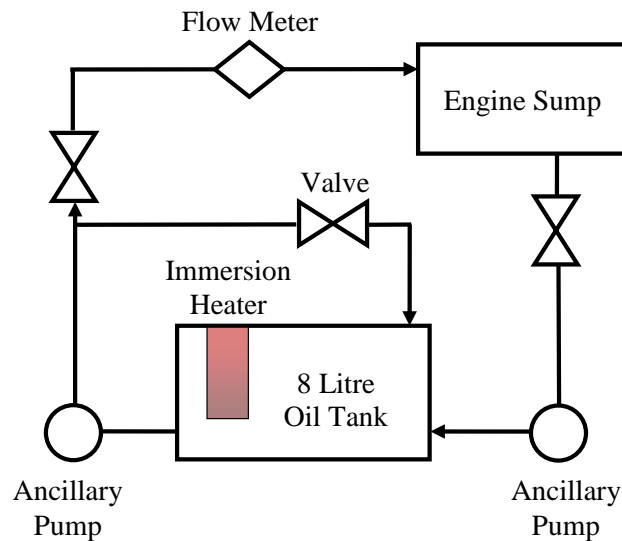

Figure 3.5 Schematic of the motored engine external oil heating circuit

3.4.3 Motored Engine Blow-by Source

Since there was very little or no compression and no combustion in this motored engine there was no blow-by introduced into the crankcase. To replicate the blow-by on a firing engine a controlled steady state flow was introduced into the crankcase at the bottom of each cylinder liner. A schematic of the crankcase flow circuit is shown in Figure 3.6.
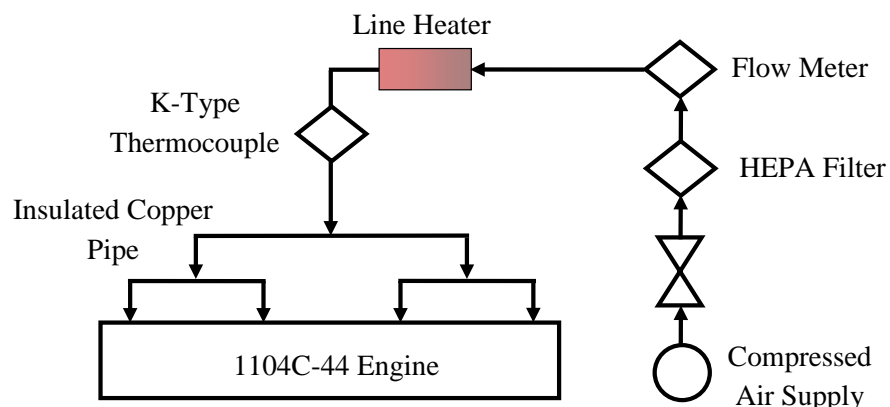
Figure 3.6 Schematic of the motored engine crankcase flow pipe work

A compressed air supply was regulated using a Chell flow meter to achieve the desired crankcase flow rate. A HEPA filter was used to remove 99% of particles $d_p > 500$ nm from the compressed air supply. The flow was then heated to 100°C using a line heater in a closed loop system, before being divided equally into four outlets and entering the engine crankcase at the bottom of each cylinder liner. 8 mm inner diameter pipe was used throughout, flexible plastic pipe was used before the line heater, after the line heater, copper pipe work with 20 mm insulation was used to reduce any heat loss. Equally spaced compression fittings were mounted on the inlet side of the engine block securing the four copper nozzles directing the crankcase flow. The four copper crankcase flow nozzles were bent to a 45° template and secured in the same orientation below the cylinder liner.
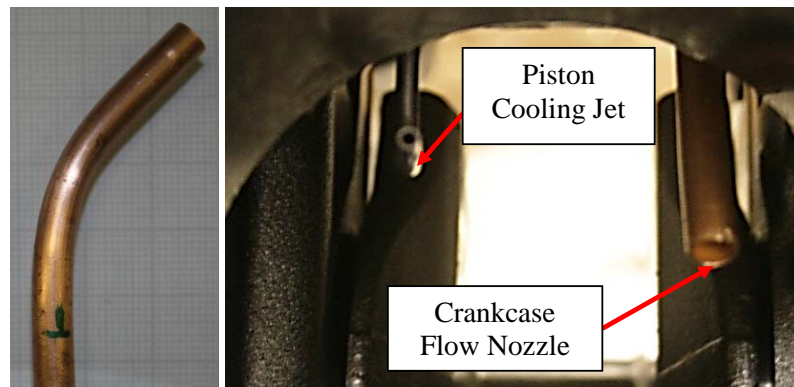
Figure 3.7 Motored engine crankcase flow nozzle

An example of the crankcase flow nozzle and its installation is shown in Figure 3.7. As the focus of this experimental work was the main crankcase body, not around the piston rings, the piston cooling jets were sealed for all tests. The oil rail pressure was measured to check the performance of the oil pump and to record the oil supply pressure around the engine.

For a total blow-by flow rate of 40 litres.min^{-1} the velocity of air leaving the each nozzle is 13 m.s^{-1}, calculated using Equation (3.1), where Q is the nozzle flow rate, A_n is the cross sectional area of the nozzle and V_a is the gas velocity within the nozzle. The crankcase flow was switched on for 10 minutes before and after the engine was run to prevent oil collecting in the pipes, and ensure the system was at a stable temperature.

Nozzle Volume Flow
Rate

$$Q = A_n V_a \qquad (3.1)$$

As discussed a series of K-type thermocouple measurements, pressures and flow rates were taken around the engine to accurately quantify the engine operating conditions. These measurements are summarised in the table and schematic of the motored engine instrumentation is shown in Figure 3.8.
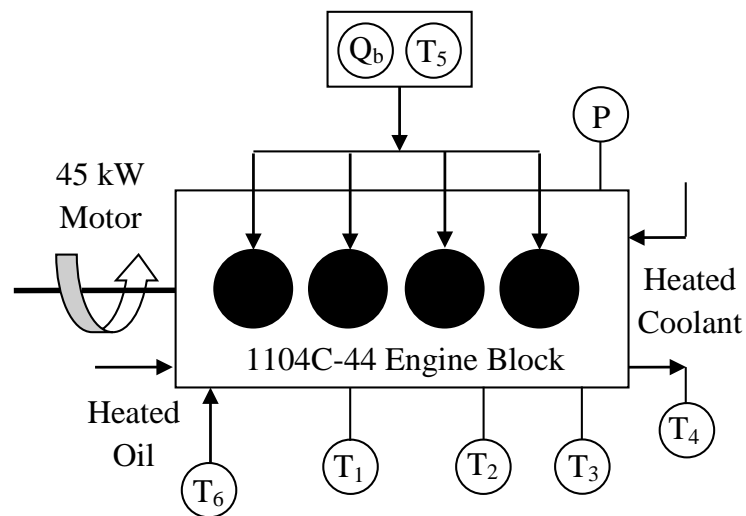
Temperature	
T_1	Oil Sump
T_2	Cylinder 3 Push Rod Gallery surface
T_3	Oil Rail Temperature
T_4	Water header tank
T_5	Crankcase flow
T_6	Oil heater
Flow rate	
Q_b	Crankcase flow

Figure 3.8 Schematic of motored engine instrumentation

3.5 Optically Accessed Motored Engine

The engine crankcase was optically accessed for qualitative and quantitative analysis of the oil distribution. For all imaging locations a calibration graticule was used in the focal plane to accurately quantify the image scale. Full optical access was gained around the valve gear in the cylinder head. The production rocker cover was replaced with a simple slab sided Perspex cover as shown in Figure 3.9. An image of the rocker cover testing is shown in Figure 3.10.

Figure 3.9 Motored engine Perspex rocker cover
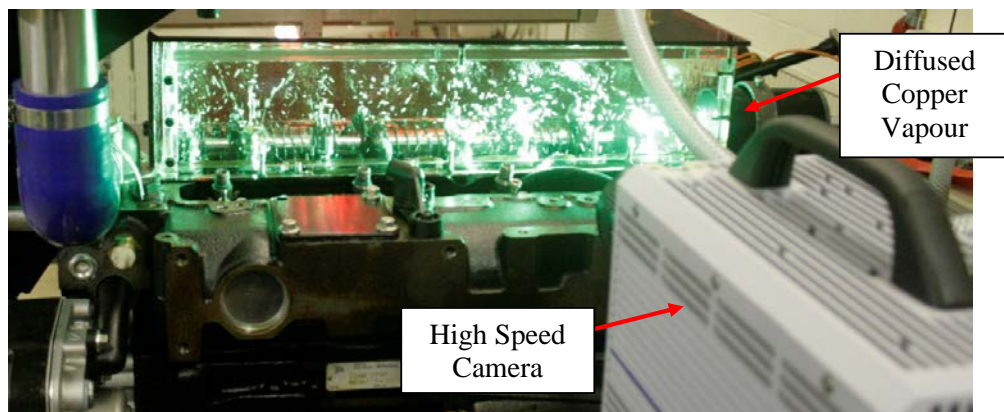
Figure 3.10 Motored engine rocker cover imaging

On the 1104C-44 the four pushrod galleries were fed by two smaller galleries above the camshaft as annotated in Figure 3.11. A window was machined over the pushrod gallery to provide optical access at all stages as the oil drained into the sump and the crankcase gas travelled into the rocker cover. A clear Perspex sheet sealed the pushrod gallery, causing minimal difference to the internal volume of the pushrod galleries. An image of the pushrod gallery testing is shown in Figure 3.12.
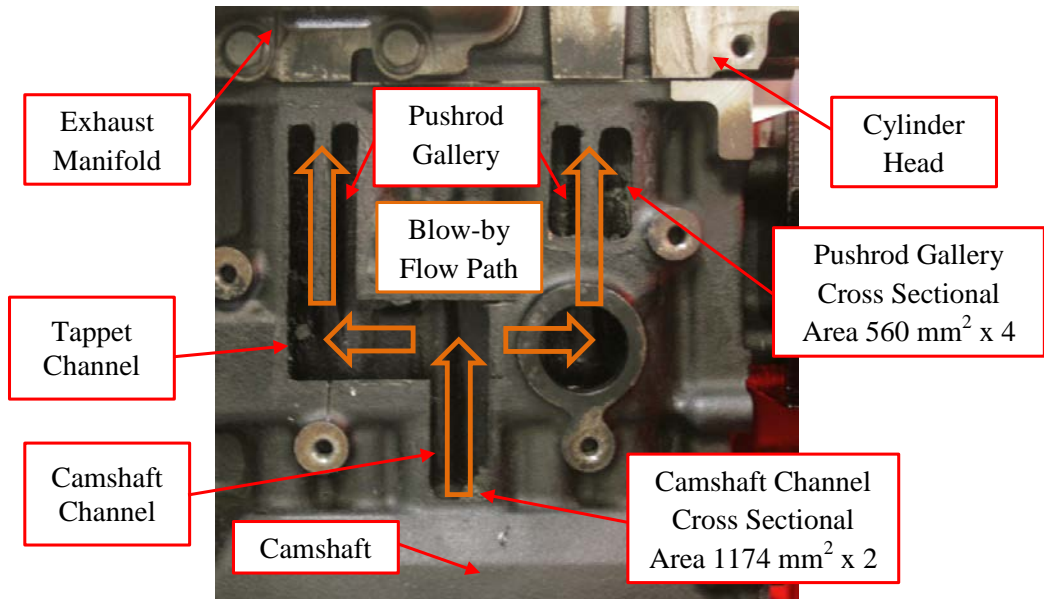
Figure 3.11 Motored engine optically accessed pushrod gallery
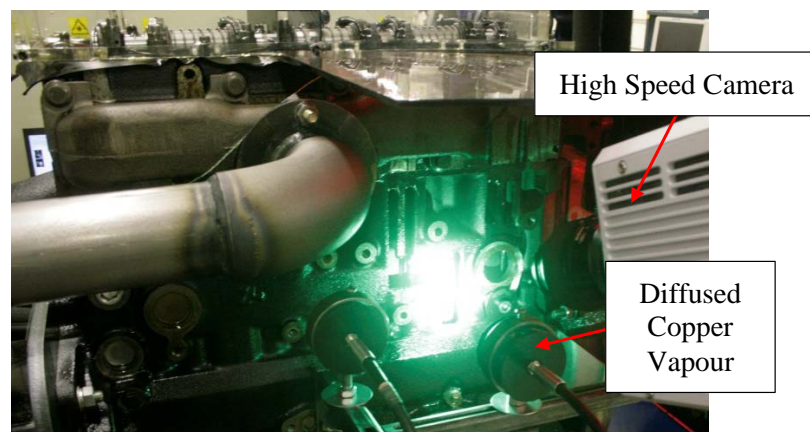
Figure 3.12 Motored engine pushrod gallery imaging

Optical access was gained in the bottom of the engine via a series of windows machined into the engine sump and block. The Perspex windows in the sump are shown in Figure 3.13 and Figure 3.14. The windows were positioned to; maximise the optical access of oil distribution in each region, minimise the reduction in structural integrity of the engine and ensure adequate sealing. Due to the high level of oil distribution within the crankcase, the windows filmed up very quickly. Where necessary the windows were extended out to reduce the film build up and improve image quality.
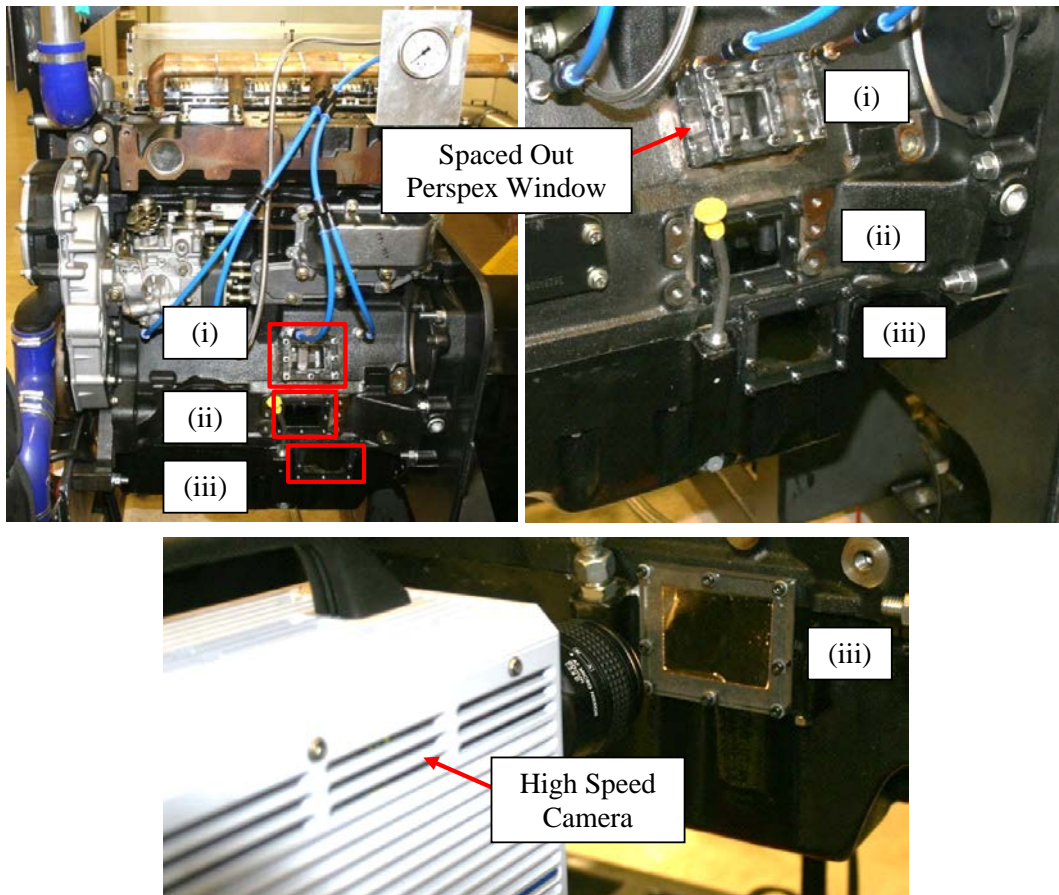
Figure 3.13 Motored engine sump optical access on the right side of the engine
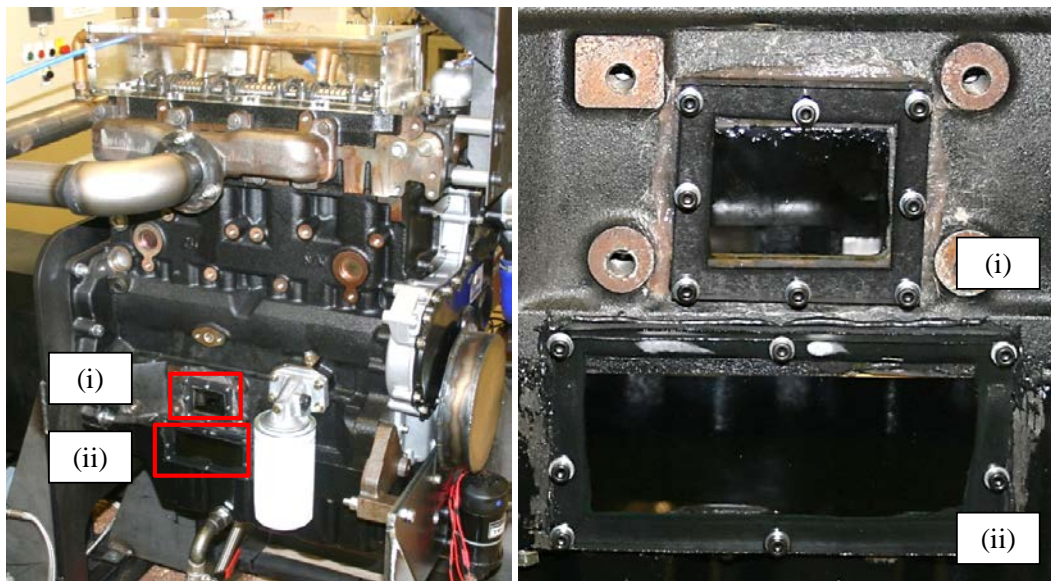
Figure 3.14 Motored engine sump optical access on the left side of the engine

3.6 Motored Engine Optical Setup and Testing

Separate high resolution and high speed cameras, plus either halogen or laser illumination, captured high quality images at each of the optically accessed crankcase locations. The details of the imaging and illumination equipment are discussed in this section, followed by the specific installations used at each crankcase location.

High resolution single shot imaging examined the oil aerosol generation in detail. An Olympus E330 DSLR camera with a maximum resolution of 7.5 megapixels (effective pixels) on a N-type Metal Oxide Sensor (NMOS) was used for high spatial resolution imaging. The camera was connected to a 30 inch LCD television to display a live image, then a separate hand held trigger was used to record the data. This camera setup made image capture and synchronisation easy to control and laser safe. The lens $f^{\#}$, sensor exposure and chip sensitivity were manually adjusted on the camera to achieve the optimum image contrast and brightness.

High speed imaging was conducted using a Photron FASTCAM APX-RS high speed camera. The Photron camera used a Complementary Metal Oxide Sensor (CMOS) sensor with a maximum full frame resolution of 1024 x 1024 pixels at 3000 fps. At a lower 512 x 512 pixel resolution, the frame rate could be increased to a maximum of 10,000 fps. The camera was operated from a laptop where the frame rate and image resolution could be selected to suit the specific oil distribution under examination. The high speed camera could be used to trigger the laser illumination and ensure that the light pulse was produced at the correct time.

Continuous white light illumination was provided from a single bulb 500 watt halogen lamp. Fluctuation in the mains light source at 50 Hz caused a variation in the high speed image brightness, therefore these images were not used for full quantitative analysis but they provided value insight into the crankcase oil distribution.

Laser illumination was provided by an Oxford Laser LS-20-50 Copper Vapour laser with wavelength split 2/3 at 511 nm and 1/3 at 578 nm. The laser was capable of producing a pulse repetition rate of 50 kHz with a 10-30 ns pulse duration. Laser

light was delivered to the test location using a fibre optic cable. The armored fibre optic cable was statically mounted at each crankcase location to ensure optimum illumination. Red acrylic or steel laser guards were positioned around the engine to meet laser safety requirements. An acrylic diffusion screen was used for both illumination sources to produce diffused light and improve the quality of the captured images.

Variable focus Nikon 105 mm and Nikon Micro Nikkor 200 mm f/4 D lenses were used for both single shot and high speed photography. Extension rings were used to adjust the lens magnification, depending on the crankcase location under investigation.

3.6.1 Sump and Crankshaft Imaging

Images were collected of the rotating crankshaft viewed through the sump using halogen illumination in forward scatter. The high speed camera was positioned at 45° to the crankshaft centre line as shown in Figure 3.15, a sample image is shown next to the optical setup. The high speed camera was also positioned perpendicular to the crankshaft centre line, viewing directly across the sump, including the oil surface within the sump. The crankshaft was viewed in isolation as shown in Figure 3.16, through the window located below the cylinder liner using the high speed camera and halogen illumination in back scatter. Fouling of the windows was particularly problematic in this region, despite the windows being spaced away from the engine block. For this reason images were only collected at low engine speeds where the oil distribution was minimised.
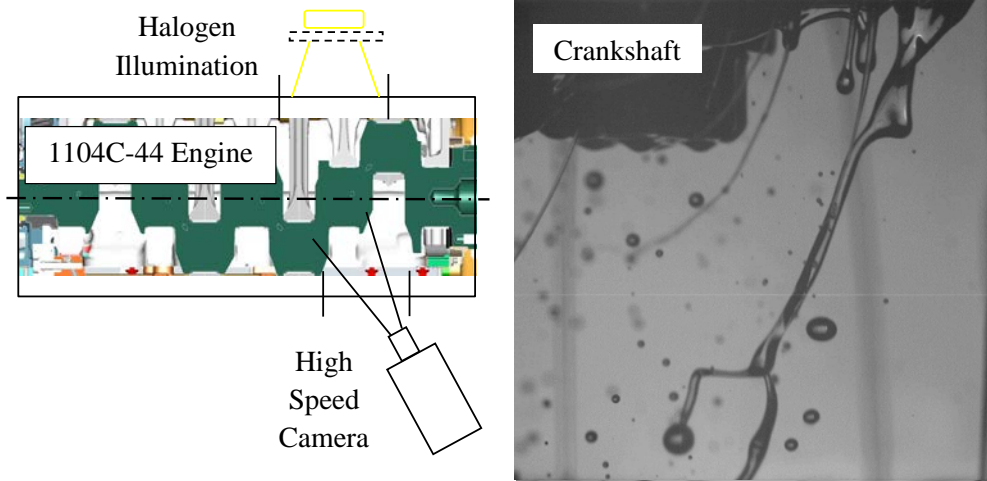
Figure 3.15 Crankshaft and sump imaging with forward scatter illumination
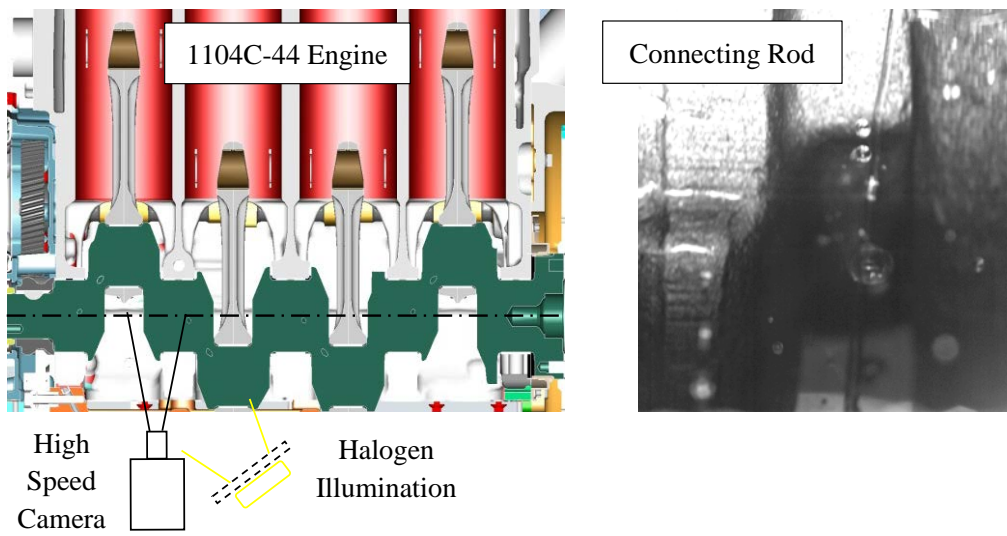

Figure 3.16 Cranksahft imaging with back scatter illumination

3.6.2   Pushrod Gallery Imaging

The pushrod gallery could only be accessed from one side of the engine, therefore only back scatter illumination was used. Both the high speed and DSLR cameras were used with white light and copper vapour illumination, to provide sequenced images with high temporal and spatial resolution. The optical setup used when imaging in the pushrod gallery is shown in Figure 3.17.
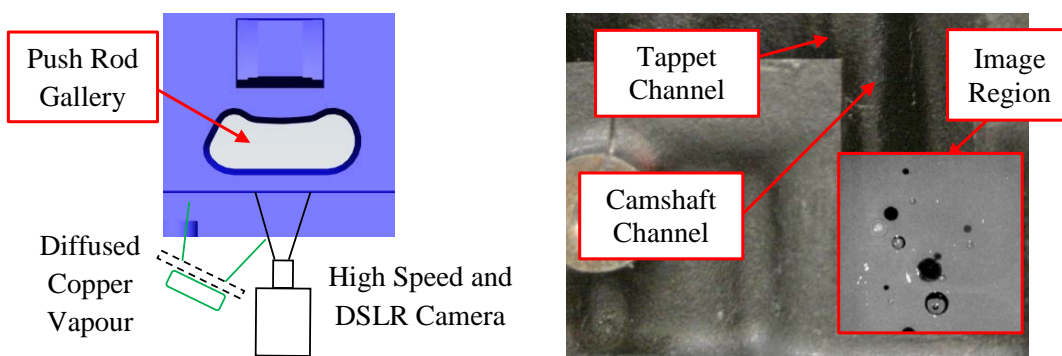
Figure 3.17 Pushrod gallery imaging with back scatter illumination

3.6.3   Rocker Cover Imaging

The rocker cover was imaged in both back and forward scatter using copper vapour illumination. Images were collected perpendicular to the centre line of the engine, from the intake and exhaust sides using both cameras. The oil distribution was examined in detail around all dynamic components within the rocker cover. The optical setup used when imaging in the rocker cover is shown in Figure 3.18.
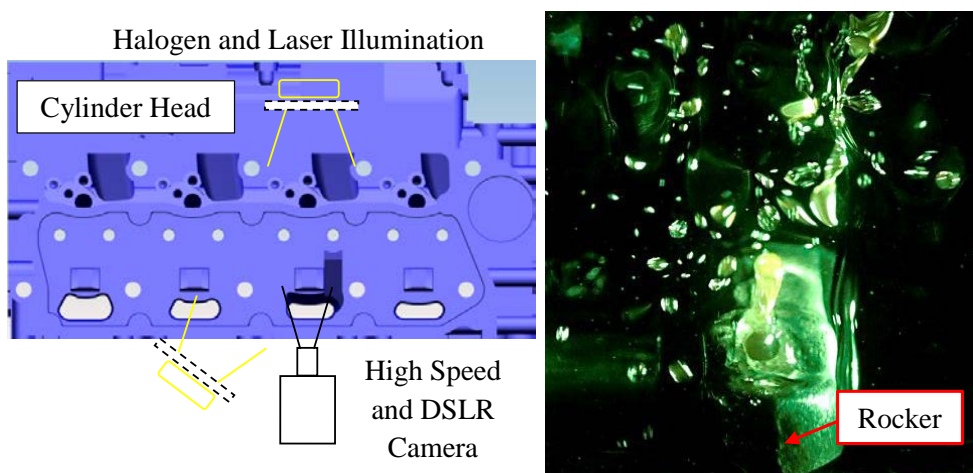
Figure 3.18 Rocker cover imaging with back and forward scatter illumination

3.6.4 Rotating Components Imaging

Rotating components within the crankcase were found to contribute substantially to the oil aerosol generation. The isolated contribution of the crankshaft to the oil aerosol present in the top of the engine was captured by imaging in the rocker cover. Figure 3.19 shows the setup of the copper vapour illumination and the high speed and DSLR cameras used to capture the oil drops that were transported up into the top of the crankcase. The pushrods, rockers, pistons and connecting rods were removed and there was no oil circulated to the top of the engine.
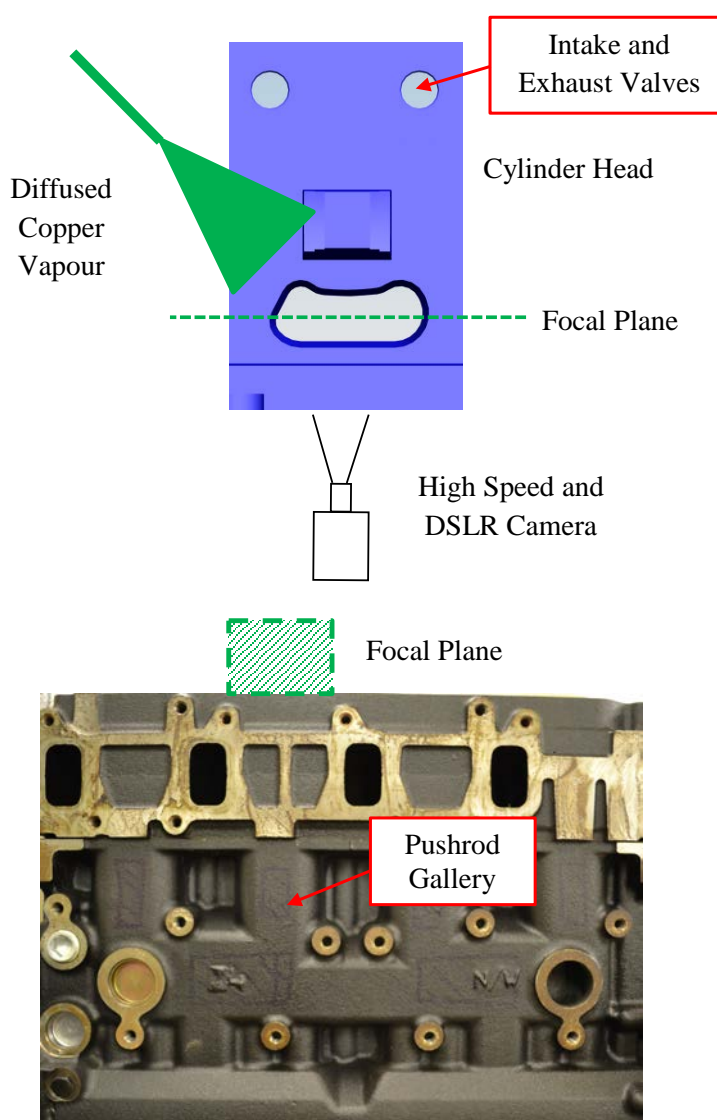
Figure 3.19 Rotating components imaging

The diffraction limited spot size, d_{diff} was calculated, as shown in Equation (3.2), where $f^{\#}$ is the f-number, M is the magnification factor and λ is the wavelength of the laser light incident on the drops (Raffel, Willert, Wereley and Kompenhans, 2001). For the optical setup shown in Figure 3.19, using the DSLR camera with a 200 mm lens, the diffraction limited spot size was $10\,\mu m$. Drops smaller than this would appear as $10\,\mu m$ in the images and therefore their precise diameter could not be resolved.

$$\begin{matrix} \text{Diffraction Limited} \\ \text{Spot Size} \end{matrix} \qquad d_{diff} = 2.44f^{\#}(M+1)\lambda \qquad (3.2)$$

3.6.5 Test Parameters

For all imaging locations, tests were completed at a range of stable engine conditions. The engine speed, oil temperature and crankcase flow rate were adjusted to replicate changes in fired engine running conditions. A summary of the motored engine optical test matrix is shown in Table 3.2.

Table 3.2 Motored engine optical test matrix

Engine Speed [rpm]	Imaging Location	Oil Temperature [°C]	Crankcase Flow Rate [litres.min^{-1}]
300	Sump and Crankshaft	20	40
600	Crankshaft	60	60
900	Sump	80	80
1000	Rocker Cover	100	100
1400	Push Rod Gallery	120	120

3.7 Crankcase Particle Sampling

The particulate matter emitted from the crankcase on both a motored and fired 1104C-44 engine were measured. The engine block and internal components within the crankcase were identical for both these engines, the motored engine specification has already been introduced in Section 3.4, details of the fired engine are shown in Appendix A Table A-3.1.

Two different engine oils were used to examine their effect on crankcase oil aerosol generation. The motored engine used SAE 5W-30 oil, whilst the fired engine used SAE 15W-40. At 100°C the kinematic viscosities of the two oils differs by $5.1 \times 10^{-6} \, m^2.s^{-1}$, the properties of both oils are listed and compared in Appendix B Table B-2.2.

Due to the sensitivity of particle sampling to thermal conditions, a stable engine and sampling equipment temperature was achieved before conducting all tests. A series of thermocouple measurements were taken on each engine to record any temperature variation. The thermocouple data was recorded using a data logger (Pico Logger USB TC-08), providing valuable information on generation and behavior of crankcase particle matter. The specific measurement points on each engine will be discussed in the next sections.

Three types of sampling equipment were used to characterise the crankcase particulate matter emissions: (i) the Cambustion DMS500 MkII fast particulate spectrometer measuring particles 5 nm - 1 µm (ii) the TSI SMPS and CPC measuring particles 15 nm - 660 nm (iii) the APS measuring particles 0.5 µm - 20 µm. The operating principles of these measurement instruments was introduced in Section 2.10. Particle sampling was conducted at a range of engine speeds and loads. On the fired engine the rated load could be varied just adjust the blow-by rate, however, on the motored engine the blow-by rate was adjusted directly by controlling the steady state flow introduced into the crankcase.

3.7.1 Motored Engine Sampling

The motored engine sampling analysis was conducted using the TSI^{TM} SMPS, CPC and the APS. Samples were taken from the same three crankcase locations tested on the fired engine, however, on the motored engine the crankcase was fully vented via the specific sampling point. To confirm the three sampling points were; the dipstick mounting hole, 100 mm down the pushrod gallery and the oil filler cap. A 300 mm length of 8 mm diameter copper pipe was connected to the sampling point, the flow was then channelled into a 25 mm rubber pipe before entering a 40 mm diameter stainless steel sampling pipe, as shown in Figure 3.20. Samples were extracted from two 90° tappings in the centre of the sampling pipe that were connected to the APS (20 mm diameter pipe) and SMPS (10 mm diameter pipe), the remaining flow was vented to an extraction system.
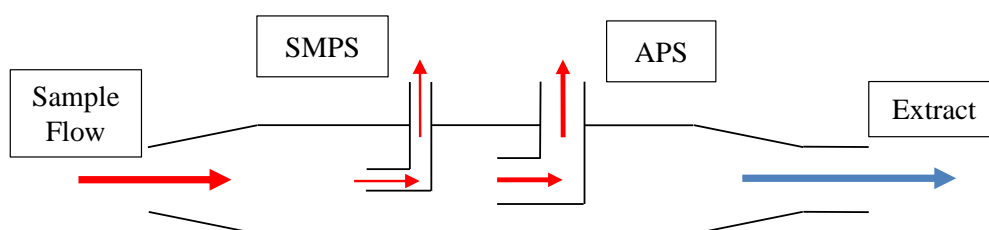
Figure 3.20 Motored engine crankcase sampling points

The APS sample was diluted using a closed system aerosol diluter in increments of 20:1 or 100:1, the sample dilution was corrected for in the data processing. Sampling tests were conducted at crankcase flow rates of 40, 60, 80, 100, 150, 200 litres.min^{-1} and speeds of 360, 600 and 900 rpm. The crankcase flow temperature and the engine coolant circuit were heated to 100°C and 90°C respectively for all tests. Temperature measurements were taken at the following locations around the crankcase using K-type thermocouples; sump oil, oil rail, oil film above the push rod gallery, gas temperature at the top and bottom of the push rod gallery, three sampling points and coolant temperature in the thermostat housing. The oil rail pressure was also monitored.

3.7.2 Fired Engine Sampling

The fired engine was directly coupled to an eddy current dynamometer within an engine test cell at Loughborough University, the engine installation is shown in Figure 3.21. The only difference between the fired and motored engine was the use of a turbocharger on the fired engine. The turbocharger was mounted below the exhaust manifold on the pushrod side of the fired engine, as shown in Figure 3.21. The central turbocharger shaft was lubricated directly from the oil rail feed as shown in Figure 3.1, the hot dirty oil was returned to the crankcase on the pushrod side of the engine where it drained down into the sump.
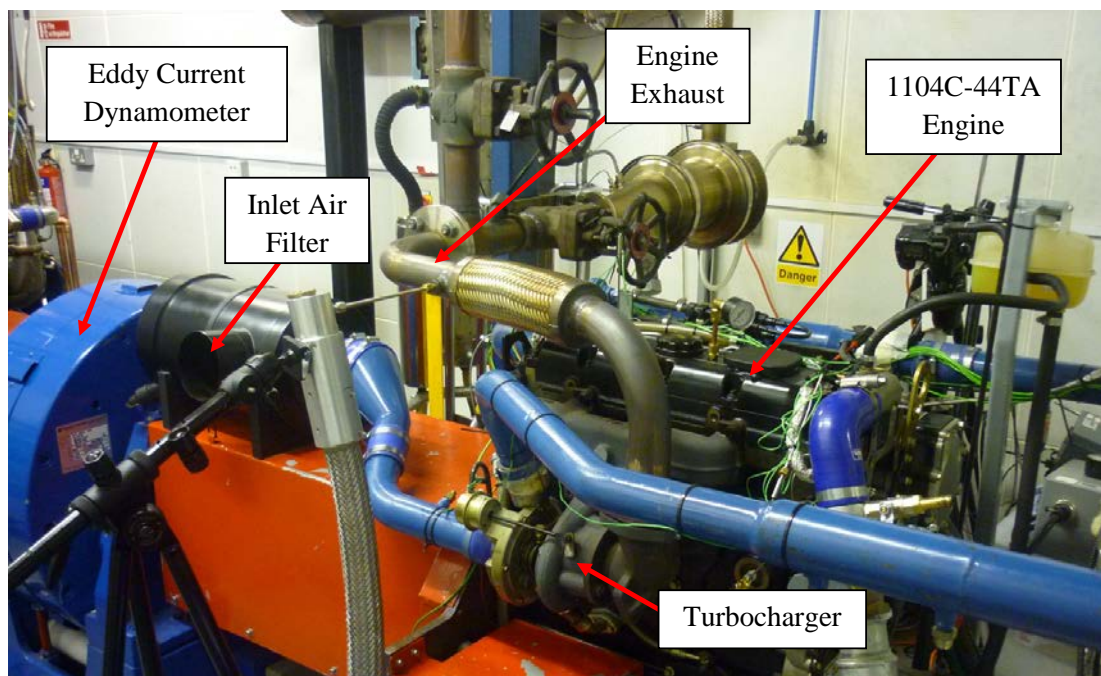
Figure 3.21 Fired engine dynamometer installation at Loughborough University

The engine speed and rated load was controlled for the steady state particle sampling tests. Thermocouple measurements were taken around the engine to ensure that the engine temperatures were stable before sampling started. Temperature measurements were taken at the following locations around the engine; sump oil, post compressor air temperature, oil film above the pushrod gallery, gas temperature at the top and bottom of the pushrod gallery, the three sampling points and the coolant temperature in the thermostat housing, the oil rail pressure was also monitored. An AVL 244 blow-by meter was used to measure the blow-by flow rate. The fired engine

particulate matter was sampled using the Cambustion DMS500 MkII fast particulate spectrometer at three crankcase locations as shown in Figure 3.22. Sampling tests were conducted at 0, 25, 50 and 75% rated engine loads and speeds of 900 and 1400 rpm.
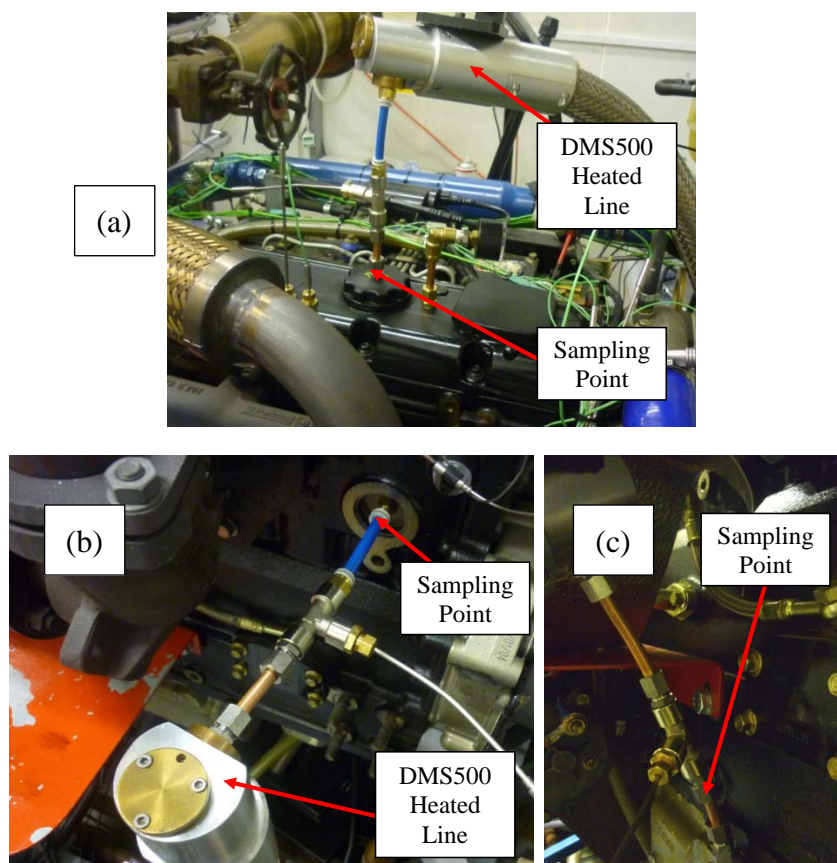

Figure 3.22 Fired engine DMS500 sampling points (a) rocker cover (b) pushrod gallery core plug (c) sump dipstick mount

The sampling locations were; the oil filler cap in the rocker cover, the pushrod gallery core plug and the dipstick mounting hole in the sump. A sample was extracted from the crankcase into a 50 mm length of 8 mm diameter pipe. A K-type thermocouple was used to measure the sample temperature via a stainless steel T-junction, a second 50 mm section of 8 mm diameter copper pipe connected the T-junction to the Cambustion DMS500 heated line. Within the heated line the sample passed initially through a heated cyclone before reaching the DMS500 fast particulate spectrometer. The engine exhaust was also sampled as shown in Figure 3.23, a 250 mm length of 6 mm diameter stainless steel pipe was positioned in the centre of the exhaust flow.
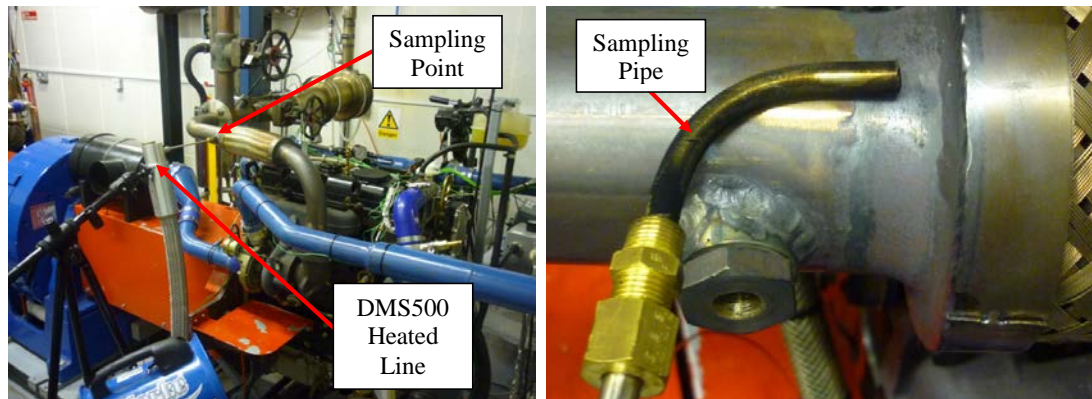
Figure 3.23 Fired engine (a) dynamometer and cell installation (b) exhaust sampling point

The DMS500 has an integrated two-stage dilution system, primary dilution occurs at the sampling point in the heated line where compressed air is passed through a HEPA filter and then used to dilute the sample. Secondary high ratio dilution is applied using a rotating disc diluter, Figure 2.8 shows a schematic of the full dilution system. Both primary and secondary dilution was used on the DMS500 when sampling from the crankcase of the fired engine. For all sampling tests on the fired engine, the crankcase was vented through the production crankcase vent in the rocker cover into the blow-by meter. A sample of 8 litres.min^{-1} was extracted from one of the three specific sampling points and diluted to an appropriate level before entering the DMS500. The DMS500 was calibrated to correct for varying dilution ratio.

3.8   Concluding Remarks

This chapter has described the thorough experimental procedure that was developed to capture high quality optical and sampling data to advance the understanding of crankcase oil aerosol generation. The data collected from the experimental rigs described in this chapter is presented and discussed in Chapters 4 and 5.

CHAPTER 4

OPTICAL ANALYSIS OF CRANKCASE OIL AEROSOL GENERATION

4.1 Introduction

The results collected from an optical investigation of crankcase oil aerosol generation are presented and discussed in this chapter. Optical diagnostics was employed to capture high quality images within the three major regions of the crankcase, namely; the sump, the pushrod galleries and the rocker cover. The main objective of this experimental study was to capture the distribution and breakup of liquid oil, and thus, identify the main contributors to crankcase oil aerosol generation.

The motored engine and experimental setup used, replicated the crankcase of a fired engine. Representative data sets were collected at a range of oil temperatures and engine speeds to demonstrate the isolated effect of each parameter on crankcase oil aerosol generation. The specific test conditions and key optical setups will be indicated throughout this chapter, however, a detailed experimental description and explanation of the motored engine and optical diagnostics techniques can be found in Chapter 3.

Customised image processing code was developed to examine the comprehensive data sets and quantify the oil distribution and atomisation. The resulting qualitative and quantitative analysis evaluated in this chapter, provides new and novel insight into both the passive behaviour of crankcase oil and the fundamental process of oil aerosol generation.

4.2 Image Processing

MATLAB and the open source Java image processing software ImageJ, were used to process captured data sets and identify the oil distribution and atomisation. Gonzalez, Woods and Eddins (2004) give a comprehensive description of the fundamental MATLAB image processing techniques. The specific image processing approach that was selected will now be discussed. An example MATLAB image processing code, that was used to process images taken around the rockers, is shown in full in Appendix D.

For each optical setup calibration images of either a microscope graticule or 1 mm x 1 mm graph paper positioned in the focal plan, was used to scale the detected oil breakup, an example calibration image is displayed in Figure 4.1.
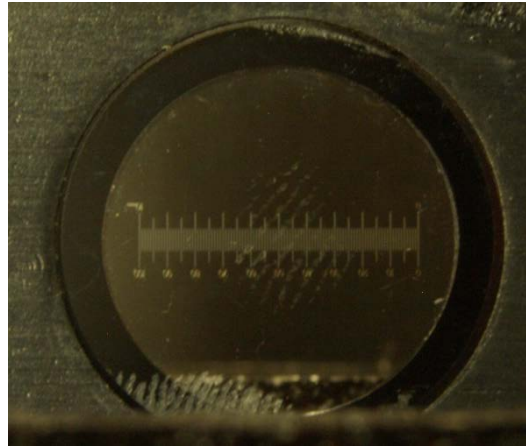

Figure 4.1 Rotating components graticule image calibration

A large number of sequenced images were taken to capture the oil distribution, consequently customised robust image processing codes were developed to process each image set and extract necessary information. The flow chart shown in Figure 4.2 represents the sequence of processes that were applied to the images. Points 1-5 were adapted to suit the specific region of interest ensuring that the oil distribution and oil drops were detected and measured correctly.
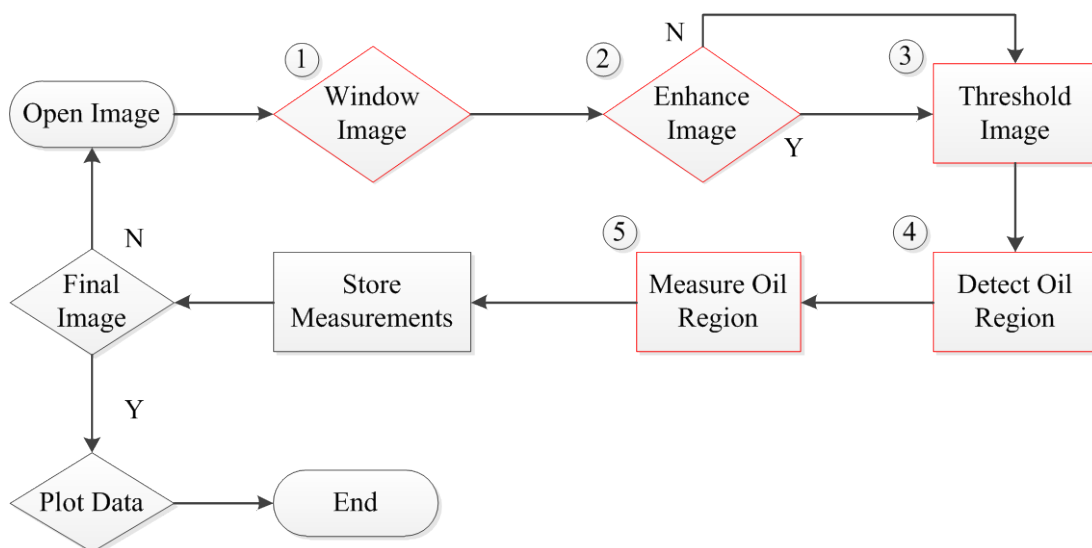

Figure 4.2 Oil detection image processing flow chart

Both the grey scale high speed camera images and RGB DSLR images were processed in an 8 bit grey scale. A selection of filters were applied to the images to remove noise and enhance the image contrast, the filters that were used are listed in Table 4.1. The strength and number of kernel passes varied between image sets, depending on the initial image quality and the required final image.

Table 4.1 Image filters (Gonalez, Woods, 2001)

Filter Name	Filter Application
Wiener	Adaptive low pass noise filter
Median	Noise flter for removing impulse or salt and pepper noise
Disk	Averaging filter
Sobel	Edge detection
Laplacian	Edge detection

For most data sets the quality of the raw images was high, therefore a threshold was applied directly to the windowed image. Either adaptive or finite threshold values were used to convert the grey scale images into binary. Figure 4.3 shows the 8 bit grey scale histogram from a raw image of the oil distribution around the rockers. The majority of the image is in the higher end of the grey scale, with the drops present in the peak at the bottom of the grey scale.
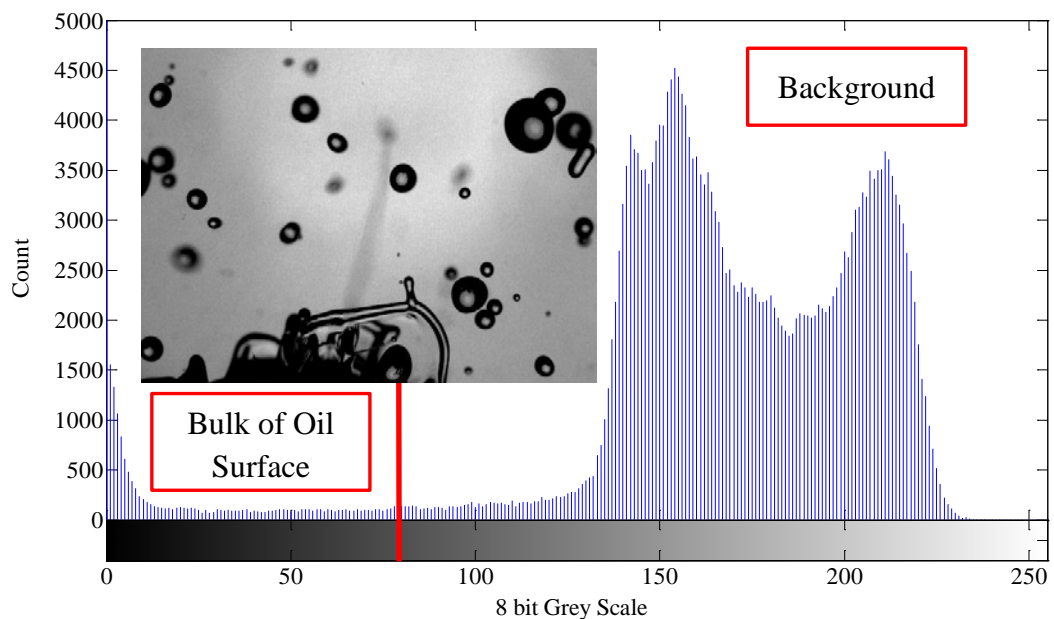

Figure 4.3 Raw image of rocker oil distribution and 8 bit grey scale histogram

A threshold value was chosen so that the oil could be detected from the background and engine components. Figure 4.4 shows the binary images resulting from both a good and bad threshold. A poor threshold has been achieved in the image on the right of Figure 4.4, as the drops at the edge of the image cannot be identified. The diffused copper vapour illumination caused excessive bias, consequently the dark background is present in the final binary image, for this reason care was taken when using an adaptive threshold value. In most circumstances, as the optical setup was constant, a fixed threshold value could be used and assessed manually.
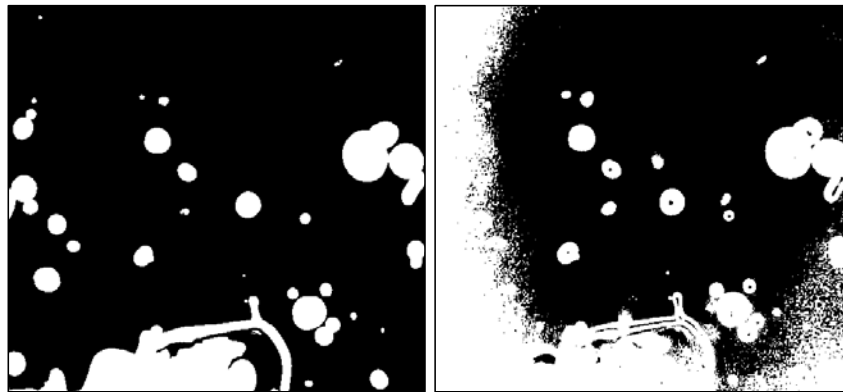

Figure 4.4 Image processing (a) good threshold (b) bad threshold

Often when using back illumination, the oil drops and ligaments had a dark boundary but a bright centre, where the incident laser light was reflected inside the oil drop. The boundary of the oil drops and ligaments could be detected but their surface was not completely filled, to overcome this the MATLAB function *imfill* was used. The *imfill* function filled in holes of background pixels that could not be reached by filling the background from the edge of the image. The returned image contained the filled oil surface, making drop and ligament detection much easier. In Figure 4.4 (a) the *imfill* function has been used, in Figure 4.4 (b) the oil drops and ligaments have not been filled. The *imfill* function was reliant on having a solid bounding edge to the oil surface, to improve the accuracy of the boundary location edge detection filters where applied.

The powerful image processing functions *bwlabel* and *regionprops* were implemented to analyse the images, the functions used a kernel with a specified shape and size, recording geometric measurements of connected pixels. The recorded

data included area, eccentricity and centroid location. The centroid location and equivalent drop diameter were plotted in the image window to indicate detected components, as shown in Figure 4.5 by the red crosses and a blue circles. Displaying the drop information in the image window enabled simple human assessment of the image processing performance for each data set. The recorded area and eccentricity values were used to differentiate between large oil films, oil ligaments and oil drops. All the geometric data from sequenced images was stored in an external Excel file. An example plot of drop diameter for one image of the rocker oil distribution is shown on the left of Figure 4.5.
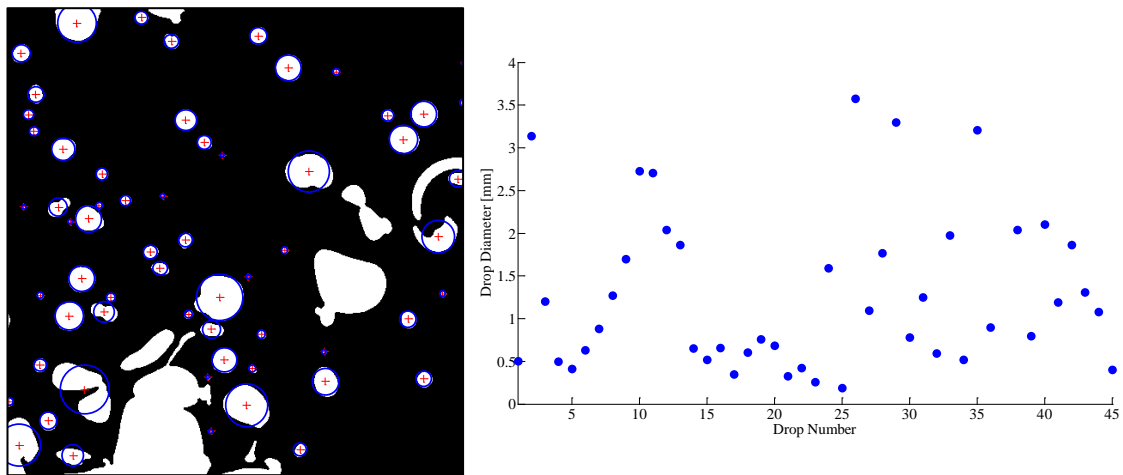

Figure 4.5 Detection and measurement of oil drops (a) detected drops (b) drop diameter

The drop velocity was measured using the series of processes listed in Figure 4.6. In a similar manner to that discussed previously, the x and y locations of drop centers for a series of consecutive images a known time apart were stored. The MATLAB function *track* was then used to connect drops between consecutive images that have similar x and y pixel locations, as the image separation and pixel calibration were known, the drop velocity between images could be calculated.
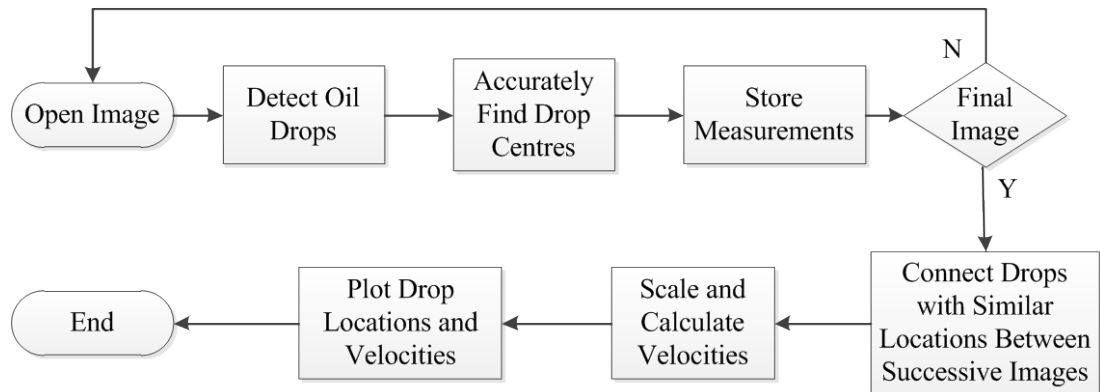
Figure 4.6 Drop velocity image process flow chart

The main image processing tools have been introduced in this section, however, as indicated the code was refined for each data set to ensure that the oil atomisation and aerosol generation was quantified correctly.

4.3 Crankshaft Imaging

Images of the crankshaft in the sump and engine block were collected using the optical setups shown in Figure 3.15 and Figure 3.16, annotation in the figures indicates the position of the high speed camera and halogen illumination. Example images are shown to the right of the optical setup. For further clarity the individual components that are visible in the recorded images are displayed in the annotated CAD assembly in Figure 4.7.
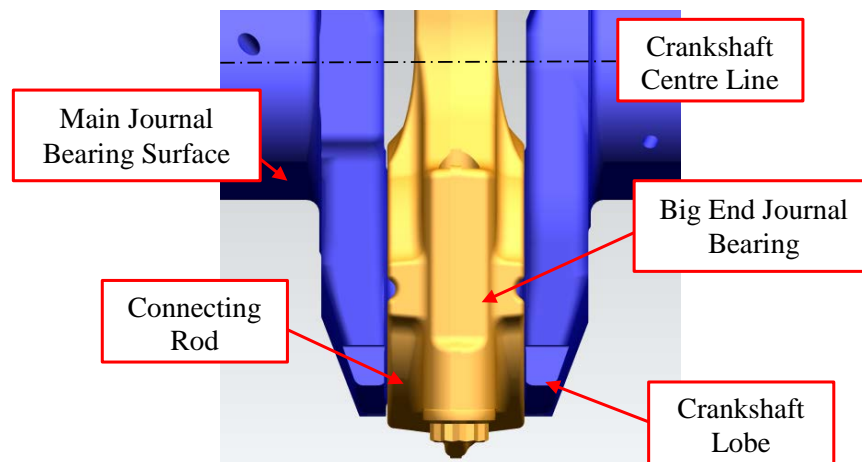

Figure 4.7 1104C-44 CAD image of crankshaft assembly

Oil pressure and flow rate are critical to the oil atomisation, on the 1104C-44 engine these values vary with engine speed as the oil pump is driven directly by the crankshaft. The oil pressures and flow rates at varying engine speeds in the oil rail, which supplies the crankshaft journal bearings, are shown in Figure 4.8. For all the images discussed in this chapter a steady state blow-by of 40 litres.min^{-1} at 100°C was introduced into the crankcase, the engine block was heated to 90°C and the oil rail temperature was 60°C, any variations from these test conditions is specified. Due to the full engine assembly being used, as highlighted in Table 3.1, the fundamental oil distribution was examined at 360, 600 and 900 rpm engine speeds.
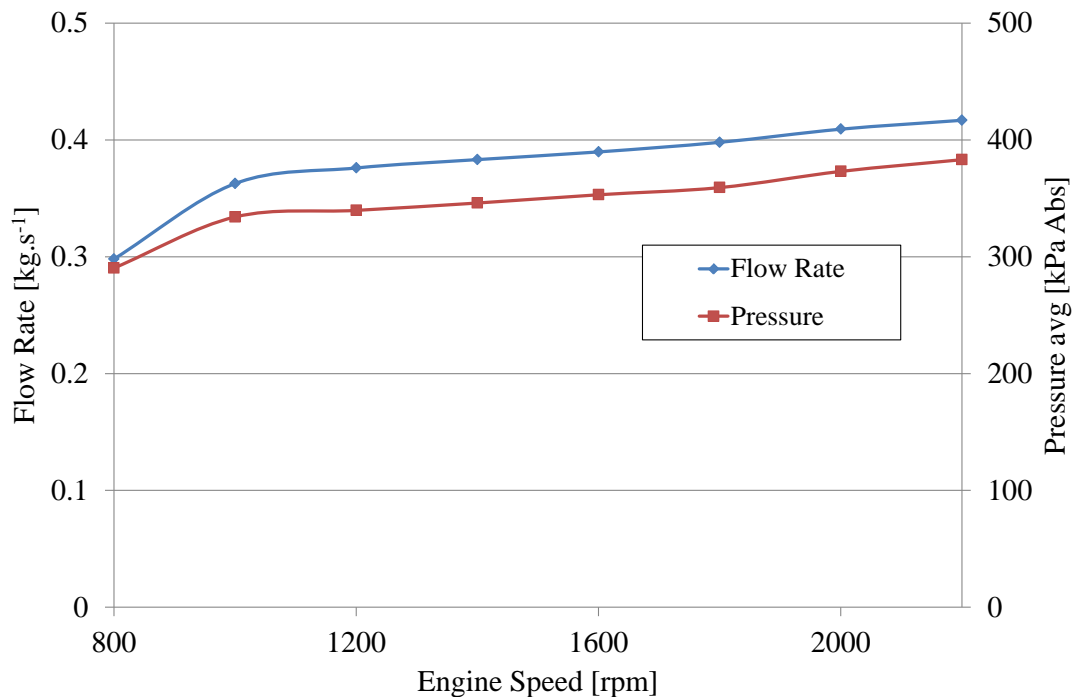
Figure 4.8 1104C-44 oil rail pressure and flow rate

4.3.1 Crankshaft Oil Atomisation

Oil at high pressure is delivered to crankshaft journal bearings, where it leaks from the bearing shells and flows out to form a film on the rotating crankshaft assembly. The thickness of the oil film on these components is controlled by the surface tension and dynamic viscosity of the oil and the crankshaft angular velocity. The corresponding values for the SAE 15W-40 oil, used for all the tests discussed in this chapter can be found in Appendix B Section B-1.

Figure 4.9 shows the substantial oil film coating the connecting rod when the crankshaft is rotating at 360 rpm. These images were collected using the optical setup shown in Figure 3.16, which consisted of a high speed camera and front halogen illumination through a window in the engine block. At a low engine speed of 360 rpm key factors of the crankcase oil distribution were clearly visible. Oil ligaments were drawn from the crankshaft as it rotated and breakup of these ligaments generated oil drops. Images captured oil ligaments and drops impacting on the crankshaft and coalescing into the oil film.
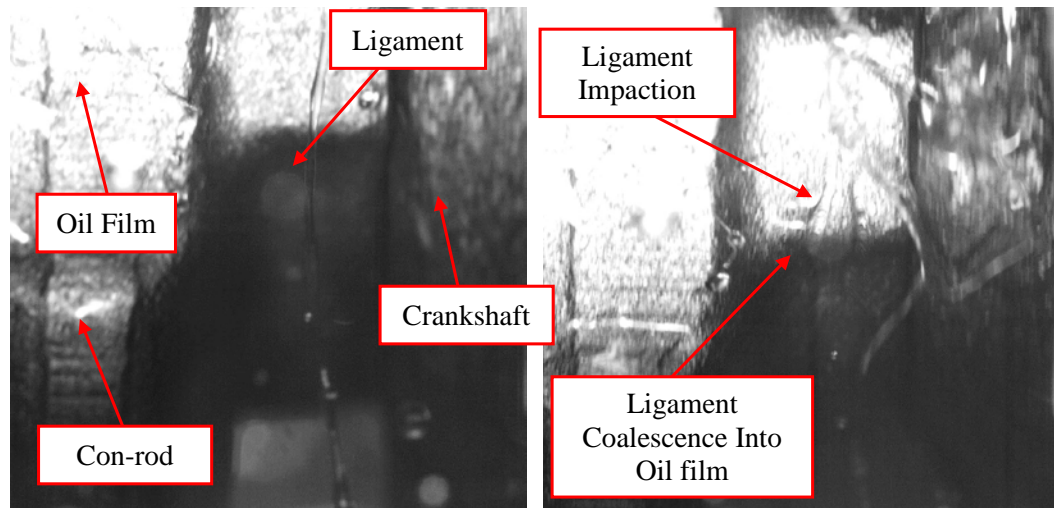
Figure 4.9 Connecting rod oil distribution and oil ligament impaction at 360 rpm

The increase in oil pressure and flow rate at higher engine speeds had a dramatic effect on the oil distribution and aerosol generation. At 600 rpm compared to 360 rpm in Figure 4.10 there is a noticeably higher level of oil around the crankshaft assembly and there are a range of different drop sizes present. Importantly small atomised drops were seen to travel vertically up the crankcase from the sump.
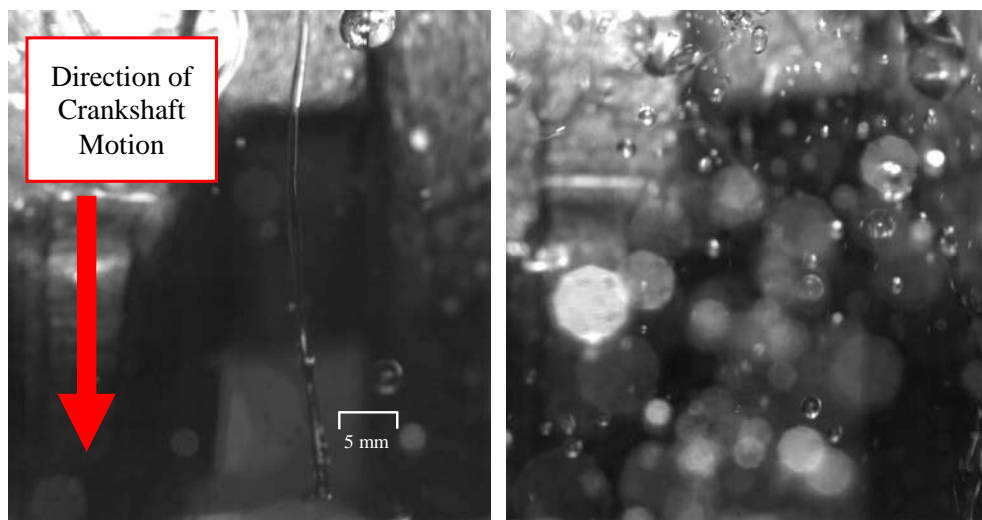

Figure 4.10 Connecting rod oil distribution (a) 360 rpm (b) 600 rpm

The high speed camera was moved to an angle of approximately 45° to the centre line of the crankshaft, so that back illumination across the sump enabled the crankshaft oil aerosol generation to be captured in more detail. A diagram of the imaging setup and a sample image is shown in Figure 3.15.

Images in Figure 4.11 show that at an engine speed of 360 rpm the angular velocity of the crankshaft was sufficient to separate the oil film from the crankshaft surface and generate oil ligaments thrown ahead of the crankshaft.
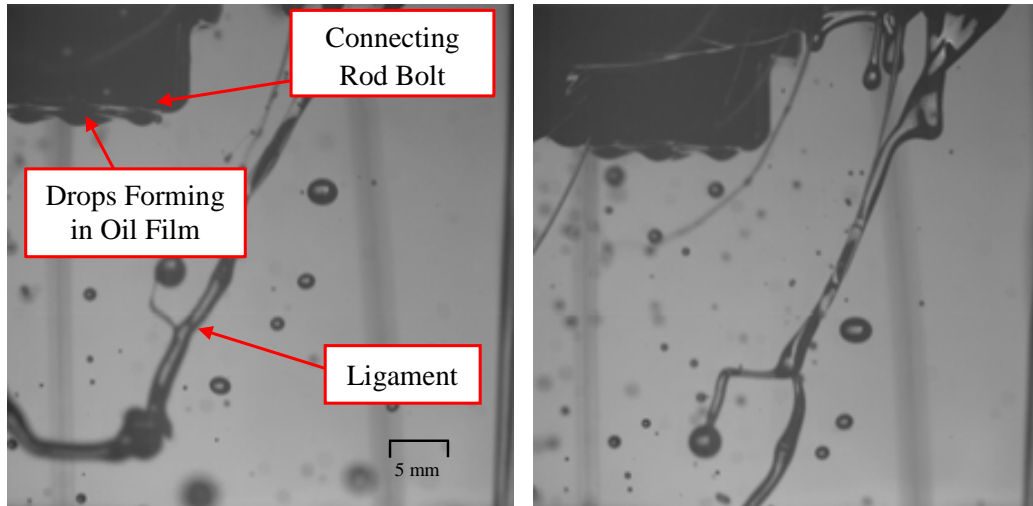

Figure 4.11 Crankshaft approach ligament formation at 360 rpm with 4 ms image separation

The images in Figure 4.12 show that thinner ligaments are generated and stretched away from the crankshaft surface as the crankshaft angle is increased and the crankshaft moves up out of the image. The ligament generation was a result of the crankshaft rotation, the mechanics of this process are discussed further in Section 4.3.4.
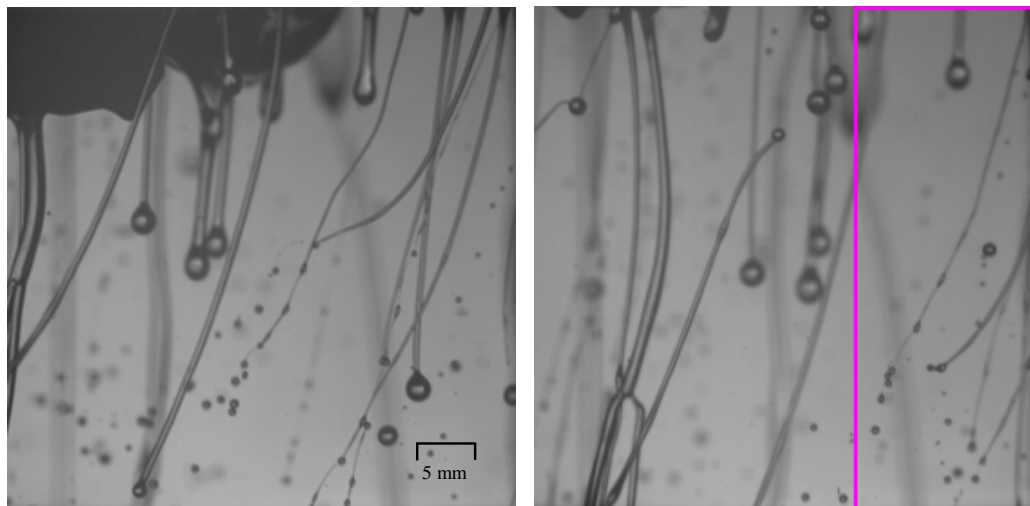

Figure 4.12 Crankshaft departure ligament growth at 360 rpm with 6 ms image separation

Following ligament generation, any blow-by present in the crankcase provides a disruptive aerodynamic force. As discussed in Section 2.5, the surface tension of the oil opposes any disruption from external forces and generates surface waves in the ligament. The capillary waves in the ligament causes necking, when the oil ligament thickness is small enough the neck breaks and drops are generated. The initial stages of Rayleigh breakup of oil ligaments has been captured in Figure 4.13, which focuses on the bounded region to the right of the last image in Figure 4.12.
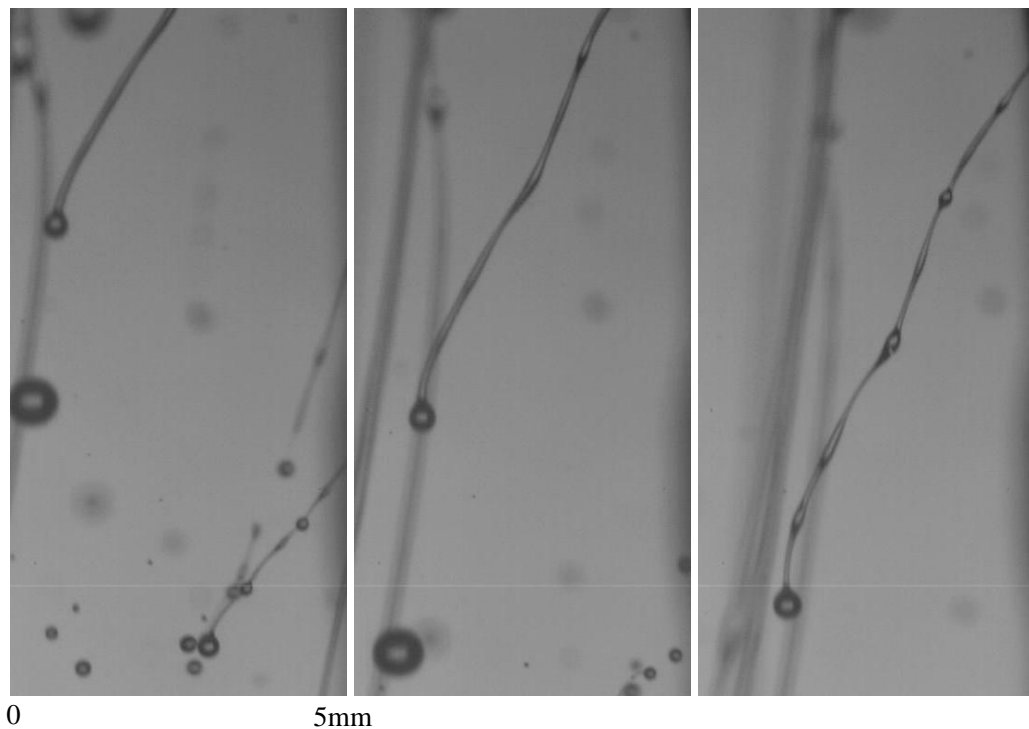

0   5mm

Figure 4.13 Oil ligament breakup at 360 rpm with 3 ms image separation

Figure 4.13 and Figure 4.14 show that as necking occurs a series of drops in the hundred micron to millimetre range form along the length of the $500\,\mu\text{m}$ thick oil ligament. Ideal Rayleigh jet breakup predicts the generation of drops in this size range as shown in Equation (4.1), which states that drops 1.89 times the diameter of the liquid jet will be generated.

Idealised Rayleigh Jet
Breakup

$$d_p = 1.89 \times 2a_L \qquad\qquad (4.1)$$
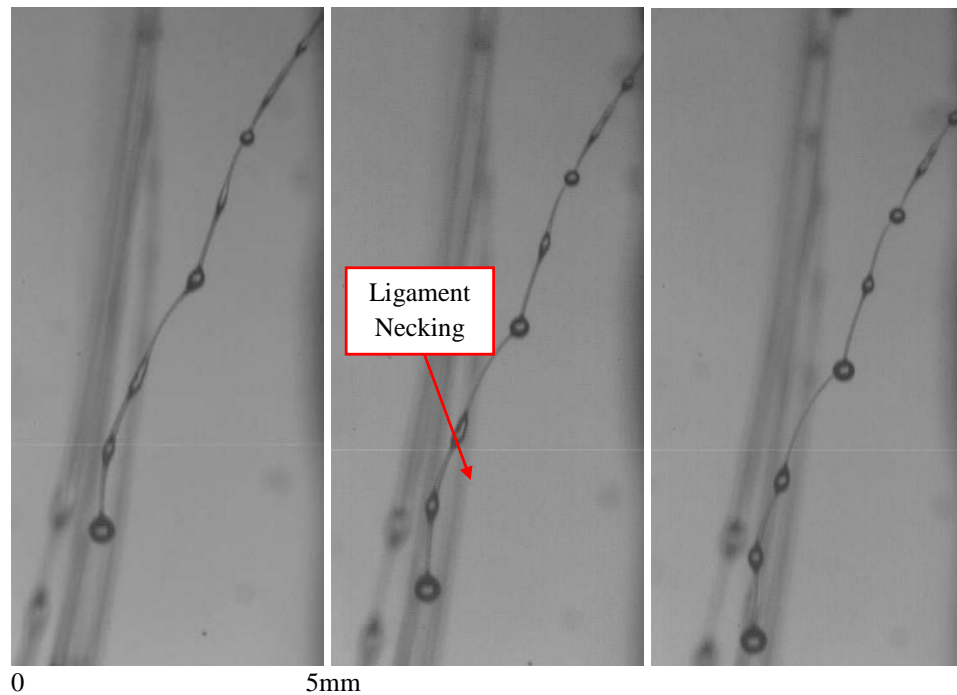
0   5mm

Figure 4.14 Oil ligament necking at 360 rpm with 1 ms image separation

Ideal Rayleigh jet breakup does not completely represent the oil aerosol generation from the crankshaft. Examining the process in more detail in Figure 4.15, reveals that breakup of the thin necks connecting the main drops generates a range of drops from $d_p = 100\,\mu m$ to $d_p = 200\,\mu m$. The surface tension of oil acts to draw the oil into the largest volume, therefore the neck connecting the drops was thickest next to the drop. When the neck broke up, as shown in the final image of Figure 4.15, the largest drops are generated closest to the main drops. Small drop generation was not always witnessed, when the neck thickness was sufficient it separated from one or both of the main drops but was drawn together to form a large drop, this process is highlighted in the top of the last image in Figure 4.15.
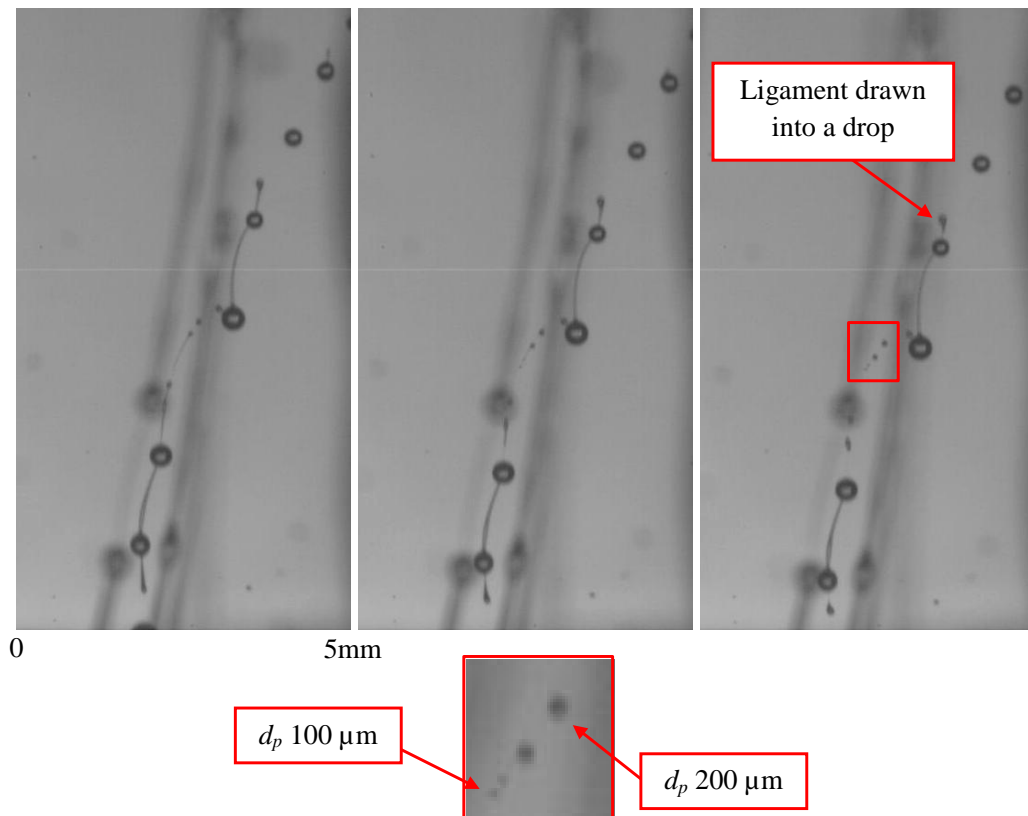
Figure 4.15 Crankshaft oil ligament breakup at 360 rpm with 0.3 ms image separation

4.3.2   The Effect of Crankshaft Speed On Drop Generation

Increasing the rotational speed of the engine from 360 to 600 and 900 rpm increased the number of ligaments and reduced the ligament thickness, therefore reducing the mean diameter of drops. The change in drop generation with engine speed is apparent when comparing the three images in Figure 4.16 which were taken at BDC. At 900 rpm there was increased blurring of the high speed images, compared to the lower engine speeds due to the higher number concentration of small drops and the presence of oil vapour in the crankcase. Table 4.2 presents the mean drop diameters for images at 0, 50 and 310° CA for varying engine speeds. The decrease in mean drop diameter was most significant between 360 and 600 rpm, falling by almost 300 μm.
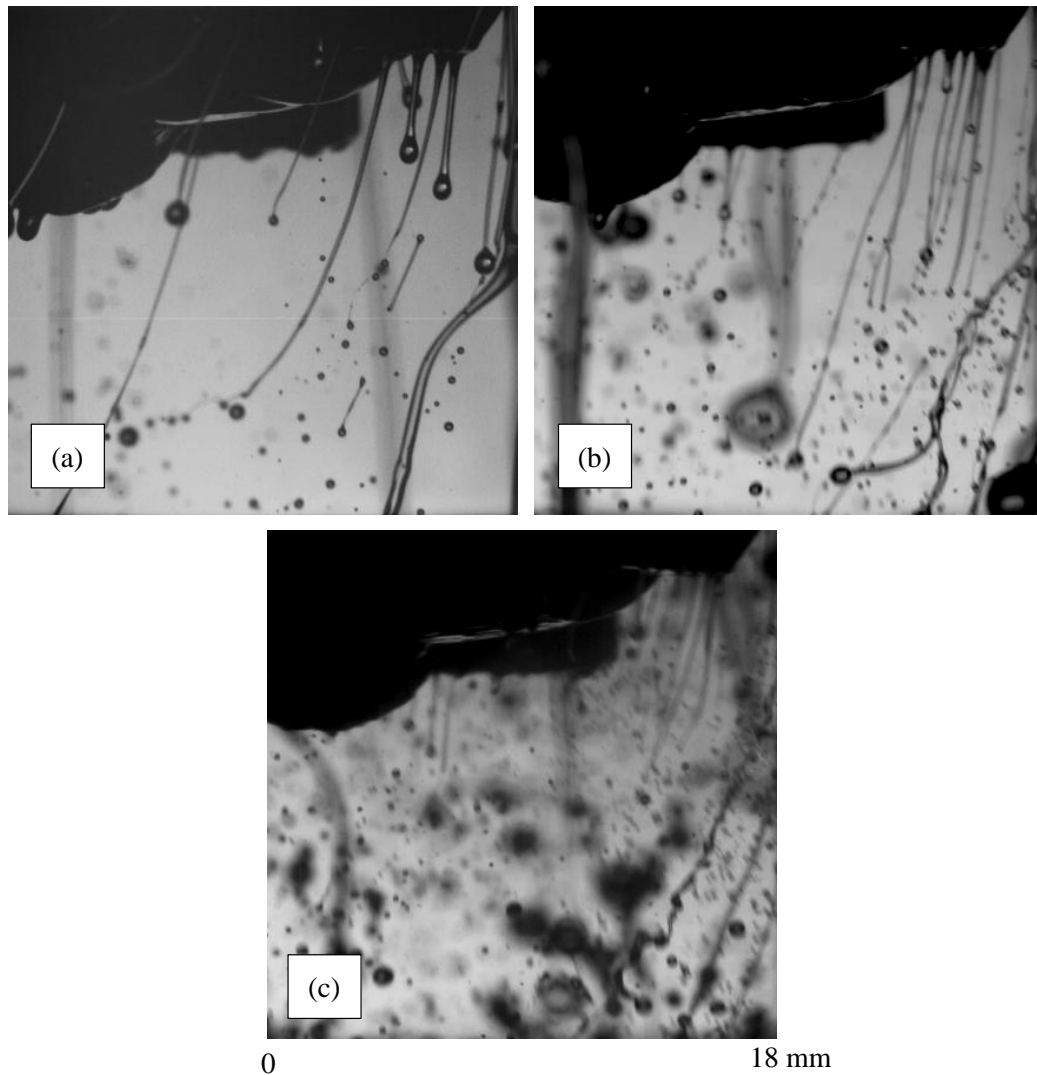
0   18 mm

Figure 4.16 Crankshaft oil drop generation speed comparison at CA BDC (a) 360 rpm (b) 600 rpm (c) 900 rpm

Table 4.2 Effect of engine speed on mean drop diameter between images at 0, 50 and 310° CA

Speed [rpm]	Mean Drop Diameter [μm]
360	803
600	526
900	496

At higher engine speeds the angular velocity and normal acceleration of the crankshaft are higher. Coupled with this the oil rail pressure and flow rate also increase, as shown in Figure 4.8, therefore more oil leaks from the crankshaft journal bearings onto the crankshaft.

The reduction in ligament thickness and mean drop diameter can be attributed to the increase in angular velocity and therefore the normal acceleration acting on the oil film. Thinner ligaments are generated by the crankshaft at a higher angular velocity and breakup into drops occurs quicker. The development and motion of the oil ligaments can be seen in Figure 4.17. Initially the curvature of the ligaments follows that of the crankshaft lobe outer diameter, but as the ligament length increases the oil weight becomes more significant when compared to the normal component of acceleration from the crankshaft and the ligaments straighten out.
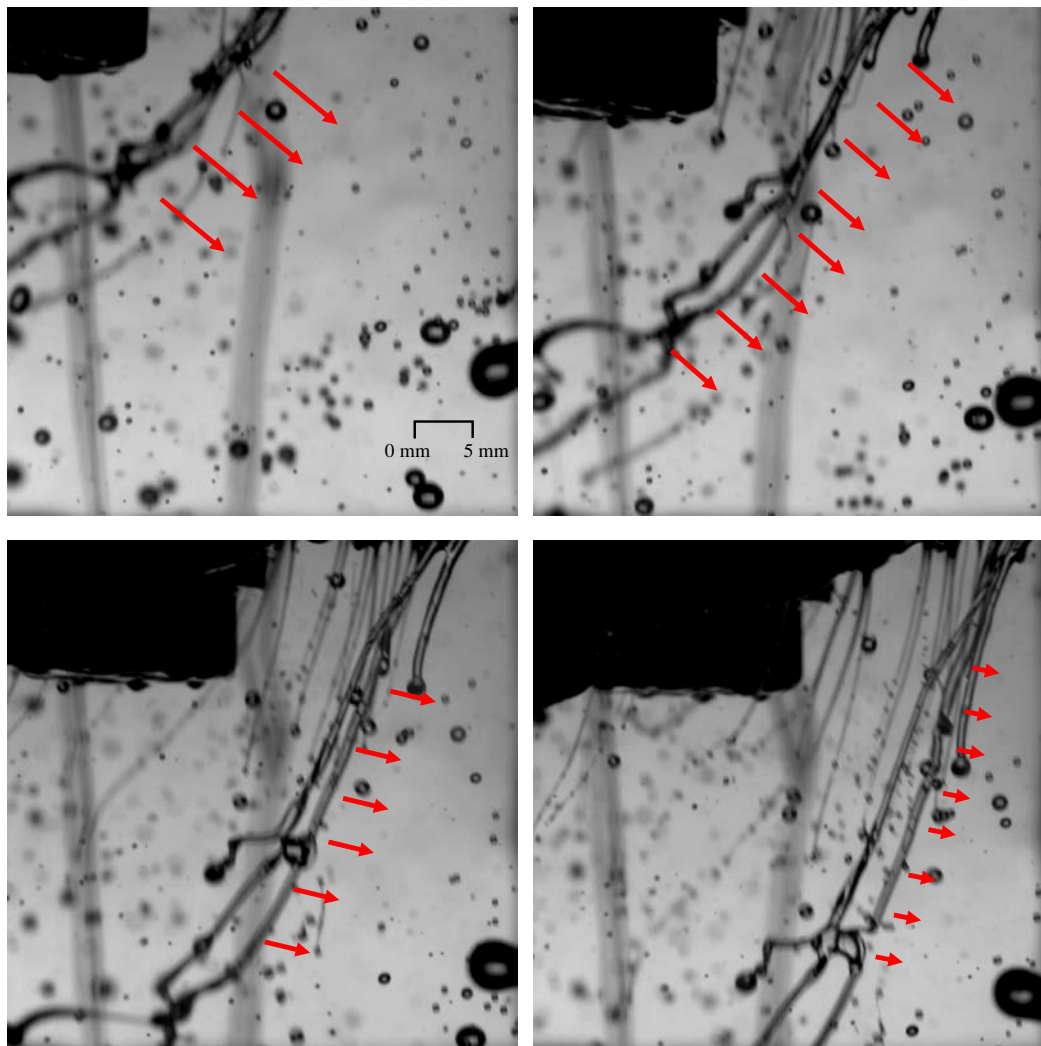

Figure 4.17 Oil ligament development at 600 rpm with 2 ms image separation

The cycle of drop generation from the crankshaft was examined at the fixed imaging position illustrated in Figure 3.16. The drop count measured over 3.5 crankshaft revolutions from BDC is plotted in Figure 4.18. Figure 4.18 illustrates the increase in drop count at higher engine speeds and also the repetitive nature of drop generation from the crankshaft.
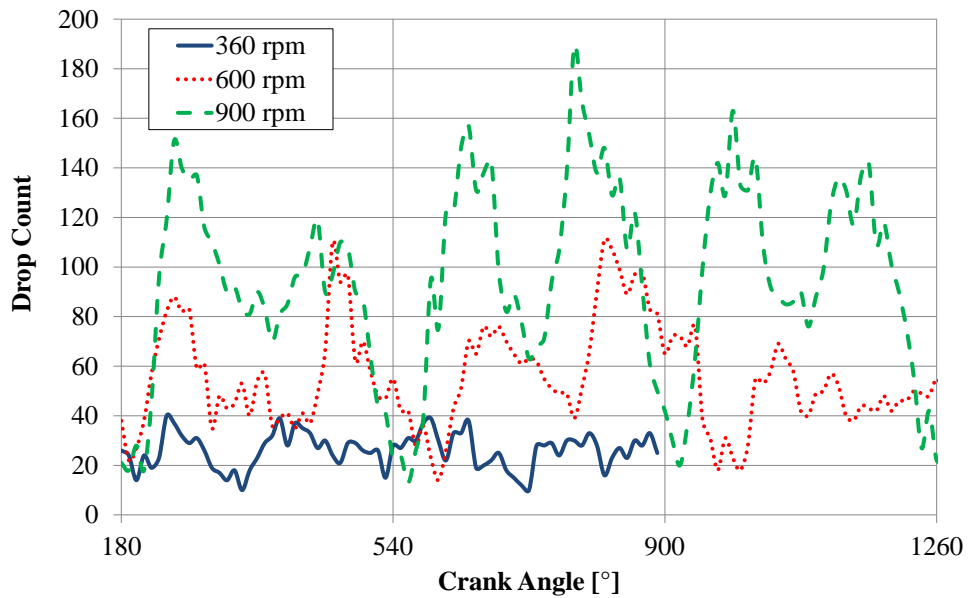

Figure 4.18 Crankshaft generated drop count for three crankshaft rotations from BDC at 360, 600 and 900 rpm
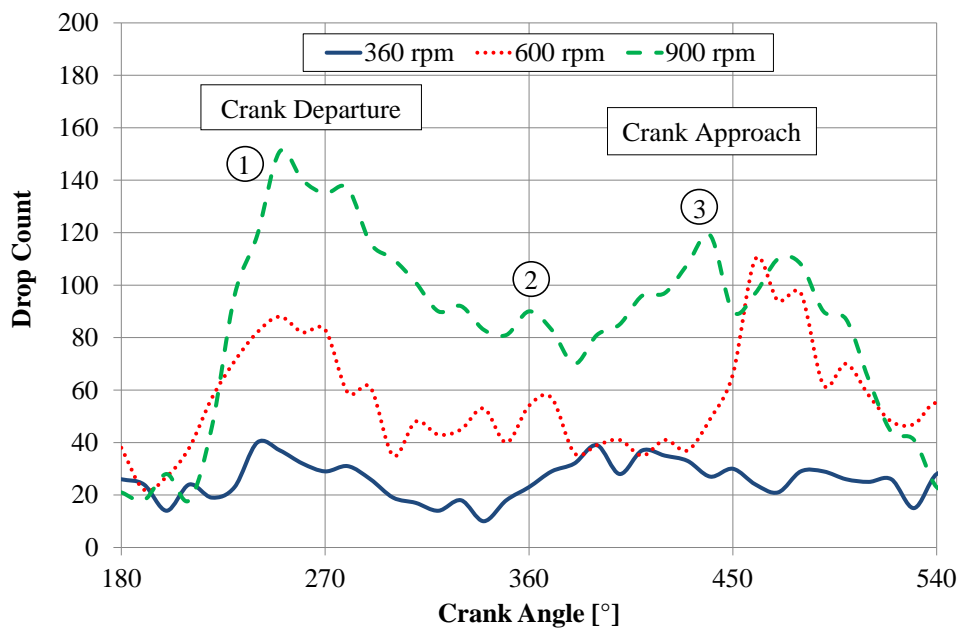

Figure 4.19 Crankshaft generated drop count for one crankshaft rotation from BDC at 360, 600 and 900 rpm

The drop count has been plotted in Figure 4.19 for one crank revolution starting at BDC for the three different engine speeds. Moving from ligament generation at 180° CA, a peak drop count can be seen at 250° CA when the majority of ligaments have been atomised into drops (Point 1 in Figure 4.19). From this first peak the drop count reduced as the drops fell into the sump (Point 2). As the crankshaft moved from top dead centre (TDC) to 450° CA the drop count increased again to another peak (Point 3), as drops thrown ahead of the crankshaft fell into the field of view. The drop count then reduced as the crankshaft approached BDC before the process repeated. Images at the significant CA positions for 600 rpm are shown in Figure 4.20, these images clearly reflect the stages of crankshaft atomisation that have been discussed.
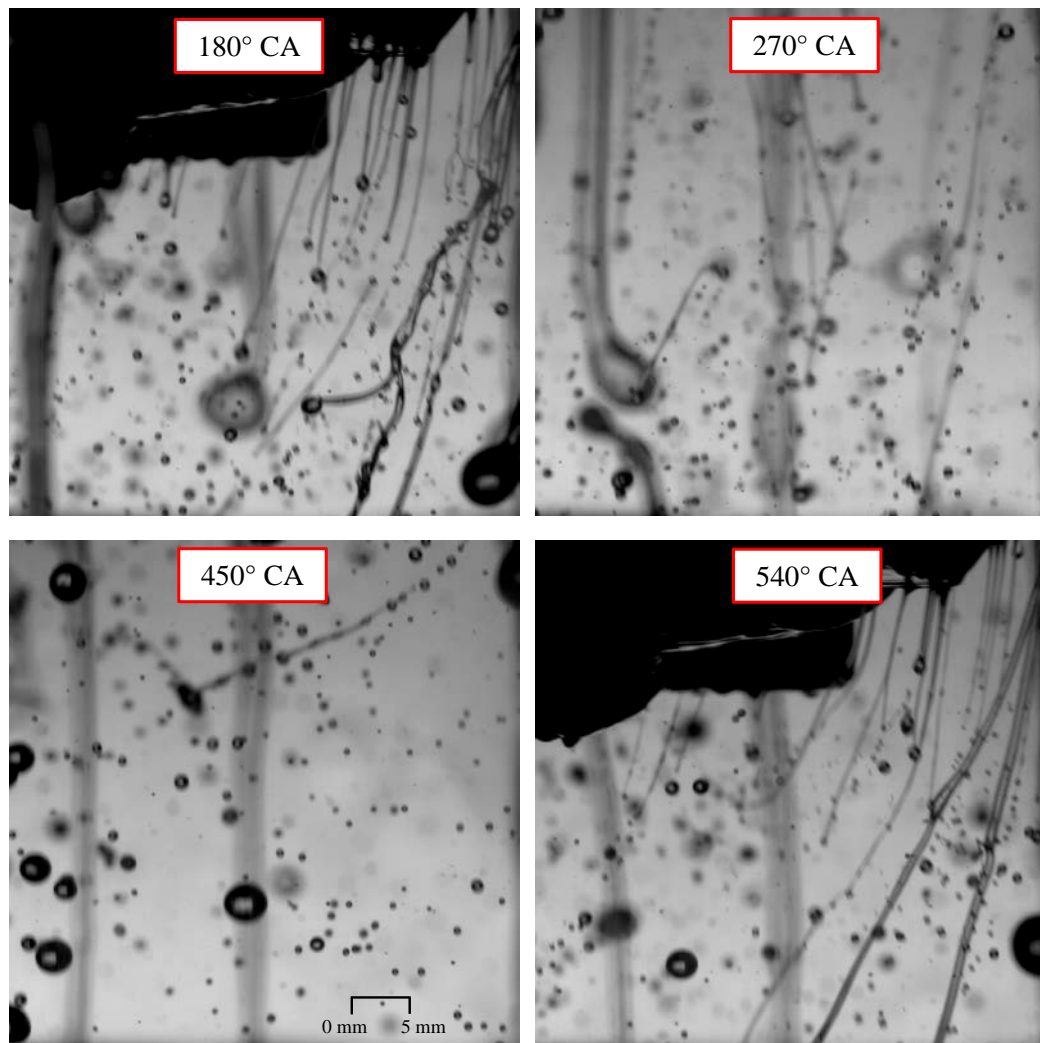

Figure 4.20 Stages of crankshaft oil distribution for a full engine rotation at 600 rpm

At the low engine speeds 360 – 900 rpm, the majority of the drops were too large to be suspended in the crankcase flow and simply fell down into the sump. The image processing techniques discussed in Section 4.2 quantified that at 900 rpm drops $d_p = 1$ mm fell down into the sump with a mean velocity of 5 m.s^{-1}. The velocity of the larger drops that fell into the sump was dependent on the crankshaft speed and drop diameter.

If we neglect drop breakup and assume that a liquid drop will remain at a specific diameter, using Stokes' Law Equation (2.14) we can calculate the aerodynamic force and the associated air velocity required to suspend that drop in equilibrium. The resultant velocity is known as the gravitational induced drop velocity U_g, and can be calculated using Equation (4.2) where ρ_l and ρ_a are the liquid and gas densities respectively, and η_a is the air dynamic viscosity (Raffel, Willert, Wereley and Kompenhans, 2001). The effect of drop diameter on U_g is plotted in Figure 4.21, and shows that for a $d_p = 1$ mm oil drop, a gas velocity of 20 m.s^{-1} would be required to suspend the drop, clearly crankcase gas velocities of this magnitude were not present in the imaged region in the sump, as drops $d_p = 1$ mm were neither suspended in the crankcase flow or atomised via secondary breakup into smaller drops.

$$\text{Gravitationally Induced Drop Velocity} \qquad U_g = d_p^2 \frac{(\rho_l - \rho_a)}{18\eta_a} g \qquad (4.2)$$
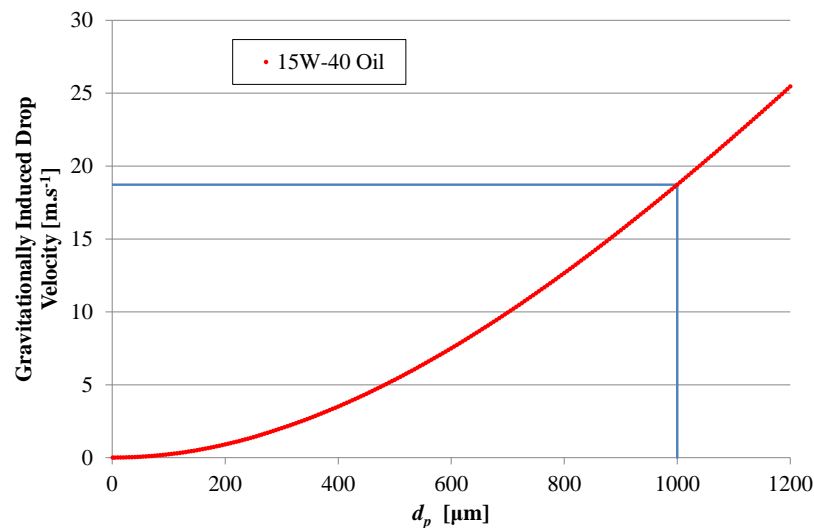

Figure 4.21 Variation in gravitationally induced drop diameter for SAE 15W-40 oil at 60°C in air

Smaller drops approaching the optical limit of the setup were suspended in the crankcase flow and transported around the sump. As discussed in Section 4.3.1, smaller satellite drops were generated from ligament breakup, the crankcase gas velocity was sufficient to suspend and transport these atomised drops around the crankcase. The velocity of the atomised drops, $d_p < 300$ μm, were resolved over a series of successive images at 900 rpm and $\approx 450°$ CA, when the drop count was highest and ligaments were not present. The resulting drop velocities are plotted in Figure 4.22 indicating that at 900 rpm atomised drops were transported with a mean velocity V_d of 1 m.s^{-1} and a maximum velocity of 3 m.s^{-1}.
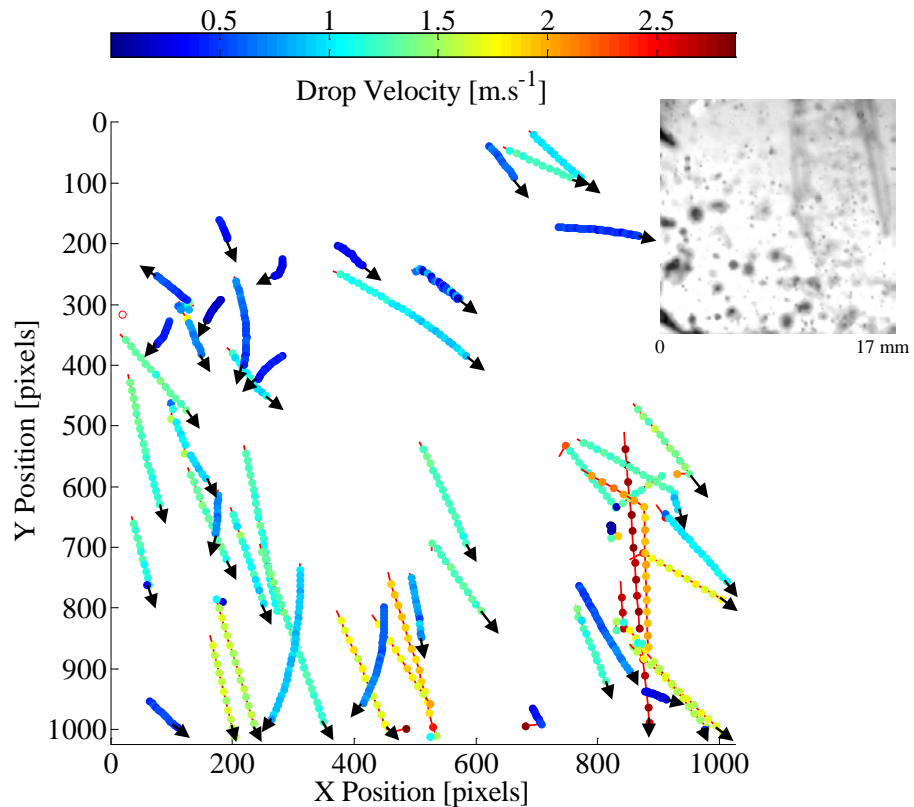

Figure 4.22 Crankshaft atomised drop velocity for 30 images at 900 rpm with 0.3 ms image separation at 450° CA. Image collected using the optical setup displayed in Figure 3.15.

The critical condition for aerodynamic breakup of a drop, in a low Reynolds number flow, is defined by the critical aerodynamic Weber number as displayed in Equation (2.11). The Reynolds number of the air flow around a drop at 77°C travelling at 1 m.s^{-1} is calculated using Equation (2.13) where ρ must be the air density ρ_a and η must be the air dynamic viscosity η_a. Once the Reynolds number is known, the drop drag coefficient C_D can be approximated using the range of

relationships presented in Appendix C Table C-1.1. The resulting critical aerodynamic Weber numbers for a drop of SAE 15W-40 oil at 77°C travelling in air at the same temperature, are plotted against drop diameter in Figure 4.23. The drop velocity required to achieve the critical aerodynamic Weber number was calculated using Equation (2.9) and is plotted in Figure 4.24 against drop diameter.

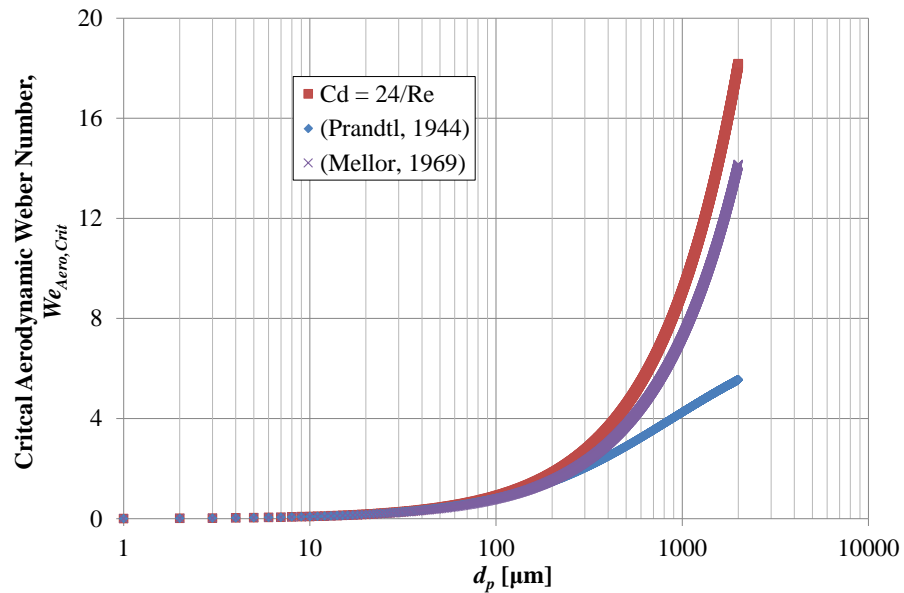**Figure 4.23 Critical aerodynamic drop Weber number based on drops travelling in air at 77°C using a range of drop drag coefficient approximations as displayed in Appendix C Table C-1.1**
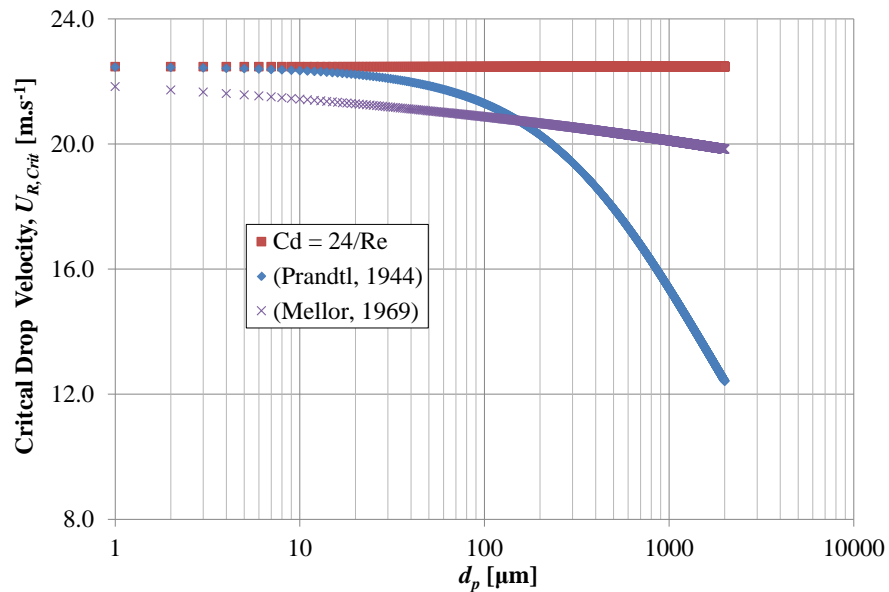

Figure 4.24 Critical drop velocity required for aerodynamic breakup of SAE 15W-40 oil drops at 77°C in air at 77°C using a range of drop drag coefficient approximations as displayed in Appendix C Table C-1.1

Although a series of approximation have been made, Figure 4.24 shows that secondary aerodynamic breakup of drops smaller than 1 mm requires a drop velocity and therefore crankcase flow velocity greater than 12 m.s^{-1}. Initial imaging work has shown that velocities fields of this magnitude are not present throughout the main body of crankcase. The fundamental fluid mechanics presented should be considered if small galleries and channels are designed into the crankcase. Reducing the cross sectional area will increase the flow velocity for a fixed flow rate, therefore potentially generating a Weber number large enough for secondary drop breakup. The blow-by gas velocity in the smallest cross section of the crankshaft is discussed further is Section 4.4.2.

4.3.3 Additional Parameters Affecting Crankshaft Atomisation

For the third and final set of crankshaft and sump images, the aligned windows in the sump and back halogen illumination were still used, however, the camera was positioned perpendicular to the centre of the crankshaft. In Figure 4.25 only one connecting rod and crankshaft lobe are visible, this single image shows more oil ligaments and oil drops in the region around the crankshaft lobe.

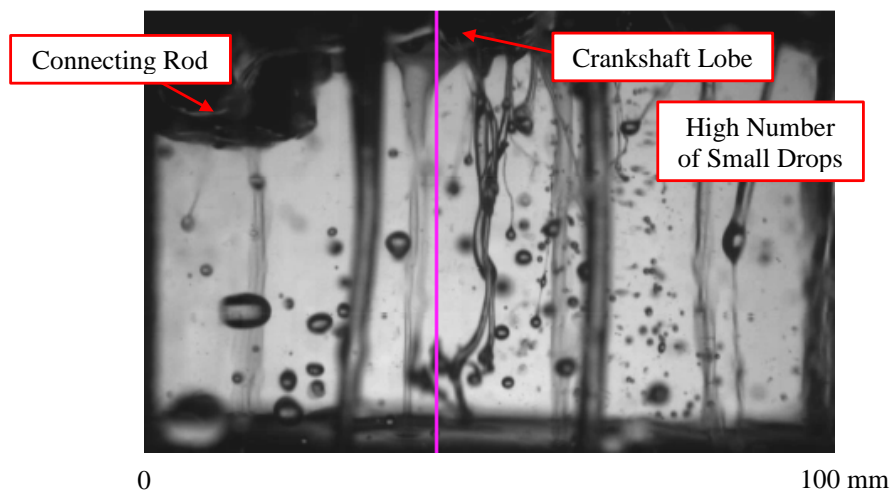**Figure 4.25 Crankshaft imaging across the sump 600 rpm 28°C oil**

To quantify the drop generation in each region, the image was split at the vertical line in Figure 4.25 and the drops on both sides of the image were counted. The drops in each region were counted every 60° CA for a single crankshaft revolution at 600 rpm, the resultant drop diameters and drop count for each region are plotted in

Figure 4.26 and Figure 4.27. The sump oil temperature was only 28°C, however, this should not affect the relative difference between the two regions, it will only affect the global total drop count. As expected the total drop count in the region around the crankshaft lobe was 50% higher and the mean drop diameter was 56% lower at $d_p = 800$ μm.
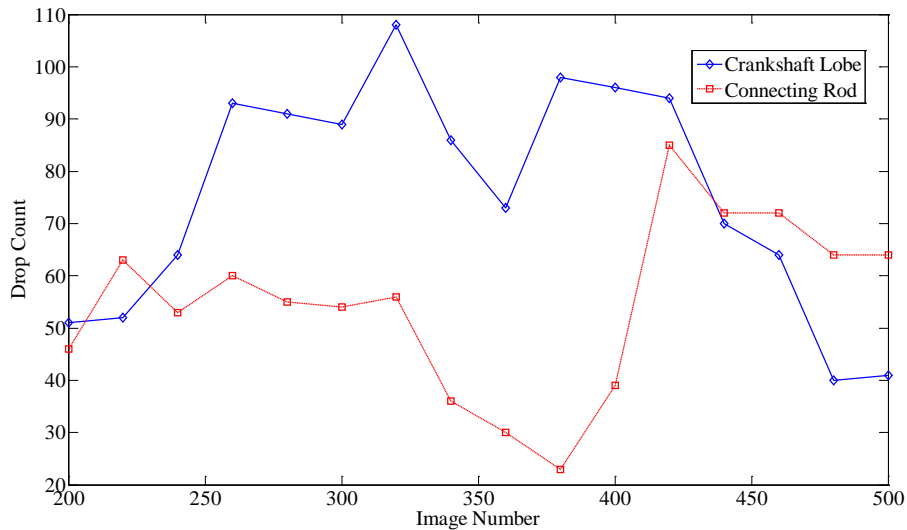

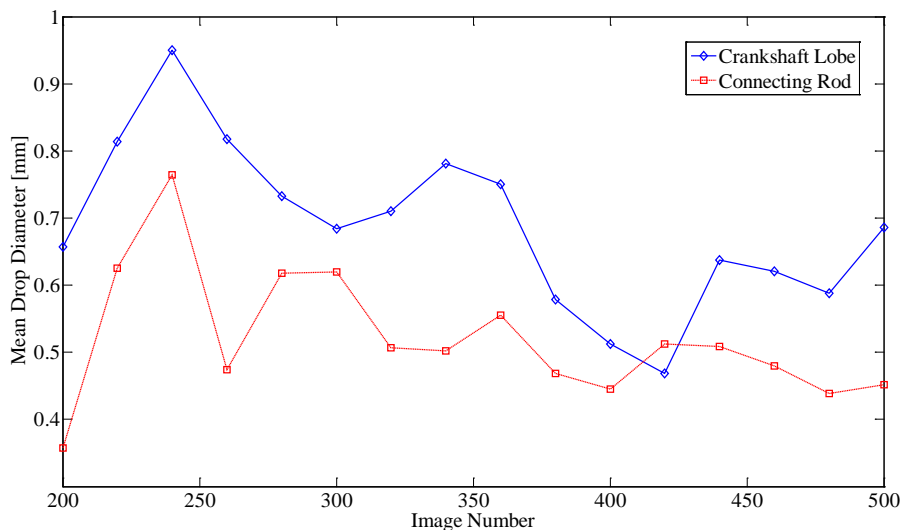**Figure 4.26 Number of drops thrown from the crankshaft at 600 rpm 28°C oil**

Figure 4.27 Diameter of drops thrown from the crankshaft at 600 rpm 28°C oil

4.3.4 Mechanics of Crankshaft Oil Atomisation

Consider the crankshaft rotating at a constant angular velocity ω, with a film of oil coating the outer edge of the crankshaft at a radius r of 99.2 mm. The acceleration (a) of the oil is made of two components as defined by Hibbeler (2004) in Equation (4.3); the normal or centripetal acceleration component a_n shown in Equation (2.6) and the tangential acceleration component a_t shown in (4.5), where v is the tangential velocity component of the oil film. As the crankshaft is rotating at a constant angular velocity the tangential velocity component is constant, therefore the tangential acceleration is zero and the oil film acceleration is composed of only the normal acceleration component.

$$a = \sqrt{a_n^2 + a_t^2} \qquad (4.3)$$

Acceleration of Oil Film

$$a_n = \omega^2 r = \frac{v^2}{r} \qquad (4.4)$$

Normal/Centripetal Acceleration

Tangential Acceleration
$$a_t = \dot{v} \qquad (4.5)$$

A free body diagram of the forces acting on the crankshaft oil film is displayed in Figure 4.28. For a constant angular velocity, the oil remains on the crankshaft when the surface tension force F_σ of the oil over its entire volume is equal to or greater than the normal component of acceleration F_n. When the mass of the oil film is large its weight F_W become significant and depending on the angular position of the oil film, it either acts radially inwards or outwards. The viscosity of the oil film resists the flow of the oil film along the crankshaft surface. The Reynolds number in Equation (2.13) gives a ratio of the inertial and viscous forces. Using the tangential velocity component and the oil film thickness as the characteristic velocity and length, a 3 mm thick SAE 15W-40 oil film at 60°C on the crankshaft rotating at 900 rpm has a Reynolds number of 607. Gohar and Rahnejat (2008) consider that in lubrication problems typically Re < 1, therefore viscous forces dominate. The high

Reynolds number of the crankshaft oil film indicates that inertial force dominates viscous force for large oil films > 1 mm on the crankshaft, therefore it is acceptable to ignore them in this explanation.
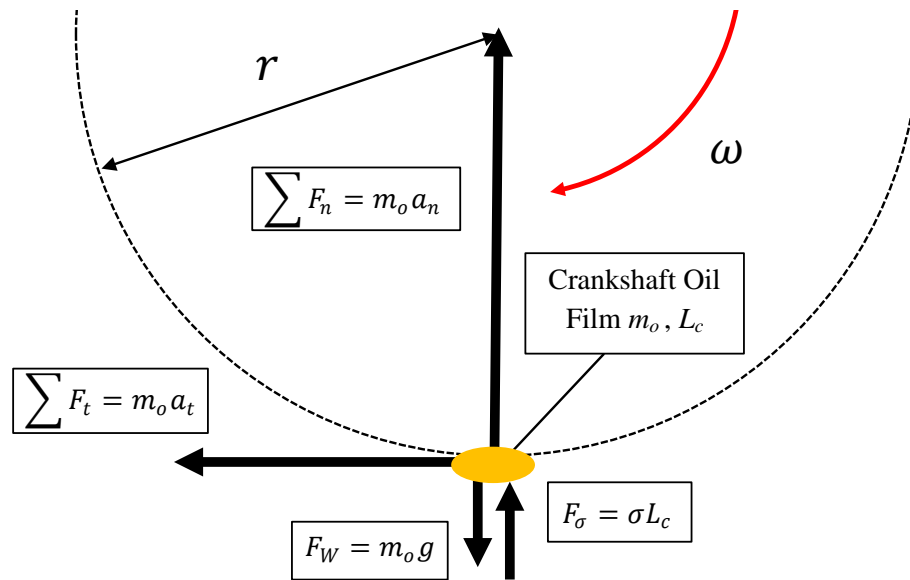
Figure 4.28 Crankshaft oil film free body diagram

Oil Film Forced into
Stable Oil drops

$$F_n > F_\sigma \tag{4.6}$$

Oil Ligaments
Generated

$$F_n \gg F_\sigma \tag{4.7}$$

As shown very clearly in Equations (4.6) and (4.7) when the centripetal force F_n, is larger than the oil film surface tension force F_σ, the oil film will adjust its shape towards an oil drop, therefore increasing the characteristic length of the oil film L_c. If the centripetal force is significantly larger than the surface tension force then oil ligaments are generated from the crankshaft oil film. Even at the lower crankshaft speeds discussed in this section, the surface tension force of the crankshaft oil film was not sufficient, therefore ligament generation was readily witnessed.

4.3.5   Crankshaft Imaging Summary

The range of recorded data clearly shows that the crankshaft is a significant generator of crankcase oil aerosols, as the thick oil films around the crankshaft assembly are atomised into drops $d_p > 100$ μm travelling with a velocity of approximately 1 m.s^{-1}. Drops with a diameter $d_p < 100$ μm and the presence of oil vapour was witnessed. The number concentration of drops increased with engine speed, accompanied by a reduction in the mean drop diameter.

The 900 rpm maximum engine speed tested for this optical study represents a low idle, however, this engine model would spend the majority of its operating life at much higher engine speeds of 1500 – 2200 rpm. Assuming that the crankshaft continues to behave as a rotary atomiser, it will contribute substantially to crankcase oil atomisation throughout the engine speed range. The interaction of the oil surface tension and viscosity against any disturbing force causes the oil atomisation, the process is complex and difficult to predict consistently. The atomisation from the crankshaft should be investigated further to characterise the atomisation processes and aerosol contribution in more detail.

4.4   Pushrod Gallery Imaging

Oil is delivered to the top of the 1104C-44 engine to lubricate the components in the valve train. The cylinder head is designed so that the oil distributed around the valve gear can drain down each of the eight pushrod galleries and return to the oil pump in the bottom of the engine via a series of channels in the engine block.

The schematic of the optically accessed pushrod galleries in Figure 4.29 shows that the eight pushrod galleries are connected horizontally above the tappets. It is only once the oil collects above the tappets that it can finally drain down one of the two channels above the camshaft and into the sump. Due to the positioning of the eight tappets, the two channels above the camshaft have a small cross sectional area of just 1174 mm^2. The oil drains down through the engine following the path described above. Conversely the blow-by generated around the pistons takes the reverse route to the oil and travels up to the top of the engine via the pushrod galleries, this flow path is highlighted by the large arrows in Figure 4.29. For discussion purposes the pushrod gallery has been divided into the three annotated sections in Figure 4.29; the pushrod gallery, the tappet channel and the camshaft channel.
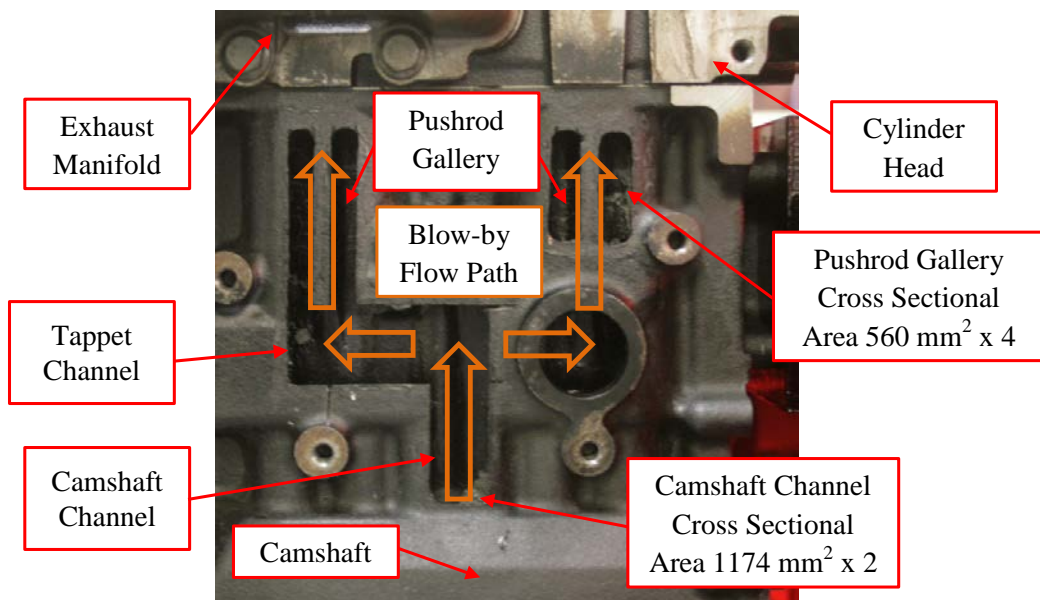

Figure 4.29 Optically accessed pushrod gallery schematic

The mass flow rate and pressure of oil supplied to the top of the cylinder head is shown in Figure 4.30, 70% of the oil pressure and only 6% of the mass flow rate of oil from the pump is supplied to the rocker shaft in the top of the cylinder head.
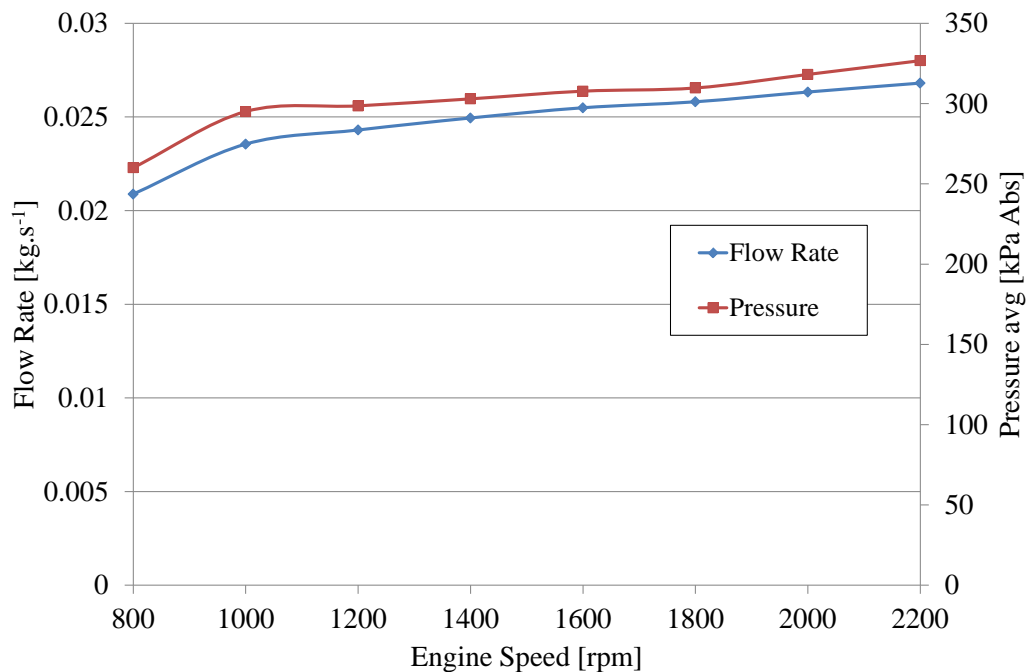

Figure 4.30 Rocker shaft oil pressure and flow rate SAE 15W-40 oil at 60°C

Although only a small percentage of oil is supplied to the top of the engine, it is important that oil is not stagnant in the pushrod galleries or any other region of the crankcase. Poor oil circulation not only increases the chance of oil pump starvation, but it also reduces the effectiveness of heat transfer in the oil circuit. Despite not being the main objective of this work, identifying deficiency in the performance of the whole oil circuit indicates design changes that can reduce the total required oil volume and therefore reduce oil aerosol generation elsewhere in the crankcase.

Imaging in the pushrod gallery was conducted at speeds of 900, 1200, 1500, 1800, 2000 and 2200 rpm. Higher speed capability was achieved by running without pistons and connecting rods, for further clarification the full engine setup is described in Chapter 3 Table 3.1. For all the images presented a steady state blow-by of 40 litres.min^{-1} at 100°C was introduced into the crankcase, the engine block was heated to 90°C and the oil rail temperature was 60°C, any variations from these test conditions is specified.

4.4.1 Fundamentals of Pushrod Gallery Oil Distribution

The high resolution DSLR images in Figure 4.31 were taken using ambient room lighting. These images show that at 1800 rpm there is significant bulk movement of oil in the pushrod gallery. As specified in Figure 4.30, the 26 g.s^{-1} of oil supplied to the top of the engine drains down the pushrod gallery creating a 1 mm oil film on the pushrods. The surface tension and viscosity of the 1 mm oil film at 60°C was sufficient to resist the acceleration of the pushrod and the aerodynamic force of blow-by, preventing oil breakup along the pushrod length. Ripples were visible in the oil film on the pushrod at all engine speeds up to 2200 rpm, but no atomisation was witnessed.
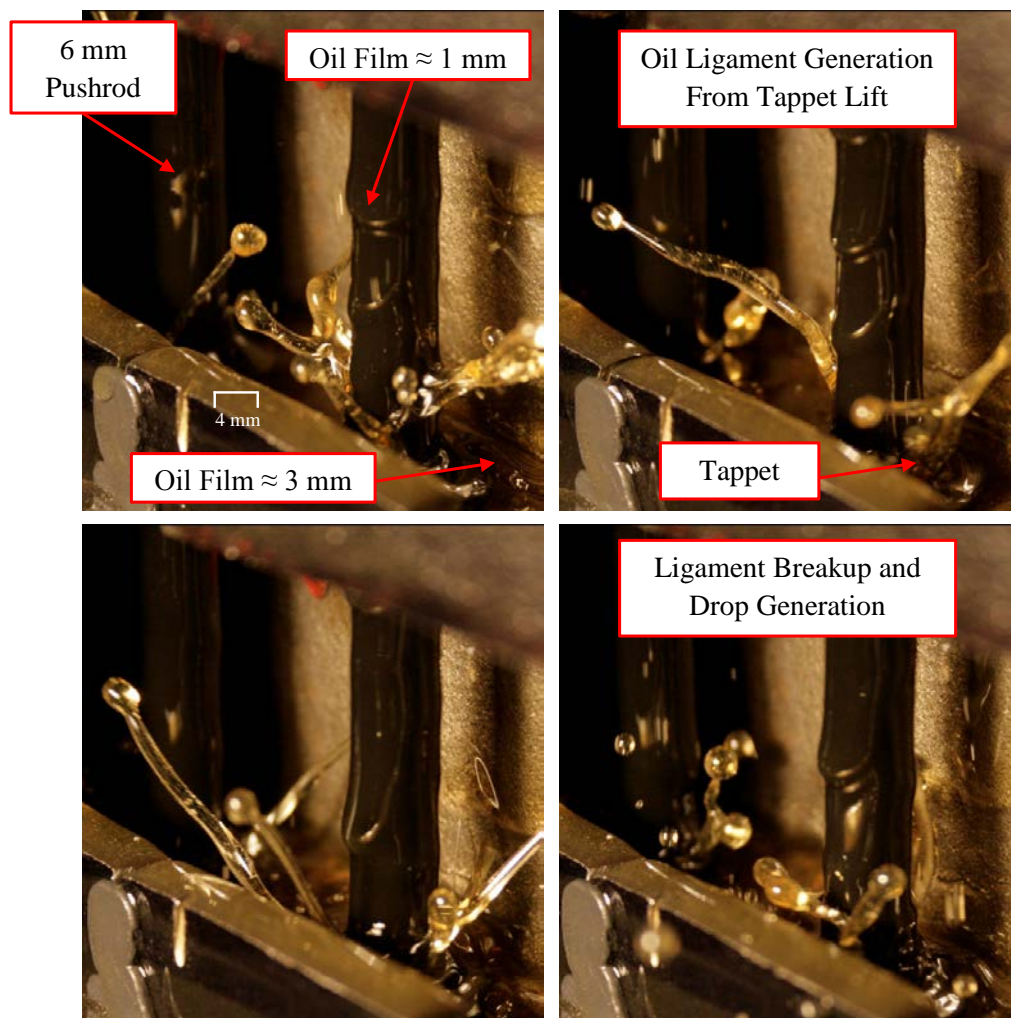

Figure 4.31 Tappet channel and pushrod gallery oil distribution at 1800 rpm

Figure 4.31 shows that the oil draining down the pushrods and the pushrod gallery surface collects above the tappets and creates a 3 mm thick oil film. The surface tension and viscosity of the oil film in this region was not sufficient to sustain the force from the tappet acceleration, large ligaments 1 - 2 mm in diameter were generated. The ligaments were seen to breakup into large oil drops ranging from $d_p = 4$ mm to 1 mm. Finally Figure 4.32 shows that the 3 mm oil film on the tappet channel drains down into the camshaft channel. The data recorded with this initial high resolution DSLR imaging did not show any oil aerosol generation resulting from the motion of the pushrods and the tappets.
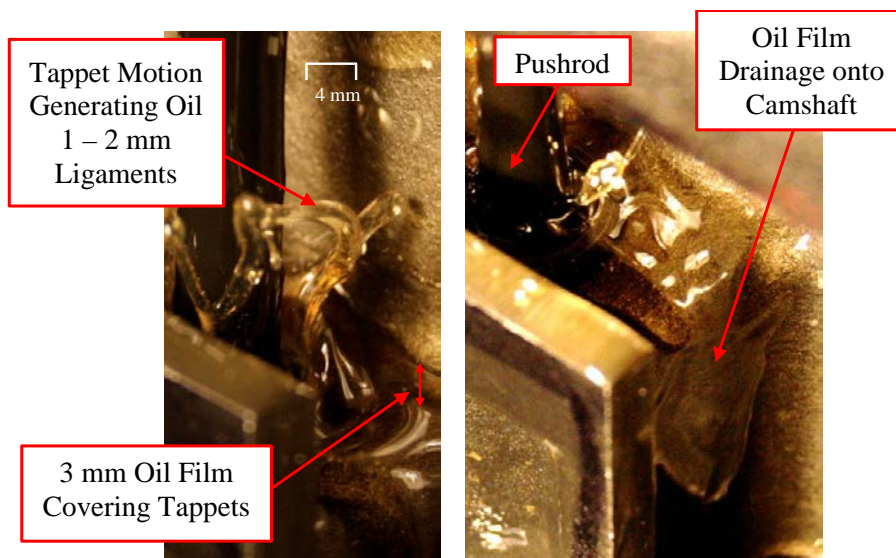
Figure 4.32 Tappet channel oil film at 1800 rpm

4.4.2   Camshaft Channel Oil Aerosol

Oil atomisation in the camshaft channel was investigated initially using high resolution DSLR images illuminated with ambient room lighting. As shown in Figure 4.32 the oil from the tappet channel drains down onto the camshaft and into the sump. Although imaging was not conducted around the camshaft, the velocity and trajectory of small drops thrown up the camshaft channel indicates that oil on the camshaft is atomised in an identical manner to that found on the crankshaft.

Atomised drops generated by both the crankshaft and the camshaft travelled up the camshaft channel. Figure 4.33 and Figure 4.34 show that drops $d_p \approx 100$ μm to $d_p \approx 1$ mm were thrown up the camshaft channel, the trajectory of these drops is

traced in the long exposure DSLR image in Figure 4.33. Drops generated by the tappet motion, on the right side of Figure 4.33, followed a parabolic trajectory across the image and did not contribute directly to the oil aerosol generation, they were simply thrown across to the other side of the camshaft channel or fell down onto the camshaft and into the bottom of the crankcase. The high resolution single shot images of the camshaft channel in Figure 4.34 indicate that for a still image at 1800 rpm the concentration of visible drops thrown up the camshaft channel was drop number $\approx 500\ N.cm^{-1}$. This number concentration measurement is by no means absolute, but it serves to indicate the significant transport of drops up the camshaft channel
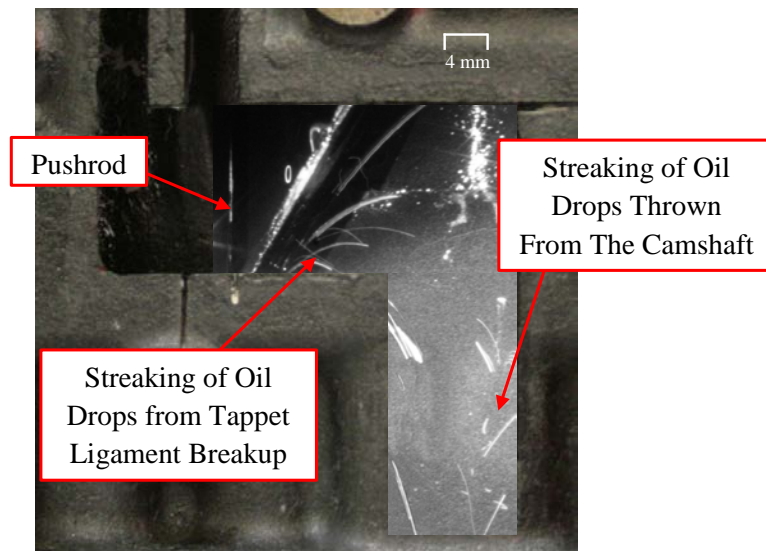

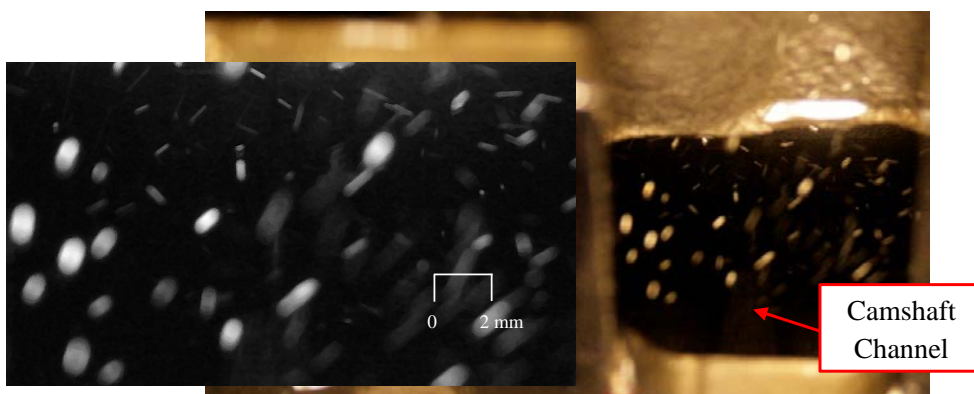**Figure 4.33 Camshaft channel oil aerosol at 1400 rpm**

Figure 4.34 Camshaft channel oil aerosol at 1800 rpm

The oil aerosol in camshaft channel was investigated in more detail using the optical setup annotated in Figure 4.35. The intensity of the illumination was improved by using single fibre copper vapour illumination and a plastic diffusion screen to diffuse the laser light. High speed images were captured at a frame rate of 3000 fps with a magnification of 30 µm per pixel using a Nikon 105 mm lens with a 52 mm expansion ring.

Push Rod
Gallery

Fibre Holder and
Diffusion Screen

105 mm Lens
31 mm and 21 mm
Expansion Rings

Copper
Vapour
Fibre

Photron High
Speed Camera
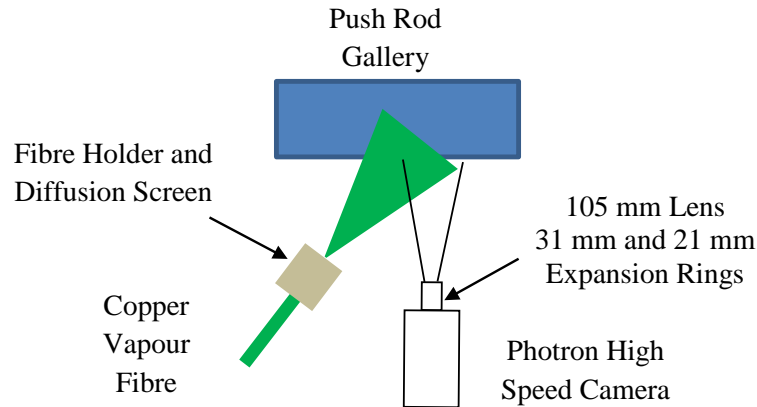
Figure 4.35 Camshaft channel imaging with forward illumination

Incident Light
Diffused
Copper Vapour
511 nm and 578 nm

Geometric Light
Scattering

$d_p = 140\lambda$
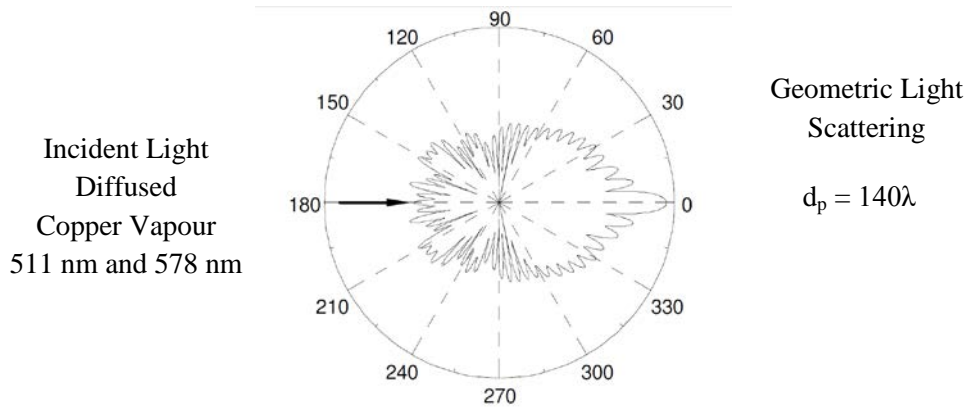
Figure 4.36 Geometric light scattering diagram for oil drops in the camshaft channel

Due to the limited optical access around the camshaft channel it was difficult to introduce sufficient forward illumination to record all the small drops atomised by the camshaft. The drops scattering sufficient light to be captured on the CMOS chip were approximately $d_p = 140\lambda$, therefore geometric light scattering principles were considered to achieve the optimal imaging setup. The scattering diagram in Figure 4.36 shows that the camera had to be positioned at 30° to the laser fibre to collect the maximum intensity of scattered light. Despite optimising the position of

components in the optical setup a large aperture of $f^{\#}$ 5.6 was required to collect sufficient scattered light. Due to the low $f^{\#}$ care had to be taken when positioning the camera as the drops would quickly move out of focus due to the small focal depth and the three-dimensional trajectory of the drops thrown up the camshaft channel.

Despite the difficulties with the optical setup, consecutive high speed images taken at 1800 rpm show that $d_p = 70$ µm drops are thrown up the camshaft channel with a velocity of 1 m.s^{-1}, an example image is shown in Figure 4.37. The recorded images captured the transport of atomised oil drops in the camshaft channel, indicating the potential contribution of the camshaft to crankcase oil aerosol generation, and the large transport of oil aerosol from the bottom of the engine up into hot pushrod galleries and the top of the engine. Qualitative analysis of the camshaft channel images showed that increasing the engine speed from 900 - 2200 rpm increased the drop number concentration and reduced the drop diameter. The small drops were generated either by the crankshaft or by the camshaft.

Oil drops
$d_{p,min}$ 70 µm
$V_{d,avg}$ 1 m.s^{-1}

2 mm
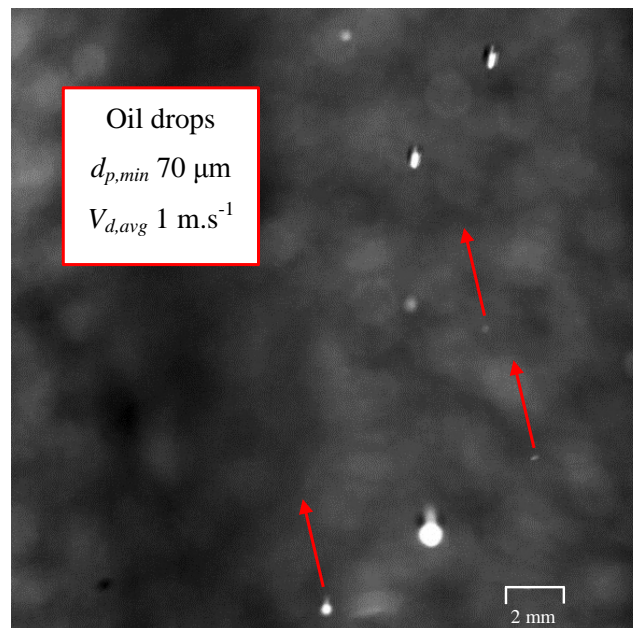
Figure 4.37 Camshaft oil atomisation at 1800 rpm

A second data set was collected with a black plastic background placed at the rear of the camshaft channel, this reduced the scattering of light from the engine block and generated a uniform oil film at the rear of camshaft channel. Drops captured by this optical arrangement were large, $d_p > 150$ µm, they were generated by the tappet and

camshaft motion. Figure 4.38 is a typical representation of the camshaft channel drop distribution. On the left of the image large drops $d_p = 700$ μm to $d_p = 5$ mm generated by the tappet motion recorded in Figure 4.31, were thrown down onto the camshaft and into the sump region. On the right of the image region smaller drops were thrown up by the camshaft. Drops would often collide with each other and depending on their diameter, velocity and therefore Weber number, would exhibit a range of outcomes. In Figure 4.39 two large drops collide and coagulate to form one large oil volume, however, the velocity of the smaller drop is too high for the surface tension and viscosity of the large drop to contain it, although a ligament forms the ligament necks and releases a smaller drop.
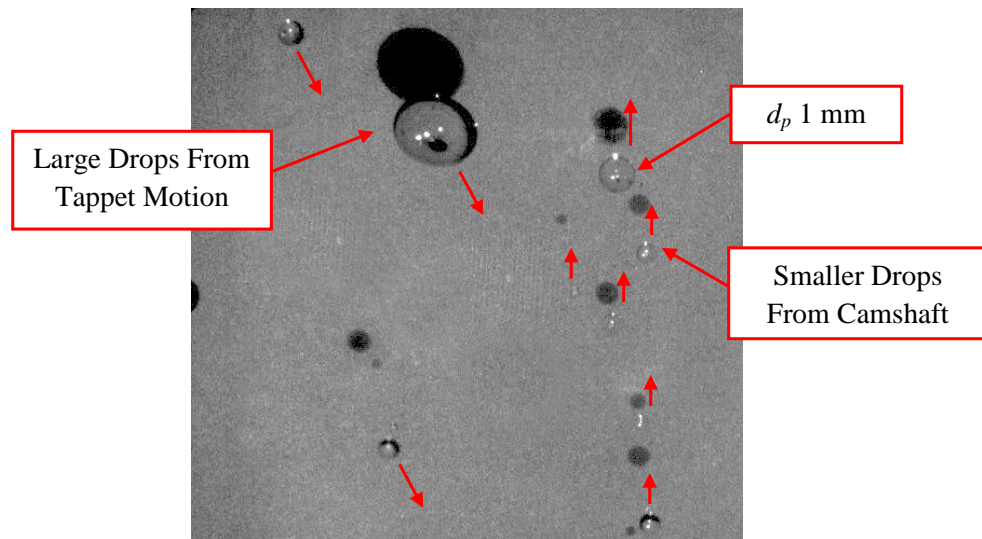

Figure 4.38 Camshaft channel at 2000 rpm
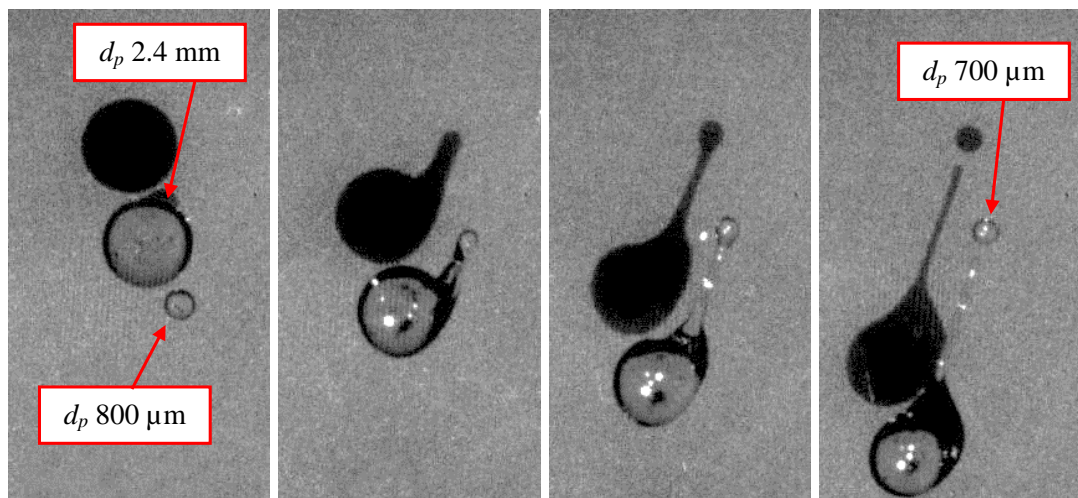
Figure 4.39 Camshaft channel drop collision at 2000 rpm with 3 ms image separation
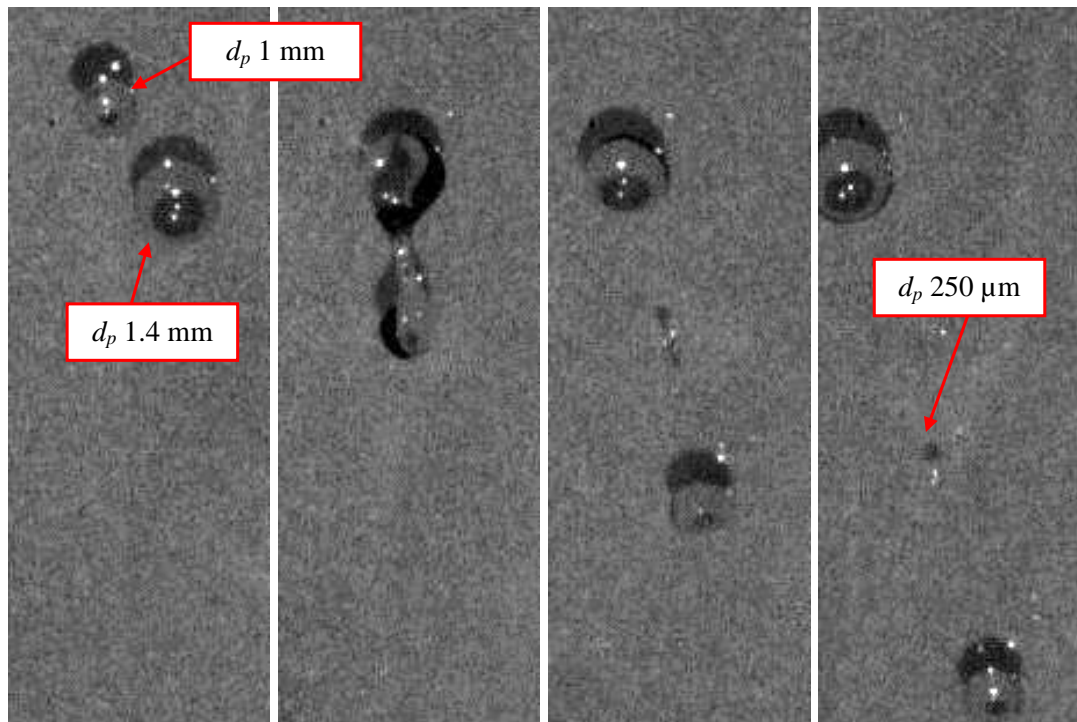
Figure 4.40 Camshaft channel drop collision at 2000 rpm with 3.5 ms image separation

The collision of two drops with a similar diameter and velocity is shown in Figure 4.40, again a ligament forms following the collision of the two drops. The ligament necks at both ends generating a drop 25% smaller than the original colliding drops. Considering the gravitationally induced drop velocity plotted in Figure 4.21, a SAE15W-40 oil drop $d_p = 250$ μm at 60°C drops requires a blow-by velocity of 1.4 m.s^{-1} to be suspended in the camshaft channel flow. Assuming half the blow-by travels up each camshaft channel, Equation (4.2) can be used to show that the blow-by rate would have to be 198 litres.min^{-1} to suspend a $d_p = 250$ μm oil drop. If the blow-by rate was 100 litres.min^{-1} then the gas velocity in the camshaft channel would be 0.7 m.s^{-1} and drops $d_p < 177$ μm would be suspended in the camshaft channel flow.

Several drops thrown up from the camshaft had a curved trajectory due to the normal acceleration of the camshaft, they moved towards the back of the camshaft channel and impacted onto the oil film. In Figure 4.41 the velocity of a $d_p = 1.3$ mm oil drop is low enough for the drop to coalesce into the oil film. Again another impaction of a $d_p = 1.3$ mm oil drop onto the oil film at the back of the camshaft channel can be

seen in Figure 4.42, however, the velocity of the drop is sufficient for the drop to impact and rebound, the drop deforms but does not fully coalesce into the oil film.
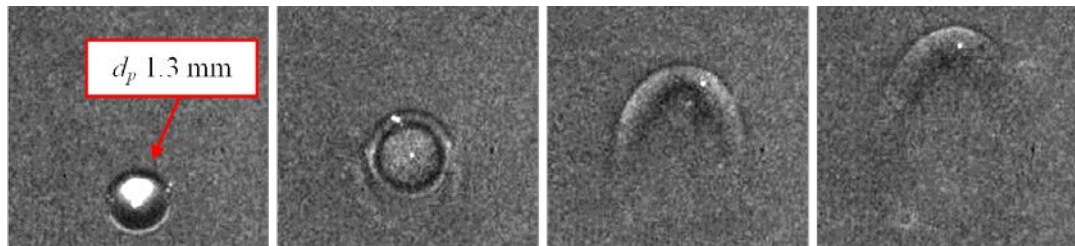
Figure 4.41 Camshaft channel oil film impaction at 2000 rpm with 10 ms image separation
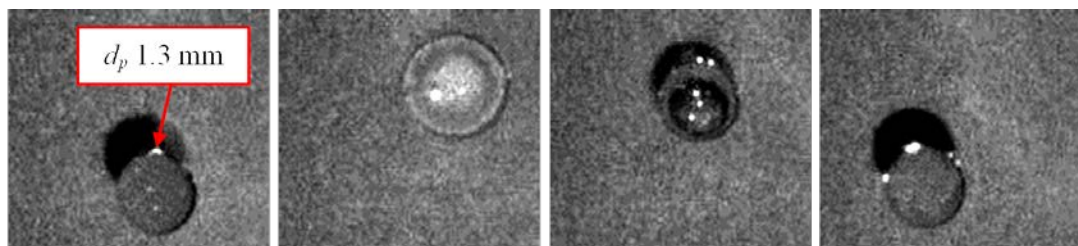
Figure 4.42 Camshaft channel oil film impaction 2000 rpm 2 ms image separation

Although the drops recorded in Figure 4.41 and Figure 4.42 are large they exhibit some of the characteristic drop impaction behaviour that has been studied intensively for much smaller drops in diesel fuel sprays. A prominent body of work in this field was conducted by Bai and Gosman (1995) who characterised seven different types of drop impact regimes, these were; stick, rebound, spread, boiling induced breakup, rebound with breakup, breakup and splash. They characterised the different regimes using Weber number, Laplace number, incidence angle of impaction, temperature, wall film thickness and wall surface roughness. The majority of these parameters have been introduced previously or are discernible directly from single measurements of the impact event. The dimensionless Laplace number should be defined in more detail though as it provides a measure of the importance of surface tension and viscous forces within a liquid. The Laplace number is calculated used Equation (4.8) where σ is the oil surface tension, ρ_l is the oil density and η_l is the dynamic viscosity of the oil.

Laplace Number
$$L_\alpha = \frac{\rho_l \sigma d_p}{\eta_l^2} \tag{4.8}$$

Equation (4.8) shows that for a fixed oil temperature the Laplace number varies linearly with drop diameter and the larger the drop the more significant viscous forces within the oil. The images collected in the camshaft channel have shown that if the correct conditions are created oil drops can be removed from the crankcase blow-by within the crankcase. This important observation indicates that steps can be taken to improve crankcase emissions control within the crankcase, the validity of this hypothesis is explored in Chapter 6.

4.4.3 Camshaft Channel Discussion

The minimum distance from the camshaft channel to a camshaft journal bearing is 80 mm, therefore the oil film on the camshaft below the camshaft channel is generated by oil flowing from the cylinder head. Assuming the total oil flow to the cylinder head drains completely down the engine and is divided equally between each of the two camshaft channels, at 1800 rpm 13 g.s^{-1} of oil flows onto the camshaft. Comparatively, the crankshaft oil film is generated by journal bearing side flow from each of the five main and the four big end bearings. On a fired engine the piston cooling jets will also contribute to the crankshaft oil film. The total side flow for a single main bearing at 1800 rpm is 19 g.s^{-1}, clearly the total oil film flow onto the crankshaft is much more significant than that for the camshaft. The crankshaft journal bearing oil flow was calculated using the equations presented in Section 2.3 assuming the oil was at 80°C, the full calculations and the assumptions made are described in Appendix A Section A-4.

Furthermore, the camshaft normal acceleration is lower than that for crankshaft, due to both a lower angular velocity and radius. In contrast the aerodynamic force from blow-by will be much higher around the camshaft, because the crankcase volume around the camshaft is much smaller than around the crankshaft. Figure 4.29 indicates the 1174 mm^2 cross sectional area of each camshaft channel.

4.4.4 Pushrod Gallery Imaging Summary

The images presented in this section indicate that when large oil films are generated on dynamic components there is significant passive motion of the oil. The oil distribution in the tappet channel does not contribute significantly to the engine lubrication or oil aerosol generation, however, oil draining onto the camshaft contributes to the crankcase oil aerosol generation. Images collected at a range of engine speeds and imaging positions around the pushrod gallery channels, indicate that steps can be taken to control the oil aerosol within the crankcase. Coalescence and accumulation of oil drops was witnessed within the pushrod gallery region. A method of controlling crankcase oil aerosol emissions within the crankcase is explored in Chapter 6 Section 6.9.

The camshaft channels are the throat in the crankcase blow-by flow path for the 1104C-44 engine tested. The oil aerosol generated at the crankshaft, camshaft and for a fired engine the piston ring pack and turbocharger oil drain, will travel up the camshaft channel. The optical data collected in this study shows that the camshaft channels are critical to the crankcase emissions and oil drainage. Oil aerosol control around the camshaft is proposed as a method of regulating crankcase emissions in Chapter 7.

4.5 Rocker Cover Imaging

For the eight valve cylinder head on the 1104C-44 oil flows into each rocker through the central rocker shaft, the valves and pushrods are then lubricated by a gallery at either end of the rocker. The full valve and rocker arrangement including the central rocker shaft for cylinder 2 is shown in Figure 4.43. An annotated diagram in Figure 4.44 shows the oil gallery outputs which feed the valve and pushrod at either end of the rocker. On the pushrod side of the rocker an oil gallery feeds the cup at the top of the pushrod and on the valve side a gallery feeds the flat surface on top of the rocker. The engine and experimental setup was the same as that described in Section 4.4, any variations to the test conditions are specified.
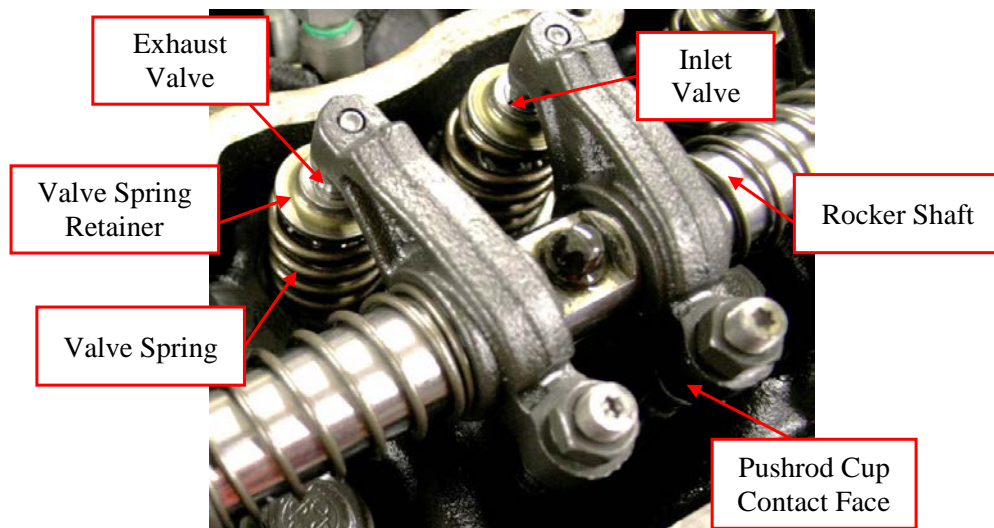
Figure 4.43 1104C-44 rocker valve train
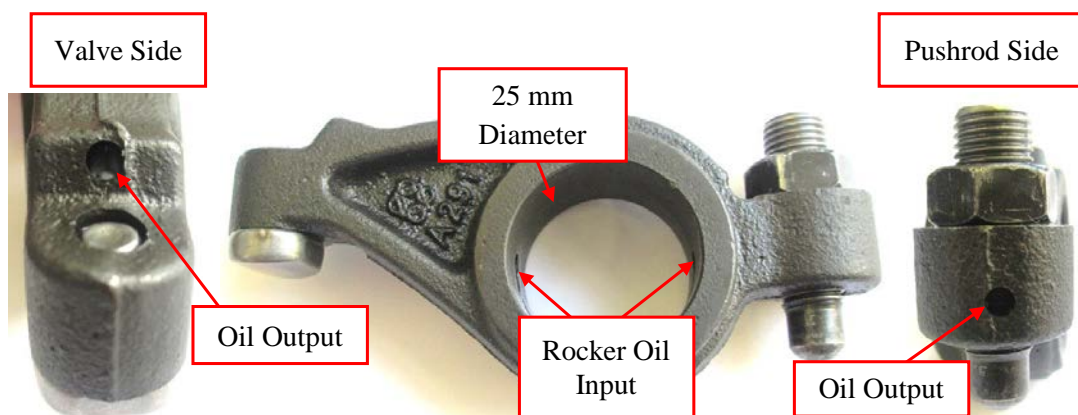
Figure 4.44 1104C-44 rocker schematic

A complete Perspex rocker cover provided excellent optical access around the rockers, therefore the illumination and camera could be positioned to collect the maximum amount of light scattered by any oil drops. The DSLR image in Figure 4.45 shows the significant oil distribution from the rockers. Rocker oil distribution has been investigated in detail and the illumination and camera positions have been adjusted to suit the particular region of interest.
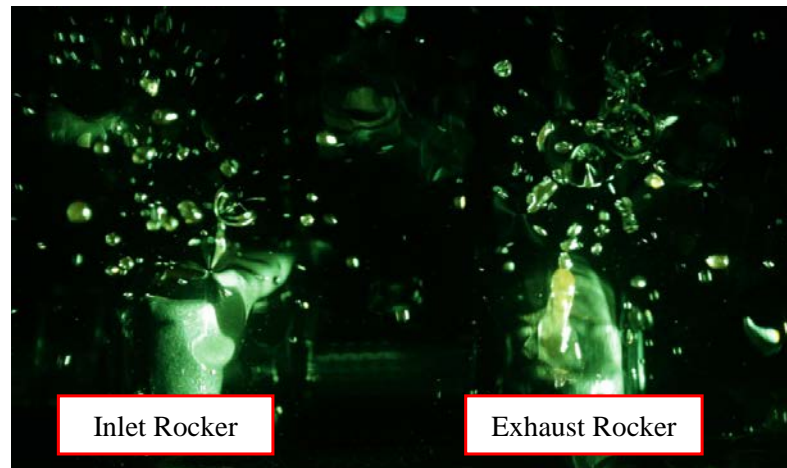
Figure 4.45 DSLR image of oil distribution from cylinder four rockers at 1800 rpm using copper vapour side illumination

The purpose of the valve side lubrication from the rocker is to lubricate the valve stem and the contacting ends of the valve spring. None of these contacting surfaces are directly lubricated as their lubrication is reliant on oil film movement or passive splash motion of the oil thrown from the rockers. At a low engine speed, the qualitative images in Figure 4.46 show that an oil film is generated on top of the rocker. The rocker acceleration during valve closure generates a ring of oil from the oil film, the ring is then separated into two oil ligaments. The trajectory of the ligaments is such that they collide and a single ligament then accelerates upwards. The acceleration of the rocker was sufficient for a large drop to separate from the ligament, however, the drop simply fell vertically back down onto the rocker. The surface tension and viscosity of the oil act against the acceleration of the rocker to control the oil motion.

Figure 4.46 also shows that the large amount of oil thrown from the front of the rocker generates an oil film over the whole rocker. Oil ligaments are generated from the oil film over the rocker length, the height of the ligament varies depending on its radial position along the rocker because the smaller the radius the lower the acceleration of the oil film.

Figure 4.46 Rocker oil film breakup at 900 rpm

As witnessed elsewhere in the engine, when the forces are sufficient ligament generation can contribute significantly to the oil aerosol generation. For this reason the rocker ligament generation was investigated with an improved optical setup in more detail, the results are discussed in Section 4.5.1.
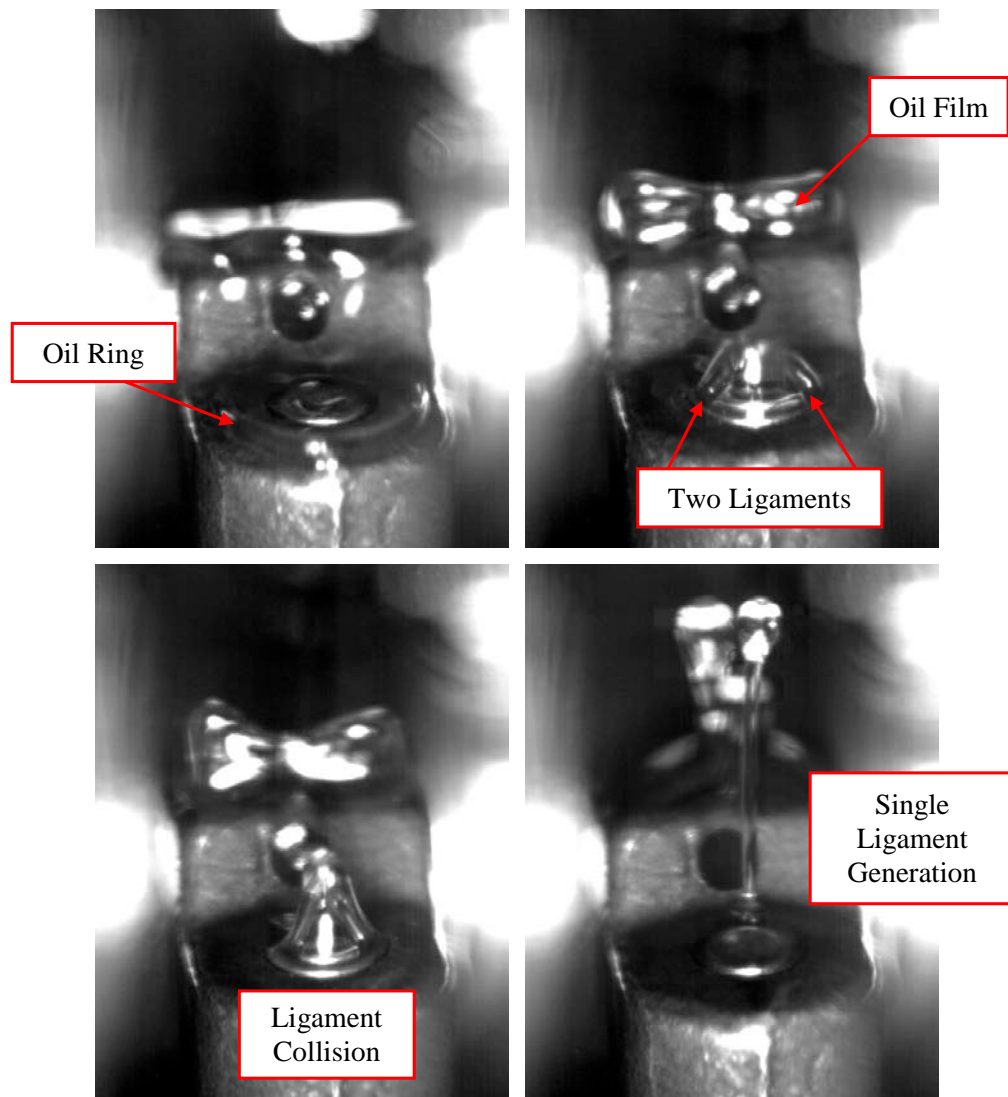
The oil distribution at the critical lubrication interface between the rocker and the valve stem was investigated. Figure 4.47 displays the oil distribution around the top of the cylinder three exhaust valve. In the first image on the top left the valve is closed and the rocker is static, before any motion a large amount of oil from the oil gallery flows down the front of the rocker. As valve opening commences the acceleration of the system forces a ring of oil up from the oil film on the valve spring retainer. The oil ring then moves up towards to rocker adding to the oil from the oil gallery. Waves are visible in the oil film on the top of the rocker as the valve is fully open. As the valve closes all the oil on the top of the rocker is forced down. At the end of the valve event thick oil ligaments are generated above the valve spring, the oil ligaments either impact on the valve spring retainer or are thrown down onto the cylinder head.

Figure 4.47 1104C-44 valve lubrication 900 rpm

Although the images discussed above did not capture any small oil drops, the oil motion was substantial. Considering that the images in Figure 4.47 were captured at only 900 rpm engine speed, with a low oil temperature of 60°C and at the exhaust valve which has a lower acceleration than the inlet valve, there is still potential for oil atomisation around the valve spring retainer at higher engine speeds and oil temperatures.

The oil distribution was also investigated on the pushrod side of the rocker. At 1500 rpm there is sufficient oil in and around the pushrod cup for the acceleration of an inlet valve event to generate a ring of oil, breakup of which generates oil drops, this event is displayed in Figure 4.48. The oil ring was generated below the pushrod cup during valve opening, disruption of the oil ring during valve closure accelerated the process of ligament necking and drop generation, drops down to $d_p \approx 250$ μm were produced. Comparing Figure 4.48 to Figure 4.31 we can see that although the acceleration and force is constant along the length of the pushrod, the increase in diameter between the main pushrod length at 8 mm and the pushrod cup at 11 mm is sufficient to generate a large volume of oil. The surface tension and viscosity of the oil at 60°C in the oil volume in and around the pushrod cup could not prevent breakup. The qualitative data presented in Figure 4.48, again highlights how excessive oil pooling and film generation on dynamic components can generate small oil drops.
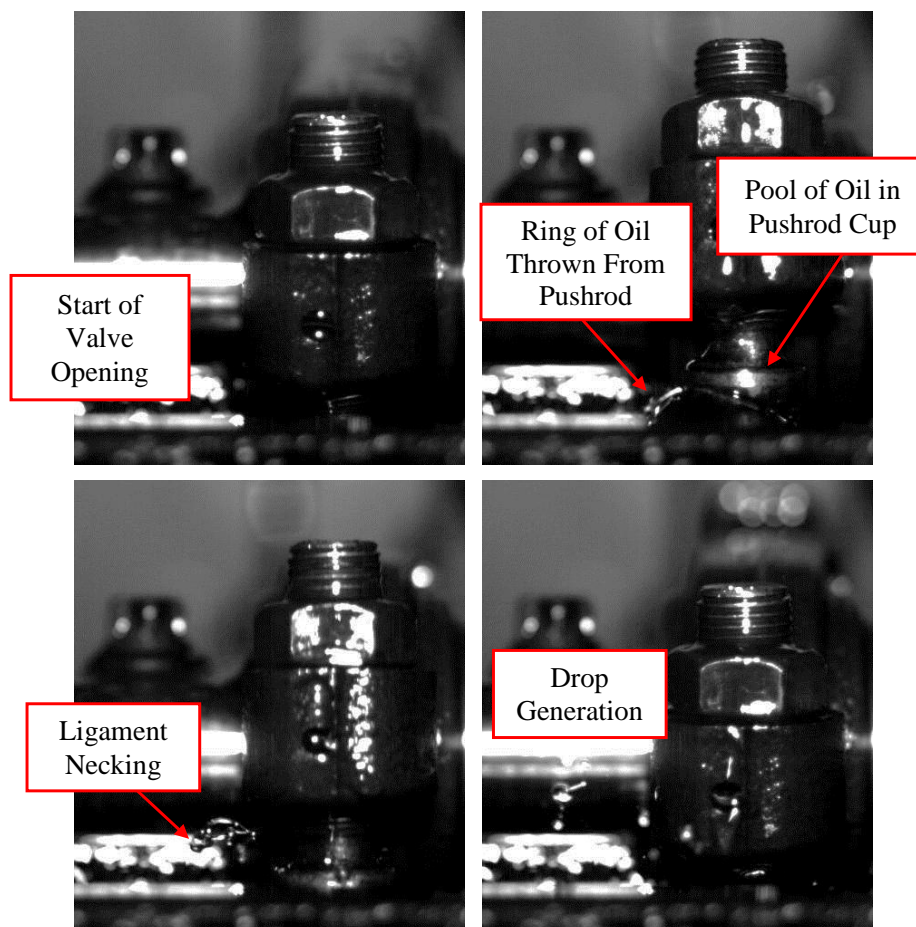
Figure 4.48 Pushrod oil atomisation at 1500 rpm

4.5.1 Rocker Oil Atomisation

The significant atomisation of oil from the valve side of the rockers was captured in more detail using the optical setup shown in Figure 4.49, which consists of a Photron high speed camera and diffused single fibre copper vapour back illumination. The effect of engine speed on oil atomisation from the rockers was investigated at 900, 1400 and 2000 rpm. Images in Figure 4.50 clearly highlight the dramatic effect that increasing the engine speed has on the rocker oil atomisation. Increasing the engine speed increased both the acceleration of the rockers and the flow rate of oil onto the rocker. The thicker oil film generated at higher engine speeds was atomised with more force. The higher speed capability was achieved by not running with pistons and connecting rods. The full engine setup is described in more detail in Chapter 3.
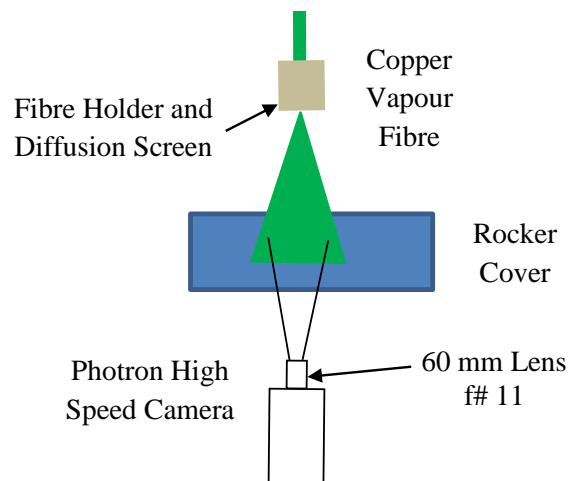
Figure 4.49 Rocker high speed back illuminated imaging setup
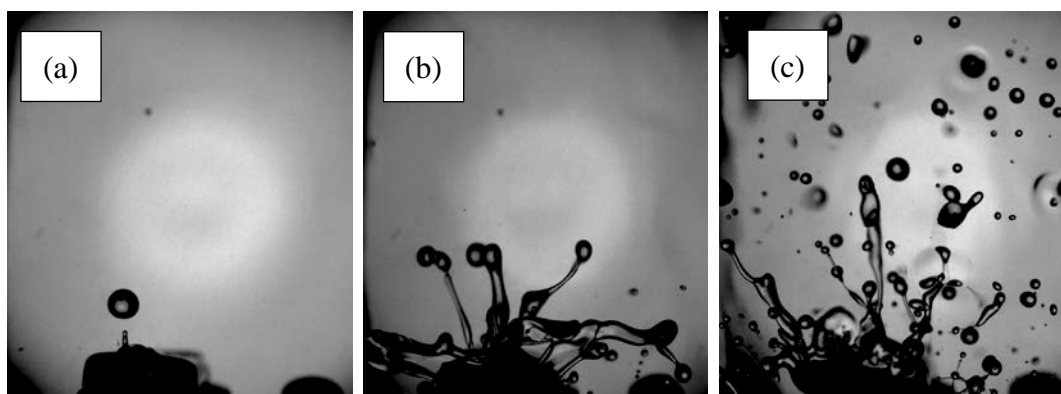
Figure 4.50 Rocker valve side oil atomisation at a fixed rocker position (a) 900 rpm (b) 1400 rpm (c) 2000 rpm

The oil ligament behaviour at 900 rpm can be clearly seen in Figure 4.51, where the acceleration of the rocker during valve closure generates a thick ligament from the oil film coating the top of the rocker. Once the rocker is static, following valve closure, the ligament length increases and a large volume drop of oil forms at the top of the ligament. The ligament then begins to neck and the ligament length decreases, before final separation of the drop and the ligament.

0   15 mm
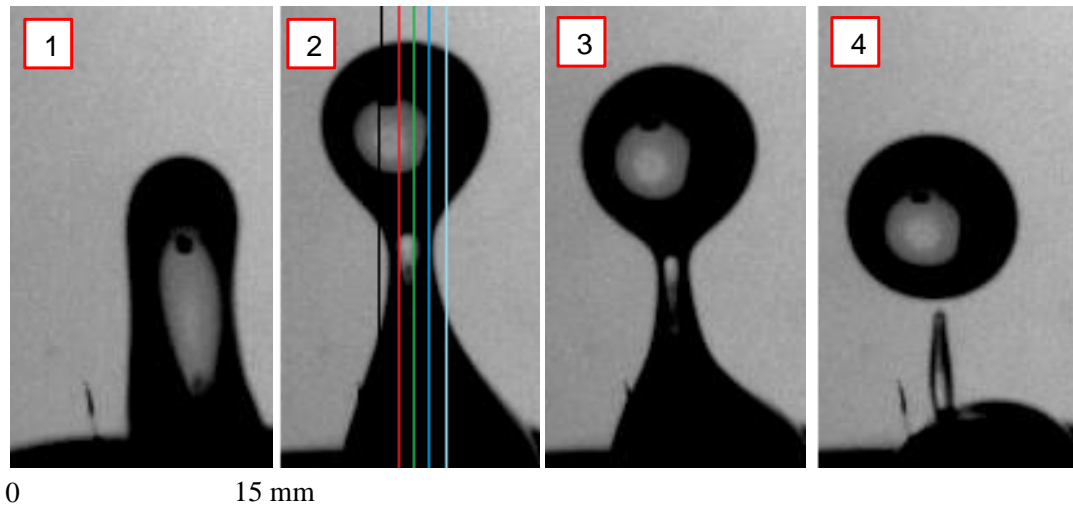
Figure 4.51 Rocker valve side oil ligament generation and breakup at 900 rpm, images collected at 3000 fps
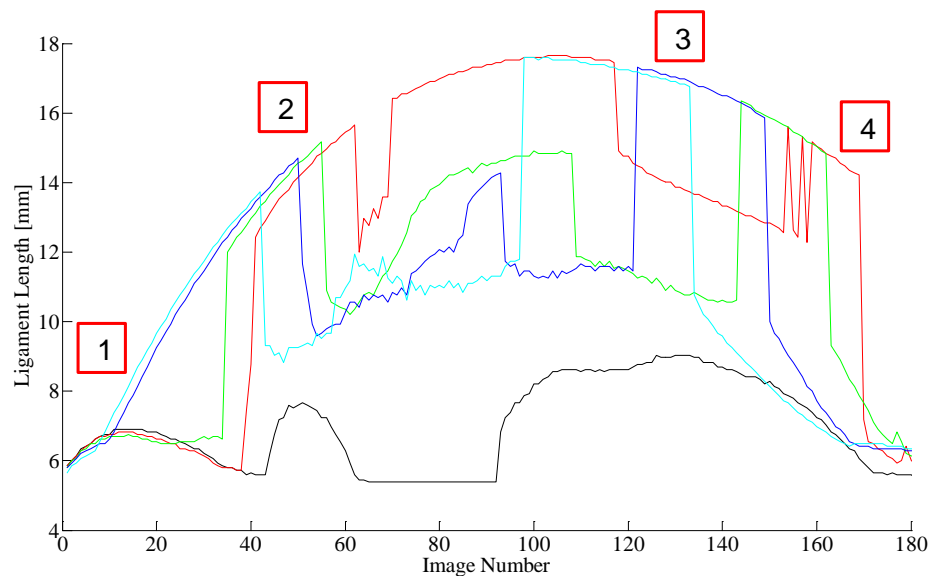
Figure 4.52 Rocker valve side oil ligament length at 900 rpm

The total ligament length for the consecutive images in Figure 4.51 over five vertical line profiles across the ligament thickness is plotted in Figure 4.52. Five line profiles were taken as the ligament moved both the vertically and horizontally. The cumulative ligament thickness over the five line profiles shows a good fit to a parabolic profile, this suggest that the generation of an oil ligament excited by a known acceleration can be predicted with reasonable confidence.

The ligament thickness prior to drop separation, shown in Figure 4.53, was also measured and is plotted Figure 4.54. The curved profile of the drop has been represented well in the graph and the drop separation can be clearly detected. The difference been consecutive lines appears consistent, again suggesting that drop generation of this type can be predicted with reasonable accuracy. The feasibility of modelling of this type of ligament behaviour is investigated further in Section 4.6.
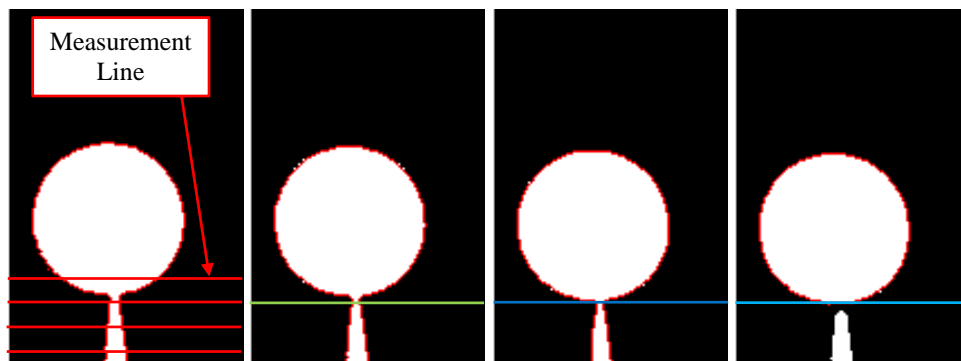
Figure 4.53 Measurement of rocker oil ligament thickness at 900 rpm
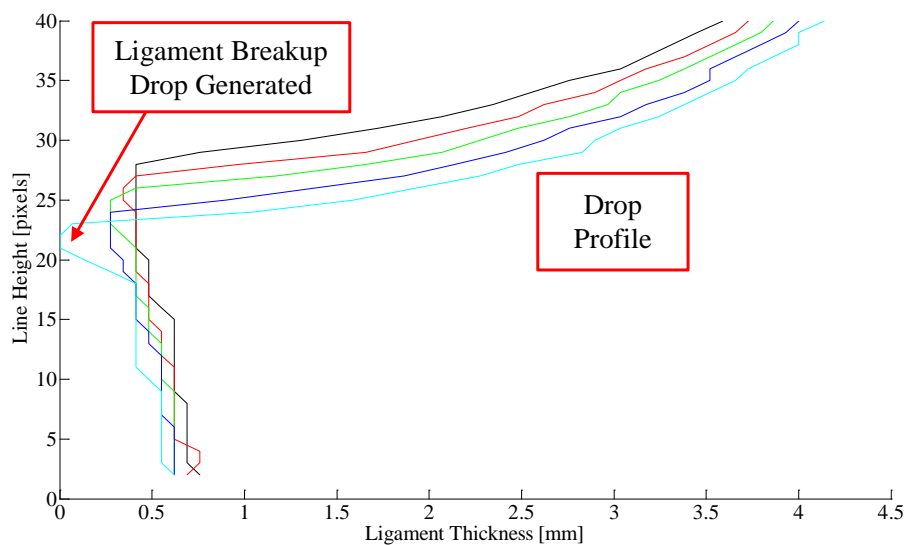
Figure 4.54 Rocker ligament thickness prior to drop generation at 900 rpm

Although no atomised oil drops were recorded at 900 rpm, analysis of the ligament behaviour and breakup provides preliminary validation of the fluid mechanics behind the ligament breakup process. At higher engines speeds the oil distribution from the rocker is significant, atomisation of the oil film occurs, initially the fluid mechanics of this process are the similar to those measured at 900 rpm but the acceleration and the volume of oil is larger.

Looking at the oil breakup in more detail revealed the added complexity that is introduced when the volume of the oil film and its acceleration are increased. In Figure 4.55 thin oil sheets with a thick bounding ligament are thrown from the rocker. Assuming that the rocker acceleration and oil film thickness are reasonably consistent, there is huge variation in the oil distribution and final drop generation between valve opening events.
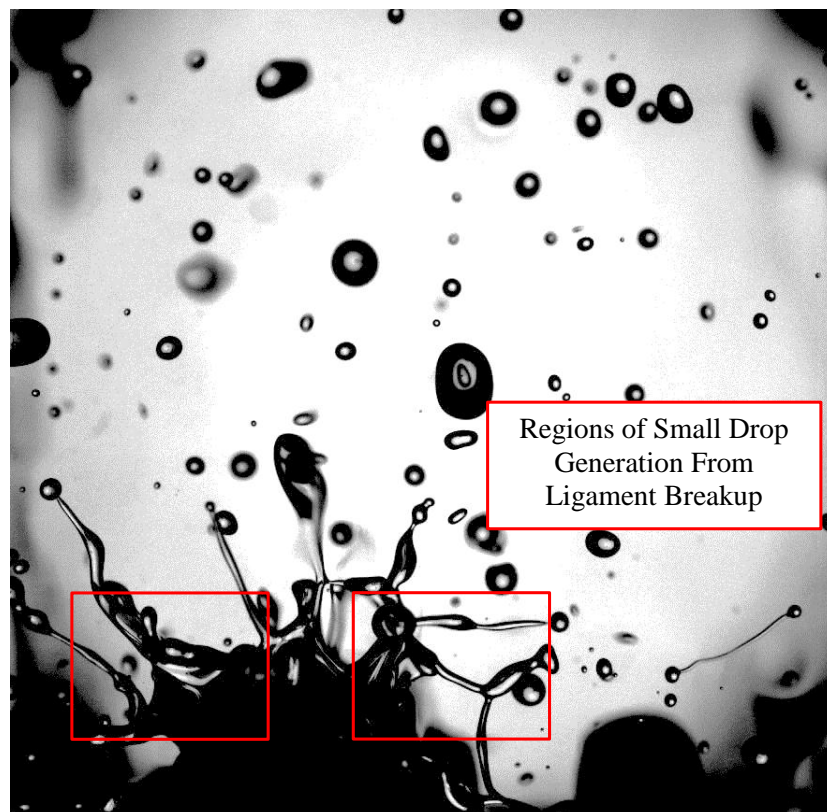
Figure 4.55 Rocker valve side oil atomisation at 1400 rpm

Figure 4.56 and Figure 4.57 show the process of ligament necking and drop formation occurring for thin ligaments generated at 1400 rpm and 2000 rpm. The small scale images in Figure 4.57 show that the capillary waves created on the

surface of the ligament generates drops along the length of the ligament not just at the head of the ligament. The smaller drops will contribute to the crankcase oil aerosol if the blow-by flow rate is sufficient.

0   50 mm
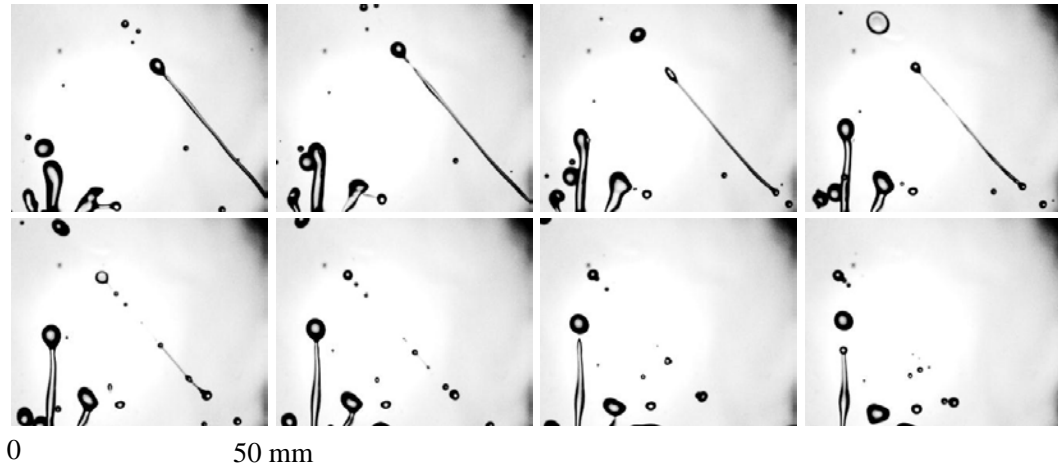
Figure 4.56 Large scale rocker valve side oil ligament breakup at 1400 rpm with 5 ms image separation

0   8 mm
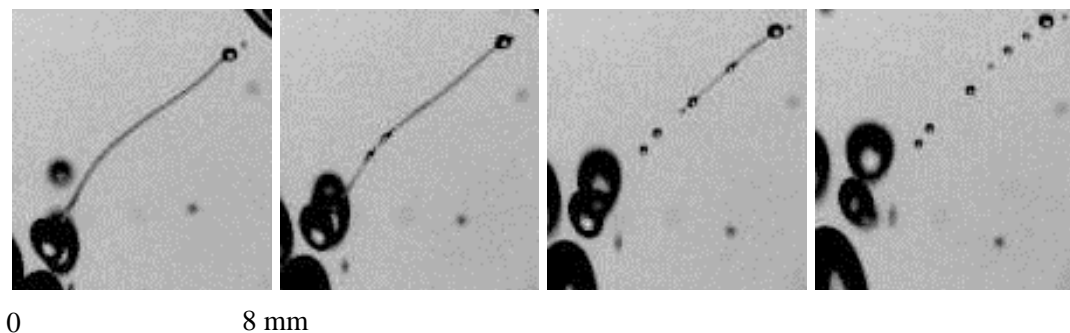
Figure 4.57 Small scale rocker valve side oil ligament breakup at 2000 rpm with 0.7 ms image separation

The drop count for drops $d_p \geq 250\,\mu\text{m}$ for over 300 images, recorded at 3000 fps covering a minimum of eight valve opening events at 1400 rpm and 2000 rpm is plotted in Figure 4.58. The presence of a peak drop count is repeatable, however, there is variation in the magnitude of the peak. The sets of sequenced images in Figure 4.60, Figure 4.59 and Figure 4.61, illustrate the complex drop generation from oil ligament and sheet breakup from the valve side of the rocker. The data sets presented in this section help to explain the large variation in drop count witnessed in Figure 4.58.
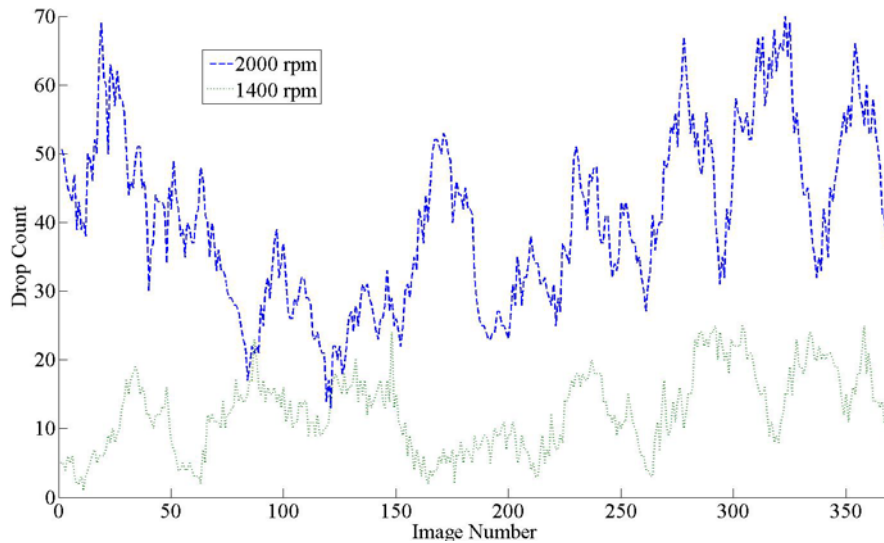
Figure 4.58 Rocker drop count against image number for a minimum of eight valve opening events, recorded at 3000 fps 1400 rpm and 2000 rpm

0   40 mm
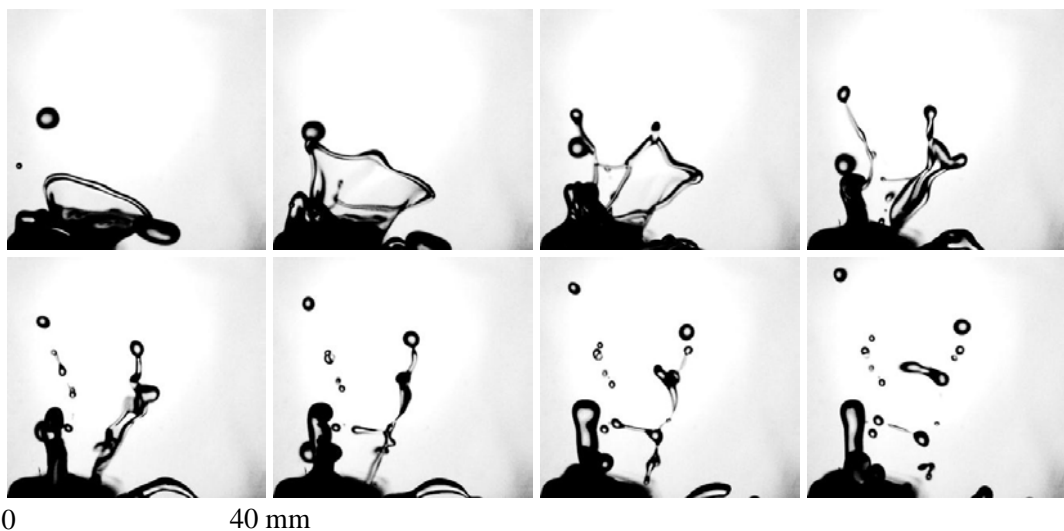
Figure 4.59 Rocker valve side oil crown atomisation at 1400 rpm with 5 ms image separation

Figure 4.59 captures the breakup of a thick bounding oil ligament that is generated at the front of the oil volume thrown from the rocker at 1400 rpm. The oil surface tension and viscosity initially tried to maintain a curved ligament, however, the acceleration of the fluid was too large to sustain the ligament. The fluid in the bounding ligament was initially drawn into three sections, each section then broke up into two separate ligaments. The final two ligaments exhibit the typical Rayleigh ligament breakup witnessed earlier. The initial stages of the bounding oil ligament formation dictate the fluid location, and therefore final ligament breakup and drop generation, this process varied between valve opening events.

0   14 mm
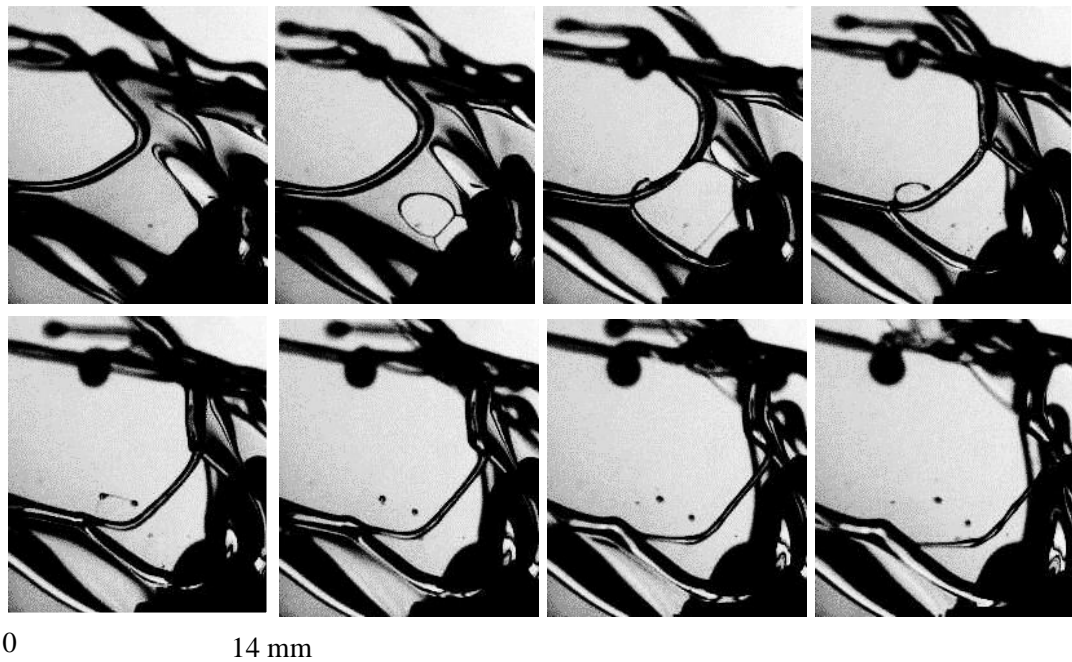
Figure 4.60 Rocker oil sheet atomisation at 1400 rpm with 0.7 ms image separation

The breakup of an oil sheet generated on the left of the rocker at 1400 rpm is shown in Figure 4.60. The oil sheet develops a central hole and very quickly begins to deform, the entire sheet breakup process occurs in 5 ms. The surface tension and viscosity of the oil cannot sustain the central disruption and the sheet surface is drawn into a ligament with a curved profile, due to the rapid change in oil surface area. The ligament eventually breaks up into a series of drops with a minimum diameter of $d_p = 250$ μm.

The breakup of another oil sheet is displayed in Figure 4.61, the sheet was generated on the right side of the rocker at 1400 rpm. The oil sheet breakup process occurs over the same time scale as that witnessed in Figure 4.60, however, as the sheet is drawn into a ligament volume the ligament is twisted. The angular momentum of the twisted ligament is carried through to the drops generated during ligament breakup, this is exhibited by the rotation of the two adjacent drops in the final six images. Drops down to $d_p = 450$ μm were generated by this extremely complex oil sheet breakup.

0   13 mm
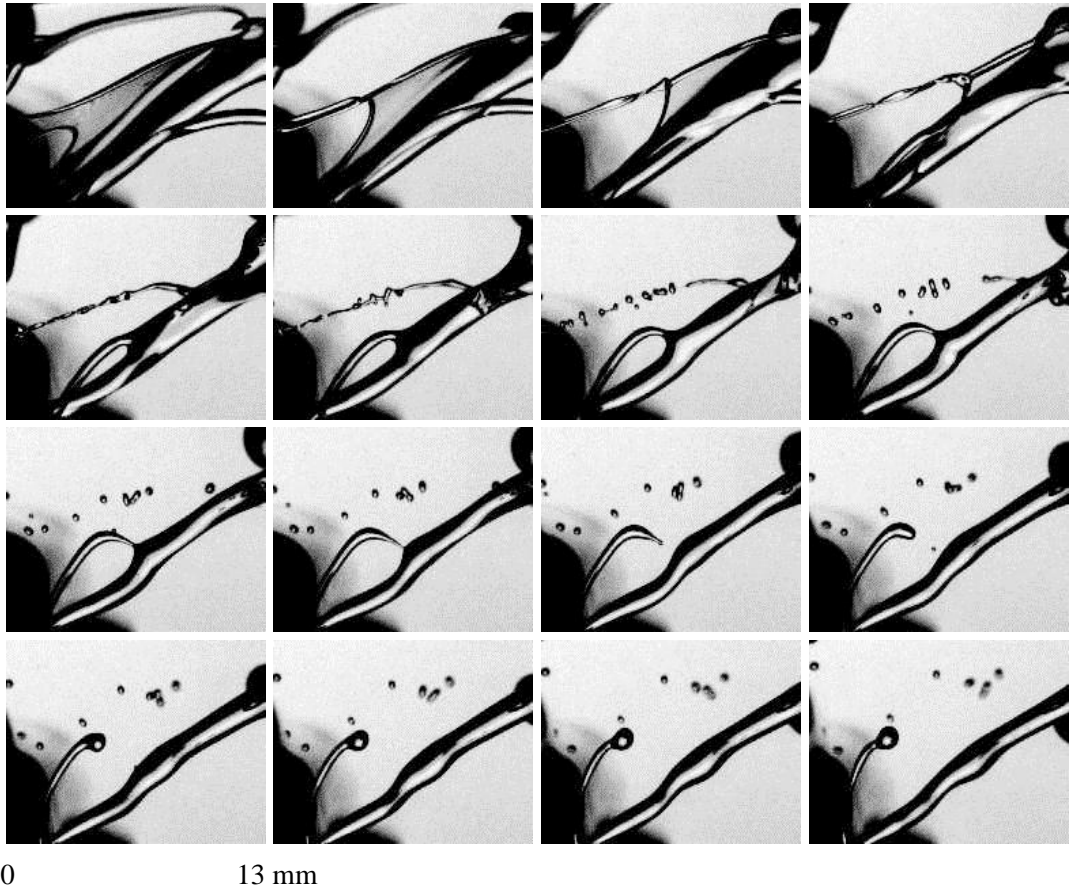
Figure 4.61 Rocker valve side oil ligament breakup at 1400 rpm with 0.7 ms image separation moving from the top left to the bottom right

Figure 4.62 Rocker valve side oil atomisation at 2000 rpm

As shown in Figure 4.58 the number concentration of oil drops increased with engine speed, the image with the highest drop count from is displayed in Figure 4.62, and the associated diameter of the measured drops is plotted in Figure 4.63. The mean drop diameter is very large $d_p \approx 1$ mm this highlights that although the drop distribution from the rocker was significant and small drops were generated, 40 litres.min^{-1} of blow-by would not be sufficient to transport the majority of the larger drops out of the crankcase.
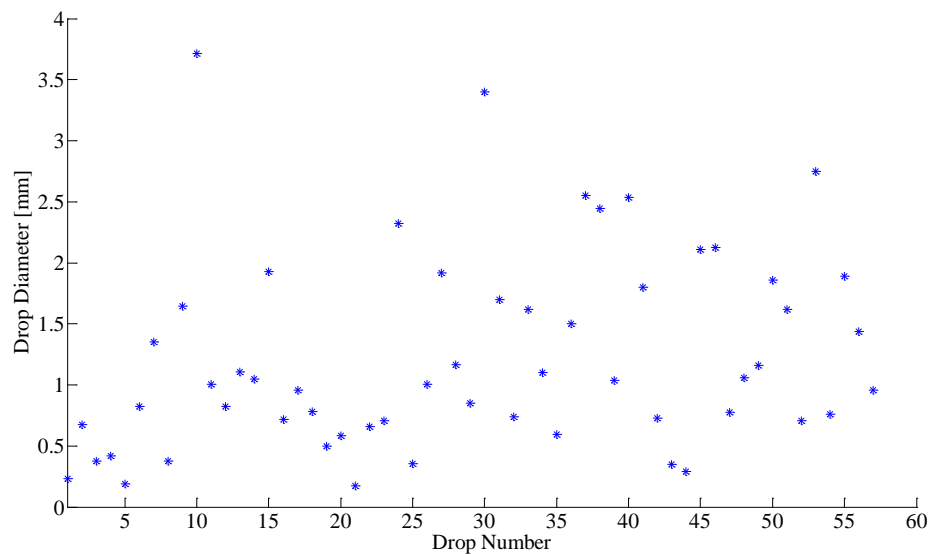
Figure 4.63 Rocker valve side drop diameter from the peak drop count image taken at 2000 rpm

4.5.2 Rocker Cover Imaging Summary

A plethora of high quality images of large scale and small scale oil ligament breakup have been captured. The wealth of data highlights the variety of breakup mechanism and suggest that some characteristics of large oil ligament breakup are analogous to those occurring for much smaller ligament sizes, further investigation and validation of this is required. Theoretical analysis of the oil distribution and breakup has been conducted using the experimental data to provide initial validation of a computational model in the next section. Potential improvements to the lubrication system based on the conclusions drawn from this work are presented in Chapter 7.

4.6   Rocker Atomisation Modelling

The feasibility of predicting rocker oil distribution using a computational fluid dynamics model (CFD) was investigated. A two phase volume of fluid model (VOF) was developed in the CFD software Star CCM+ Version 7.02.011. To minimise the computational processing time a two-dimensional sealed profile on the valve side of the rocker was modelled. The rocker and the CFD fluid domain are displayed in Figure 4.64. A trimmer prism layer mesh containing 54868 cells was generated over the fluid domain, the mesh is shown on the right of Figure 4.64, the minimum cell size was 15 μm.

Figure 4.64 Rocker oil ligament breakup modelling (a) valve side of rocker (b) 2D CFD flow domain and mesh

An implicit, unsteady, segregated, turbulent, isothermal model with gravity was applied. As information on the effect of turbulence on the two phase model was limited, the widely acknowledged and validated K-Eplison turbulence model was implemented. Two phases were modelled, these were liquid SAE 15W-40 oil at 60°C and air at ambient temperature. A Eulerian multiphase solver was applied to set the properties of each phase and track the volume fraction of the oil and air in each cell. A multiphase interaction was applied so that the surface tension force could be resolved. The primary phase was selected as liquid oil so that the surface tension and contact angle between the oil and the rocker surface could be specified.

The surface tension of the oil at a specified temperature was measured by Intertek Testing Services, the result is displayed in Appendix B Table B-2.2. The surface

tension of the oil at 60°C in air was evaluated using a gradient approximation based on results by Ross (1950), the results are displayed in Appendix B Figure B-1.1. The contact angle (θ_c) of the oil against the rocker surface was measured from the image displayed in Figure 4.65. A 1 mm oil drop was dropped from a needle containing a reservoir of heated oil 200 mm above a rough surface selected to replicate the rocker. The impact of the drop onto the surface was captured using a high speed camera and diffused halogen back illumination. The image displayed in Figure 4.65 was taken once the drop surface tension and viscosity had stabilised the oil volume. The contact angle for SAE 15W-40 oil at 60°C oil temperature was 25°.
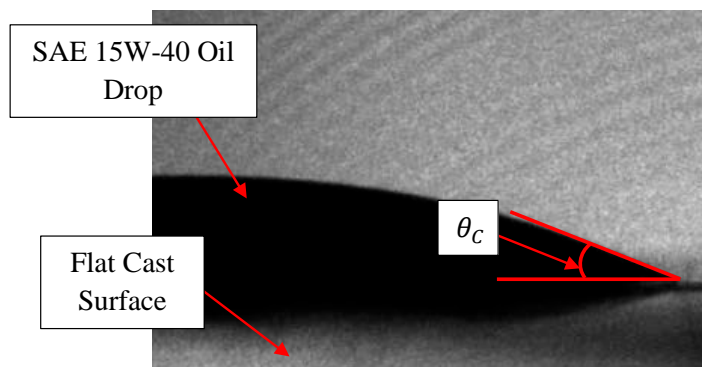
Figure 4.65 SAE 15W-40 oil contact angle for 60°C oil temperature

The VOF properties could be adjusted to modify the diffusion of each phase within the cells. The effect of these values on the final results was not investigated in detail, however, it should be noted that adjusting these values is a potential way of refining the computational solution to match experimental data. For reference the specific VOF properties used are displayed in Table 4.3.

Table 4.3 Rocker ligament CFD model VOF properties

Volume of Fluid (VOF) Properties	
Convection	2nd-order
Sharpening Factor	1
Angle Factor	0.05
CFL_I	0.5
CFL_u	1

The linear kinematic acceleration of the rocker was calculated from the camshaft angular acceleration profile. The linear acceleration profile used is displayed in Figure 4.66, a reference arrow in the figure indicates the direction gravity was specified to act in, as -9.81 m.s^{-2} was added to all the linear acceleration values. The linear acceleration profile was applied to the fluid domain by adjusting the reference value of gravity using a field function. The field function specified the linear acceleration every 1° CA or every 185 ns at 900 rpm. The time step for the implicit unsteady solver was 46 ns. 10 iterations were completed every time step, therefore 40 iterations were completed every 1° CA.
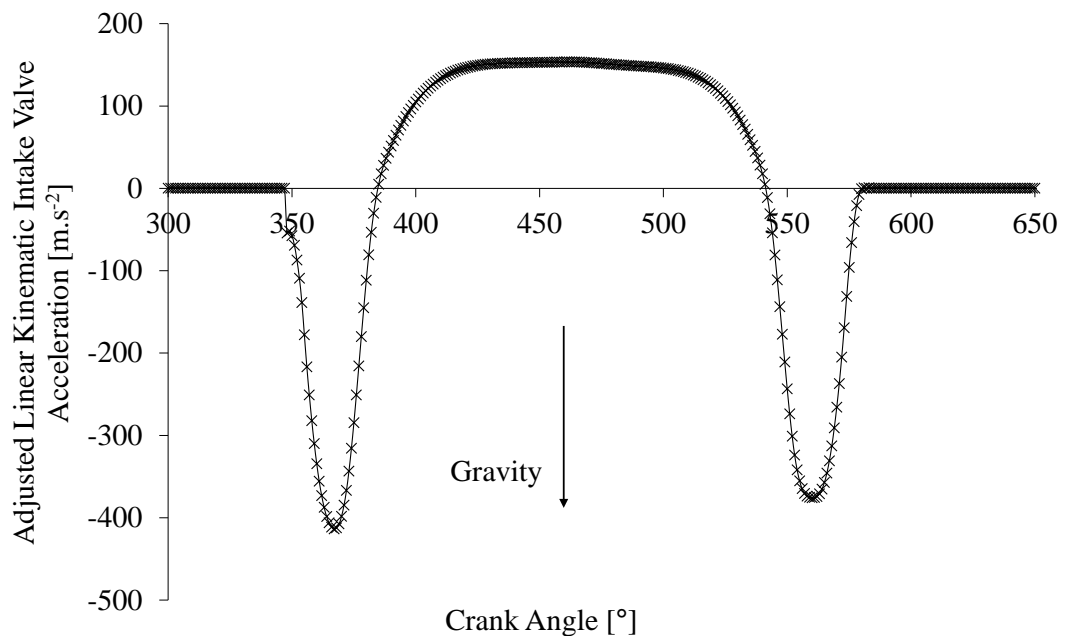
Figure 4.66 1104C-44 adjusted inlet valve kinematic valve acceleration at 900 rpm
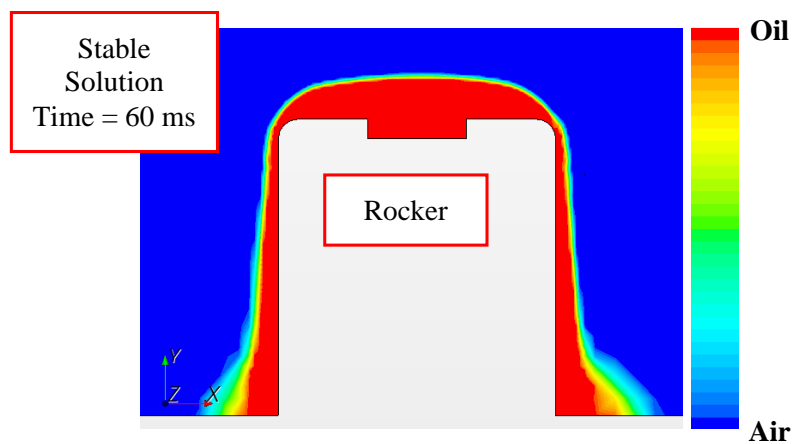
Figure 4.67 Stable rocker oil film prior to valve opening

The model ran for 200 ms, for the first 60 ms only gravity was applied. The valve event took 44 ms, following which the model was left to run for a further 96 ms. A 22 core computer was able to complete the solution in a matter of hours. A field function was used to specify the initial volume of oil on the top of the rocker, the oil film was left to stabilise over the initial 60 ms when only gravity was acting. The stable oil film on the rocker at 60 ms prior to the valve event is displayed in Figure 4.67.

4.6.1 Rocker Atomisation CFD Results

The results of the CFD model in Figure 4.68 show excellent agreement with the initial high speed images, where two ligaments are formed at the edges of the rocker. Simulating accumulation of the two ligaments and the subsequent separation of a drop from the large central ligament was more difficult to achieve.
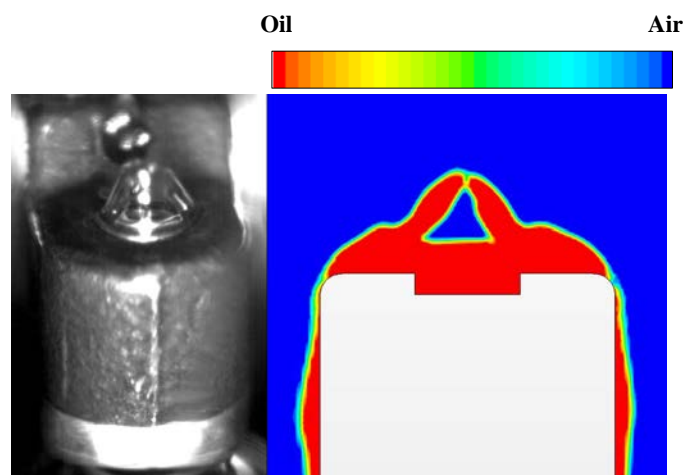
Figure 4.68 Rocker ligament model 900 rpm

Several simulations were completed for different oil film levels in an attempt to achieve the desired ligament breakup and drop generation. The oil film level displayed in Figure 4.67 provided results that were most comparable to high speed images. Secondly, the linear acceleration profile was adjusted, considering that the smooth kinematic acceleration profile was modelled, not the noisy dynamic acceleration profile that is the most accurate representation of the actual valve event. The linear kinematic acceleration was magnified by a constant until representative accumulation and ligament breakup was witnessed.
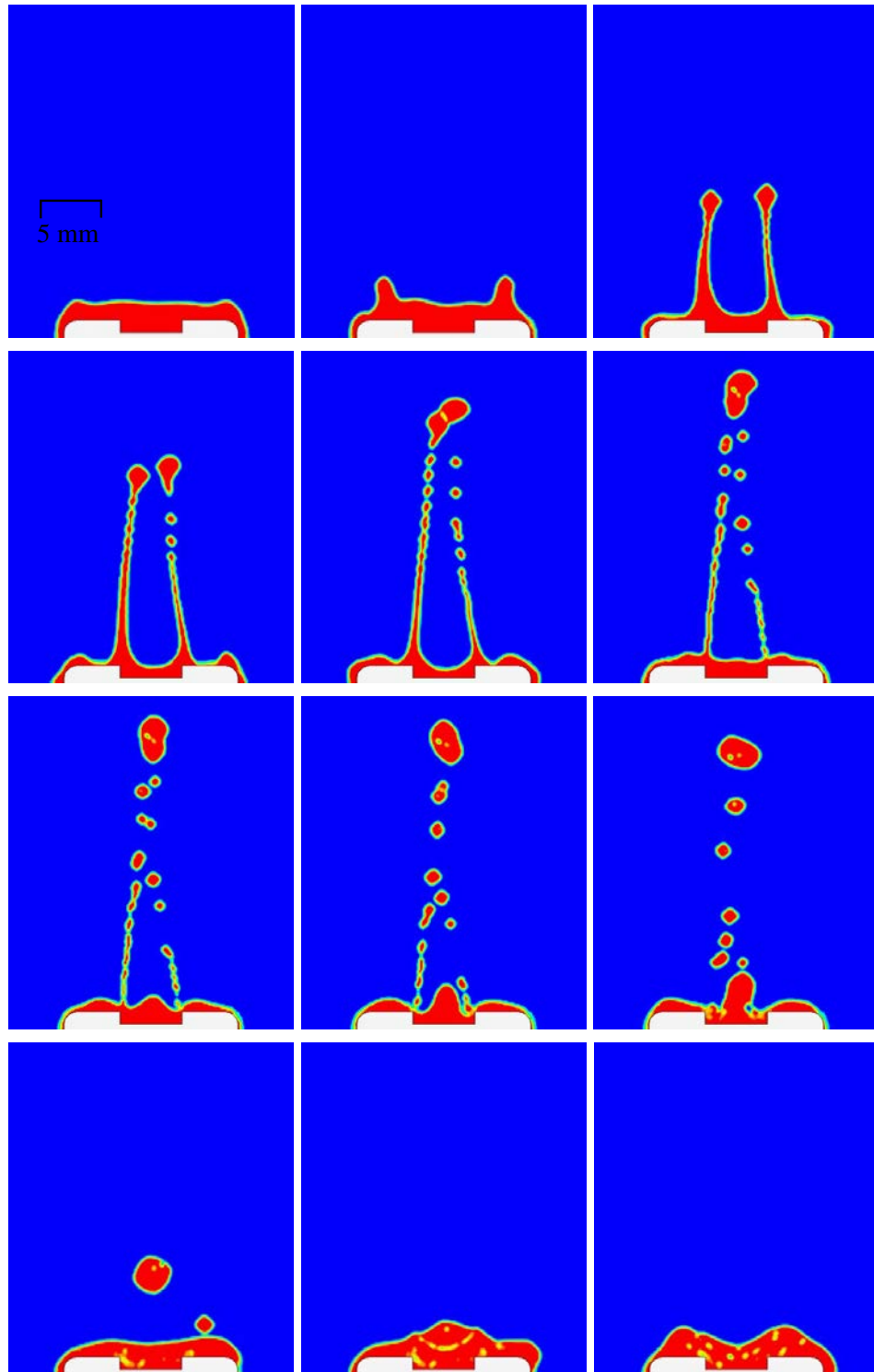
Figure 4.69 Rocker ligament model 900 rpm, adjusted linear acceleration profile, images taken at a varying time separation

The results displayed in Figure 4.69, highlight the success of the VOF model to predict oil ligament breakup. The ligament generation can be clearly seen, as the ligament length increases the ligament begins to neck below the large oil drop at the head of the ligament. This qualitative analysis agrees well with the plots of ligament development in Figure 4.52 and Figure 4.54. Capillary waves generated along the ligament forced the oil into a series of drops, this Rayleigh type breakup was witnessed throughout the experimental data presented in this chapter. Although small satellite drops were not generated, the simulation results presented in Figure 4.69, indicate that predicting satellite drop generation with a CFD simulation is plausible, provide the acceleration, cell size and time step are optimised.

Drop accumulation and coagulation was captured well by the simulation. The images displayed in Figure 4.69, not only capture the accumulation of the drops but also the angular motion of the drops caused by their relative motion prior to impact. The model illustrated the action of the oil surface tension and viscosity reacting to generate a large stable oil volume. Again this interesting and complex behaviour was witnessed in the experimental images in Figure 4.61.

4.6.2 Rocker Atomisation Modelling Summary

The simulation results produced were better than expected. As the cell size was much smaller that the ligament thickness, the model was able to predict the capillary waves and necking in the ligament very well. The CFD model parameters did not perfectly match the experimental test conditions for the rocker oil distribution, therefore it is unrealistic to expect the simulation results to agree completely with experimental images. A computational model was developed to assess the feasibility of predicting crankcase oil aerosol generation, and ensure that the processing demand was not prohibitive. The simulation results show good agreement with the experimental data and the oil ligament breakup shows good agreement with the theory, suggesting that crankcase oil aerosol generation can be successfully predicted. Further investigation is required, it should focus on modelling the physical phenomena captured experimentally, when all the experimental parameters have been recorded accurately and therefore they can be replicated in the model.

4.7 Rotating Components

The results of an optical investigation of crankcase oil aerosol generation have been presented in this chapter, the most significant mechanism of oil atomisation and aerosol generation was ligament breakup and drop formation from oil films present on dynamic components. Oil films present on the crankshaft, camshaft and rockers were atomised by the acceleration of these components, consequently the atomisation process was strongly affected by engine speed, and thus, increasing the engine speed increased the drop number concentration and reduced the drop diameter. The imaging setups used have highlighted the critical atomisation of oil films, but have not readily captured the small oil drops $d_p < 100\,\mu\text{m}$ produced by the primary atomisation process.

The excellent optical access around the top of the engine was utilised and the optical setup shown in Figure 3.19 was installed to capture images of oil drops $d_p \geq 10\,\mu\text{m}$ that were generated in the crankcase and transported up the pushrod gallery in the 100 litres.min^{-1} of 100°C blow-by. The focal plane was positioned in the centre of the cylinder three pushrod gallery. Drops $d_p \leq 10\,\mu\text{m}$ were captured in the images, however, as the diffraction limited spot size of the images was $10\,\mu\text{m}$ their precise diameter could not be resolved. The diffraction limited spot size was discussed in more detail in Chapter 3.

Oil was only supplied to the main journal bearings supporting the crankshaft, and the three camshaft journal bearings. The connecting rod journal bearings were clamped in place on the crankshaft as there were no connecting rods or pistons. The oil supplied to the top of the engine was circulated back to the external heating tank. Oil was pumped directly into the oil rail using an external oil pump, therefore the oil rail pressure and flow rate could be regulated to achieve the correct values at the fixed engine speed despite the variations in back pressure on the oil circuit. The experimental setup used to investigate the contribution of the crankshaft and camshaft to oil aerosol generation is described further in Section 3.6.4.

0   10 mm
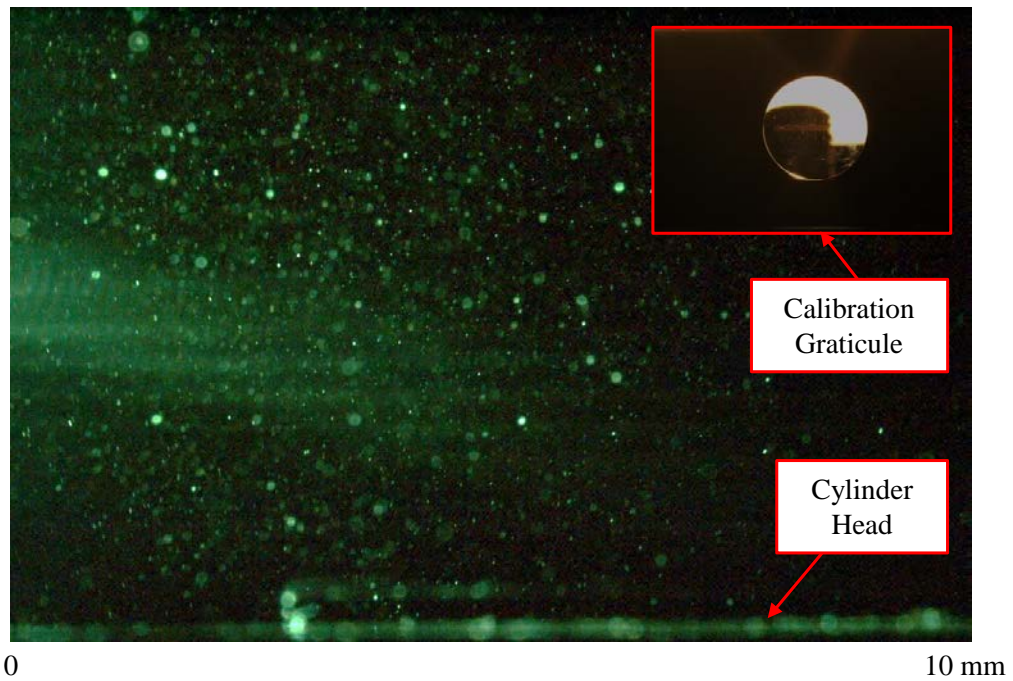
Figure 4.70 DSLR image across the cylinder head of the oil aerosol generated by the crankshaft and camshaft at 1400 rpm

0   10 mm
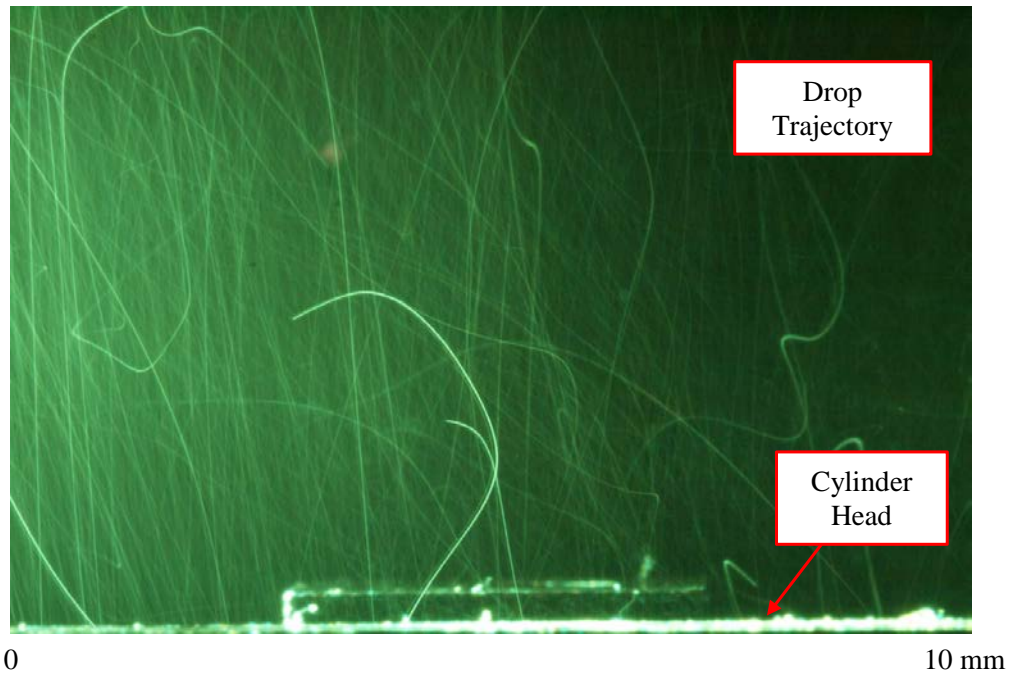
Figure 4.71 Long exposure DSLR image across the cylinder head of the oil aerosol generated by the crankshaft and camshaft at 1400 rpm

Figure 4.70 shows the high number concentration and small diameter of atomised drops present in the rocker cover for a sump oil temperature of 60°C. There are over

2000 drops $10\,\mu m \geq d_p \leq 400\,\mu m$ in the single $10\,mm \times 10\,mm$ image shown in Figure 4.70. Due to the lack of oil supplied to the cylinder head and valve gear these drops were generated predominantly by the crankshaft and transported up through the pushrod galleries suspended in the crankcase flow. The single long exposure image in Figure 4.71 captures the strongly vertical trajectory of the drops that are thrown up the pushrod gallery. Increasing the engine speed increased the drop number concentration with a less significant reduction in the mean drop diameter, speed effects are investigated in more detail later in this section.

A single image was chosen to represent the high resolution data set collected at 1400 rpm. The drop diameters present in the representative image are plotted in Figure 4.72, the mean diameter of drops captured was $d_p = 32\,\mu m$ with a standard deviation of. The graph in Figure 4.72 highlights the range of drop diameters that were witnessed in the images.
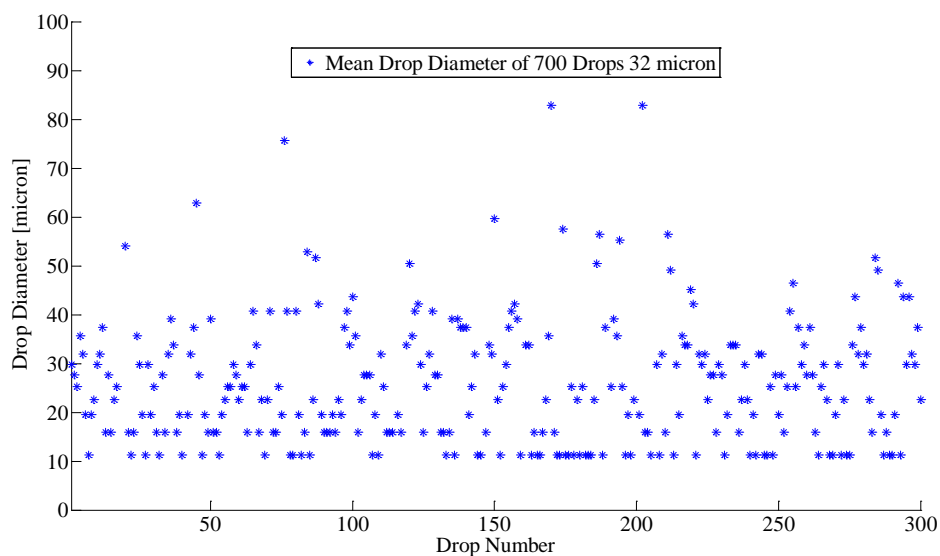
Figure 4.72 Range of drop diameters transported from the crankshaft and camshaft into the rocker cover

The purposely restrictive experimental setup meant that the primary atomisation mechanism generating oil was either the crankshaft or camshaft. The images displayed throughout this chapter demonstrate the complexity and large variability in the ligament breakup process that occurs at the crankshaft and camshaft. The variation in the ligament breakup process alone explains the range of drop diameters that were witnessed in the top of the engine.

Additionally, the temperature and blow-by velocity around the crankcase will affect the primary and secondary breakup of oil drops witnessed in the top of the engine. Oil evaporation due to the elevated temperatures at the journal bearings will generate oil vapour, subsequent homogenous or heterogeneous condensation of the oil vapour within the crankcase has the potential to increase the drop number concentration and mean drop diameter. Aerosol evaporation and condensation are discussed in more detail in Chapter 5. Further secondary breakup will occur at higher blow-by rates because the aerodynamic Weber number of atomised oil drops will be higher, therefore potentially altering the diameter and number of oil drops in the top of the engine.

Engine Valves

0

90 mm
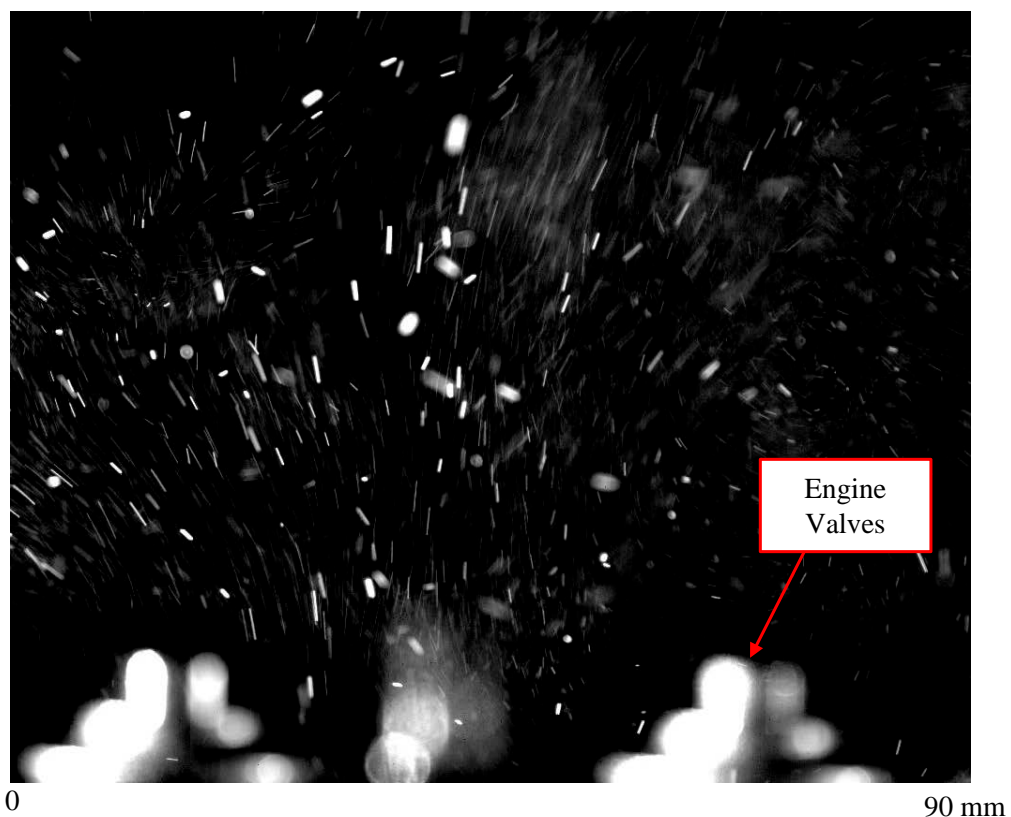
Figure 4.73 High speed image of the oil aerosol generated by the crankshaft and camshaft at 1400 rpm

The effect of engine speed on drop generation was evaluated by measuring the drop count for over 1000 high speeds images collected at 500 fps for engine speeds of 900, 1400 and 2000 rpm. The smaller resolution of the high speed camera meant that only drops $d_p \geq 100$ μm could be resolved and counted in the images an example image and the resultant drop counts are displayed in Figure 4.73 and Figure 4.74

respectively. The drop number increased with engine speed but the difference between engine speed is not as significant as that seen at the source of the drop generation around the crankshaft and camshaft. The low variability suggests that the drop count stabilises over the length of the pushrod gallery as there are no additional sources of primary atomisation.
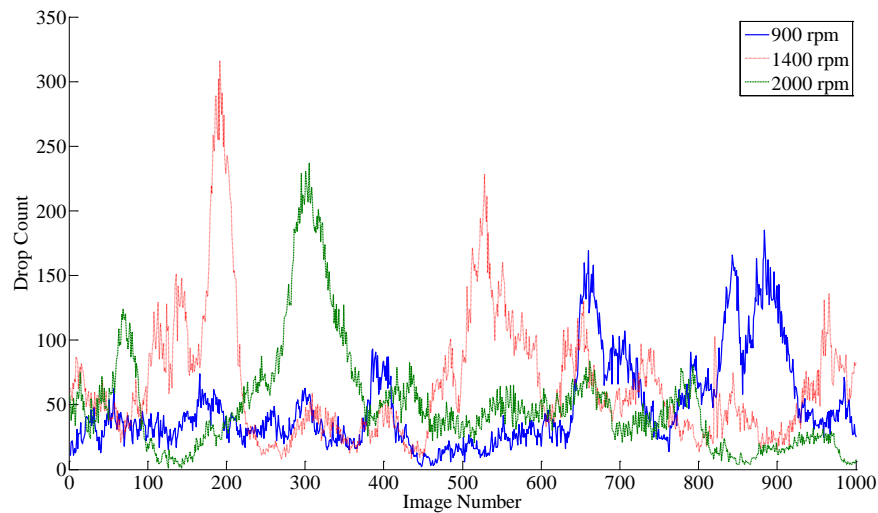
Figure 4.74 Effect of engine speed on drop number for oil drops $d_p \geq 100$ µm in the cylinder head

Interestingly oil drops were present in the high speed images even when there was no blow-by flow introduced into the crankcase, the drop number concentration was much lower but drops were still generated at the crankshaft and carried up the pushrod gallery. The transport of the drops was caused by the flow induced by the crankshaft rotation. The large crankshaft volume and its high angular velocity meant that pressure differences were generated by the crankshaft motion, this resulted in a pulsating flow within the crankcase that transported the atomised oil drops.

Figure 4.75 shows a single high speed image with improved resolution taken at 250 fps capturing the trajectory and indicating the high 4 m.s^{-1} velocity of large oil drops $d_p \approx 60$ µm thrown up from the pushrod gallery. The majority of the oil drops behaved like fine seeding, tracing the blow-by flow around the top of the cylinder head with a velocity of the 2 m.s^{-1} which is equal to the blow-by gas velocity expected across the pushrod gallery. The high velocity of these drops indicates that they are accelerated by forces additional to the blow-by. Although drops down to

$d_p = 60$ µm were below the optical limit of the previous imaging work, this data set again shows that the crankshaft and camshaft contribute significantly to the oil aerosol present near the crankcase vent.
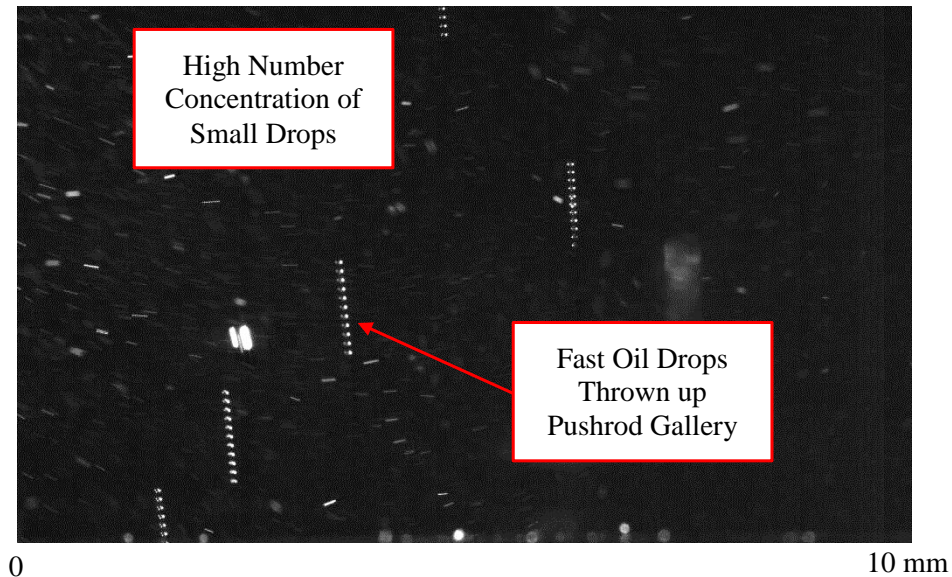
Figure 4.75 Long exposure high speed image across the cylinder head of the oil Aerosol generated by the crankshaft and camshaft at 2000 rpm

4.7.1 Rotating Components Summary

The images presented are extremely valuable as they provide evidence that the crankshaft and camshaft are major contributors to crankcase oil aerosol generation. The number concentration of drops witnessed was significant even with the low blow-by rate and oil temperature of 100 litres.min^{-1} and 60°C respectively. Higher values of both parameters will be generated on a firing engine, therefore primary and secondary oil atomisation will be more likely and the number concentration of oil drops will increase. Although the diameter of the drops captured was small, with careful utilisation of the crankcase surfaces and oil films, forced impaction and coalescence of the oil drops may prevent the oil aerosol leaving the crankcase. Further investigation of this potentially valuable and effective control strategy is required.

4.8 Concluding Remarks

A detailed optical analysis of crankcase oil atomisation has been presented and discussed in this chapter. Imaging was conducted at a range of engine speeds and locations around the crankcase to capture the generation and transport of atomised oil drops. The main mechanism of oil drop generation was from the atomisation of oil films on rotating components most notably the crankshaft and thus crankcase oil atomisation was highly dependent on engine speed. Oil ligament necking and breakup was the most significant mechanism of primary oil breakup and drop generation. The range of optical data collected has been used to assess the validity of predicting oil distribution and ligament breakup using a computational model. An initial volume of fluid model has showed promising results, which indicate that oil ligament breakup and drop generation can be predicted, provided the fluid domain is specified accurately.

The next chapter documents a comprehensive sampling study focussing on submicron crankcase emissions. The crankcase particulate and oil drops were sampled from the motored test engine used in this optical study and an equivalent fired engine. The combination of the optical data presented in this chapter and the quantification of the crankcase emissions from the data presented in the next chapter provides a thorough characterisation of crankcase emissions.

CHAPTER 5

CRANKCASE PARTICLE SAMPLING

5.1   Introduction

Diesel particle emissions are classified as carcinogenic (IARC, 2012), consequently governing bodies will continue to regulate their production with increasing severity. Historically, diesel particulate matter was only legislated by particle mass, but in 2011 Regulation 692/2008 defined the maximum particle number emissions from on-highway diesel engines in Europe. The mass of emission inhaled is important, however, it is the particles size that dictates the level of human ingestion. The current off-highway particulate mass measurement standard provides little information on particle size.

The diagram of the human respiratory tract shown in Figure 5.1 illustrates the size range of aerosol particles that will be trapped when inhaled. The problematic size range is 5 nm – 7 µm, because when inhaled these particles will be absorbed by the human respiratory tract (Lobo, 2002).
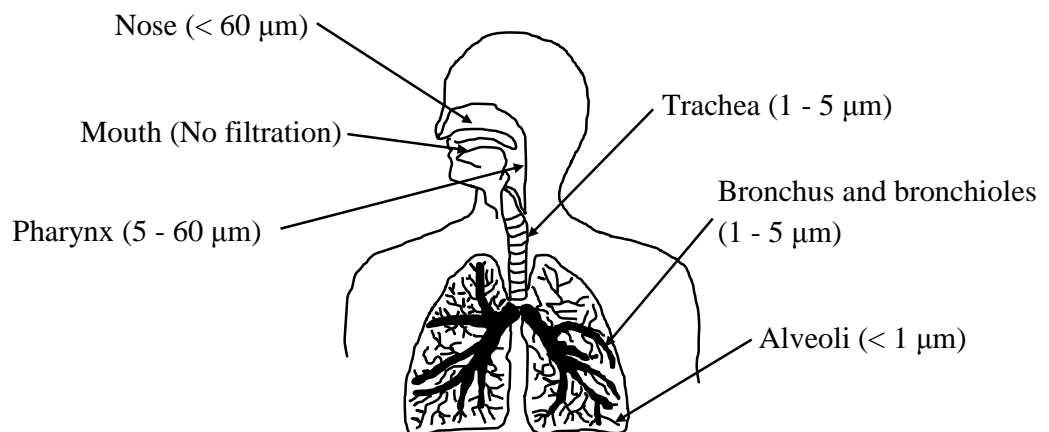
Figure 5.1 Depository characteristics of particulate in the human respiratory tract. Adapted from Lobo (2002)

If a closed crankcase system is used to reduce the crankcase emissions, then the crankcase emissions must still be filtered. In CCV system the high particle number in the re-circulated crankcase gas will foul the turbocharger and other engine components, substantially reducing the engine efficiency. Any vapour generated from volatile fuel and oil components may condense in the high pressure volute of the turbocharger causing further fouling problems.

In Chapters 1 and 2 discussed the paucity of work that has been published on crankcase emissions and highlighted that crankcase particulate emissions are very sensitive to crankcase design (Tatli and Clark, 2008). Information quantifying crankcase particulate emissions is sparse, and there is deficiency in the understanding of how lubricating oil contributes to the crankcase emissions.

To address this absence of understanding, a detailed particle sampling study was conducted on the fired and motored engines introduced in Section 3.7. Testing was completed at a range of engine speeds, blow-by rates and crankcase locations.

Sampling instruments were used to measure the crankcase emissions in the size range 5 nm – 20 µm. The chosen instruments were; the Cambustion DMS500 fast particulate spectrometer, the TSI Scanning Mobility Particle Sizer (SMPS), the TSI Condensation Particle Counter (CPC) and the TSI Aerodynamic Particle Sizer (APS). The operating principles of the sampling equipment is described in Section 2.10. Full details of the sampling and engine setup are given in Section 3.7. Critical information regarding the equipment and test condition is presented in this chapter.

Over 380 sampling tests were completed, the results quantify the crankcase particulate emissions from a specific engine and sampling setup, including the isolated contribution of the lubricant oil to crankcase particulate emissions. The particle number distributions and the effect of parameter changes on crankcase oil emissions have been evaluated. Results highlight the main mechanisms generating the crankcase oil emissions. The sampling data has been correlated with optical data presented in Chapter 4 in order to provide supplementary information on the major mechanisms of crankcase oil aerosol generation.

5.2 Acknowledged Sources of Crankcase Emissions

Data collected in this chapter and Chapter 4 identifies the main mechanisms of crankcase oil aerosol generation. Atomisation of lubricating oil driven by the relative velocity or acceleration acting on the oil, generates oil drops $1\,\mu\text{m} \le d_p \le 700\,\mu\text{m}$. Images in Chapter 4 captured oil atomisation driven by the acceleration of oil films on the crankshaft, camshaft and rockers which generated drops $d_p \le 10\,\mu\text{m}$. Figure 5.2 indicates the high number of oil drops that are atomised by the crankshaft and transported up into the top of the engine.

Calibration
Graticule

Cylinder
Head

0   10 mm
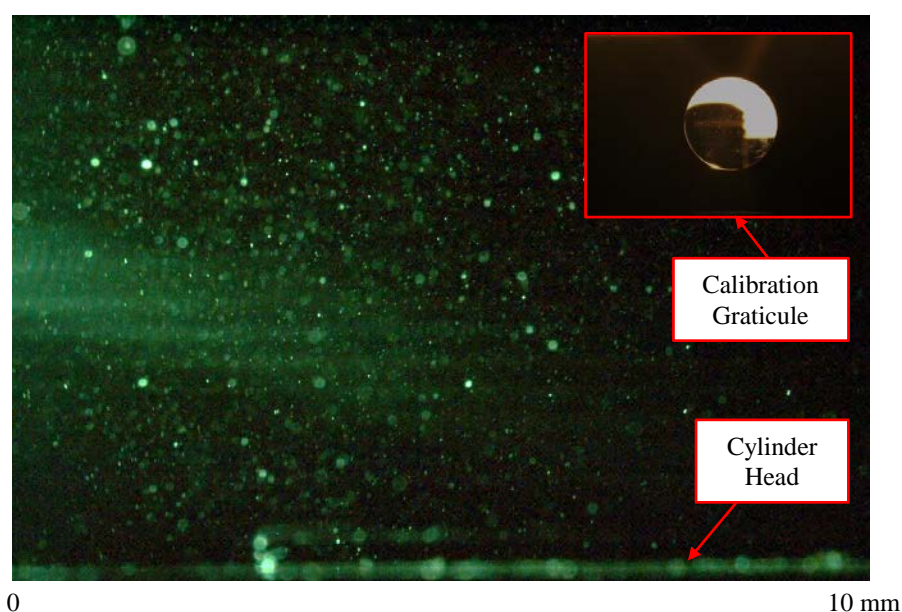
Figure 5.2 Image across the cylinder head of the oil aerosol generated by the crankshaft and camshaft at 1400 rpm

A separate body of work by Dyson, Priest and Lee (2010) focussed on oil atomisation from the piston rings and captured oil drops $4\,\mu\text{m} \le d_p \le 120\,\mu\text{m}$ generated by the sonic gas velocity around the piston rings. The contribution of ring pack oil atomisation was minimised during the motored engine sampling study by removing the blow-by past the piston rings and sealing the piston cooling jets.

Unpublished work completed by Lotus Engineering highlighted the significant contribution of the turbocharger oil drain to crankcase emissions. Investigating turbocharger oil atomisation was outside the scope of the work completed in this study. However, considering the increasing trend in turbocharger boost pressure,

turbocharger oil atomisation is identified as a region for further investigation in Chapter 7.

Focussing on the combustion process, it is well documented that primary soot particles typically sized between 20 – 50 nm are generated in the rich regions of diesel diffusion flames (Virtanen, Ristimaki, Vaaraslahti and Keskinen, 2004). Excess oxygen that is present due to the high air fuel ratio of the total combustion mixture, means there is significant oxidation of the soot, this provides a mechanism for reducing particle size (Harris and Maricq, 2002). Agglomerates of primary soot particles are formed in the engine exhaust and blow-by. Primary and agglomerated soot particles generated by diesel combustion can act as condensation sites.

Submicron accumulation mode particles present in diesel combustion products are primarily composed of carbonaceous agglomerates and absorbed material, most of the submicron particle mass occurs in the accumulation mode (Kittelson, 1998). Smaller nucleation mode particles consist mainly of volatile organic species formed, from unburned fuel and unburned oil including small amounts of solid carbon and metallic compounds (Kittelson, Watts and Johnson, 2002; Sakurai *et al.*, 2003). Volatile fuel and oil particle species emitted from diesel engines will remain in the gas phase, condense on existing solid particles or nucleate to form new particles (Burtscher, 2005). Crankcase gas temperature will strongly effect the crankcase particle size number distribution, as the behaviour of volatile species depends largely on temperature. Sulphur from the fuel can also contribute to the nucleation mode particles. Ultra-low sulphur diesel with 15 ppm sulphur was used on the fired engine tested in this study. The contribution of sulphur particles to the particulate matter emissions can be considered negligible in the results presented in this thesis.

The trimodal Whitby model shows that total submicron particle number concentration of 1.38×10^4 N.cm^{-3} have been found in urban locations (Whitby, 1978). The contribution of anthropogenic activities to atmospheric aerosols is carefully regulated. Engine emissions legislation is discussed in Section 1.3 and Section 1.4, additionally to this the Environmental Health Organisation provides an exposure limit to oil mist. The oil mists exposure limits for the oils used on the fired and motored engines are shown in Table 5.1.

Table 5.1 Oil mist exposure limits

Oil	Regulations	Exposure Duration	Exposure Limit [mg.m^{-3}]
SAE 15W-40	ACGIH	TWA	5
SAE 15W-40	ACGIH	STEL	10
SAE 5W-30	ACGIH	TWA	5
SAE 5W-30	OSHA	TWA	5

Submicron crankcase particulate matter from both oil and combustion products is the main focus of this particle sampling investigation. Information on the generation of submicron crankcase particles and drops is scarce, due to their complex behaviour and sensitivity to measurement. Developing a better understanding of submicron particles is crucial to the sustainable future of the internal combustion engine as a prime mover.

Submicron particles are extremely difficult to filter and they present significant detrimental health effects. Non-serviceable components that are effective at removing oil drops down to 5 µm have been successfully developed by Long *et al.* (2009) and Gokten *et al.* (2008), but the removal of submicron particles requires complex, expensive and consumable components that increase parasitic losses. Any knowledge gained on the evolution and behaviour of submicron crankcase particles is extremely beneficial, as it will assist the design and implementation of crankcase filtration devices.

5.3   Overview of Experimental Setup

Separate fired and motored engines were used in this study. The internal crankcase components and oil circuit were identical for both engines, however, the fired engine was turbocharged and accordingly there was an oil feed from the oil rail to the turbocharger and an oil return into the crankcase in the side of the engine block. The full specifications for these engines and a detailed description of the oil circuit can be found in Appendix A Table A-1.1, Table A-3.1 and Section A-2 respectively.

Two different engine oils were used to examine their effect on crankcase oil aerosol generation. The fired engine used SAE 15W-40 and the motored engine used SAE 5W-30. At 100°C the kinematic viscosities of the two oils differs by 5.1×10^{-6} m^2.s^{-1}. Noack volatility tests were conducted to ASTM D5800 B, on both oils to measure the percentage weight loss of the oil that evaporated at 250°C. The results of the Noack tests were very similar for both oils, for the SAE 15W-40 oil 11.3% m.m^{-1} and for the SAE 5W-30 oil 12.0% m.m^{-1}. Further properties of both oils are listed in Appendix B Table B-2.2.

Due to the similarities in oil properties and the results from the experimental investigations presented throughout this thesis, using different lubricating oil was found to have a negligible effect on the mechanisms and trends of crankcase oil aerosol generation. It is expected that the number concentrations and final drop diameters will vary with the physical properties of the oil, but the initial breakup and thermal processes will be consistent.

Three types of sampling equipment were used to characterise the crankcase particulate matter emissions. On the fired engine the Cambustion DMS500 MkII fast particulate spectrometer was used to measure particles $d_p = 5$ nm - 1 µm. Comparatively on the motored engine the TSI SMPS and CPC were used to measure particles $d_p = 15$ nm – 660 nm and the TSI APS to measure particles $d_p = 0.5$ µm - 20 µm. The operating principles of this equipment are described in Section 2.10 and full details of the sample extraction and dilution are described in Section 3.7.

For all sampling tests, the results collected were not intended to be a total emissions measurement. The experimental setup was designed around the operating requirements of the sampling equipment and it was kept consistent. Any variation in the results was attributed to changes in engine parameters or sampling location only, thus highlighting factors which influence crankcase particulate generation.

Thermocouple measurements were taken at various locations around each engine. K-type thermocouples were used to record any temperature variation and ensure the engine temperature was stable before sampling tests started. The thermocouple

measurement points were; the sump oil, the oil film above the pushrod gallery, the gas temperature at the top and bottom of the pushrod gallery, the sampling points and the coolant temperature in the thermostat housing. On the fired engine the air temperature after the turbocharger compressor was also measured. The oil rail temperature and pressure was monitored on both engines.

5.3.1 Fired Engine Sampling

The fired engine particulate matter was sampled using the Cambustion DMS500 at the three crankcase locations; the oil filler cap in the rocker cover, the pushrod gallery core plug and the dipstick mounting hole in the sump. The engine exhaust was also sampled to indicate the contribution of the combustion products to the crankcase particulate emissions. Sampling was conducted at the range of engine speeds and rated loads shown in Table 5.2.

Table 5.2 Fired engine sampling test matrix

Fired Engine				
Crankcase and Exhaust	Rated Load [%]			
Speed [rpm]	0	25	50	75
900	x	x	x	x
1200	x	x	x	x
1400	x	x	x	x
1600	x	x	x	x

For all fired engine sampling tests the crankcase was vented through the production crankcase vent in the rocker cover into an AVL blow-by meter. The DMS500 requires a sample of 8 litres.min^{-1}, an appropriate sample was extracted from one of the three specific sampling points and diluted to an appropriate level before entering the DMS500. Since combustion products in the blow-by generated a high crankcase particle number concentration, the crankcase was always vented via the main

crankcase sampling point into the AVL blow-by meter, and the sampling instrument was connected directly to one of the three sampling test points.

5.3.2 Motored Engine Sampling

The objective of the motored engine study was to understand the contribution of lubricating oil to crankcase particulate emissions. A series of sampling tests were conducted at the range of test conditions listed in Table 5.3, to provide novel information on the influence of engine parameters and sampling location on crankcase oil aerosol emissions.

Table 5.3 Motored Engine Sampling Test Matrix

Motored Engine						
Crankcase	Crankcase Flow Rate [litres.min^{-1}]					
Speed [rpm]	40	60	80	100	150	200
360	x	x	x	x	x	x
600	x	x	x	x	x	x
900	x	x	x	x	x	x

The motored engine sampling analysis was conducted using the TSI SMPS, CPC and the APS. Samples were taken from three locations around the crankcase of the engine; the dipstick mounting hole, 100 mm down the pushrod gallery and the oil filler cap. The entire crankcase was vented through each sampling point on the motored engine, then a sample was drawn from that total flow, the sample extraction is illustrated in Figure 3.21. Results provide important information on the evolution of the crankcase oil aerosol. Further details of the sample extraction on the motored engine can be found in Section 3.7.1.

The motored engine was driven by a 30 kW electric motor to a maximum speed of 900 rpm. The inducted cylinder volume was vented via the fuel injector and glow plug holes, and a temperature controlled steady state crankcase flow was introduced

below the piston skirt to replicate blow-by. The crankcase flow temperature was kept at 100°C and the engine coolant circuit was heated to 90°C for all tests.

5.4 Data Presentation

The particle sampling results are presented as plots of normalised number concentration against lognormal particle diameter d_p. The full range of measured particle diameters is plotted in Figure 5.3, to show that the particle size range of the SMPS and CPC used on the motored engine fell within that of the DMS500 used on the fired engine. Unfortunately, the same particle sampling equipment could not be used on both the fired and motored engines. The DMS500 and SMPS instruments were chosen so that the submicron crankcase particle measurements from the fired and motored engines were in the same size range and could be compared.
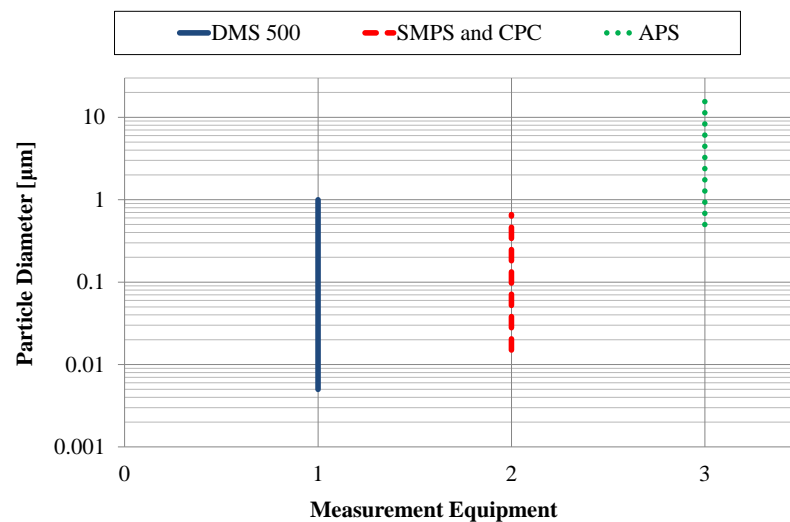
Figure 5.3 Size range of particle sampling equipment

The APS measured the aerodynamic particle diameter, which represents the diameter of a standard density ($\rho_0 = 1000$ kg.m^{-3}) sphere that has the same gravitational settling velocity as the measured particle (Kulkarni, Baron and Willeke, 2011). The aerodynamic diameter standardises for particle shape and density. The particle diameter d_p can be calculated from the aerodynamic diameter D_{Aero} using the particle density ρ_l and standard density ρ_0, as shown in Equation (5.1). For SAE15W-40 oil at 80°C the particle diameter d_p, is 0.922 of the aerodynamic diameter, D_{Aero}. All the APS data has been plotted against aerodynamic particle diameter in microns.

Aerodynamic Diameter $$D_{Aero} = d_p\sqrt{(\rho_l/\rho_0)} \qquad (5.1)$$

As discussed in Chapter 1 and displayed in Equation (1.1), the normalised number concentration enables comparison of aerosol size number distributions between different aerosol sizing instruments. For the submicron particle measurements, the number of particles in each size range was calculated from the voltage at the electron rings in the DMS500 and using the CPC following the SMPS differential mobility analyser. The APS measured the aerodynamic particle diameter and particle count using a pulse of scattered light from two laser beams with a fixed separation. These measurements provide a number concentration of particles per cubic centimetre (cm^3), as shown in Equation (5.2). With knowledge of the particle density and shape factor the normalised mass concentration of particles in milligrams (mg) per cubic centimetre (cm^3) can be calculated as shown in Equation (5.3). Particles from the motored engine crankcase were only oil drops. Assuming a shape factor of one, the density of the oil at the specified temperature can be used to calculate the mass concentration. The same oil density and shape factor was used to calculate the fired engine mass to provide a comparable measurement, however, this assumption is less accurate as combustion products of agglomerated diesel soot particles and condensed unburned fuel vapour will be present in the crankcase sample.

Particle Number Concentration per cm^3 $$dN/d\mathrm{log}D_p/cm^3 \qquad (5.2)$$

Particle Mass Concentration mg per cm^3 $$dM/dlogD_p \ mg/cm^3 \qquad (5.3)$$

Geometric mean diameters (d_g) and geometric standard deviations (σ_g) of the size number distributions have been used to compare data sets. Geometric values were used as they normalised the lognormal particle size number distributions. Geometric mean diameter and geometric standard deviation can be calculated using

Equation (5.4) and Equation (5.5) respectively, where n_i is the number of particles in the ith group, d_i is the midpoint diameter of the ith group and N is the total number of particles (Hinds, 1999).

<table>
<tr><td>Geometric Mean
Diameter</td><td>$$\ln d_g = \frac{\sum n_i \ln d_i}{N}$$</td><td>(5.4)</td></tr>
</table>

<table>
<tr><td>Geometric Standard
Deviation</td><td>$$\ln \sigma_g = \left(\frac{\sum n_i \left(\ln d_i - \ln d_g \right)^2}{N-1} \right)^{1/2}$$</td><td>(5.5)</td></tr>
</table>

A total flow of 8 litres.min^{-1} was drawn into the DMS500 at 90°C. Primary and secondary dilution was then available to dilute the sample, ensuring that the particle concentration was not too large. The principles of DMS500 sample dilution are described in Section 2.10. The DMS500 data processing MS Excel Macro corrected for the sample dilution by multiplying the spectral data by the dilution ratio. Adjusting the dilution ratio was found to have no marked effect on the sampling results from the DMS500. The APS used sample dilution as described in Section 2.10, the SMPS and CPC did not use any dilution. The TSI Aerosol Instrument Manager software was used to process the SMPS, CPC and APS results, the APS instrument dilution ratio was specified and corrected for in the final results.

5.5 Repeatability

The sampling instruments and the test engines were warmed to the specified temperatures before each test to minimise the effect of temperature variations on the sampling results. Temperature drops in the sampling lines were controlled by minimising the length of the sampling pipe work and using pipe insulation. The effectiveness of these control measures, and the repeatability of the sampling equipment was assessed by comparing a minimum of three data sets collected at a fixed test point over a 20 minute test. The repeatability results from the fired engine collected at a fast idle speed of 900 rpm sampling from the pushrod gallery at various engine loads using the DMS500 are shown in Figure 5.4.
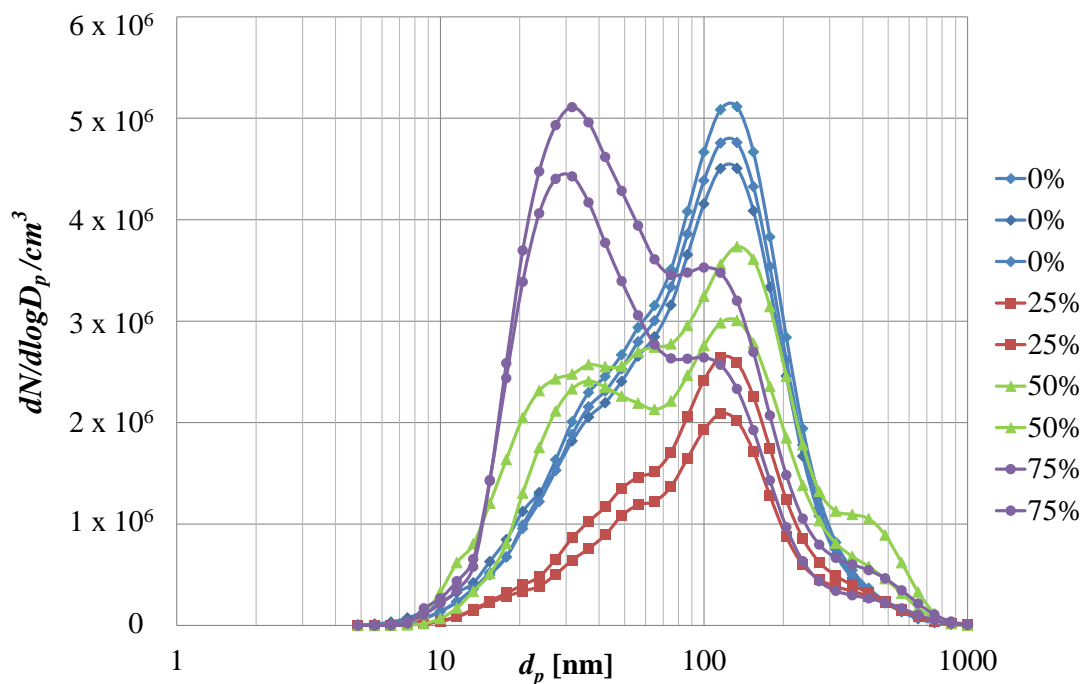
Figure 5.4 DMS500 fired engine size number distribution of crankcase particulate matter for varying engine load at 900 rpm sampling from the pushrod gallery

Variation in number concentration was significant for all engine loads, but the trend across the measured particle size range was consistent. Geometric means of the distributions shown in Figure 5.4 are plotted in Figure 5.5. The minimum standard deviation between data sets was 0.6 at 50% load, the maximum standard deviation of repeat data sets was 4.5 at 75% load. At 75% load the lognormal size number distribution was bimodal, the difference in the geometric mean diameters was caused by differences in the position of an accumulation mode peak around 100 nm. The size number distribution was also bimodal at 50% load, the standard deviation of the geometric means was very low as the data sets showed good agreement, however, Figure 5.4 clearly shows a difference in the data sets around 65 nm and 420 nm. The variations in the 50% load data sets cancelled each other out and no change was reflected in the geometric means. The difference in the size number distribution can be identified by comparing the total particle number concentration. At 50% load the standard deviation of the total particle number was 121% of the mean total particle number concentration.
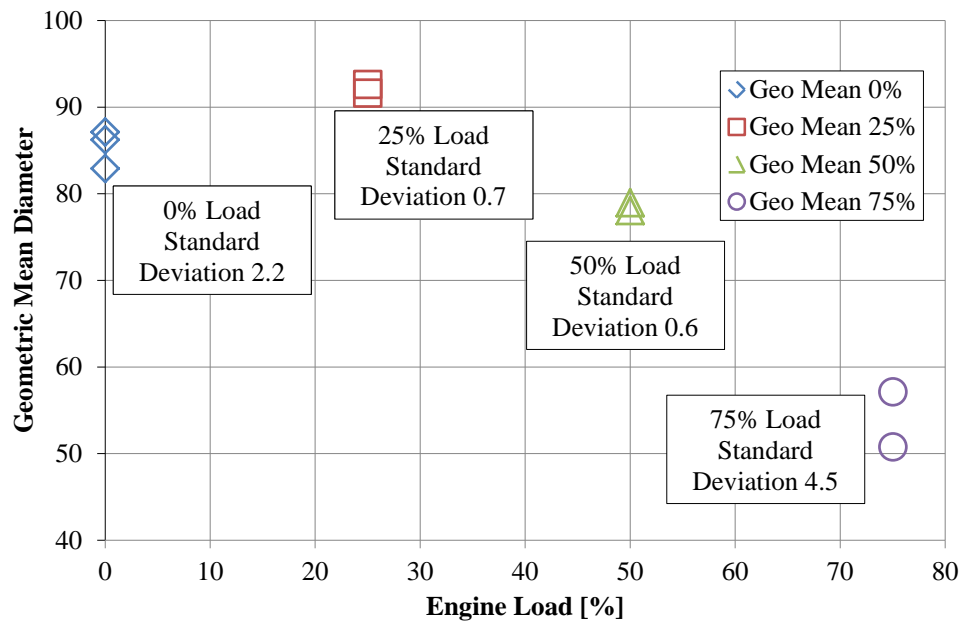
Figure 5.5 Geometric mean diameters of data plotted in Figure 5.4

A typical contour plot of the data sets shown in Figure 5.4 is presented in Figure 5.6, to show the little fluctuation in the sampling equipment for stable engine conditions of 900 rpm 0% load over a 20 minute test. The contour plot in Figure 5.7 shows the same test conditions but at 75% engine load, the plot is less stable over the 20 minute test. The instability in the submicron particle number concentration at 900 rpm 75% load is also reflected by the large standard deviation of the geometric means between the two identical tests, as plotted in Figure 5.5.
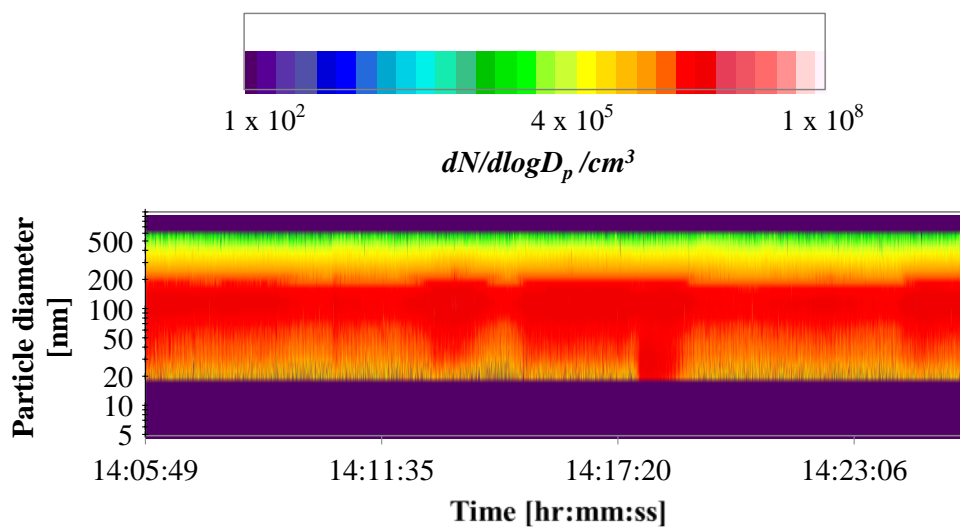
Figure 5.6 DMS500 fired engine contour plot at 900rpm 0% load sampling from the pushrod gallery
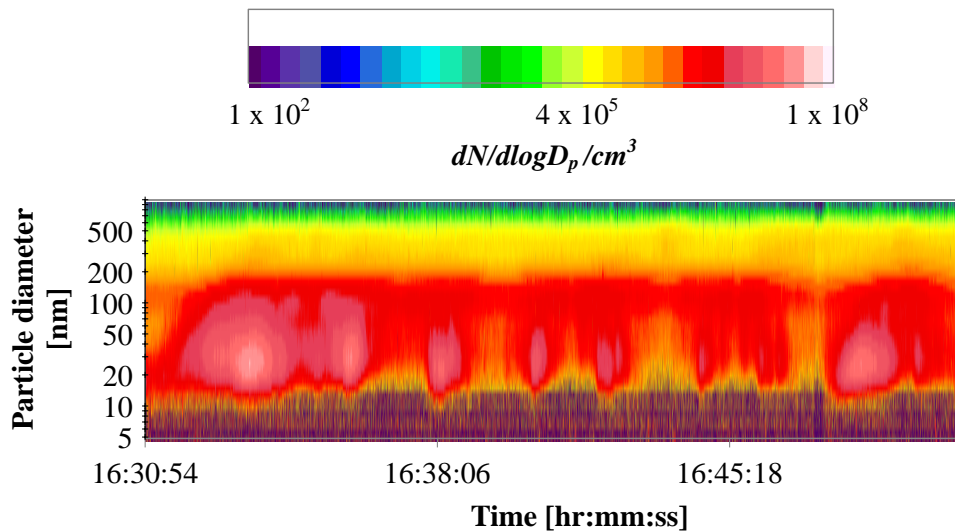
Figure 5.7 DMS500 fired engine contour plot at 900 rpm 75% load sampling from the pushrod gallery

The repeatability assessment indicated that the number concentration measurements should be interpreted with care. The signal to noise ratio was low due to the high dilution ratio used to avoid instrument damage, this was acknowledged and each data set was examined clearly to ascertain if a repeat test was required.

The results discussed thus far quantified the repeatability of the sampling instruments over the measured size range for a 20 minute test duration. To increase the range of test conditions the test duration was dropped to 15 minutes, then with continued repeatability 10 minutes.

5.5.1 Repeatability Summary

The repeat tests show that the size number distributions and the location of peak particle diameters can be confidently evaluated. The acceptable variation in geometric mean and standard deviation between data sets at fixed engine conditions is presented in Figure 5.5. Any significant variation outside these values can be attributed factors other than the sampling system, most importantly physical processes occurring within the engine. The SMPS and APS equipment used on the motored engine showed similar repeatability to that of the DMS500 for repeat tests at stable engine conditions. Three repeat 10 minute tests were completed and compared during the data collection for each test point to enable better assessment of the data.

5.6 Load Variation

The variation of blow-by flow rate with engine speed and engine load is plotted in Figure 5.8. The figure shows that the crankcase flow rates of 40, 60 and 80 litres.min^{-1} used on the motored engine, provided a good representation of the variation in blow-by from the fired engine, the best match was at 1400 rpm.
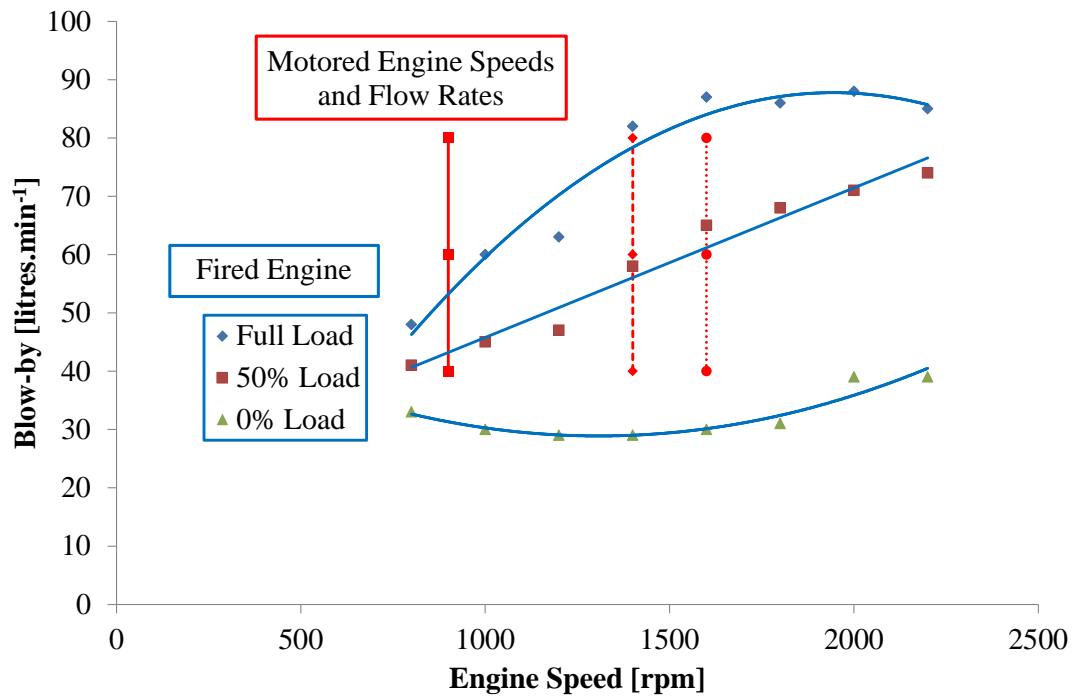
Figure 5.8 1104C-44 crankcase blow-by rates for varying engine speed and load

The fired engine data in Figure 5.9 highlights the significant effect of varying the engine load on the size number distribution of submicron particles from the pushrod gallery at 900 rpm. Increasing the engine load caused the peak number concentration of particles to shift from the accumulation mode ($d_p = 100 – 1000$ nm) to the nucleation mode ($d_p = 5 – 100$ nm). There are several published nucleation mode and accumulation mode size ranges, with slight differences between them. For the work presented in this thesis the size ranges defined by Kulkarni, Baron and Willeke (2011) stated above have been used.
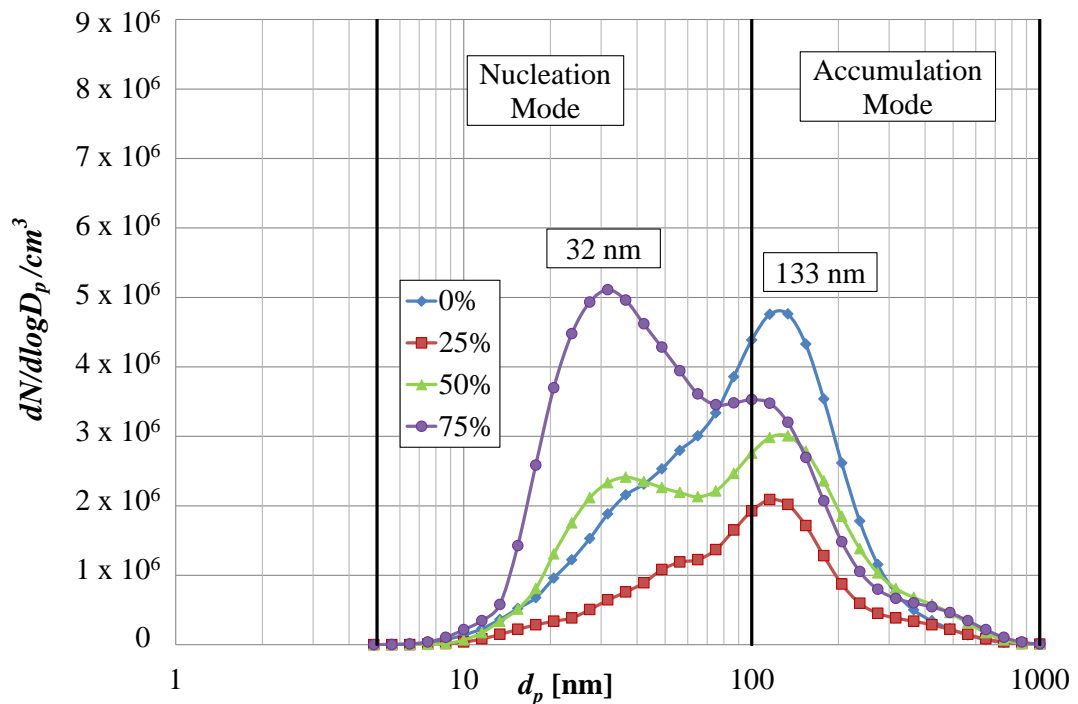
Figure 5.9 DMS500 fired engine size number distribution of crankcase particulate matter for varying engine load at 900 rpm sampling from the pushrod gallery

Initially on the fired engine with no load and therefore the lowest blow-by rate of 30 litres.min^{-1}, there was a lognormal distribution of particles with a peak centred at 133 nm. As load was applied the peak particle diameter remained at 133 nm but the number concentration of particles in the accumulation mode reduced. At 50% and 75% load the number concentration of particles in the nucleation mode increased and the lognormal size number distribution of particles became bimodal. At 75% load, the highest tested load, a small peak remained at 133 nm but a large peak was generated in the nucleation mode at 32 nm. The shift in peak particle diameter caused by increasing the engine load, can again be identified by comparing the contour plots of size number distribution in Figure 5.6 and Figure 5.7. At higher the engine load shown in Figure 5.7, the size number distribution is less stable over the test duration, but remains bimodal for the majority of the test.

Figure 5.10 DMS500 fired engine size number distribution of crankcase particulate matter for varying engine load at 900 rpm sampling from the rocker cover

Varying the engine load had the same effect on the fired engine rocker cover emissions, as shown in Figure 5.10. Initially at low load the size number distribution of particles was single mode with a peak at 133 nm, a second nucleation mode peak at 37 nm was generated at 50% and 75% load. In contrast to the pushrod gallery, at 50% load the number concentration of particles in the rocker cover was four times the magnitude of the results at other engines loads. The large variation in the size number distributions was greater than that witnessed in Section 5.5, thus factors other than variability in the sampling equipment were affecting the sampling results. As the data was evaluated during testing, three additional repeats tests were collected at this notable test condition of 900 rpm 50% load.

The size number distribution of fired engine rocker cover particulates at 900 rpm with 50% load for six tests is shown in Figure 5.11. There was substantial variation in the number concentration and size number distribution over the six tests, the geometric mean and total particle number values are shown in Figure 5.12. The standard deviation of the geometric mean diameters between the six data sets was 35% of the mean. The standard deviation of the total particle number concentration

was 86% of the mean. These very high values were caused by the shift between the accumulation mode and the nucleation mode and the large variation in particle number. Potential causes of these complex trends are discussed in Section 5.11.1 once all the sampling data has been presented.
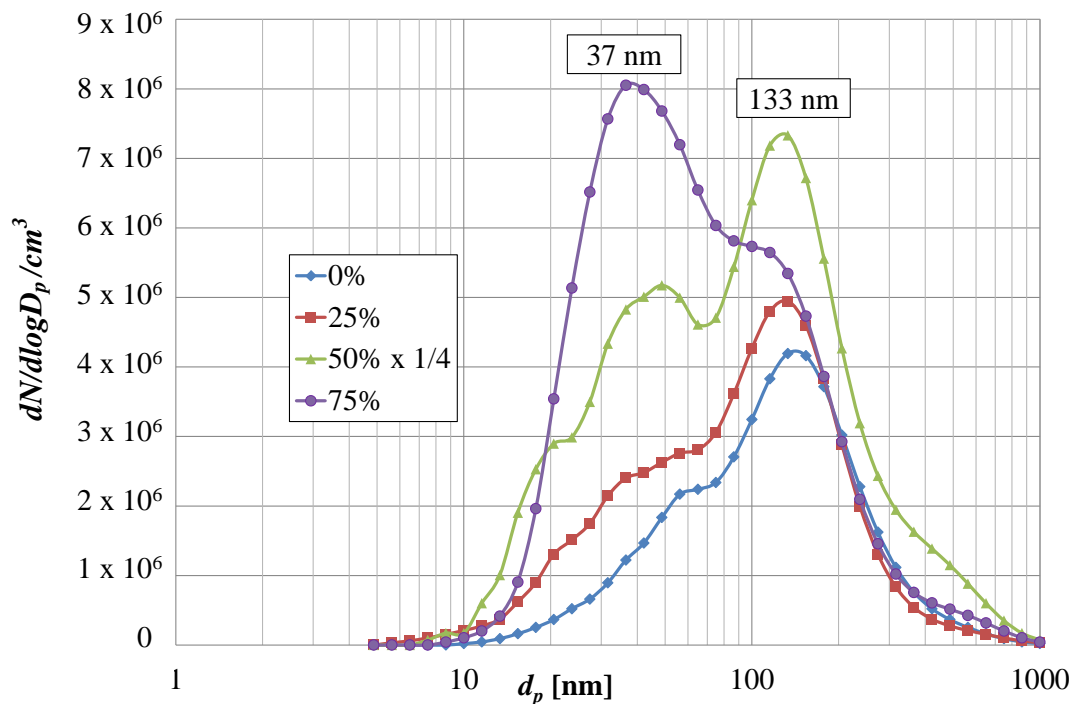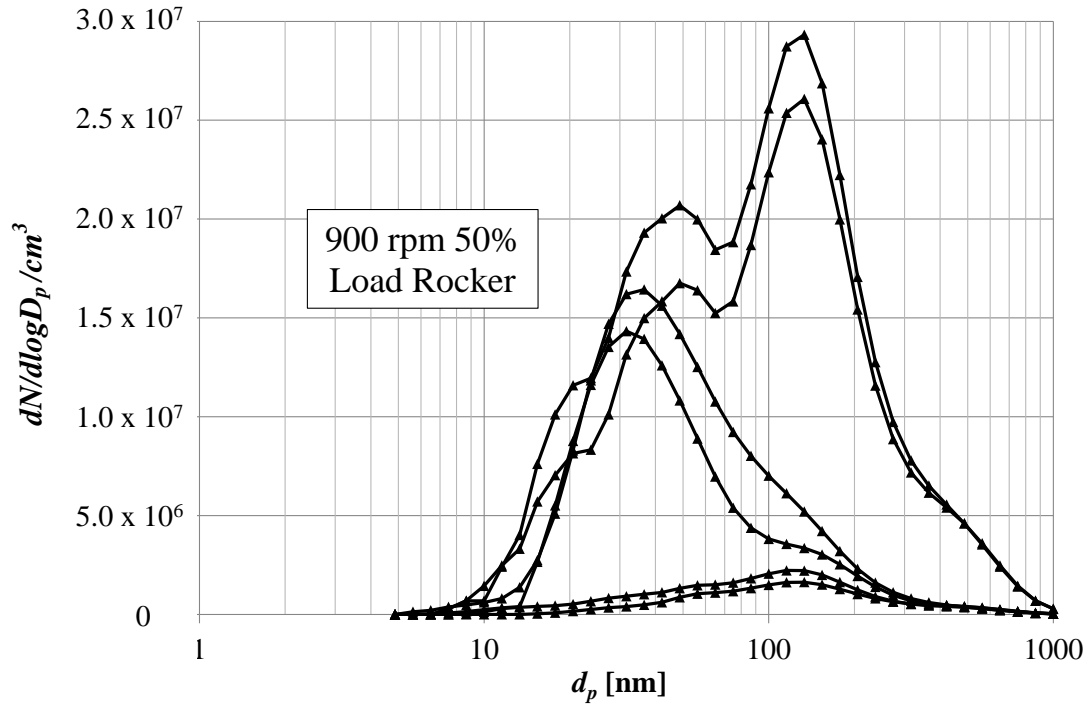

Figure 5.11 DMS500 fired engine size number distribution of crankcase particulate matter at 900 rpm and 50% load sampling from the rocker cover
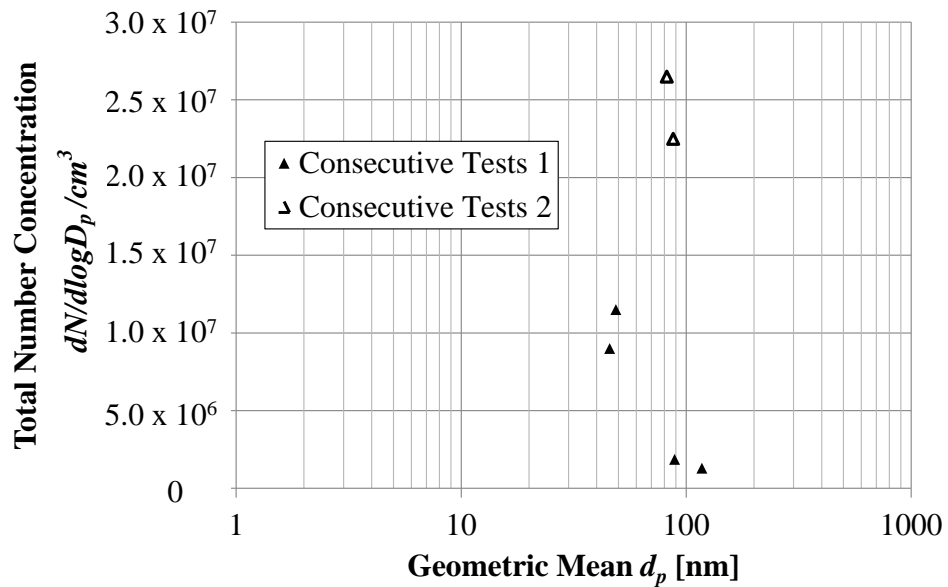
Figure 5.12 DMS500 fired engine 900rpm 50% load rocker cover repeat test statistics

The contour plot in Figure 5.13 at 900 rpm 50% load shows the transitional stage between the accumulation and nucleation mode. The signal strength varied over the 10 minute test shown in Figure 5.13, and whenever the nucleation mode peak was strong there was a lower accumulation mode peak. The accumulation mode peak was also present without a strong nucleation mode peak at certain points during the test. At higher engine speeds the shift to a strong nucleation mode peak at 50% load was not present. The results at other engine speeds are shown in Figure 5.20 and are reviewed in Section 5.8.
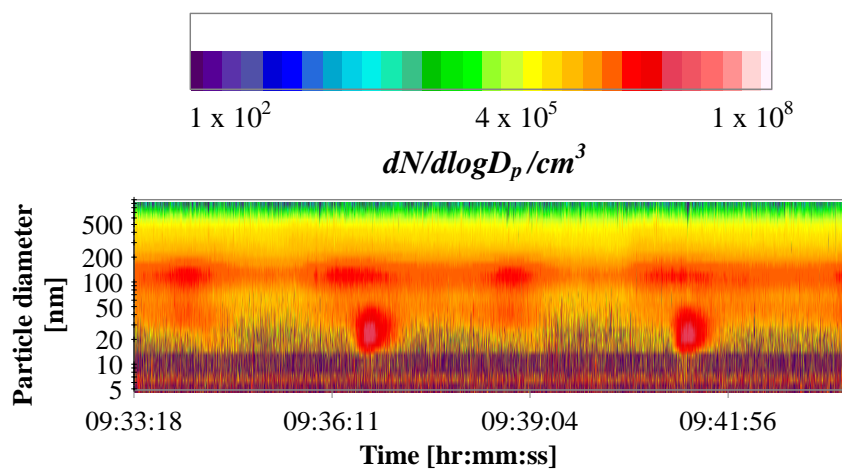
Figure 5.13 DMS500 fired engine contour plot at 900 rpm 50% load sampling from pushrod gallery

The six data sets shown in Figure 5.11 and Figure 5.12 were collected in two groups, one set of four consecutive tests and one set of two consecutive tests. The sump oil temperature, engine coolant temperature and rocker cover sampling point temperature were stable for all the tests plotted in Figure 5.11. The maximum standard deviation of the temperatures was 2% of the mean or 1.6°C for 80°C temperature. The temperature of the sampled gas in the pushrod gallery for varying engine load is shown in Figure 5.14, as expected the gas temperature increased with engine load.

Engine Load [%]	Pushrod Gallery Gas Temp [°C]
0	64
25	77
50	78
75	83
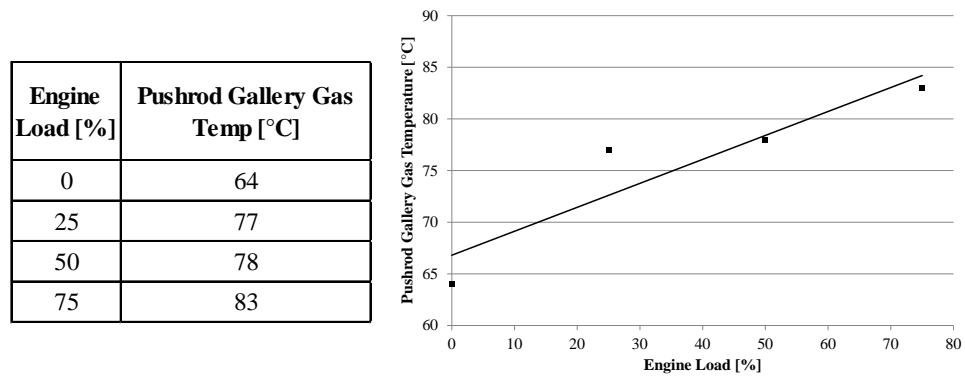
Figure 5.14 Fired engine pushrod gallery gas temperature for varying engine load at 900 rpm

On the motored engine increasing the crankcase flow rate caused the same shift between the accumulation mode and the nucleation mode but at 1% of the peak number concentration. The data in Figure 5.15 shows that the single mode peak at 250 nm shifted to a bimodal distribution with the largest peak in the range $d_p = 10 - 100$ nm and a secondary smaller peak at 250 nm.
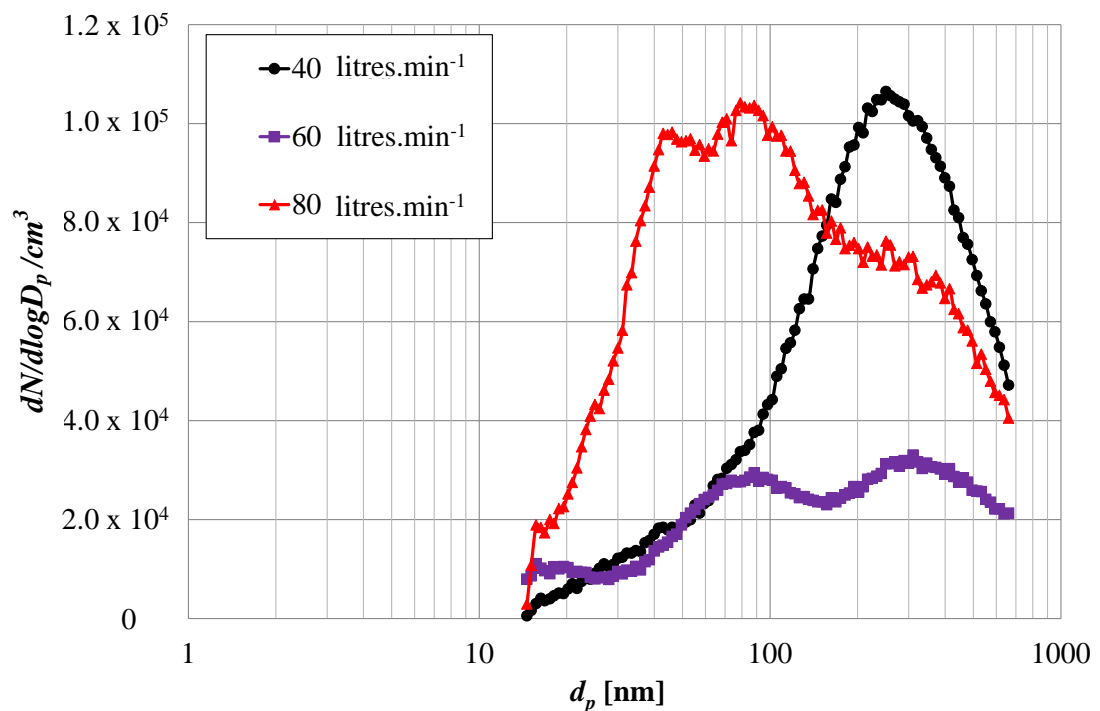
Figure 5.15 SMPS motored engine size number distribution of crankcase particulate matter for varying crankcase flow rate at 600 rpm sampling from the pushrod gallery

The effect of crankcase flow rate on the large particle size range measured by the APS is shown in Figure 5.16. Increasing the crankcase flow rate from 40 litres.min^{-1} reduced the particle number concentration present in the rocker cover, however, the

number concentration of particles captured was extremely small, thus suggesting that these results are not very robust. The low particle number concentration of particles was caused by a poorly designed particle sampling tube. Coarse crankcase particles impacted inside the 90° bend of the sampling tube shown in Figure 3.21, therefore only when the particle number concentration was very high were there sufficient particles to obtain a representative measurement on the APS.
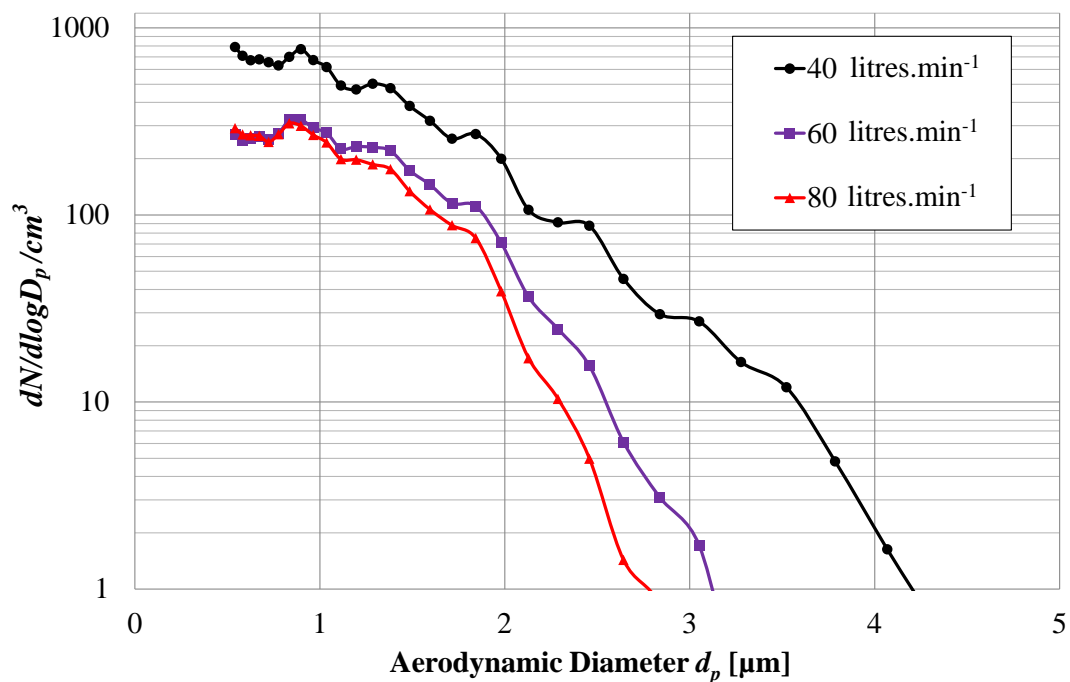
Figure 5.16 APS motored engine size number distribution of crankcase particulate matter for varying crankcase flow rate at 600 rpm sampling from the pushrod gallery

5.6.1 Load Variation Summary

Critically at low engine speed varying the engine load on the fired engine, and the crankcase flow rate on the motored engine, shifted the peak number of submicron particles from the accumulation mode to the nucleation mode, this shift is illustrated in Figure 5.10 and Figure 5.15. The submicron particles measured on the motored engine were generated by condensation of oil vapour. The physical conditions generated for vapour condensation and the respective conditions created within the crankcase of both the fired and motored engines are discussed in Section 5.11, once all the sampling data has been presented.

At this stage it is valuable to recognise that the shift in submicron particle size number distribution, with varying engine load, is present in the fired and motored engine results. This result demonstrates that lubricating oil affects the submicron crankcase aerosol emissions.

5.7   Location Variation

Recalling that the crankcase gas was sampled from three locations; the sump, the pushrod gallery and the rocker, the results of varying the sampling location on particle size number distributions are now presented. As shown in Figure 5.17 at 900 rpm the complex bimodal size number distribution described in Section 5.6 was witnessed at all three crankcase locations on the fired engine. A lognormal single mode distribution with a strong accumulation mode peak at 133 nm was present for 0% and 25% load and a small shoulder in the nucleation mode was also present. Increasing the engine load to 50% and 75% load generated a stronger nucleation mode peak at 32 nm. At 50% load the fired engine crankcase location had the most significant effect. Although as discussed in Section 5.6, a large variation in the size number distribution was also witnessed at 50% load and 900 rpm on the fired engine, even when the sampling location was fixed. When sampling from the sump and pushrod gallery, lower in the engine, the size number distribution was strongly bimodal with two prominent peaks. Sampling data from the rocker cover typically fell within the existing bimodal size number distribution found in sump and pushrod gallery.

Variation in absolute number concentration for varying sampling location on the fired engine was witnessed, but it was not higher than the levels discussed in the Section 5.5, therefore the variability in number concentration could not be confidently attributed to changing the sampling location.

Figure 5.17 DMS500 fired engine size number distribution of crankcase particulate matter for varying sampling locations and load at 900 rpm (a) 0% (b) 25% (c) 50% (d) 75%

Figure 5.18 DMS500 fired engine size number distribution of crankcase particulate matter for varying sampling locations and load at 1400 rpm (a) 0% (b) 25% (c) 50% (d) 75%

The results at 1400 rpm in Figure 5.18 show that the variation between the accumulation mode and the nucleation mode was not witnessed. At 50% load there was good agreement between the size number distributions and number concentrations at all three crankcase locations, with only a small shoulder present in the nucleation mode for the rocker cover sampling results. The final plot in Figure 5.18 shows that at 75% load the total number concentration of particles in the pushrod gallery was 83% higher than in the rocker cover.

The motored engine submicron particle sampling results in Figure 5.19 show that the total number concentration of particles was also 90% higher in the pushrod gallery than the rocker cover for 40 litres.min^{-1} blow-by at 600 rpm. It should be noted that the total particle number on the motored engine was 2% of fired engine data at 1400 rpm. The distribution of particles in the motored engine results was again lognormal, with a single prominent peak occurring in the accumulation mode at 230 nm. Changing the motored engine crankcase sampling location had little effect on the number concentration and distribution of particles measured by the APS.
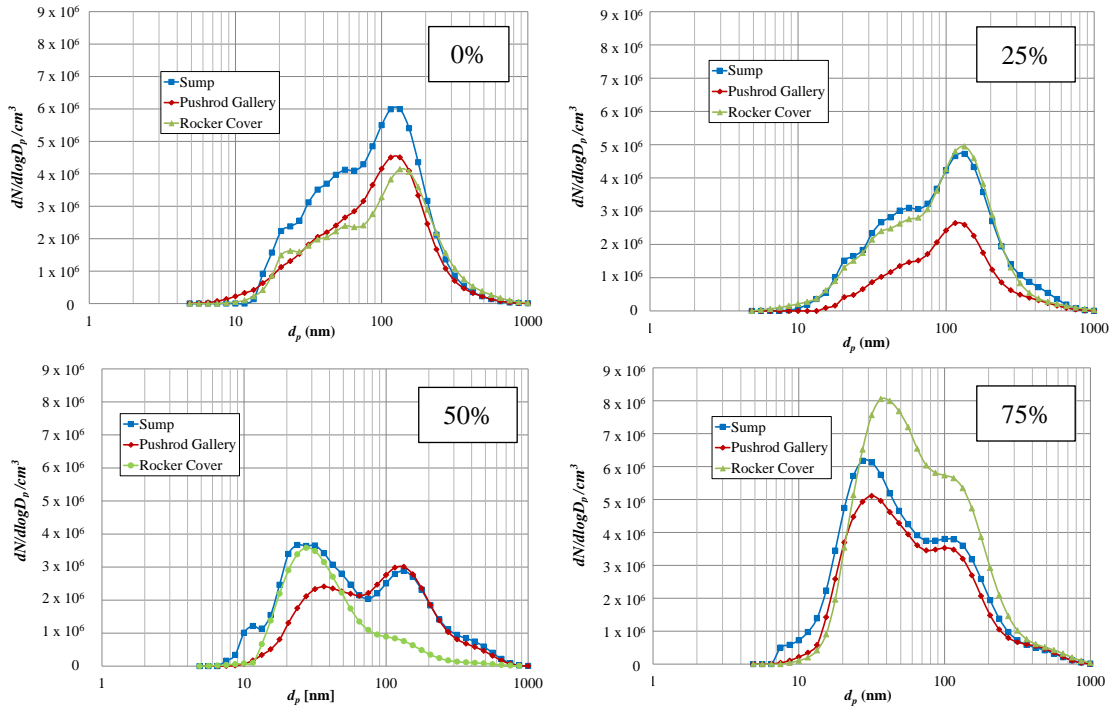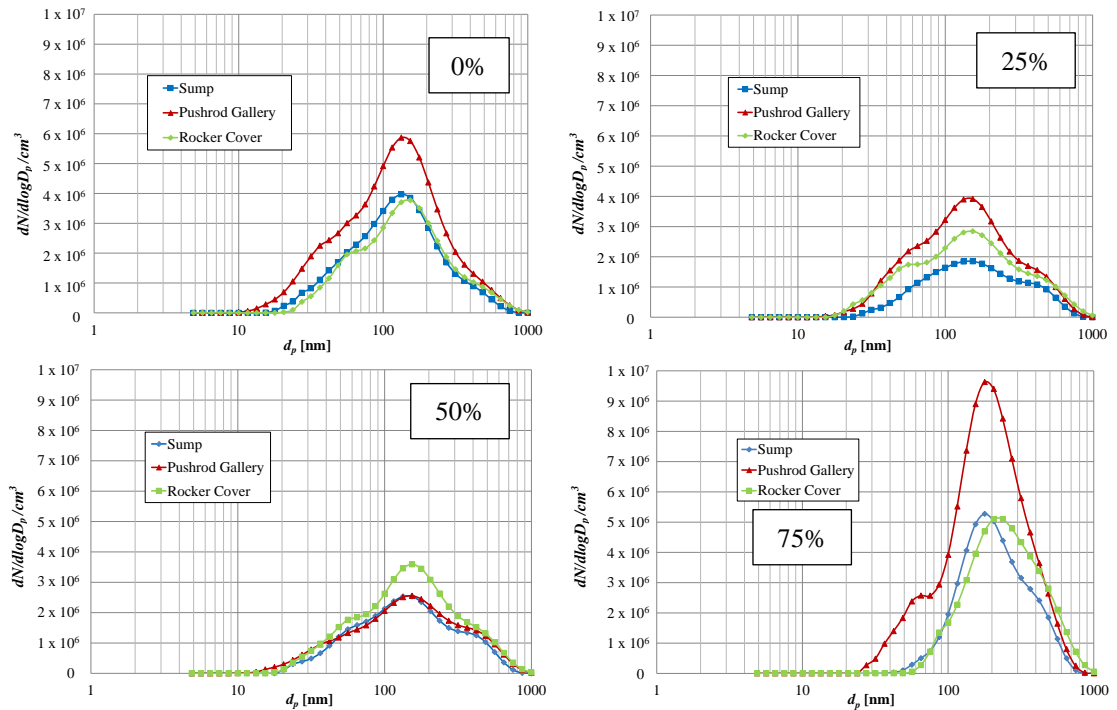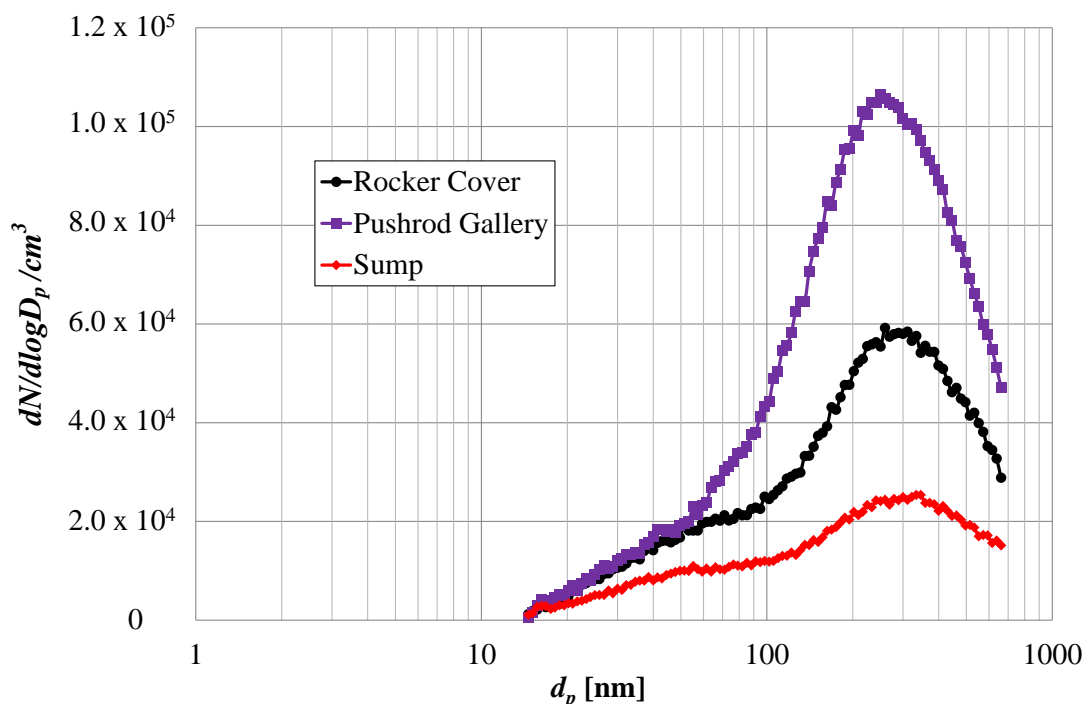

Figure 5.19 SMPS motored engine size number distribution of crankcase particulate matter for varying sampling locations at 600 rpm 40 litres.min^{-1} crankcase flow

5.7.1   Location Variation Summary

The shift between the accumulation and nucleation modes at low engine speed, occurs at all locations around the crankcase of the fired engine. Figure 5.17 and Figure 5.18 show that generally there is good agreement between the submicron size number distributions for varying engine locations, loads and speeds. Specifically it is important to note that; at 900 rpm 50% load the size number distribution switches between a peak in the nucleation or accumulation mode, at 1400 rpm there is always a single broad peak in the accumulation mode and finally the peak number concentration at high engine loads alternates between the pushrod gallery and the rocker cover. It is also essential to remember that combustion products will contribute to the submicron fired engine crankcase measurements, their isolated contribution is investigated in Section 5.9.

Motored engine results, although at a much lower total particle number concentration, consistently show variation in the number concentration of particles with sampling location. Oil vapour condensation, which is generating the submicron particles on the motored engine, is strongly affected by any variations in the physical conditions within the crankcase. Figure 5.19 shows that only a small number of submicron particles are in the sump. A higher number of particles are present in the pushrod gallery, as opposed to the rocker cover at the top of the engine. This result reinforces the dramatic effect of thermal conditions on submicron crankcase oil particles. Temperature measurements showed a drop in gas temperature of 20°C from the bottom to the top of the pushrod gallery.

Location variation data reinforces the presence of a shift in size number distribution from the accumulation mode to the nucleation mode, at low engine speed and high engine load. Data also emphasises the strong influence of crankcase temperature and pressure on the generation of submicron crankcase emission.

5.8 Speed Variation

The effect of increasing the engine speed on the fired engine submicron crankcase emissions is displayed in Figure 5.20, samples were taken from the rocker cover at speeds of $900 - 1600$ rpm and loads of $0 - 75\%$. The results at 1200, 1400 and 1600 rpm show similar size number distributions for all the measured engine loads. The consistent size number distribution exhibited a strong accumulation mode peak at 133 nm and a shoulder in the nucleation mode at 56 nm. It is at 900 rpm 50% and 75% load when there are significant differences in the results. The increased presence of a nucleation mode peak dramatically altered the particle size number distribution and the number concentration.
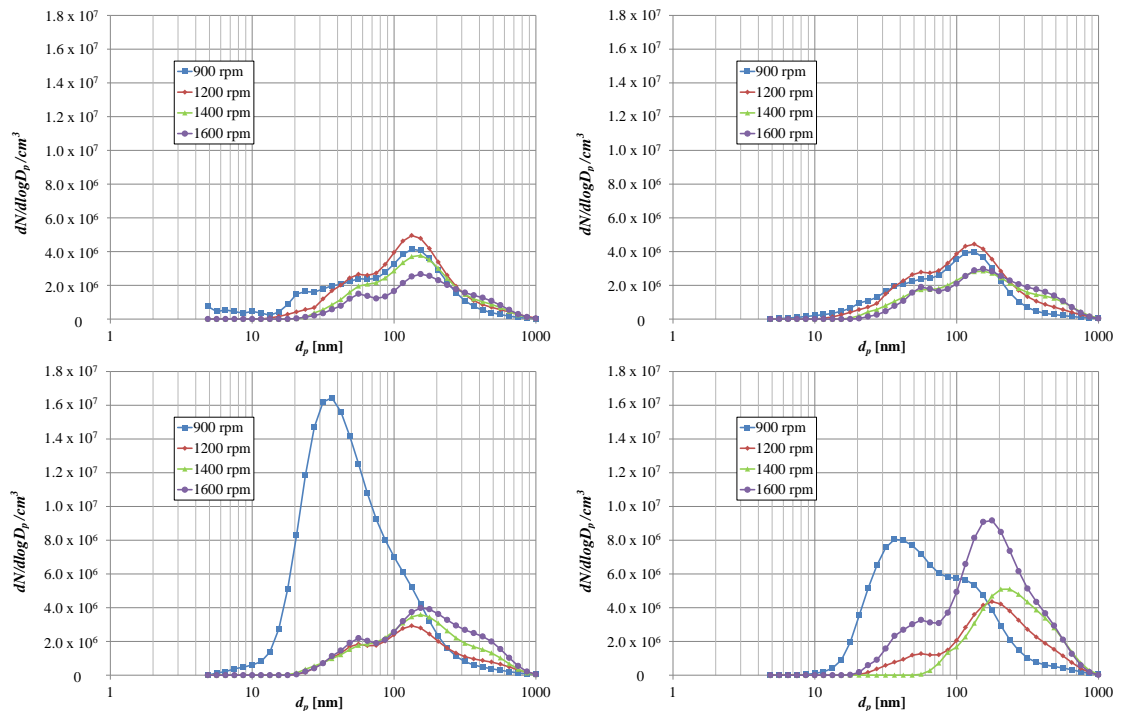
Figure 5.20 DMS500 fired engine size number distribution of crankcase particulate matter from the rocker cover for varying engine speed and load (a) 0% (b) 25% (c) 50% (d) 75%

The results of varying the engine load at 1400 rpm are plotted in Figure 5.21. The peak particle diameter was within the accumulation mode for all the tested engine loads, it peaked at 133 nm for $0 - 50\%$ load and 177 nm at 75% load. There was a notable variation in the particle size number distribution with engine load at 1400 rpm in the pushrod gallery, but the difference was not as significant as that shown in Figure 5.9 at 900 rpm.

Figure 5.21 DMS500 fired engine size number distribution of crankcase particulate matter for varying loads at 1400rpm sampling from the pushrod gallery
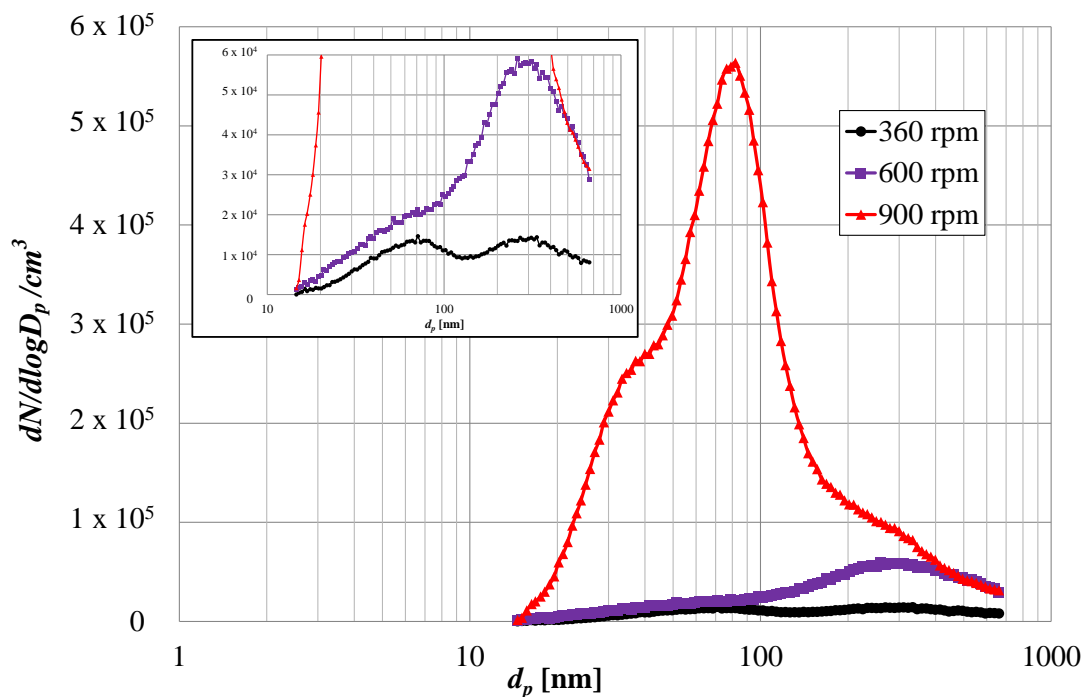
Figure 5.22 SMPS motored engine size number distribution of crankcase particulate matter for varying engine speed sampling from the rocker cover with 40 litres.min^{-1} crankcase flow

Figure 5.22 shows that increasing the engine speed had a significant effect on the SMPS results from the motored engine. The increase in engine speed altered the bimodal distribution of particles. At 360 rpm there were peaks at 62 nm and 270 nm, when the engine speed increased to 600 and 900 rpm the strongest peak at 270 nm shifted to 76 nm, and the number concentration of particles increased by an order of magnitude.

The APS results in Figure 5.23 show the increase in number concentration around 1 μm, however, throughout the rest of the measured particle diameter range the number concentration of particles was extremely low due to the poor sample extraction.
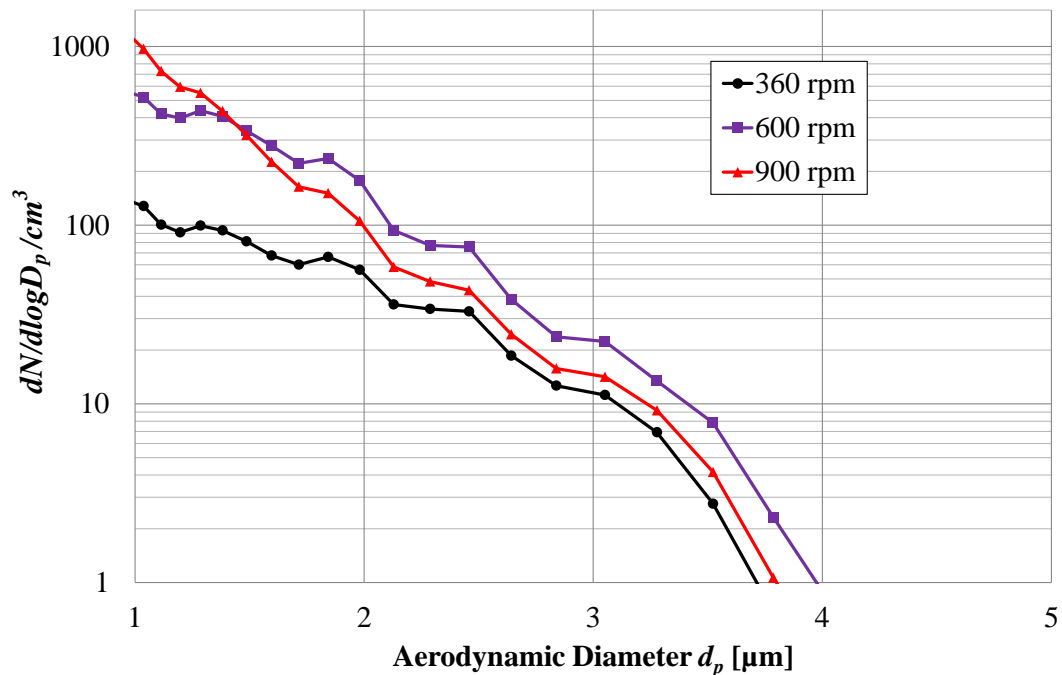
Figure 5.23 APS motored engine size number distribution of crankcase particulate matter for varying engine speed sampling from the rocker cover with 40 litres.min⁻¹ crankcase flow

5.8.1 Speed Variation Summary

Varying the engine speed on the fired engine showed that the shift between the accumulation and nucleation modes was only present at engine speeds at or below 900 rpm. For low engine loads the size number distribution of submicron particles was consistent for varying engine speeds, as shown in Figure 5.20. Above 50% load

when the blow-by flow rate increased and there was an increase in the amount of fuel burned, the highest total number of submicron particles for 50% load was at 900 rpm. At 75% load the total number of submicron particles was similar at 900 rpm and 1600 rpm. These results indicate that the crankcase aerosol on the fired engine was strongly affected by the complex blow-by around the piston ring pack and combustion. However, simply increasing the engine speed and load did not progressively increase the number of submicron particles.

For the motored engine, the effect of engine speed on submicron crankcase oil particle generation is clearly visible in Figure 5.22. Increasing the engine speed from 360 rpm to 900 rpm increased the total number concentration of submicron oil particles. At the higher engine speeds journal bearing temperatures are higher, therefore the oil temperature is higher and more oil vapour is generated. Subsequent condensation of this vapour generates submicron particles. This hypothesised explanation for the change in motored engine results is explored further in Section 5.11.

5.9   Contribution of Exhaust

The engine exhaust was sampled to investigate the magnitude and distribution of particulate matter from combustion and provide information on the contribution of the combustion products to the total crankcase emissions. At 900 rpm the exhaust particulate emissions for varying load in Figure 5.24 show a consistent log-normal and bimodal size number distribution, with a peak in the accumulation mode at 133 nm and shoulder in the nucleation mode at approximately 56 nm. At 0% load there was a strong nucleation mode peak at 9 nm, but as the load and exhaust temperature increased this nucleation mode peak disappeared and the accumulation mode particles became dominant. The total exhaust particle number concentration was different for each engine load at 900 rpm.
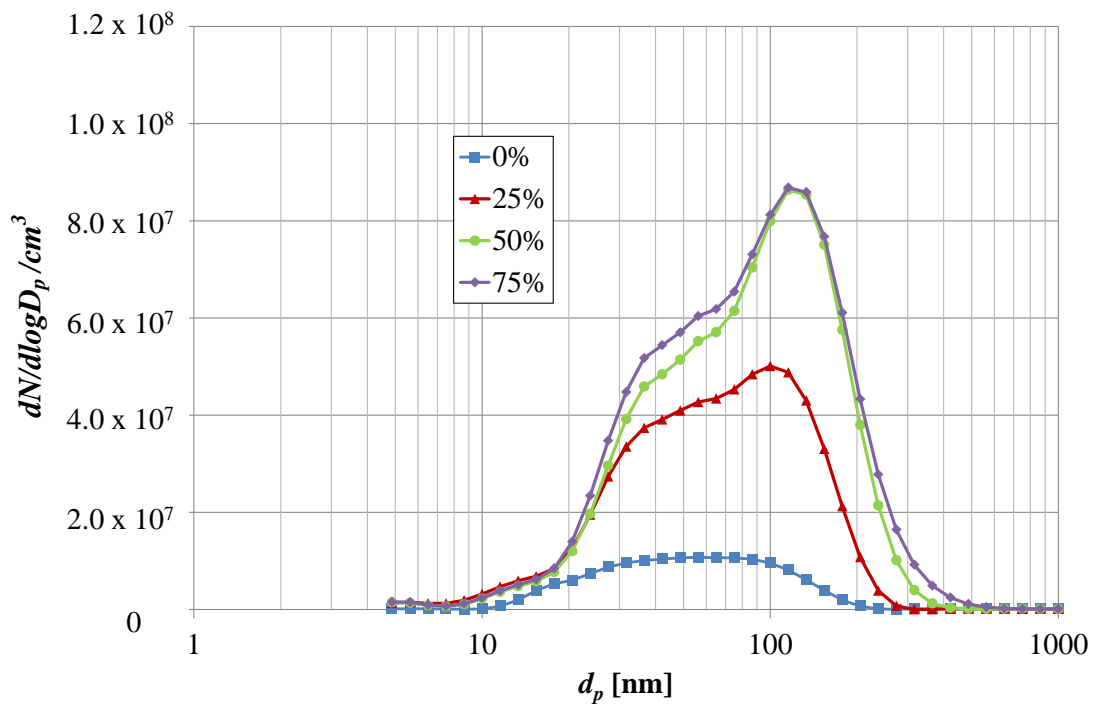
Figure 5.24 DMS500 fired engine size number distribution of particulate matter for varying load at 900 rpm sampling from the exhaust
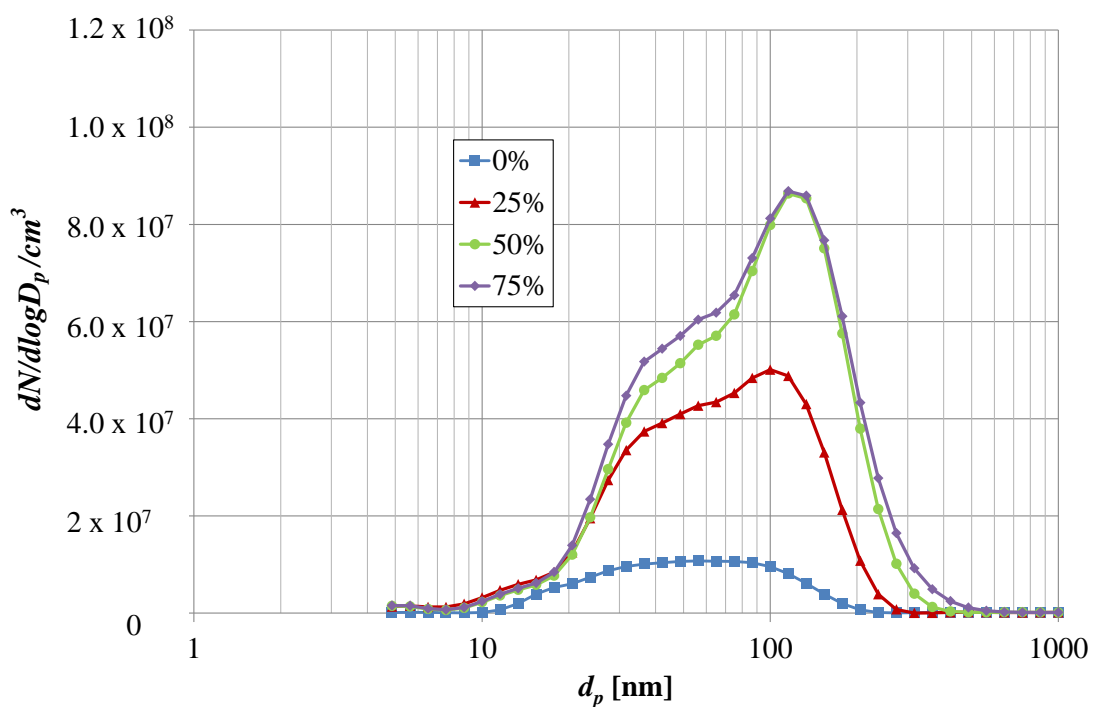
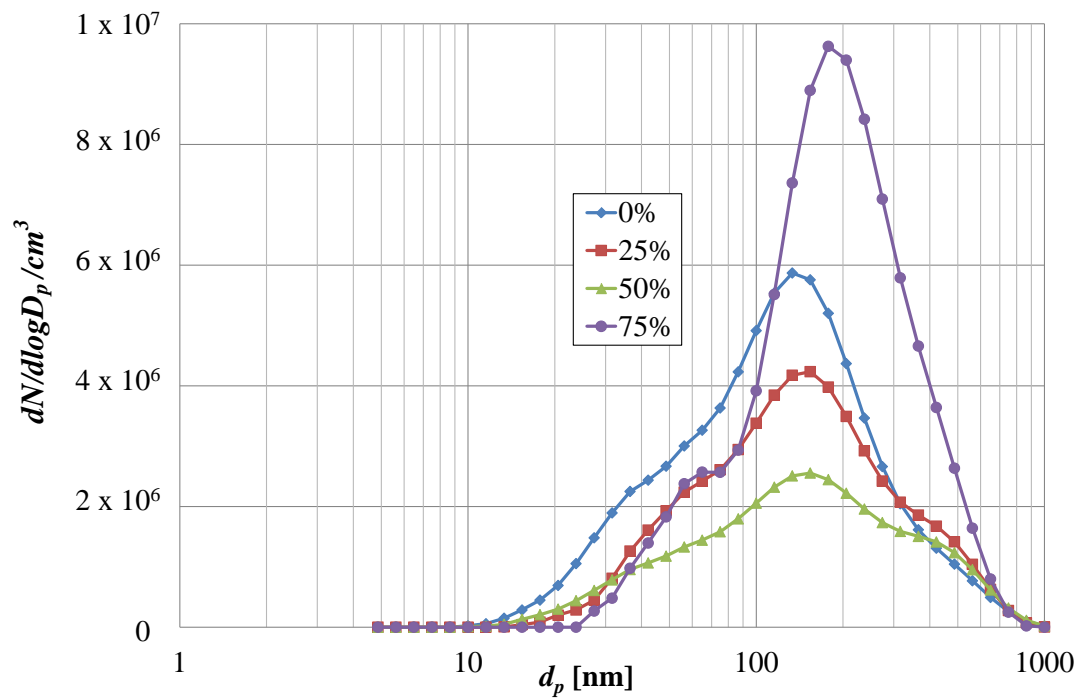**Figure 5.25 DMS500 fired engine size number distribution of particulate matter for varying load at 1200 rpm sampling from the exhaust**

At 1200 rpm and 50 - 75% load, as shown in Figure 5.25, the total number concentration of particles was consistent. When the engine speed was increased further to 1400 rpm 0% load there was a broad peak from $d_p = 27 - 100$ nm. At all the other engine loads the number size number distribution was bimodal, with a single strong peak around 133 nm and a large concentration of particles $d_p = 36 - 100$ nm. The peak number concentration of particles in the exhaust is approximately 6 times that found in the crankcase of the fired engine.
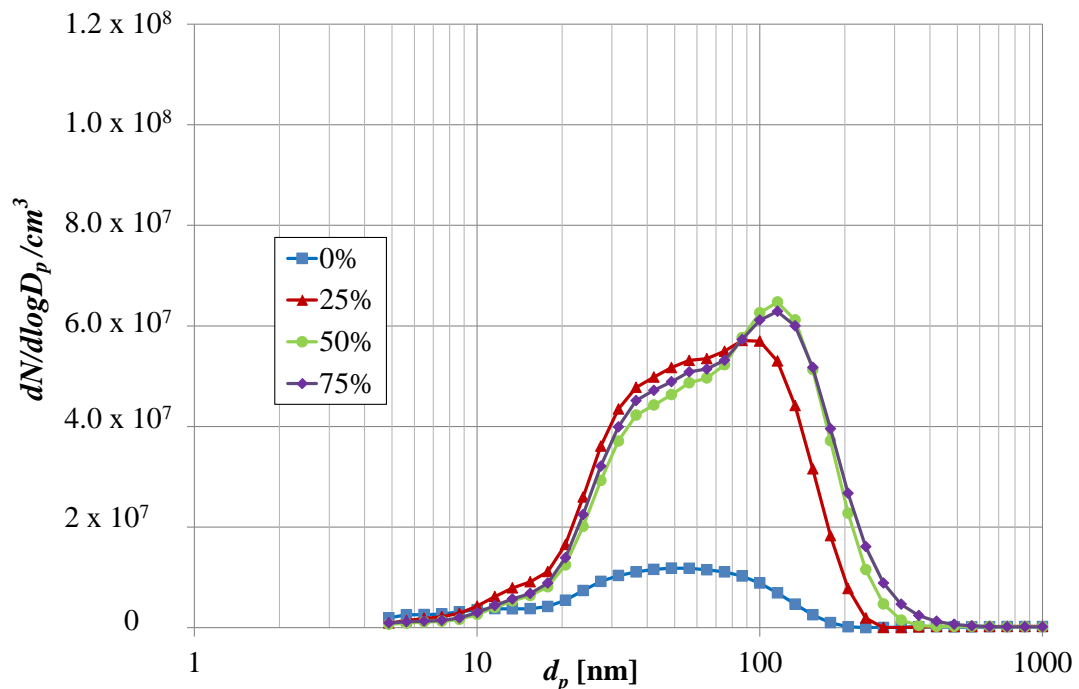
Figure 5.26 DMS500 fired engine size number distribution of particulate matter for varying load at 1400 rpm sampling from the exhaust

5.9.1 Contribution of Exhaust Summary

At 900 – 1200 rpm the total number of submicron exhaust emissions increased with engine load. This corresponds to the increased rate of fuel injection, and therefore the presence of more soot agglomerates generated by diesel combustion. The exhaust results at 1400 rpm in Figure 5.26 do not show the same shift in submicron size number distribution with engine load, above 0% the total number of submicron particles and the size number distribution does not change with engine load.

5.10 Mass Comparison

Section 1.3 highlights that particle matter emissions from diesel engines are legislated by a total gravimetric measurement. To facilitate a thorough understanding of the sampling data, the total mass concentration of submicron particle matter has been plotted in mg.m^{-3} for both the crankcase and exhaust emissions. The resulting plot in Figure 5.27 shows that moving from the motored engine crankcase to the fired engine crankcase, and then increasing the fired engine speed and load increases the total mass concentration of submicron particles. For each step there is more oil vapour generated, due to the increase in temperature. Additionally, in the fired engine crankcase there is soot from diesel combustion and unburned fuel. Interestingly the total mass of submicron particles in the exhaust was only slightly higher than in the crankcase, this demonstrates the magnitude of the crankcase emissions problem.
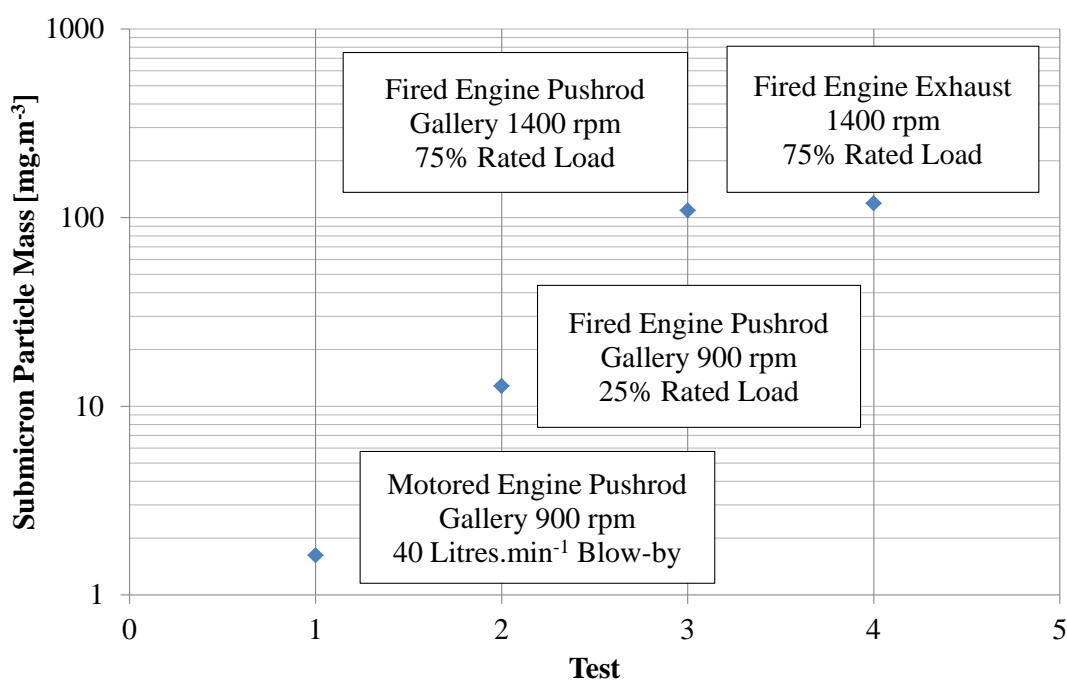
Figure 5.27 Total mass concentration of submicron particulate for varying test engines, sampling location and engine conditions
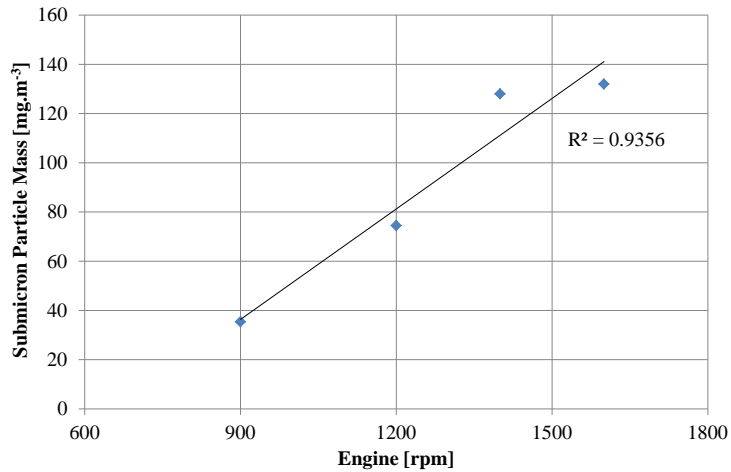
Figure 5.28 Fired engine submicron total mass concentration at 75% in the rocker cover for varying engine speed
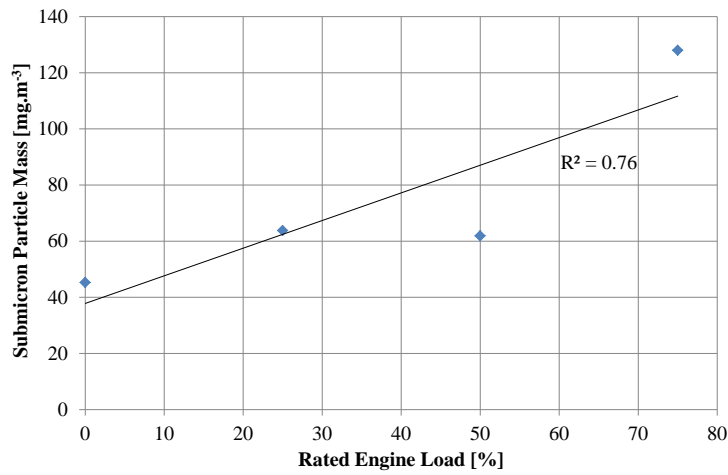
Figure 5.29 Fired engine submicron total mass concentration at 1400 rpm in the rocker cover for varying engine load
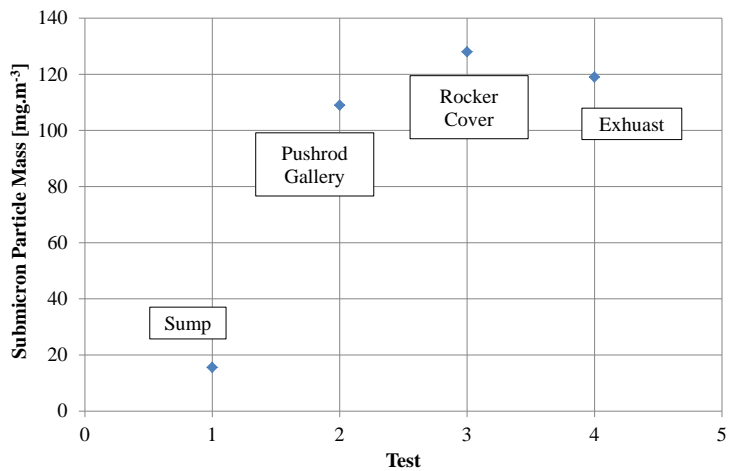
Figure 5.30 Fired engine submicron total mass concentration at 1400 rpm 75% for varying sampling location

Plotting submicron particle size mass concentration distributions provides limited information, as the size number distribution is skewed towards the larger diameter particles due to their larger mass. A sample size mass concentration plot is shown Appendix E Figure E-1.1. The submicron total mass concentration results at the range of engine and crankcase parameters tested on the fired engine are summarised in Figure 5.28, Figure 5.29 and Figure 5.30. The three figures indicate that the particle mass in the fired engine rocker cover increased with engine speed and load. The highest mass of submicron particles was found in the rocker cover at 1400 rpm 75% load.

5.11 Discussion of Submicron Crankcase Emissions Data

Many factors are known to effect crankcase emissions, these include piston ring pack design, valve stem and turbocharger oil seal design, engine wear and age, oil viscosity and age and crankcase temperature and humidity. These parameters have been assumed to be approximately stable throughout all tests unless otherwise specified.
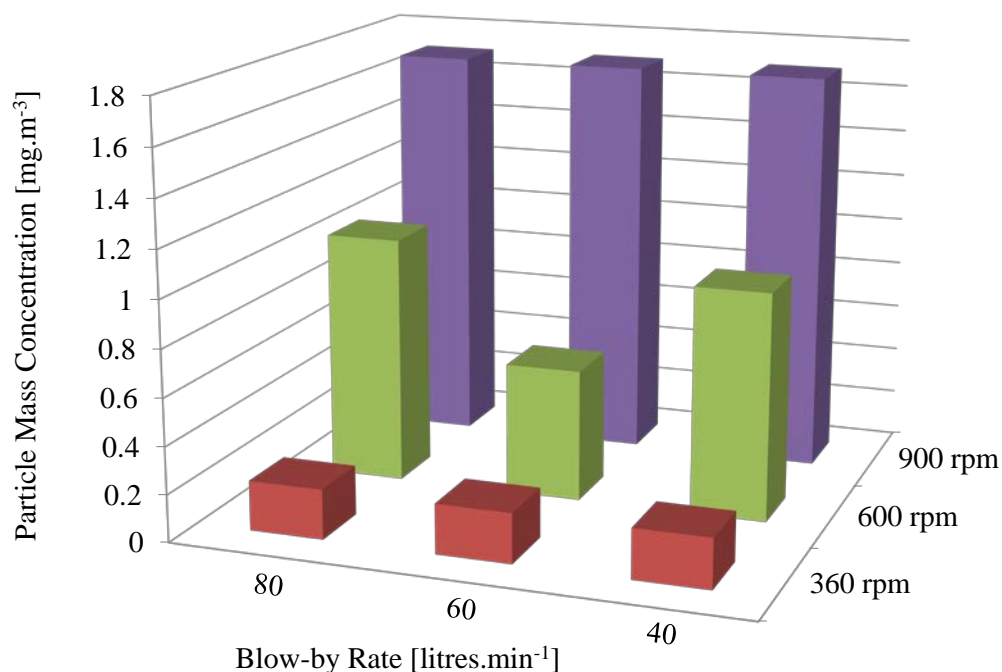
Figure 5.31 Speed load plot for motored engine total mass concentration of rocker cover emissions

Figure 5.31 is a three-dimensional plot of the total mass concentration of submicron particles generated in the crankcase of the motored engine. The plot in Figure 5.31 quantifies the isolated contribution of the lubricating oil to submicron crankcase emissions for the specific engine setup described in Chapter 3.

The submicron crankcase oil emissions from the motored engine are plotted in Figure 5.32, against the American Conference of Governmental Industrial Hygienists (ACGIH) exposure limits, as specified in the oil safety data sheet and summarised in Table 5.1. When considering only submicron oil particles, with a low blow-by rate of 40 litres.min^{-1}, oil temperature of 80°C and engine speed of 900 rpm, we can see that the emissions are 35% of the maximum exposure limits.
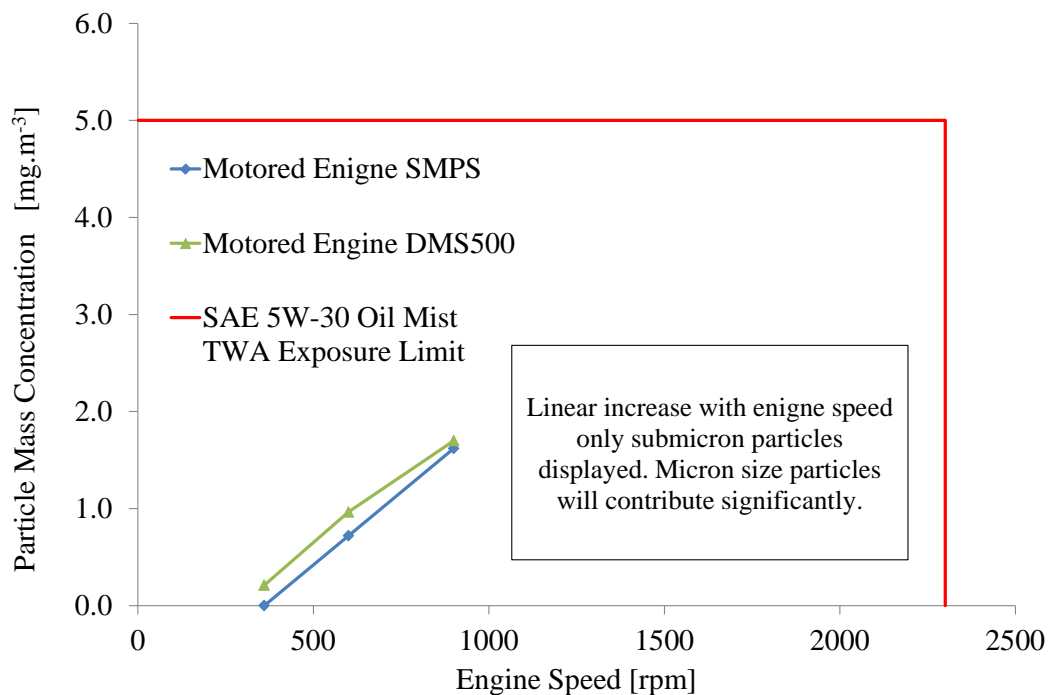
Figure 5.32 Total motored engine submicron crankcase oil mass concentration against ACGIH exposure limits

A higher mass of submicron oil drops was generated in the motored engine crankcase at higher engine speeds and blow-by rates, coupled with this the larger micron size oil particles that will contribute more mass. It is clear that open crankcase oil aerosol emissions alone will require filtration to meet the human exposure limits as defined by the ACGIH. Although the ACGIH human exposure limits do not govern the off-highway diesel engine emissions, they serve to illustrate that oil aerosol

emissions contribute significantly to the crankcase emissions. With the inevitable reduction in legislated particulate matter emissions and the introduction of a particle number measurement, controlling crankcase emissions is of vital importance to engine manufacturers.

In a similar manner to the previous three dimension plot, Figure 5.33 shows the total mass concentration of submicron particles generated in the crankcase of the fired engine at a range of engine conditions. Fired engine exhaust emissions are also shown in Figure 5.34 to indicate the contribution of diesel combustion products and unburned fuel to the crankcase emissions. Note that the engine load was varied in Figure 5.33 and Figure 5.34, whereas in Figure 5.31 the blow-by rate was adjusted directly. Furthermore note the difference in the y-axis due to the increased mass of submicron particles generated by soot, unburned fuel and oil.
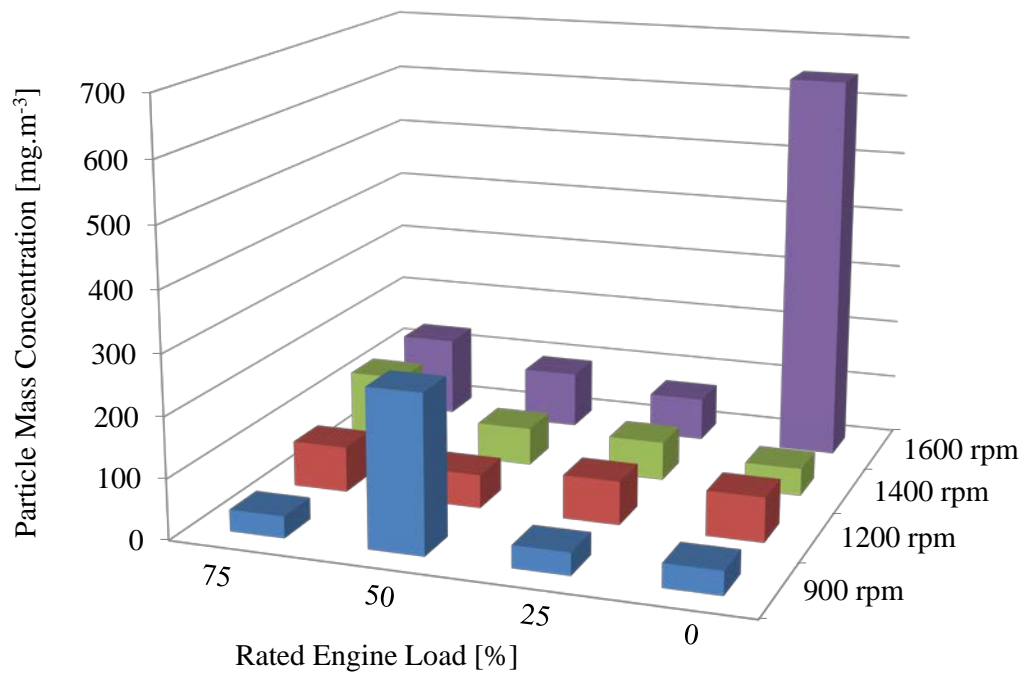
Figure 5.33 Speed load plot for fired engine total mass concentration of rocker cover emissions. Note different z-axis scale
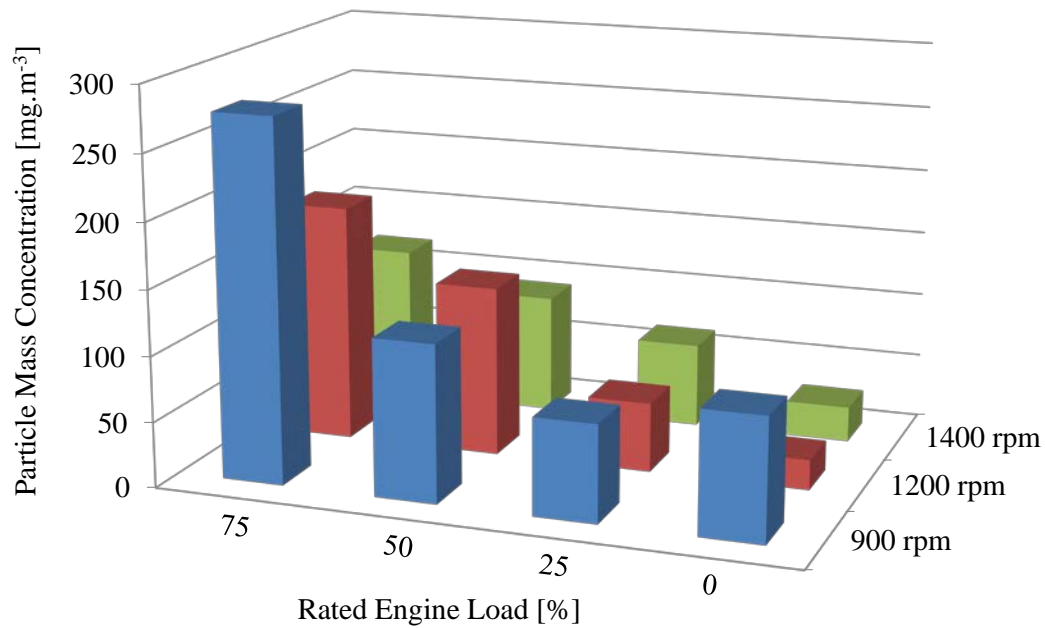
Figure 5.34 Speed load plot for fired engine total mass concentration of exhaust emissions

The submicron particle mass concentration varies with engine load and speed for all three data sets plotted in Figure 5.31, Figure 5.33 and Figure 5.34. Although no clear trend was consistently visible across all the three-dimensional plots, generally increasing the engine speed and blow-by, increased the mass of submicron crankcase emissions. In the crankcase at high engine speeds and load conditions the enthalpy of the crankcase gas will be highest. At higher blow-by rates more soot agglomerates and unburned fuel will be carried into the fired engine crankcase and more oil vapour will be generated.

For the motored engine the enthalpy of the crankcase gas will also increase with engine speed and blow-rate, condensation of crankcase oil vapour created at higher engine speeds and loads will generate the increased mass of submicron oil particles.

For the fired engine exhaust emissions the mass concentration of submicron particulate was highest at 900 rpm 75% load. At the higher load the increased rate of fuel injection and the presence of more soot agglomerates explain the high submicron particle mass. The occurrence of the peak mass concentration of submicron particulate at the lowest engine speed is not clear, one possible cause is lower exhaust gas temperature.

5.11.1 Accumulation Mode and Nucleation Mode Shift

The reviewed fired and motored engine crankcase sampling results have highlighted an interesting shift between the accumulation mode and nucleation mode at high engine load and low engine speed. There are several factors that affect the generation of particles in these two modes, their contribution has been analysed and discussed to facilitate a better understanding of the submicron results, and indicate potential mechanisms for the regulation and control of these particles.

As discussed previously fired engine nucleation mode particles are mainly volatile organic species formed from unburned fuel and unburned oil (Kittelson, Watts and Johnson, 2002; Sakurai *et al*., 2003). Volatile fuel and oil particle species emitted from diesel engines will remain in the gas phase, condense on existing solid particles or nucleate by homogenous or heterogeneous nucleation to form new particles (Burtscher, 2005).

Homogenous nucleation requires very high saturation ratios, whereas heterogeneous nucleation requires low saturation ratios, but nuclei or ions serves as nucleation sites. Diesel combustion generates primary soot particles typically sized between 20 - 50 nm, agglomerates of these particles are formed (Virtanen, Ristimaki, Vaaraslahti and Keskinen, 2004). The primary and agglomerated soot particles generated by diesel combustion can act as nuclei or condensation sites for heterogeneous nucleation

On the fired engine at higher engine loads more fuel was injected, therefore it can be conjectured that the amount of volatile organic species from unburned fuel increased and the amount of oil vapour increased due to the higher combustion and cylinder liner temperatures (Audette and Wong, 1999). Oil evaporation is discussed later in this section by examining the motored engine sampling results. At this stage it is sufficient to assume that the amount of oil vapour in the crankcase increases with engine load. The condensation of oil vapour will contribute to the accumulation and nucleation mode crankcase particles. To analyse the crankcase results in more detail the conditions required for oil evaporation and condensation have been calculated.

Condensation is controlled by the saturation ratio, the particle size and the time between particle collisions i.e. the number concentration of particles and their relative velocity. The saturation ratio of the oil vapour in the crankcase was calculated using Equation (2.28), where p_d is the partial pressure of the oil vapour at the drop surface and p_s is the saturation vapour pressure of the oil at the vapour temperature. The crankcase pressures for varying engine conditions are shown in Figure 5.35. The saturation vapour pressures for SAE 15W-40 oil were provided by the oil manufacturer Shell-UK and are displayed in Appendix B Table B-1.1.

Saturation Ratio $$S_R = \frac{p_d}{p_s}$$ (5.6)
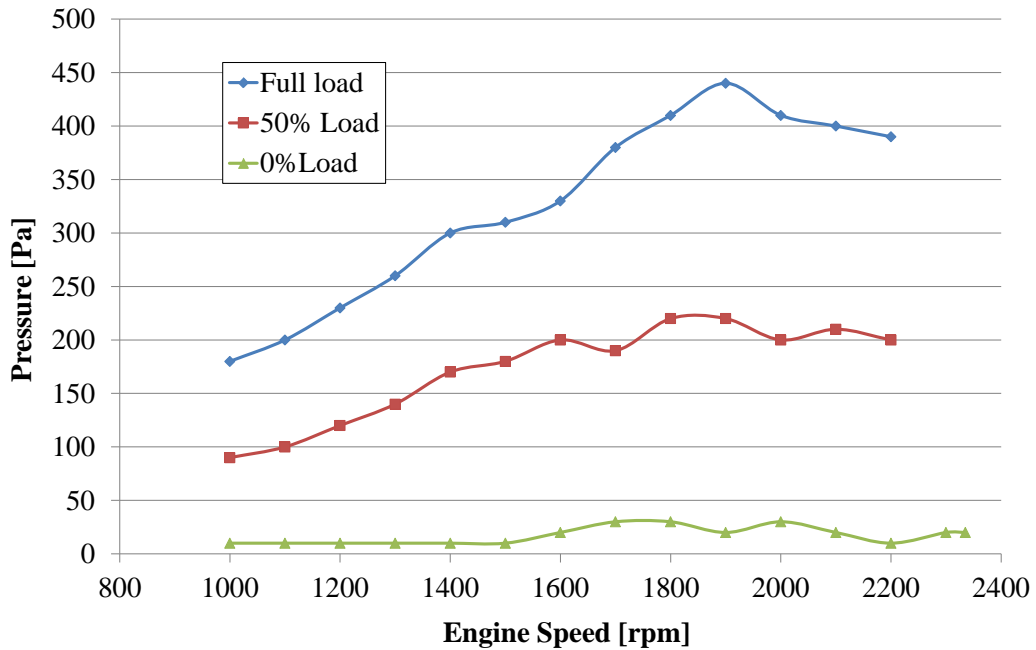
Figure 5.35 1104C-44 fired engine crankcase pressures open breather

It is widely acknowledged that homogenous nucleation is the less likely form of drop formation, as it requires very high saturation ratios, typically $S_R = 2 - 10$ (Kulkarni, Baron and Willeke, 2011). For homogenous nucleation of a super saturated vapour to occur, there must be sufficient nucleus sites of vapour molecules with a diameter greater than the Kelvin diameter d^*. The Kelvin diameter defines the diameter of a drop that will neither evaporate nor grow when the partial pressure of vapour at the drop surface is p_d.

Thomson-Gibbs Equation

$$S_R = \exp\left(\frac{4\sigma M}{\rho_l R T_A d^*}\right) \qquad (5.7)$$

The Kelvin diameter can be calculated using Equation (2.30) assuming a partial pressure of the crankcase oil vapour, where σ is the oil surface tension, M is the molecular weight of the oil, ρ_l is the oil density, R is the gas constant and T_A the oil vapour temperature.

The crankcase pressures on the fired engine were known, however, there was limited knowledge of the crankcase oil vapour volume fraction and therefore the partial pressure of the oil vapour. The maximum and minimum crankcase pressures at which sampling data was collected were considered, namely 1600 rpm 50% load and 900 rpm 0% load respectively. The effect of varying oil vapour volume fraction on the saturation ratio of the crankcase oil vapour has been plotted in Figure 5.36. Figure 5.36 indicates that for crankcase oil vapour volume fractions greater than 20% the saturation ratio of the oil vapour is greater than $S_R > 2$, this suggests that homogenous nucleation will occur provided there are sufficient nuclei.
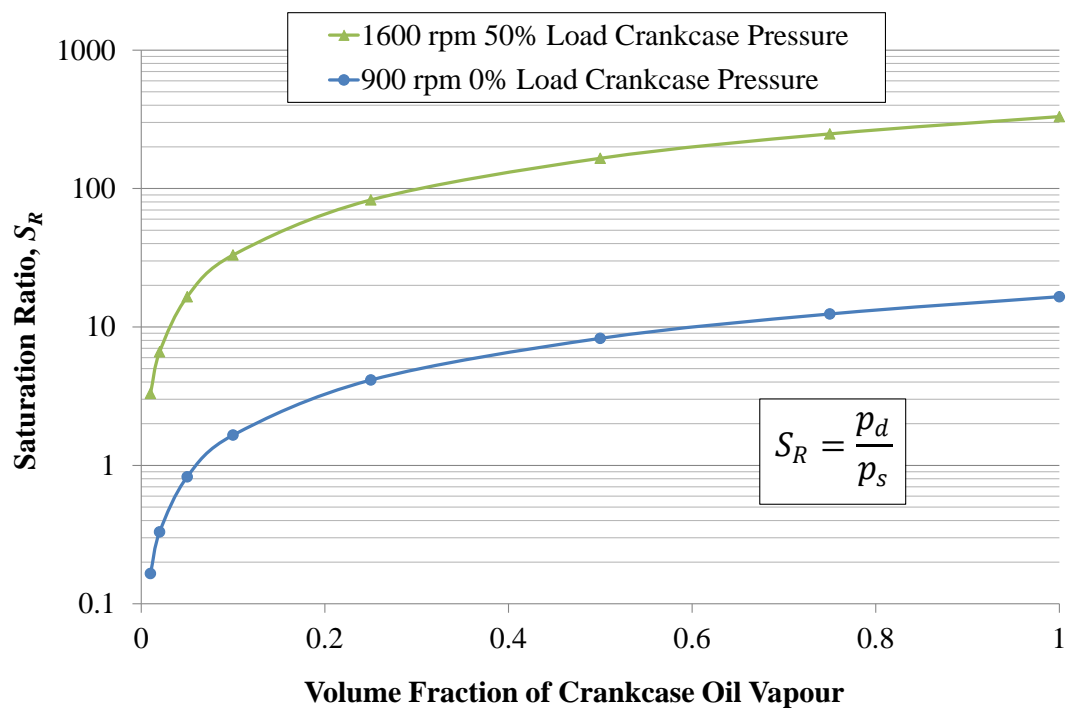
Figure 5.36 1104C-44 fired engine crankcase saturation ratio of 100°C oil vapour for variable oil vapour volume fraction

The Kelvin diameters of the nuclei required for homogeneous nucleation for varying oil vapour volume fractions are plotted in Figure 5.37. A molecular weight of 0.514 kg.mol^{-1} and a gas constant of 8.314 J.mol^{-1}.K^{-1} was used to calculate the Kelvin diameters. The molecular weight was taken from work by Tian and Cho (2004), ideally the exact range of molecular weight components in SAE 15W-40 is required, however, assuming a value of 0.514 kg.mol^{-1} is sufficient to illustrate the points pertinent to this discussion.
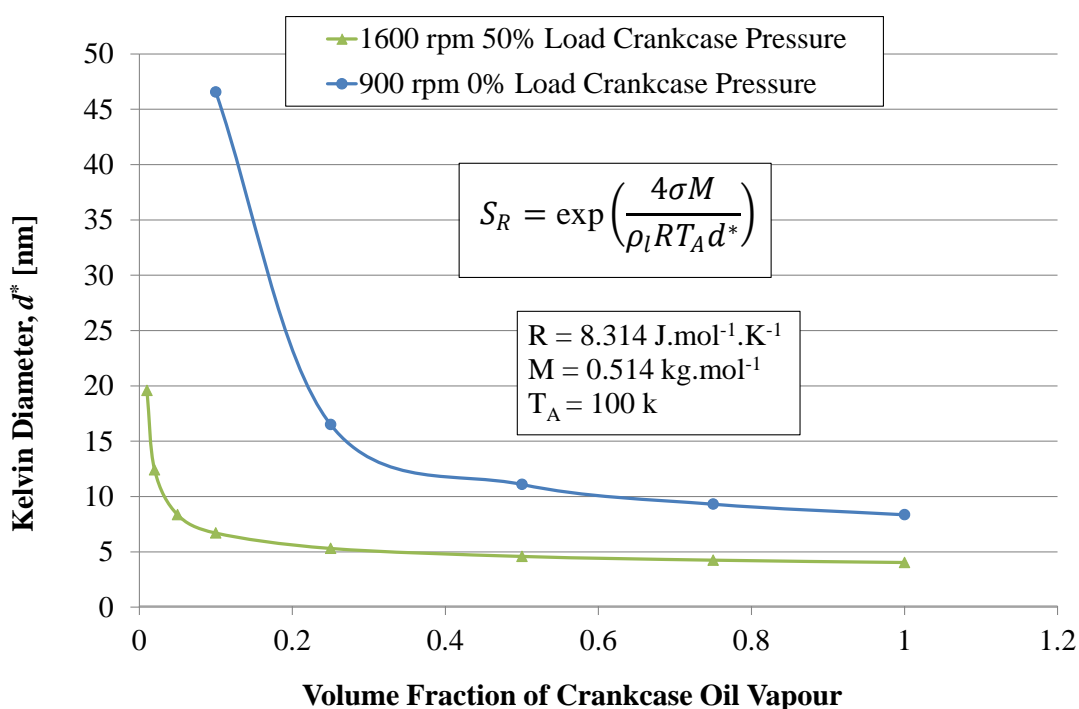
Figure 5.37 1104C-44 fired engine crankcase Kelvin diameters with 100°C oil vapour and variable oil vapour volume fraction

The Kelvin diameters for homogenous nucleation at minimum crankcase pressure range from $d^* = 8 – 46$ nm and at maximum engine conditions $d^* = 5 – 20$ nm. If homogenous nucleation of crankcase oil vapour occurred in the fired engine crankcase during sampling tests then molecular clusters from $d^* = 5 – 46$ nm were required.

The complex formation of molecular cluster within supersaturated vapours has been investigated intensively for many years, Becker and Doring (1954) provide an example of this work. Theoretical and experimental analysis by Gelbard and Seinfeld (1979) and Seinfeld and Pandis (2006) has shown that homogenous

nucleation of supersaturated vapours can occur due to agglomeration of molecular clusters with an individual diameter below the Kelvin diameter. High local concentrations of the larger molecular components present in the oil vapour may agglomerate to sufficient size to initiate homogenous nucleation, and therefore the generation of particles in the nucleation mode. Homogenous nucleation helps to explain the generation of submicron particles in the crankcase of the motored engine where there were no agglomerated soot particles for the oil vapour to heterogeneously condense on.
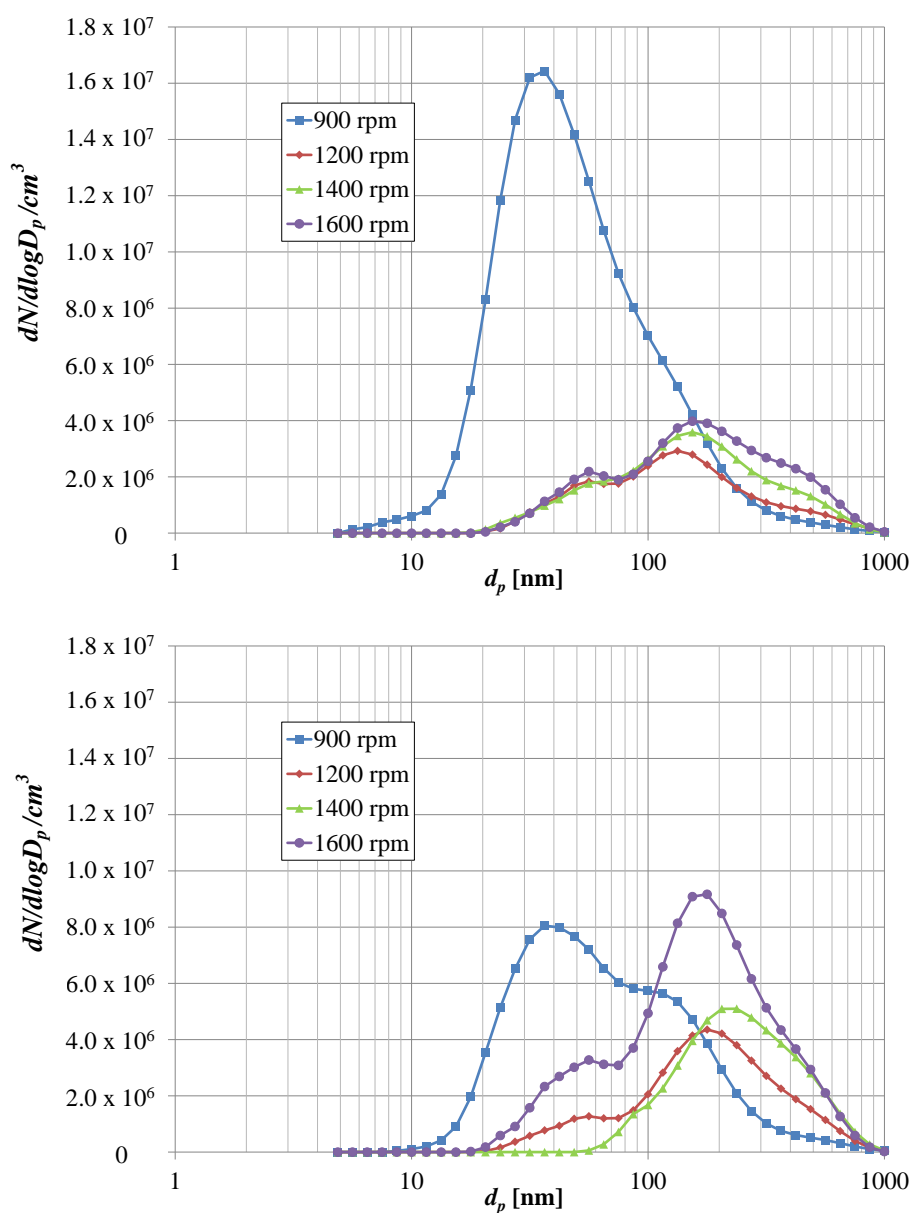
Figure 5.38 DMS500 fired size number distribution of crankcase particulate matter from the rocker cover for varying engine speed and load (a) 50% (b) 75%

At 900 rpm 50% load the crankcase pressure on the fired engine was 82 Pa which corresponds to a Kelvin diameter range of 12 - 186 nm for oil vapour volume fractions of 1% to 100%. The fired engine sampling results in Figure 5.38 show that at 900 rpm 50% load there are a large number of particles centred around 35 nm. Either these particles were generated by homogenous nucleation of oil vapour, as discussed in the previous paragraph, or they were solid soot particles generated by combustion acting as sites for vapour condensation, this is known as heterogeneous nucleation.

At higher engine speeds the blow-by and crankcase pressure increase, as shown in Figure 5.8 and Figure 5.35 respectively, the increase in both parameters is not as significant as with engine load. Again it can be conjectured that more unburned fuel and oil vapour is generated at higher engine speeds. The increase in crankcase pressure and therefore oil vapour saturation ratio from 0 – 50% load, was more significant at 1400 rpm compared to 900 rpm. If homogenous nucleation of oil vapour at high saturation ratios is the main mechanism for generating fired engine crankcase nucleation mode particles, then there should be a large number of nucleation mode particles at all engine speeds, this is not reflected in the results plotted in Figure 5.38.

At higher engine speeds and loads more solid carbon nuclei are generated by combustion and carried into the crankcase acting as sites for heterogeneous nucleation. Figure 5.26 shows that at 1400 rpm sampling from the fired engine exhaust, for all tested engine loads there were 5.21 x 10^7 N.cm^{-3} particles from 30 - 110 nm. These particles will be generated by the condensation of fuel and oil vapour and most significantly solid carbon.

The lack of nucleation mode particles in the fired engine crankcase at 75% load and 1400 rpm can be explained by the presence of the strong accumulation mode peak. At 1400 rpm 75% load compared to 900 rpm 75% load there is more unburned oil and fuel vapour, there may be more nucleation. However, there are more soot particles with a diameter greater than the Kelvin drop diameter. The soot particles act as condensation sites and grow due to the presence of the fuel and oil vapour

condensing on their surface, hence the increased accumulation mode peak at 1400 rpm.

To reiterate, for the motored engine results there are no soot particles present. For the fired engine results the concentration of agglomerated soot particles increases with engine speed and load. On both engines increasing the load and blow-by rate increases the crankcase pressure and reduces the Kelvin drop diameter as shown in Figure 5.37. With a lower Kelvin drop diameter and higher saturation ratio there is increased potential of homogenous nucleation on the motored engine, and both heterogeneous and homogenous nucleation on the fired engine. The improved conditions for both types of nucleation explains the increased number of motored engine nucleation mode particles, as shown in Figure 5.15, and the increased number of fired engine nucleation and accumulation mode particles, as shown Figure 5.38.

5.11.2 Additional Motored Engine Testing

An additional set of specific sampling tests were conducted on the motored engine crankcase, to provide supplementary information on the contribution of lubricant oil to submicron crankcase particles. The DMS500 was used as it measures a broader range of the nucleation mode down to 5 nm, compared to the SMPS which only measured particles down to 15 nm. Unfortunately, the DMS500 was only available to test in the motored engine rocker cover at 900 rpm.

The results of the motored engine DMS500 tests are compared to the motored engine SMPS results and plotted in Figure 5.39. Acknowledging the potential variation in the total particle number between identical tests as discussed in Section 5.5, and the smaller measurement range of SMPS ($d_p = 15$ nm – 660 nm) compared to the DMS500 ($d_p = 5$ nm - 1 µm), the results show good agreement around 80 nm. At 20 nm there is a large nucleation mode peak generated by the oil vapour that was not fully represented in the SMPS results, where only a shoulder in the size number distribution was present around 40 nm. Homogeneous nucleation of oil vapour within the motored engine crankcase initiates the condensation process, and generates the large number of nucleation mode particles measured by the DMS500 witnessed in Figure 5.39. The large nucleation mode peak quantifies the contribution

of lubricating to this particle size mode, and reinforces the discussion of nucleation and condensation covered in the Section 5.11.1. Given sufficient time and settling volume the large number of nucleation mode particles will coagulate into the accumulation mode.
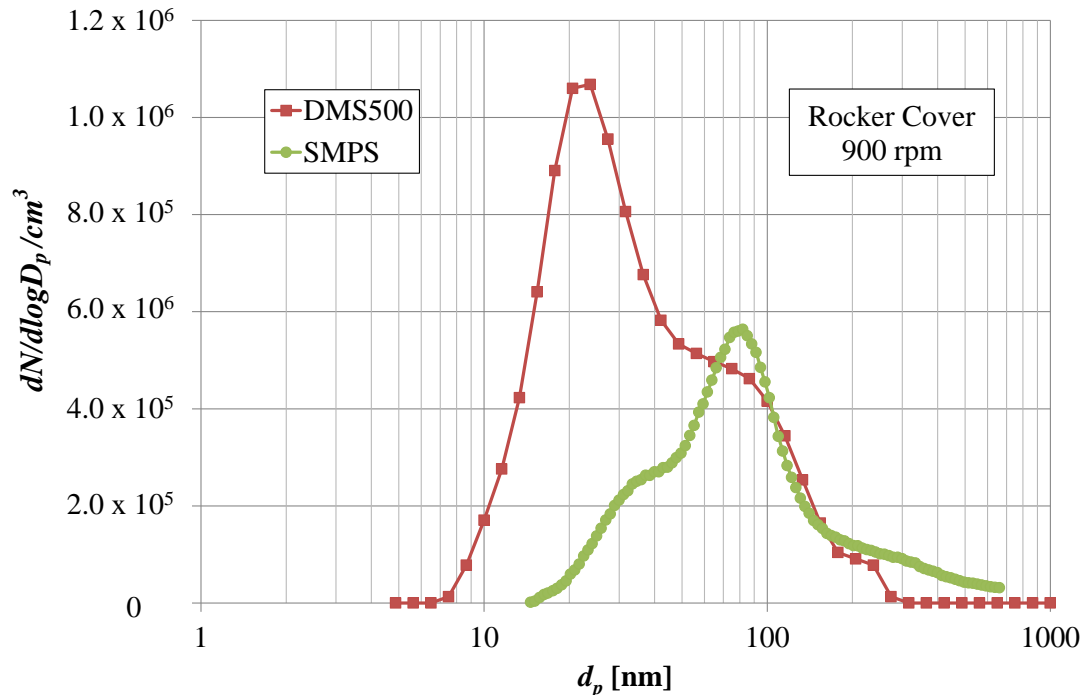
Figure 5.39 Motored engine 900 rpm submicron rocker cover emissions measured by the SMPS and DMS500 with 40 litres.min⁻¹ of crankcase flow

The evolution of submicron particles is influenced dramatically by temperature, as temperature controls oil evaporation, vapour generation and subsequent condensation of that vapour. Sampling tests were conducted on the motored engine crankcase at two different sump oil temperatures, the results are plotted in Figure 5.40. Increasing the sump oil temperature by only 25°C from 60 - 85°C increased the total number of crankcase particles by a factor a three. The plot in Figure 5.40 shows that the size number distribution of the particles did not change dramatically with increasing oil temperature, indicating that the condensation mechanism generating the accumulation mode particles did not change.
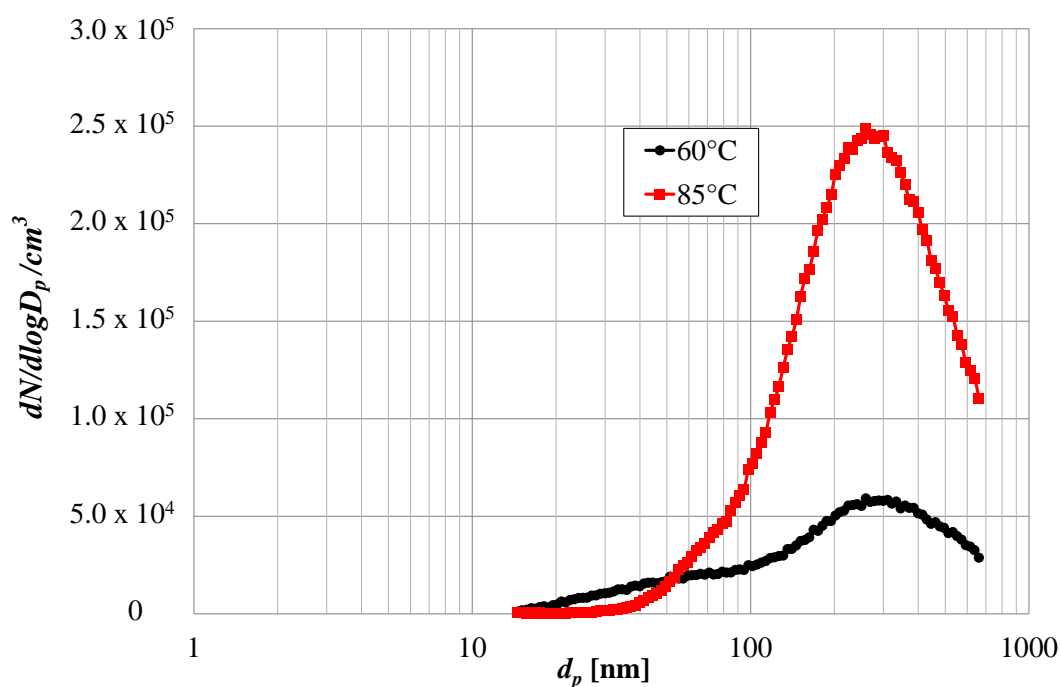
Figure 5.40 SMPS motored engine size number distribution of motored engine crankcase particulate matter for varying oil temperature at 600 rpm sampling from the rocker cover with 40 litres.min^{-1} crankcase flow

Chapter 4 indicated that oil atomisation at the crankshaft and camshaft was strongly affected by engine speed. At higher engine speeds more oil drops are generated with a smaller mean diameter, as discussed in Section 4.3.2. At higher engine speeds the journal bearing temperature is higher, and at higher blow-by rates the enthalpy of the crankcase gases is higher. The atomisation of the oil is controlled by its surface tension, density and viscosity as shown by Equation 2.9, 2.20, 2.22 and 2.23. All these physical parameters of the oil reduce with temperature, therefore there is more oil atomisation at higher temperatures.

The APS sampling setup was modified for a series of short tests on the motored engine. Impaction of atomised drops in the APS sampling lines was minimised by sampling directly from the window in the side of the engine block that was used to image around the crankshaft and connecting rods. The window position is displayed in Figure 3.13, the images in Figure 5.41 collected at 360 and 600 rpm show the increase in oil atomisation at higher engine speeds. Motored engine APS results from sampling at this location at 360 and 600 rpm are shown in Figure 5.42, they also

reflect the increased number concentration of oil drops $d_p = 1$- 10 μm that are generated by increased oil atomisation at higher engine speeds.
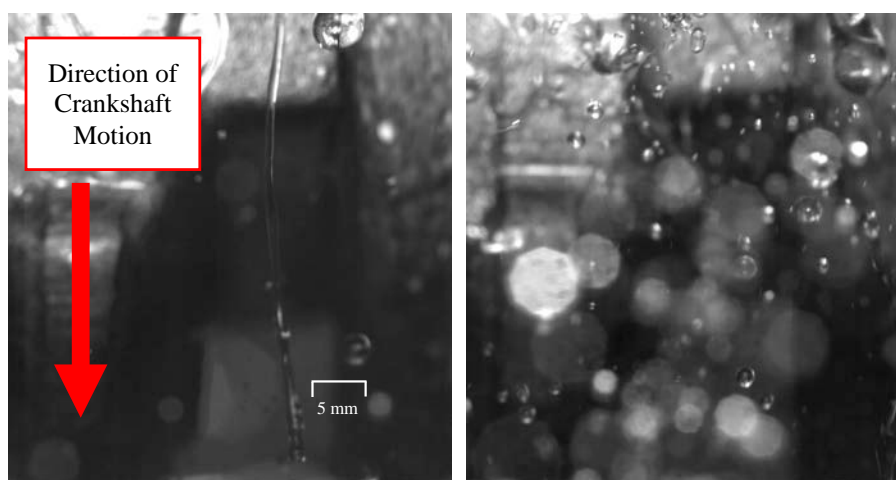
Figure 5.41 Motored engine connecting rod window oil distribution (a) 360 rpm (b) 600 rpm
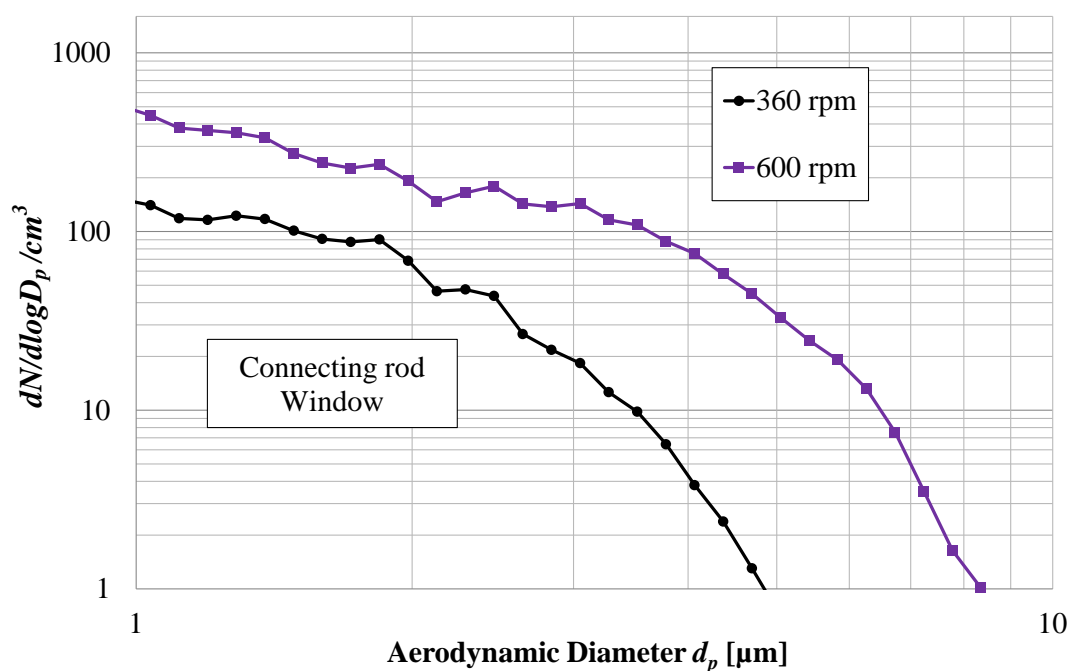
Figure 5.42 APS motored engine size number distribution of crankcase particulate matter for varying engine speed sampling from the connecting rod window with 40 litres.min^{-1} crankcase flow

For low crankcase pressures on the motored engine, the 100°C of crankcase blow-by and the oil temperature, may be sufficient to generate oil vapour from the atomised oil drops. Therefore, as the number concentration of atomised oil drop increases there is more vapour generation from evaporation at the surface of the oil drops. At

higher engine speeds and oil temperatures more oil drops and oil vapour is generated. Condensation of this oil vapour generates the motored engine nucleation and accumulation mode particles witnessed in Figure 5.40.

The behaviour of a 10 μm oil drop, for varying oil drop temperature and oil vapour partial pressure has been calculated and plotted in Figure 5.43. Figure 5.43 demonstrates that conditions exist within the crankcase for the conjectured evaporation and condensation of oil vapour from the surface of atomised oil drops. The high local temperatures at the journal bearings and the enthalpy of the blow-by gas provides sufficient heat for oil evaporation. On a fully fired engine condensation of the oil will occur in cooler low pressure regions within the crankcase and critically in the turbocharger and intake components.
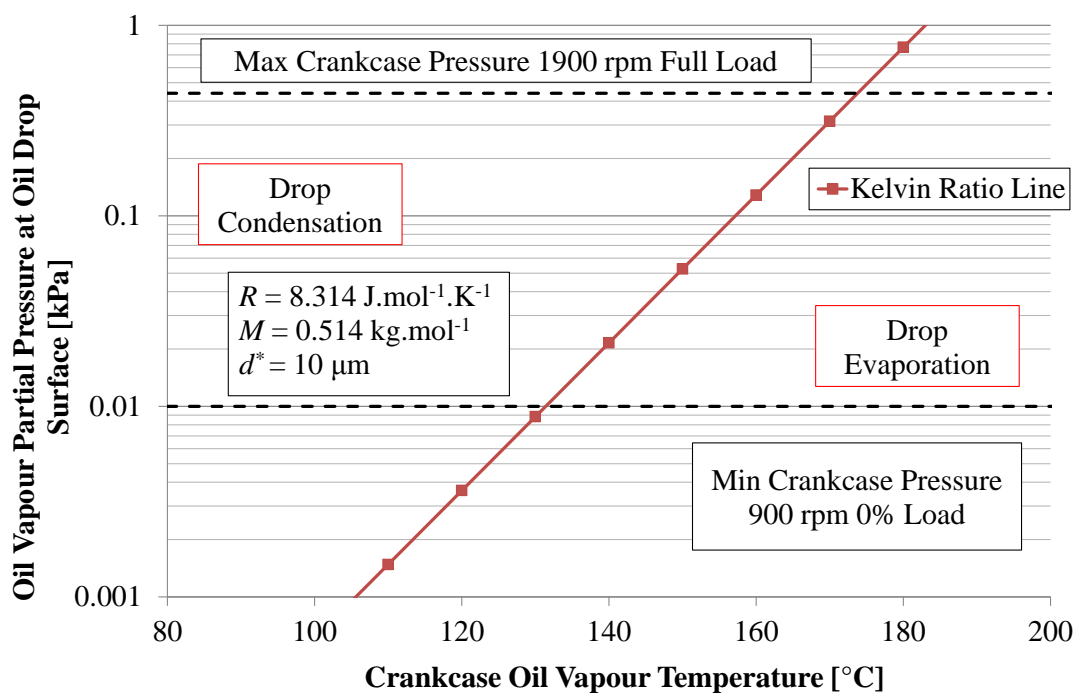
Figure 5.43 Behaviour of 10 μm oil drops for varying oil drop temperature and oil vapour partial pressure

Work on aerosols of inorganic ions by John *et al.* (1990) identified a condensation particle mode with an average aerodynamic diameter of 200 nm, this coincides with the peak in Figure 5.40 at 300 nm. John *et al.* (1990) stated that particles in this mode are formed either directly from the condensation of vapour or through coagulation with nucleation mode particles such as those witnessed in Figure 5.39.

The motored engine crankcase results, particularly those shown in Figure 5.15, exhibit the same shift between the two submicron modes that was witnessed in the fired engine crankcase results. This observation reinforces the contribution of lubricating oil to the submicron crankcase emissions and helps not only to comprehend the complex interaction between the accumulation and nucleation mode, but also indicates steps that can be taken to regulate and control the submicron oil particle generation and behaviour.

5.12 Concluding Remarks

Results from a thorough and novel crankcase particle sampling study have been examined in this chapter. Sampling data collected from a motored and fired engine crankcase quantifies the crankcase emissions and highlights the contribution of lubricating oil. The mechanisms generating submicron oil particles have been theorised and validated against experimental data presented in this chapter and Chapter 4.

The experimental results collected thus far indicate that oil atomisation at the crankshaft generates the majority of the crankshaft oil aerosol mass, and oil evaporation from the surface of these drops generates oil vapour which condenses generating submicron oil particles. Crankshaft oil atomisation is investigated in more detail in Chapter 6 to fully characterise the oil atomisation and transport around the crankshaft.

Unburned fuel vapour in the crankcase will also contribute to the generation of submicron particles and cause fouling problems. With a focus on future diesel engine design, very late fuel injection events are proposed to assist the performance of after treatment devices. Any additional unburned fuel vapour that is present in the crankcase will magnify the problem of submicron crankcase particle generation. Careful attention should be paid to the blow-by rate during the late fuel injection event, as this will dictate the amount of additional unburned fuel that is transported into the crankcase. Investigating crankcase fuel vapour was beyond the scope of the work conducted in this thesis. However, the knowledge gained from the experimental

studies in this chapter assists in understanding the complex generation and behaviour of all submicron crankcase particles.

Knowledge gained on the generation and evolution of submicron crankcase oil particles has identified that their generation and behaviour can be controlled by adjusting the crankcase pressure, temperature and atomised oil drop number concentration and diameter. Details of further investigation required to validate this proposed control strategy are listed in Chapter 7.

CHAPTER 6

CRANKSHAFT OIL ATOMISATION

6.1   Introduction

Experimental results presented in Chapter 4 and Chapter 5 indicated that oil atomisation from the crankshaft contributes significantly to the mass and number of crankcase oil particles. The optical investigation in Chapter 4 discussed the atomisation of an oil film present on the surface of the crankshaft, breakup of ligaments generated from the oil film generated small oil drops that were transported in the crankcase blow-by. The optical access and setup used in this initial study captured the generation of oil drops down to 100 µm. Further optical investigation in the top of the engine and particle sampling around the crankshaft, demonstrated that the breakup of ligaments formed at the crankshaft generates oil drops down to 1 µm.

Rotary atomisation and ligament breakup has been the subject of significant research as described in Section 2.4 and Section 2.5, however, automotive crankshaft atomisation has only recently been investigated in detail. Begg, Sercey, Miche and Heikal (2010) characterised the oil drop diameters and velocities generated by an automotive crankshaft rotating at 6000 rpm. This study noted different regimes of drop generation, but did not characterise the extremely complex ligament breakup process as it was focussed on the global size and velocity of the atomised drops.

Based on the knowledge gained from the reviewed literature and the experimental data presented in previous chapters, it is clear that predicting crankshaft oil drop generation with confidence was an unrealistic demand for un-validated computational models. An experimental programme was developed to capture crankshaft oil atomisation from a heavy duty diesel engine throughout its operating speed range, providing valuable information on oil aerosol generation and transport.

Improved optical access around the crankshaft on the 1104C-44 motored engine and modification of the oil circuit facilitated an intensive optical study of crankshaft oil atomisation. High speed images quantify the oil ligament generation and breakup, providing valuable information for modelling and indicating potential mechanisms to control crankshaft oil atomisation. High speed digital particle image velocimetry (HSDPIV) was employed to characterise two-dimensional vector fields of the air flow around the crankshaft, and quantify the flow transporting the atomised drops.

6.2 Experimental Setup

The main objective of this third experimental investigation was to fully characterise crankshaft oil aerosol generation. The individual objectives were:

- Understand the oil breakup mechanism

- Understand the transport of oil drops

- Compare experimental results to modelling

6.2.1 Motored Engine

The motored engine described in Chapter 3 was used for the crankshaft oil atomisation investigation. Modifications were made to the engine to improve the optical access and provide control of the oil pressure that was independent of engine speed. To test the full range of engine speeds the pistons and connecting rods were removed and the big end journal bearings were secured in place using jubilee clips, in an identical setup as that used for imaging in the rocker cover in Chapter 4.

The oil circuit was modified to regulate the oil pressure and oil film generation on the crankshaft. A schematic of the modified oil circuit is shown in Figure 6.1, the circuit is similar to that displayed in Figure 3.5, but with modifications to the engine oil feed. The production oil pump that is driven off the crankshaft was replaced by an external feed pump and hot oil was supplied directly to the oil filter head at the start of the engine oil circuit. SAE 15W-40 at a temperature of 80°C was used for all tests discussed in this chapter. The oil rail pressure was monitored and controlled by adjusting the back pressure on the feed pump, the production oil rail pressures are displayed in Appendix A Figure A-2.2. Cold dirty oil was lifted from the sump and returned to the external heating tank using a return pump. The external oil tank, engine oil rail and engine sump temperature were monitored using K-type thermocouples to ensure a uniform oil temperature was maintained.
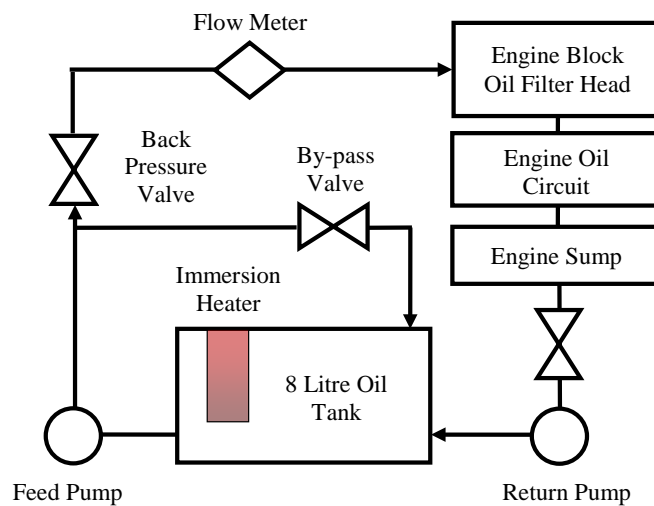
Figure 6.1 Crankshaft atomisation 1104C-44 motored engine heated oil circuit
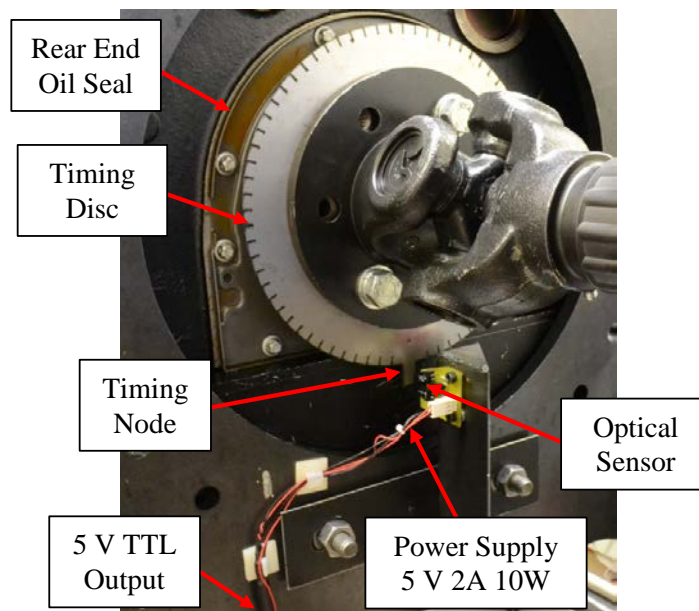
Figure 6.2 1104C-44 motored engine imaging trigger

A voltage trigger was used to initiate the high speed image capture. A steel disc with a single node was attached to the crankshaft output at the back of the engine and the front edge of the timing node was aligned with the desired crankshaft position. The crankshaft rotation was detected using an optical sensor which delivered a 5 V Transistor-Transistor Logic (TTL) signal to the high speed imaging signal processing box. An annotated assembly of the timing disc and sensor installed on the back of the engine is displayed in Figure 6.2. The trigger signal and therefore engine speed was monitored using an data logger, there were fluctuations of 1 – 3 Hz in the engine

speed, therefore it was critical that the trigger signal corresponded to the start of image capture and no delay was added.

6.2.2 Crankshaft Optical Access

Improved optical access was gained around the crankshaft lobes of cylinder one at the front of the engine, by removing the timing cover and a large section of the engine block. The sump was replaced by a customised slab sided Perspex sump as shown in Figure 6.3.
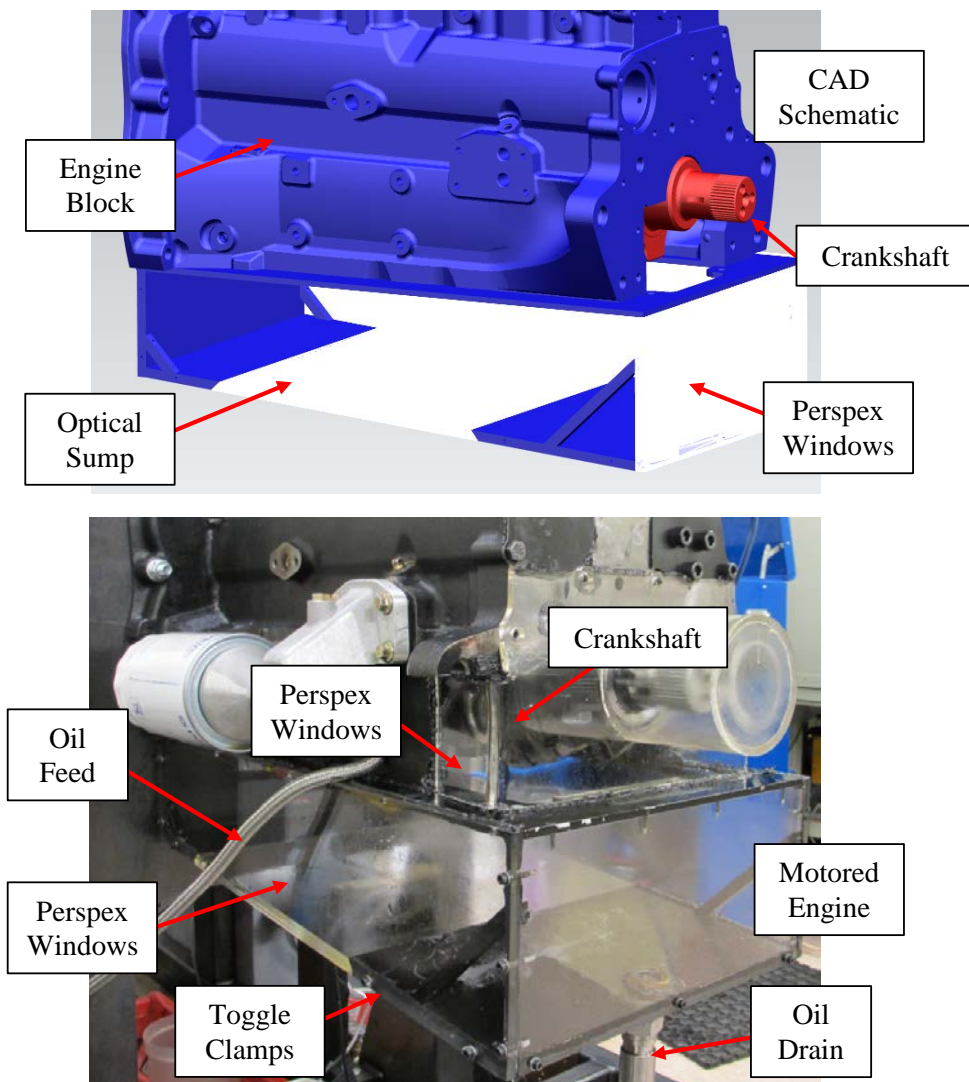
Figure 6.3 Optically accessed 1104C-44 motored engine and sump

The sump was designed so that the oil distribution in the bottom of the engine and the crankshaft oil atomisation could be captured. The base of the sump was angled 5° to horizontal so that the oil drained down to the front edge of the sump and returned to the external heating tank. The bottom Perspex window in the sump was secured in place using four toggle clamps to allow easy access to the inside of the windows for cleaning.
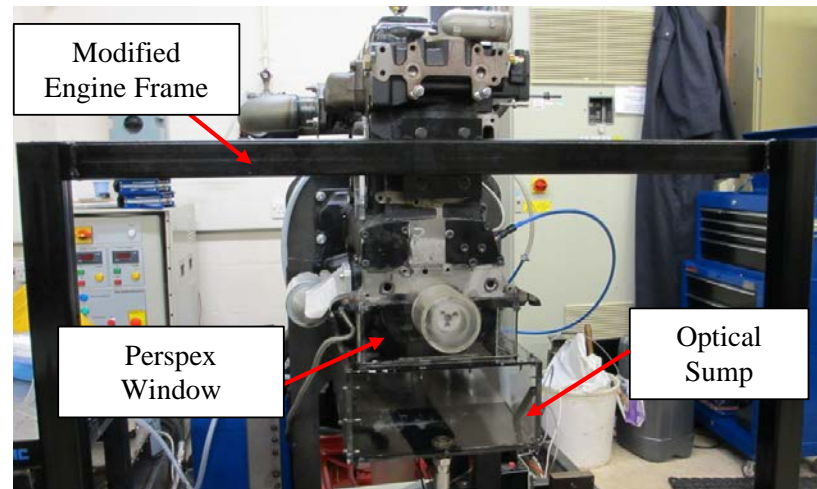
Figure 6.4 1104C-44 motored engine front mounting modification
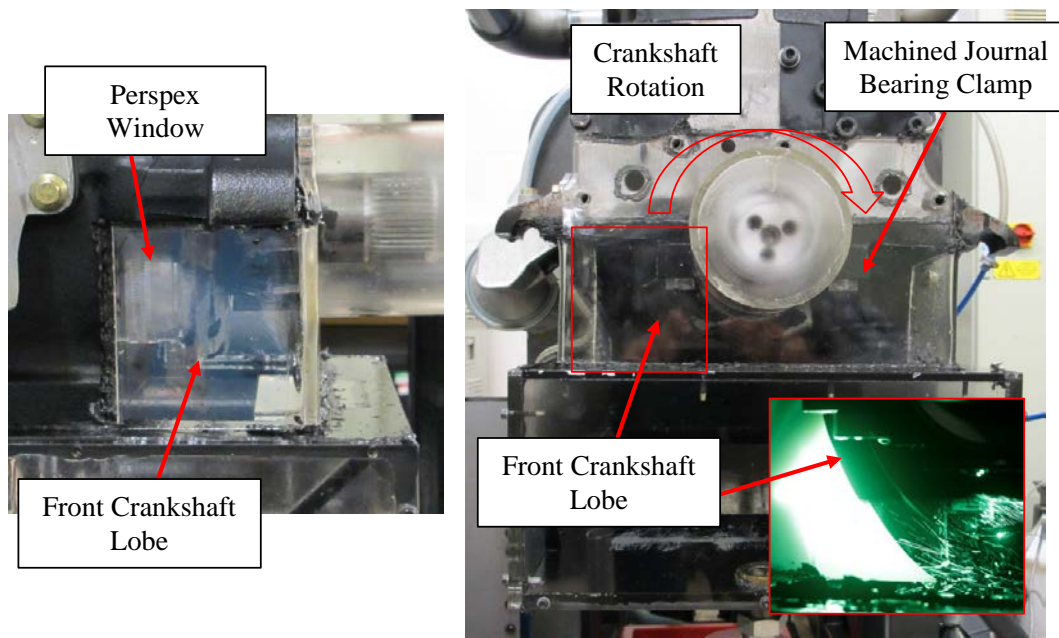
Figure 6.5 1104C-44 motored engine crankshaft optical access

A new front engine mount shown in Figure 6.4, was used to hold the engine without obscuring the optical access around the crankshaft. A large section at the front of the engine block was machined away and a Perspex shield mounted off the front of the engine was then moulded in place maintaining the internal profile of the crankcase. Any additional sealing was achieved using Loctite gasket sealant. The final Perspex window is displayed in Figure 6.5. Additionally, the clamp holding the front main crankshaft journal bearing was machined down to improve the optical access. As the engine was motored not fired and there were no pistons or connecting rods, this modification to the journal bearing clamp presented no structural problems.

6.3   Oil Ligament Illumination

High speed imaging of the crankshaft oil atomisation was conducted using the Photron FASTCAM APX-RS high speed camera and diffused single fibre copper vapour back illumination. Specific details of the imaging equipment were introduced in Section 3.6, but the image region and optical setup used for this experimental study are shown in Figure 6.6 and Figure 6.7, respectively. Images in Section 4.3.3 showed that the majority of oil drops were generated from the crankshaft lobe, consequently this is where the high speed imaging was focussed.
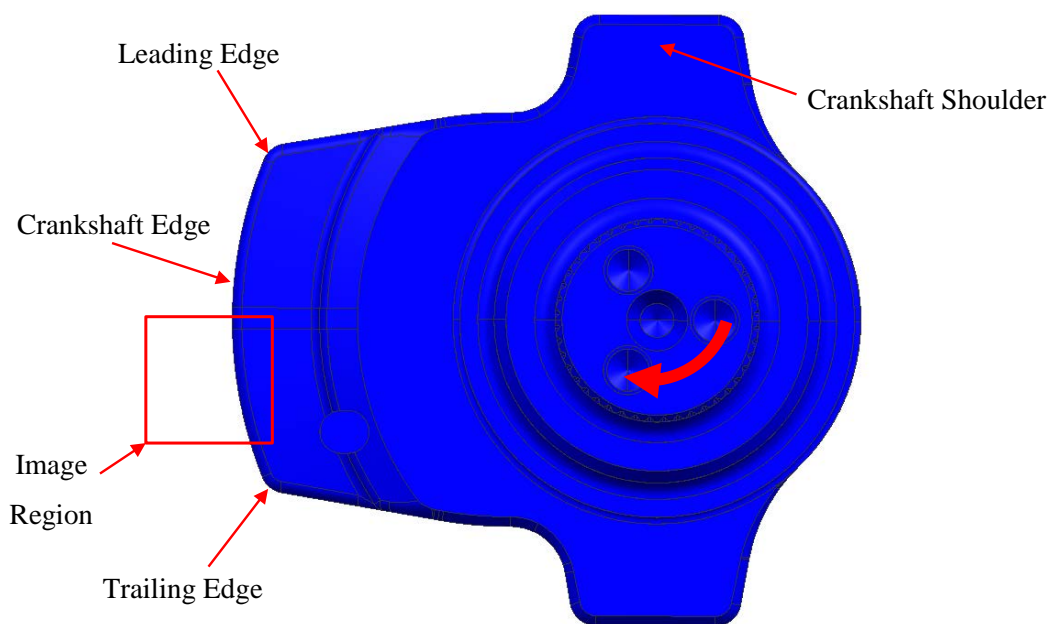
Figure 6.6 1104C-44 crankshaft oil atomisation image region and annotation
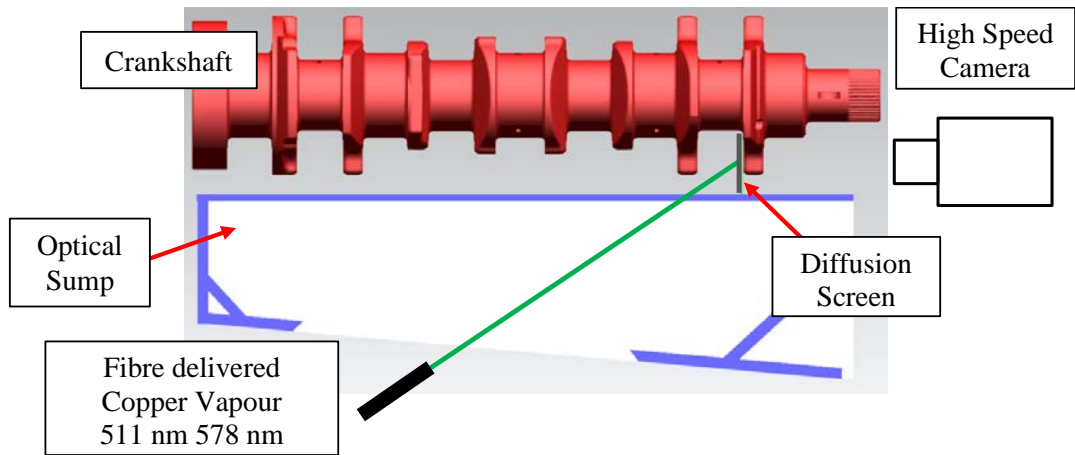
Figure 6.7 Crankshaft oil atomisation optical setup perpendicular to crankshaft centre line

(a) Optical setup parallel to crankshaft centre line
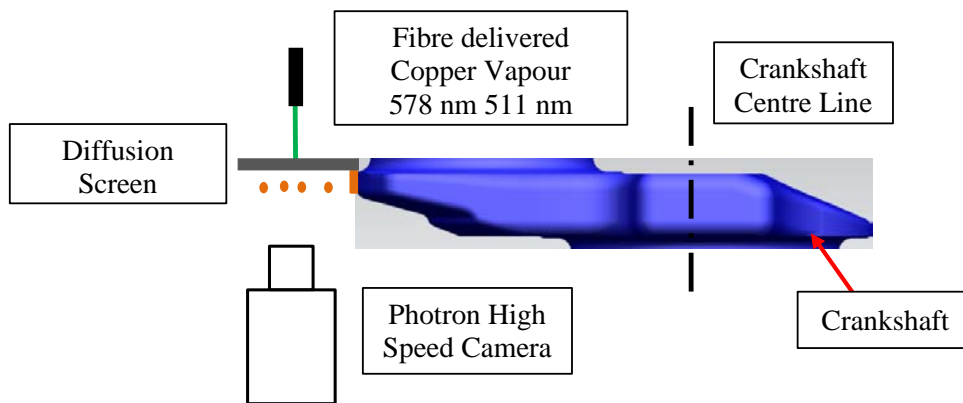
(b) Sample images
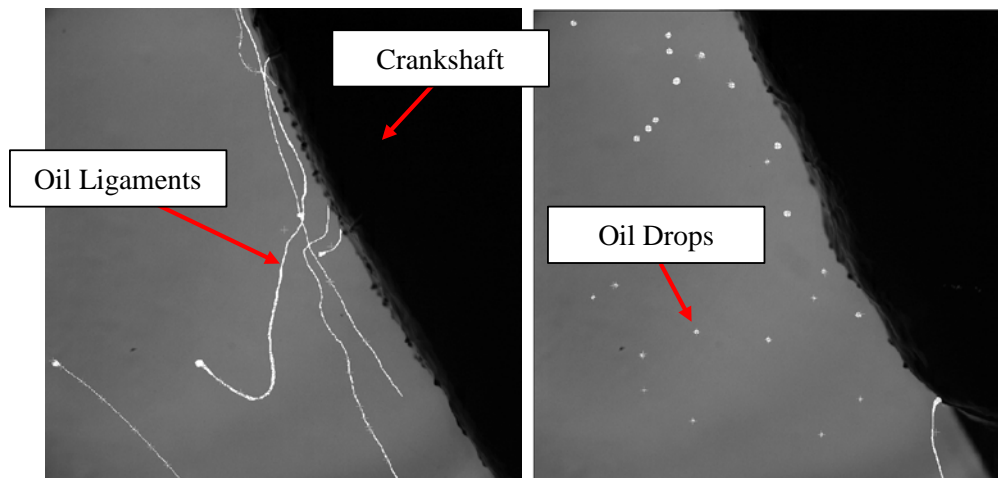
**Figure 6.8 (a) crankshaft oil atomisation optical setup perpendicular to the crankshaft centre line
(b) crankshaft oil atomisation sample images**

The Photron high speed camera was positioned parallel to the centre line of the crankshaft to capture the oil atomisation from 190 - 270° CA on the left side of the crankcase. A single copper vapour fibre illuminated the atomised oil through the bottom Perspex window in the sump, a plastic diffusion screen was positioned behind the crankshaft lobe perpendicular to the crankshaft centre. An additional schematic of the optical setup including samples images of the oil ligaments and atomised drops is shown in Figure 6.8.

A La Vision high speed controller synchronised the copper vapour laser and the high speed camera once the 5 V TTL signal from the optical sensor was received. La Vision DaVis software controlled the hardware and stored the high speed images. The engine oil pressure was regulated to ensure that there was only a thin film of oil on the crankshaft and the atomisation process could be analysed in detail without excessive blurring of the windows. Data was collected with production oil pressures but the distribution of oil was significant making it very challenging to capture useful images.

Table 6.1 Crankshaft oil atomisation test matrix

Oil Distribution			
Engine Speed [rpm]	ΔCA °	Image Size [mm]	Lens [mm]
2200	4.4	20 x 20	200
1800	3.6	20 x 20	200
1500	3	20 x 20	200
1000	2	20 x 20	200
Micro Measurement			
2200	4.4	10 x 10	200
2000	4	10 x 10	200
1800	3.6	10 x 10	200
1500	3	10 x 10	200

A test matrix is shown in Table 6.1, data was collected for two images sizes 20 mm x 20 mm and 10 mm x 10 mm at a range of engine speeds. The camera capture frequency was set to maintain the maximum image resolution of 1024 x 1024 pixels at 3000 fps. A 200 mm Nikon lens was used for the 20 mm x 20 mm images, 104 mm extension rings were required for the 10 mm x 10 mm images consequently a larger aperture was essential due to the lower signal.

Table 6.2 Crankshaft oil atomisation diffraction limited spot sizes

Wavelength	λ	nm	527
No. Active Pixels on CMOS Camera		pixels	1024
CMOS Camera Active Chip Size	A_c	mm	17.41
Imaged Area Size	A_I	mm	20.00
f-Number	$f^{\#}$		**8**
Difraction Limited Spot Size	$d_{diff} = 2.44\,(M+1)\,f^{\#}$	μm	19.24
Difraction Limited Spot Size		pixels	1.13

The diffraction limited spot size for the large imaging setup shown in Figure 6.7 and Figure 6.8 was calculated using Equation (3.2), the results are shown in Table 6.2. The diameter of any drops smaller than the diffraction limited spot size for the specific optical setup could not be resolved and would appear on the camera chip to have a diameter equal to the diffraction limited spot size.

6.4   High Speed Digital Particle Image Velocimetry

Particle Image Velocimetry (PIV) is a non-intrusive optical diagnostics technique that was developed to measure two-dimensional velocity fields. The term Particle Image Velocimetry was first introduced by Pickering and Halliwell (1984) and Adrian (1984). High Speed Digital Particle Image Velocimetry (HSDPIV) was used to collect high spatial and temporal resolution velocity vector fields of the flow around the crankshaft of the 1104C-44 motored engine. The operating principles of HSDPIV and the experimental setup employed to measure crankshaft flow structure are now described.

6.4.1   Seeding

PIV calculates the velocity of tracer particles seeding a flow, by resolving their displacement between two images captured with a known time separation. This indirect flow velocity measurement is reliant on two characteristics of the seeding particles:

1. Particle diameters are small enough for them to faithfully follow the flow and track any turbulent structures.

2. Particles must scatter sufficient incident light to enable their location to be resolved accurately.

The flow within the crankcase of the motored engine was seeded using a TSI six-jet air blast atomiser which generated a polydisperse aerosol of olive oil particles with a nominal diameter of $d_p = 1 - 2$ μm.

The ability of the seeding particles to follow the flow was assessed by first calculating the gravitationally induced velocity of a seeding particle using Stokes' drag law as shown in Equation (6.1) (Raffel, Willert, Wereley and Kompenhans, 2001), where ρ_l and ρ_a are the olive oil and crankcase gas densities respectively, and η_a is the air dynamic viscosity. The gravitationally induced drop velocity of 1 μm olive oil particles in air at 20°C is very small at 2.8×10^{-4} m.s^{-1}, this indicates that gravitational effects on the olive oil particles are very small.

Gravitationally Induced

Drop Velocity

$$\boldsymbol{U_g} = d_p^2 \frac{(\rho_l - \rho_a)}{18\eta_a} \boldsymbol{g} \qquad (6.1)$$

The frequency response of the seeding particles relative to velocity fluctuations in the surrounding fluid can be calculated by neglecting shear effects and centripetal forces. Initially assuming that the seeding particle velocity can differ from the local mean flow velocity by 0.1%, Drain (1980) showed that the size of the required seeding particles is defined by Equation (6.2), where a_p is the seeding particle radius, f_u is the maximum frequency the particles can follow, η_a is the density of the flow being measured and ρ_l is the density of the seeding particle.

Seeding Particle Frequency
Response

$$a_p^2 > 0.1 \frac{\eta_a}{f_u \rho_l} \qquad (6.2)$$

Frequency Response

1 µm Olive Oil

Particles in Air at 20°C

$$f_u = 0.1 \left(\frac{1.79 \times 10^{-6} [kg.m^{-1}.s^{-1}]}{1.205 [kg.m^{-3}] \times 2.5 \times 10^{-13} [m^2]} \right) \qquad (6.3)$$

$$f_u \approx 594 \, kHz$$

The maximum frequency 1 µm olive oil particles are capable of following has been calculated using Equation (6.2) and is displayed in Equation (6.3) as 594 kHz. Considering the existing published work on crankcase and crankshaft flows by Edelbauer (2007) and Begg, Sercey, Miche and Heikal (2010) the crankshaft flow frequencies are expected to be well within the 0.1% frequency response limit of 1 µm olive oil seeding particles.

Figure 6.9 Motored engine crankcase copper ring seeding jet

A copper ring was placed below the number one cylinder liner to introduce the olive oil seeding into the crankcase. Images of the copper ring are displayed in Figure 6.9 to illustrate the nineteen 3 mm diameter holes positioned around the ring to inject the olive oil seeding into the crankcase. The uniform seeding spray generated by the seeding jet is shown on the right of Figure 6.9.

6.4.2   Light Source

Light scattering from drops has been discussed previously in Chapter 4, the light scattering diagram for 1 μm particles is displayed in Figure 6.10. Diffraction of light on drops and particles is critical to non-intrusive optical techniques as it enables sub-pixel particle locations to be resolved. Careful attention must be paid to diffraction limits when using PIV, if the location and therefore displacement of seeding particle centres is not resolved accurately then large errors can occur in the PIV measurements.
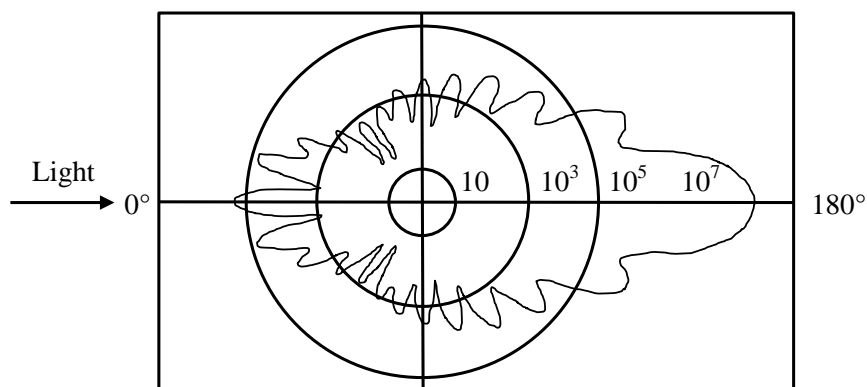
Figure 6.10 Light scattering from a 1 μm oil particle in air. Adapted from Raffel, Willert, Wereley and Kompenhans (2001)

PIV requires illumination of a two-dimensional region of seeded particles, the high spatial and temporal resolution capabilities of HSDPIV are achieved by the significant advances in laser illumination and high speed imaging. Seeding particle illumination is provided by a sheet of high energy density monochromatic light generated by a laser and suitable optics. High Speed PIV is reliant on a high frequency laser and camera capable of producing and recording illumination at a sufficient repetition rate, so that an image pair records the frequency of flow fluctuations.

A New Wave Research Pegasus-PIV Neodynium:yttrium lithium fluoride (Nd:YLF) laser was employed to measure the crankshaft flow, the full specification of the laser is listed in Table 6.3. The laser has a dual-head and is diode pumped, each head has a fundamental wavelength of 1053 nm which is combined and passed into an intra-cavity second harmonic generator which frequency doubles the infrared waves

into visible green 527 nm. The two laser heads were each capable of producing pulse energies of either 10 mJ per pulse at 1 kHz, or 2 mJ at 5 kHz.

Table 6.3 Nd:YLF laser specification

Nd:YLF Laser	
Property	**Specification**
Wavelength [nm]	1053 and 527
Pulse Engergy [mJ]	10
Pulse Duration [ns]	180
Peak Power [W]	20
Pulse Frequency [kHz]	10
Beam Diameter [mm]	1.5

A light sheet was generated from the collimated 1.5 mm beam emitted from the Nd:YLF laser using a cylindrical 50 mm lens and a spherical lens with a 1000 mm focal length. The sheet waist was positioned in the PIV imaging region and the 1000 mm focal length lens ensured there was only a small change in the beam thickness over the imaging region.
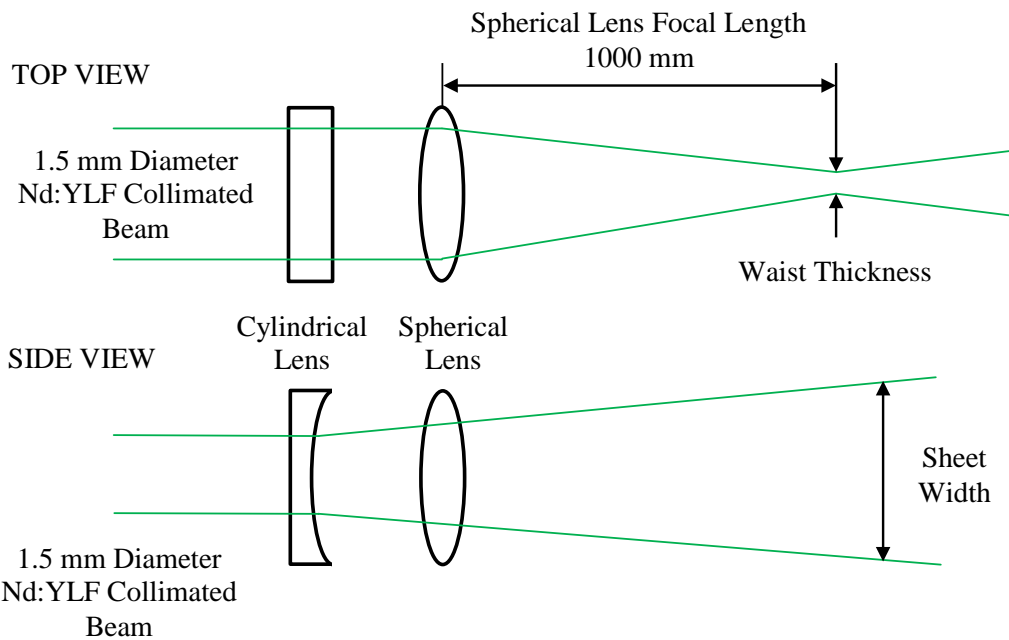
Figure 6.11 Nd:YLF PIV laser optics

6.4.3   Cross Correlation

To evaluate the velocity vectors from double-frame single-exposure images the image pair must first be divided into spatially matched interrogation regions. The interrogation region size was selected to suit the particle density and velocity gradient, the chosen value is presented in Section 6.4.6. A statistical cross-correlation between each interrogation region pair determines the average particle displacement. The cross-correlation process shifts an interrogation region with respect to its matched pair and calculates the associated correlation. Plotting the correlation for all possible spatial interrogation region shifts results in a peak correlation plane that corresponds to the average particle displacement.

For digital images the correlation peak is locked to an integer shift value, to resolve sub-pixel displacement a peak-fitting algorithm is applied to the cross-correlation peak and its surrounding points. For particles 2 – 3 pixels a Gaussian peak fit of typically three points has been shown to be highly accurate (Raffel, Willert, Wereley and Kompenhans, 2001), a schematic representing the PIV cross correlation process is displayed in Figure 6.12.
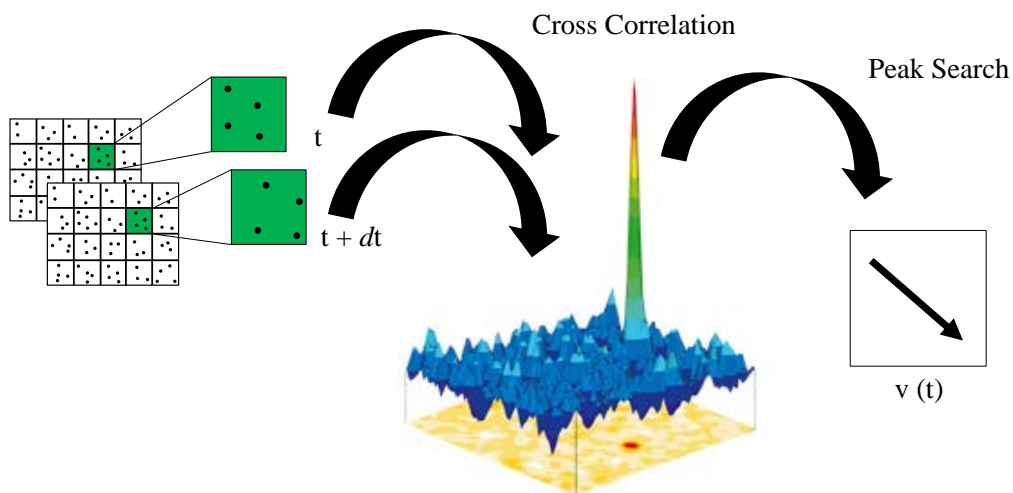
Figure 6.12 PIV cross correlation adapted from La Vision (2011)

Most commercial PIV systems generate the correlation plane in the frequency domain using Fast Fourier Transforms (FFT). The FFT is based on the cross correlation of two functions, in this case it is the complex conjugate multiplication of each functions Fourier transforms (Raffel *et al.*, 2001). FFTs are used as they reduce

the computational processing demand of the cross correlation compared to processing in the spatial domain, with only a small increase in the error. The La Vision DaVis 8.0 software used in this study completed two frame cross-correlation using a 2D FFT of the particle image pairs.

6.4.4 Image Capture

The Photron FASTCAM APX-RS high speed camera's CMOS sensor captured raw PIV images. A CMOS sensor has a charge-to-voltage conversion for each pixel enabling high image capture rates. In a high speed flow, to freeze the motion of the seeding particles a short exposure, beyond the capabilities of the high speed camera is required. The high frequency of the Nd:YLF laser was utilised to provide short bursts of illumination.

A very short interval between PIV images was achieved by frame straddling, where the laser pulse for the first image occurred at the end of the first camera exposure whilst the pulse for the second image occurred at the start of the second camera exposure. A timing diagram for the image capture is displayed in Figure 6.13, where *dt* is separation between PIV images.
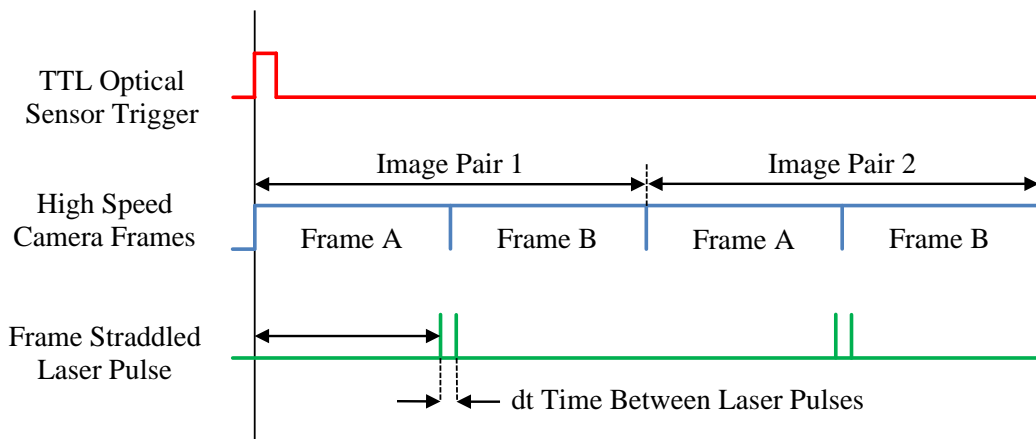
Figure 6.13 HSDPIV timing diagram

The PIV hardware was synchronised again using the La Vision high speed controller. The timing diagram in Figure 6.13 and the schematic in Figure 6.14 show the setup of the PIV hardware from the 5 V TTL trigger signal through to image storage in the La Vision DaVis 8.0 software.
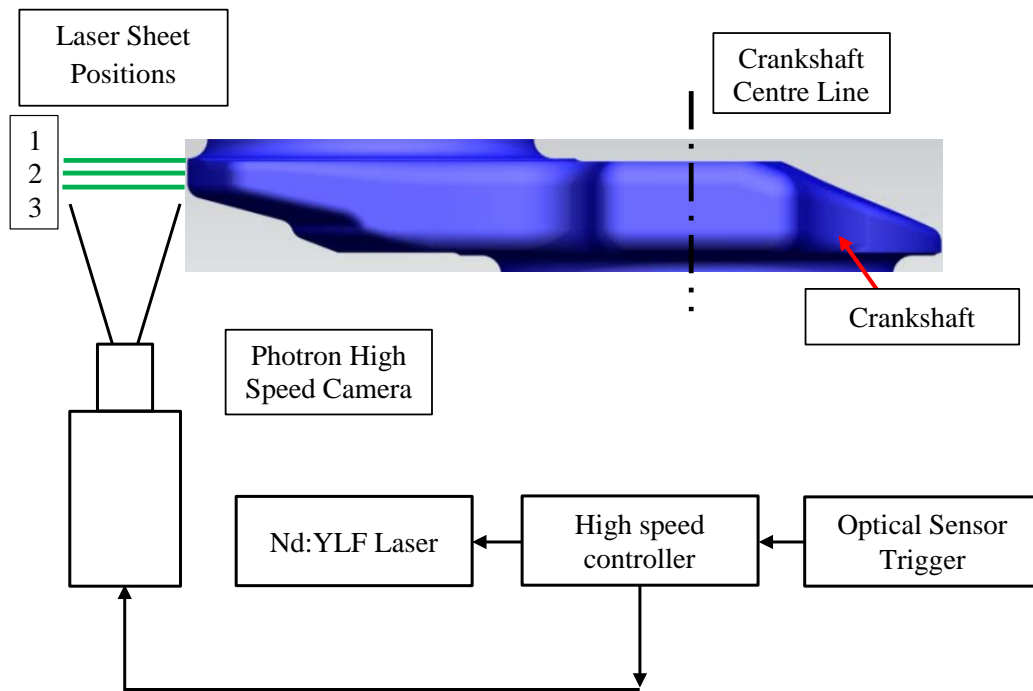
Figure 6.14 Crankshaft HSDPIV schematic
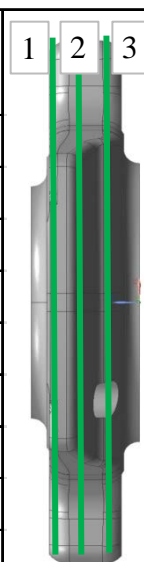
6.4.5 HSDPIV Test Matrix

As the air flow around the crankshaft was examined at a range of engine speeds the HSDPIV capture frequency was selected to maintain a consistent CA displacement (ΔCA) between PIV image pairs. The engine speed sweep was divided into two groups 2200 – 1500 rpm and 1400 – 1000 rpm maintaining a constant ΔCA between image pairs in each group. A complete test matrix for the HSDPIV is displayed in Table 6.4 including the maximum image resolution available at the fixed ΔCA. The crankshaft flow structure was examined over two different image sizes and three laser sheet position across the lobe of the crankshaft. The image region parameters and laser sheet plane positions are displayed in Table 6.5.

Table 6.4 Air flow PIV parameters

Air Flow					
Engine Speed [rpm]	dt [μs]	ΔCA °	PIV Frequency [Hz]	Capture Frequency [Hz]	Image Resolution [pixels]
2200	10	7.38	1790	3580	640 x 640
2000	12	7.38	1626	3252	640 x 640
1800	17	7.38	1463	2926	768 x 768
1600	20	7.38	1301	2602	768 x 768
1500	23	7.38	1219	2438	768 x 768
1400	24	4.69	1790	3580	640 x 640
1200	28	4.69	1534	3068	640 x 640
1000	31	4.69	1279	2558	768 x 768

Table 6.5 Air flow test parameters

Air Flow			
Engine Speed [rpm]	Laser Sheet Position	1 2 3	Nominal Image Size [mm]
2200-1500	1		24 x 24
2200-1500	2		24 x 24
2200-1500	3		24 x 24
1400-1000	1		24 x 24
1400-1000	2		24 x 24
1400-1000	3		24 x 24
Micro Measurement			
2200-1500	1		8 x 8

6.4.6   Sources of Error Present Within PIV

PIV is an extremely powerful non-intrusive fluid diagnostics technique, however, measurement errors exists. The errors present within PIV measurement can be attributed to either systematic bias errors or random errors. A number of factors contribute to the random errors within PIV measurement, they are listed and discussed below, including experimental considerations made to minimise their impact:

Optimisation of the Particle Image Diameter

If the seeding particle image size is too small the PIV data is described as peak locked. The Gaussian light distribution of the particle is lost and the cross-correlation routine cannot resolve sub-pixel particle displacement. The resultant particle displacements can only be resolved to the nearest integer pixel value. The DaVis 8.0 software was used to check for peak locking by examining the Probability Density Function (PDF) of the vector components and ensuring there was not a strong bias towards integer values for the crankshaft flow data. Conversely when the particle size is too large the correlation peak is broad reducing the accuracy of the Gaussian fit to evaluate the mean particle displacement.

Raffel, Willert, Wereley and Kompenhans (2001) showed that the optimum particle image size for high location accuracy is just over two pixels. The diffraction limited spot size was calculated using Equation (3.2) to provide an initial optical setup. The image region size and aperture were then adjusted to achieve approximately 2.8 pixels per seeding particle in the raw HSDPIV images.

Particle Image Shift

If the particle shift between consecutive images is too great then a large amount of error will be introduced in the measurement, as some particles will leave the interrogation region and new ones will enter. It is advisable to keep particle displacements below a quarter of the interrogation region. In an identical manner if the particle motion in the plane of the laser sheet is large compared to the time

interval then particles will again enter and leave the image causing a reduction in correlation pairs.

An interrogation region of 32 x 32 pixels was used and the *d*t was adjusted to maintain a quarter of an interrogation region displacement between PIV image pairs for the crankshaft air flow HSDPIV. Out of plane particle motion and large velocity gradients in the crankshaft flow approached the bandwidth of the PIV technique making it difficult to consistently achieve particle shifts of a quarter of an interrogation region. Multiple interrogation region passes and smoothing of the PIV data meant that any spurious vector values could be averaged out providing a representative result.

The engine vibration was quantified to ensure that excessive vibration did not affect the PIV measurements as the camera was mounted externally to the engine frame. Any excessive engine movement that occurred over the same time scale as the *dt* PIV frame separation would significantly affect the PIV measurements. The engine vibration was measured at all the test engine speeds of 1000, 1500, 1800 and 2200 rpm. The high speed camera recording at 3000 fps was focussed onto a 10 mm x 10 mm square piece of graph paper secured onto the front crankshaft bearing housing. The engine displacement at 1000 rpm is plotted in Figure 6.15.
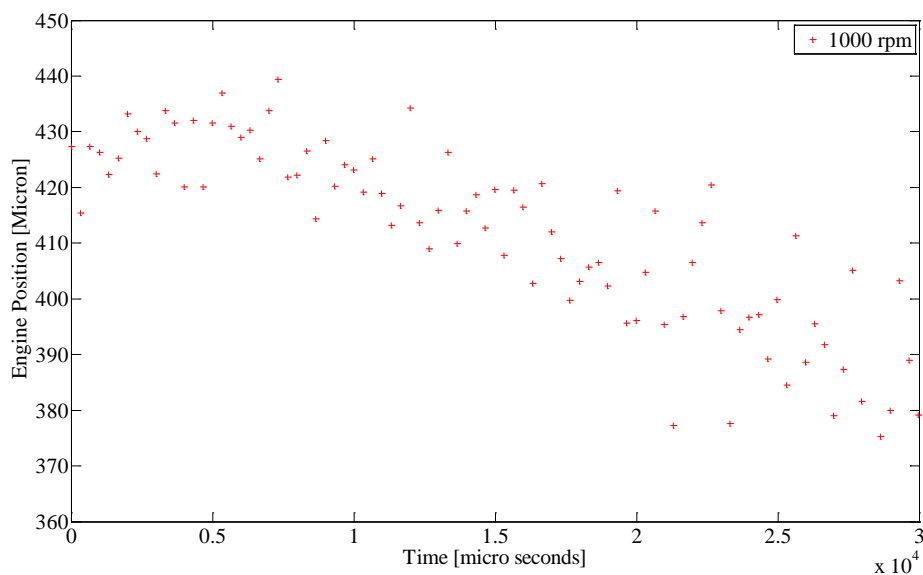
Figure 6.15 1104C-44 motored engine vibration at 1000 rpm

The mean engine displacement over 33 μs was 9 μm which is sub-pixel displacement on a HSDPIV image. The *dt* value was never larger than 30 μs and the particle displacement for a 32 x 32 pixels interrogation region was 8 pixels. For these reasons it can be concluded that the engine vibration will not significantly affect the PIV measurements.

Particle Image Density

A sufficient signal must be generated in the PIV images, a low particle number reduces the probability of accurate displacement detection, however, excessive particle density results in overlapping particles which interfere with the cross-correlation signal. For the crankshaft oil atomisation measurement the regulator pressure in the six jet atomiser was adjusted to achieve an appropriate particles seeding density over the 32 x 32 pixel interrogation region.

Particle Illumination

Non-uniformity in the particle illumination can alter the intensity of particle images leading to bias error. Non-uniformity is caused by a number of factors: obstructions in the image region, reflection off surfaces and diffraction of the light sheet caused by in-homogeneity in the windows. Similarly the signal-to-noise ratio must be sufficient to overcome any background noise.

Any variation in particle illumination was minimised by generating identical conditions for each HSDPIV data set. The optical access was not modified during testing and minimal lubrication was used to reduce fouling of the windows, when necessary the windows were carefully cleaned.

Gradient of Particle Displacement

If all the particles within an interrogation region are travelling with the same velocity then a well-defined Gaussian peak will be produced from cross-correlation. For most flow fields there is a velocity gradient across the flow and therefore the interrogation regions will generate a broader flatter cross-correlation peak. Significant problems arise when the difference in displacement across the interrogation region is larger than a single seeding particle, as the cross-correlation splinters into a number of

peaks. As only the highest correlation peak is used to calculate the particle velocity, when the peak broadens or splinters a very inaccurate measurement is made.

The pixel shift over each 32 x 32 pixel interrogation region could be analysed within the La Vision DaVis software. Example two-dimensional and three-dimensional plots of pixel shift are plotted in Figure 6.16. The plot shows that in the free stream region of the flow the cross correlation generates a single strong Gaussian peak.
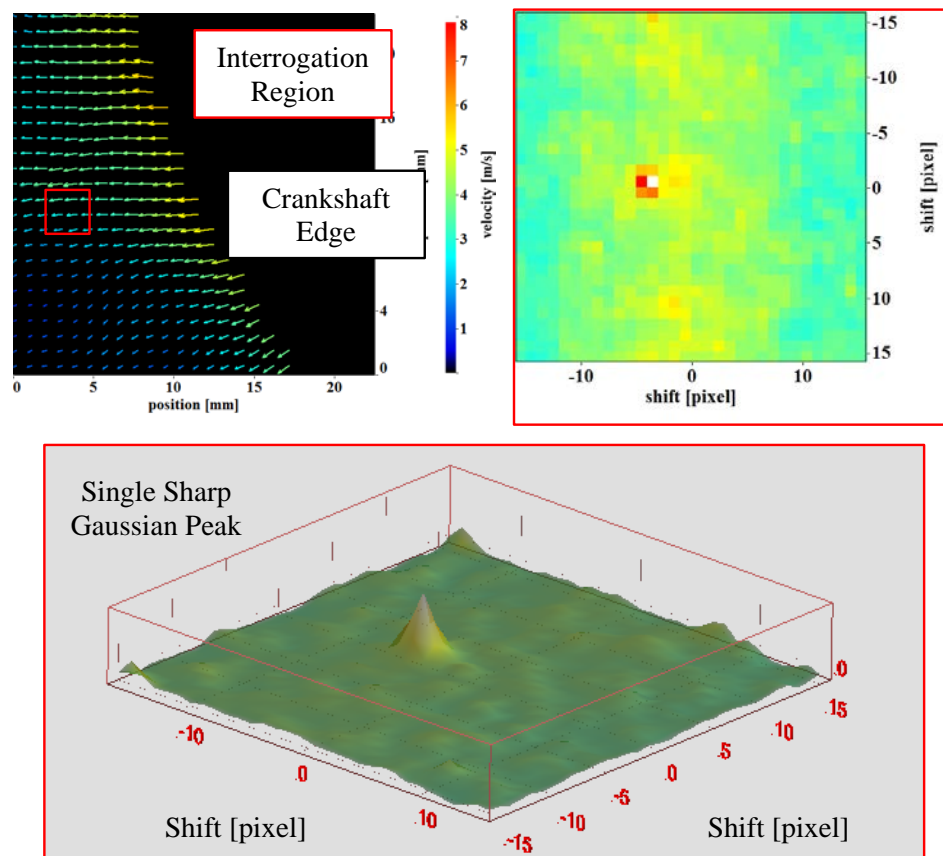
Figure 6.16 Crankshaft HSDPIV pixel shift for a single 32 x 32 pixel interrogation ratio

A boundary layer is expected near the crankshaft surface, moving over the boundary layer close to the crankshaft edge there is some splintering of the Gaussian peak, as shown in Figure 6.17. Peak splintering in this region can be minimised by reducing the interrogation region size, however, this will affect the particle image shift, particle image density and reduce the signal to noise ratio. A smaller image region was used to reduce peak splintering in the boundary layer close to the crankshaft surface. In the larger image region 1 pixel = 30 µm and for the smaller image region 1 pixel = 10 µm.
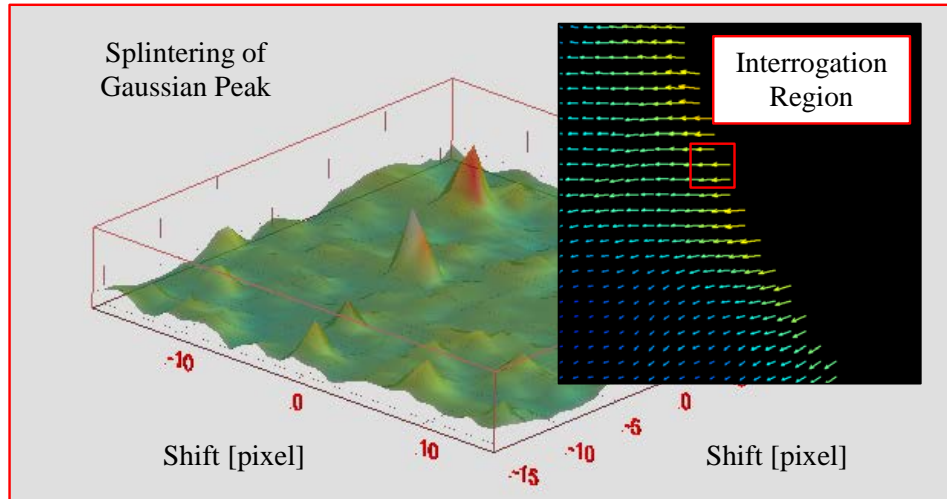
Figure 6.17 Crankshaft HSDPIV pixel shift for a single 32 x 32 pixel interrogation ratio

The gradient of pixel shift between interrogation regions was plotted against interrogation region number. A HSDPIV image of the flow behind the crankshaft was chosen as it contained a boundary layer, but the crankshaft was not present in the image. The selected HSDPIV image and the resulting plot are displayed in Figure 6.18. The shift gradient was measured over the horizontal red line in the HSDPIV image. Recalling that 1 pixel = 30 µm for the 32 x 32 pixel interrogation region, the gradient of the pixel shift between interrogation regions is within the 2.8 pixel limit even in the boundary layer region.
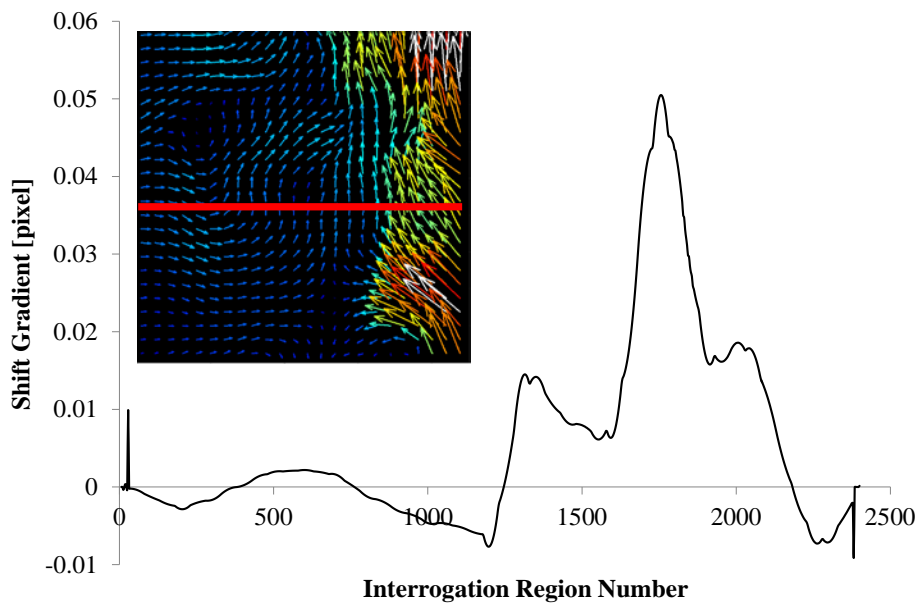
Figure 6.18 Crankshaft HSDPIV pixel shift for each interrogation region across a horizontal line

6.5 High Speed Analysis of Crankshaft Oil Atomisation

A thin 400 μm ± 50 μm oil film was consistently generated on the motored engine crankshaft lobe at the start of each test. The oil film was generated by motoring the engine for 2 minutes at an engine speed of 100 rpm with a fixed oil pressure and flow rate, no oil was fed to the engine during the 1 second test duration. The effect of engine speed on the distribution and atomisation of the oil film is displayed in Figure 6.19. Oil drops were formed along the surface of the crankshaft lobe at all engine speeds. The acceleration of the crankshaft opposed the surface tension of the oil and forced it into the series of discrete drops that were witnessed over the crankshaft lobe.
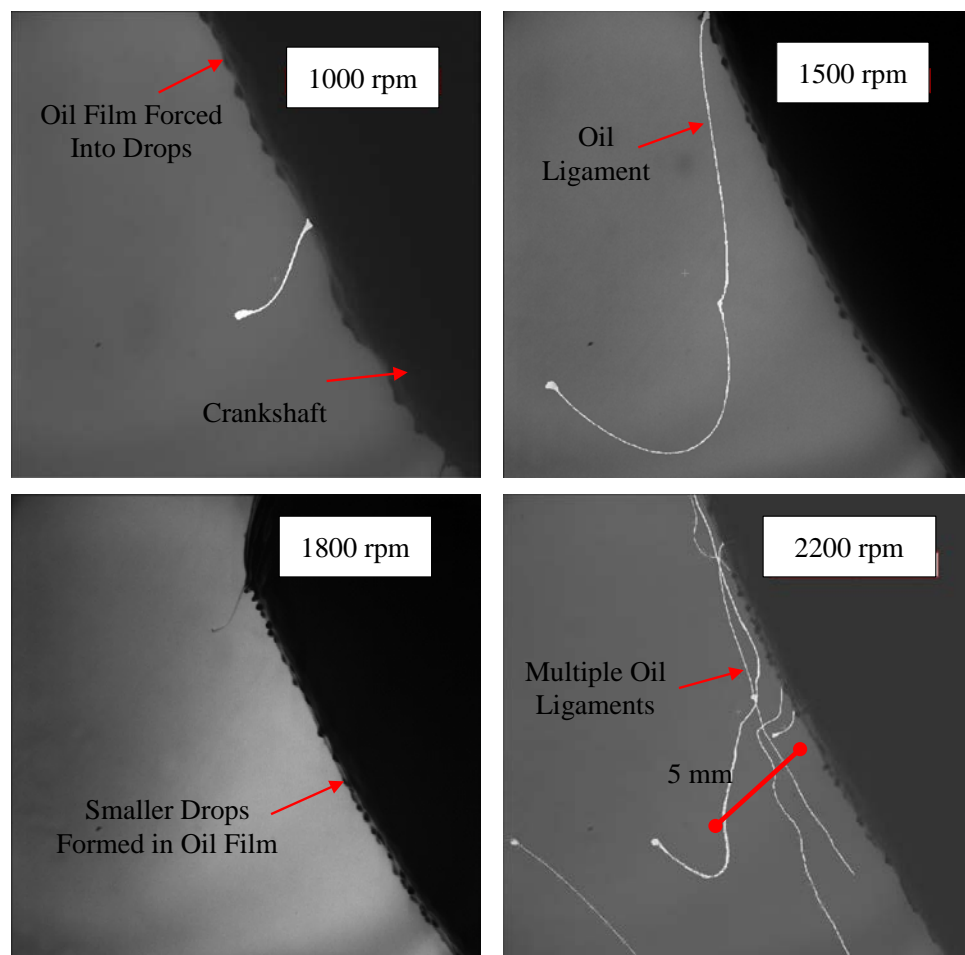
Figure 6.19 Crankshaft oil ligament generation at a range of engine speeds

6.5.1 Crankshaft Oil Film Behaviour

The crankshaft oil film profile at a fixed CA for four engine speeds was measured from the high speed images and compared to a surface profile plot of the dry crankshaft that is displayed in Appendix A Figure A-5.1. The resulting oil profiles are compared in Figure 6.20. Increasing the engine speed from 1000 rpm to 1500 rpm reduced the maximum oil film thickness on the crankshaft from 480 μm to 230 μm, but from 1500 - 2200 rpm there was minimal difference in the oil film. As the original oil film thickness was consistent, variation in the thickness means that the oil is either distributed elsewhere on the crankshaft or as is witnessed in Figure 6.19, more of the oil film is thrown off the crankshaft at higher engine speeds.
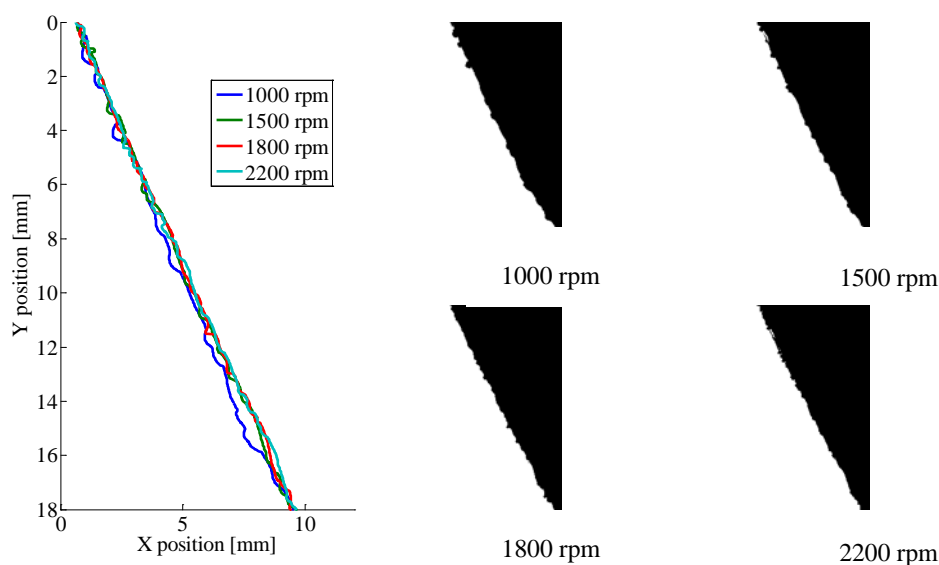
Figure 6.20 Crankshaft oil film measurement

As discussed in Chapter 2, Hege (1964) derived the expression in Equation (2.18) which shows that the oil film thickness on the surface of a rotating disc (*a*) is controlled by the balance of surface tension and centripetal forces. The measured oil film thickness ratio has been plotted in Figure 6.21 and compared to Heges' (1964) prediction. The experimental oil film thickness values were higher than that predicted by Hege (1964) as Equation (2.18) does not account for the oil flow rate onto the disc. However, the effect of the angular velocity on the crankshaft oil film is consistent, this result illustrates the strong but predictable influence of centripetal forces.

Oil Film Thickness
$$a = \left(\frac{4\sigma}{D\rho_l\omega^2}\right)^{\frac{1}{2}}$$
(6.4)
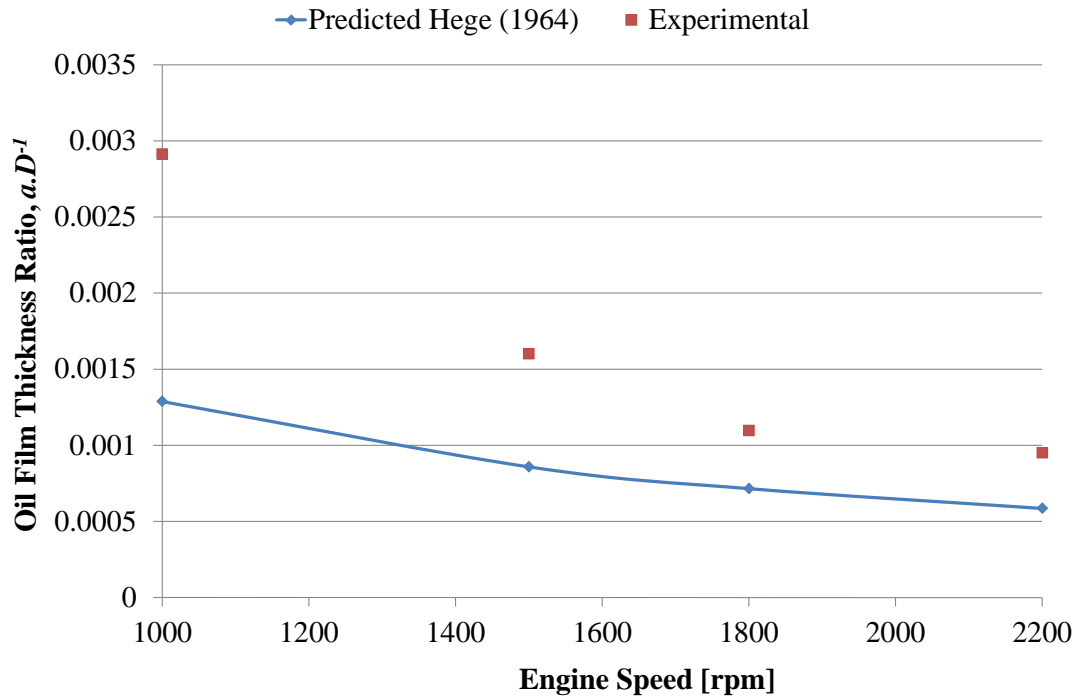
Figure 6.21 Crankshaft oil film experimental and predicted

6.5.2 Crankshaft Oil Ligament Generation

Analysis of the high speed images does not provide an absolute measurement of the total oil volume present, but it does provide valuable quantification of the effect of angular velocity on the oil drop generation. Critically the lower oil film thickness at higher engine speeds suggests that more of the oil is atomised following ligament breakup. The oil ligament generation at 1000 rpm is displayed in Figure 6.22, which illustrates oil ligaments thrown from the crankshaft. Critical to this investigation is the breakup process and the final drop generation from the crankshaft.
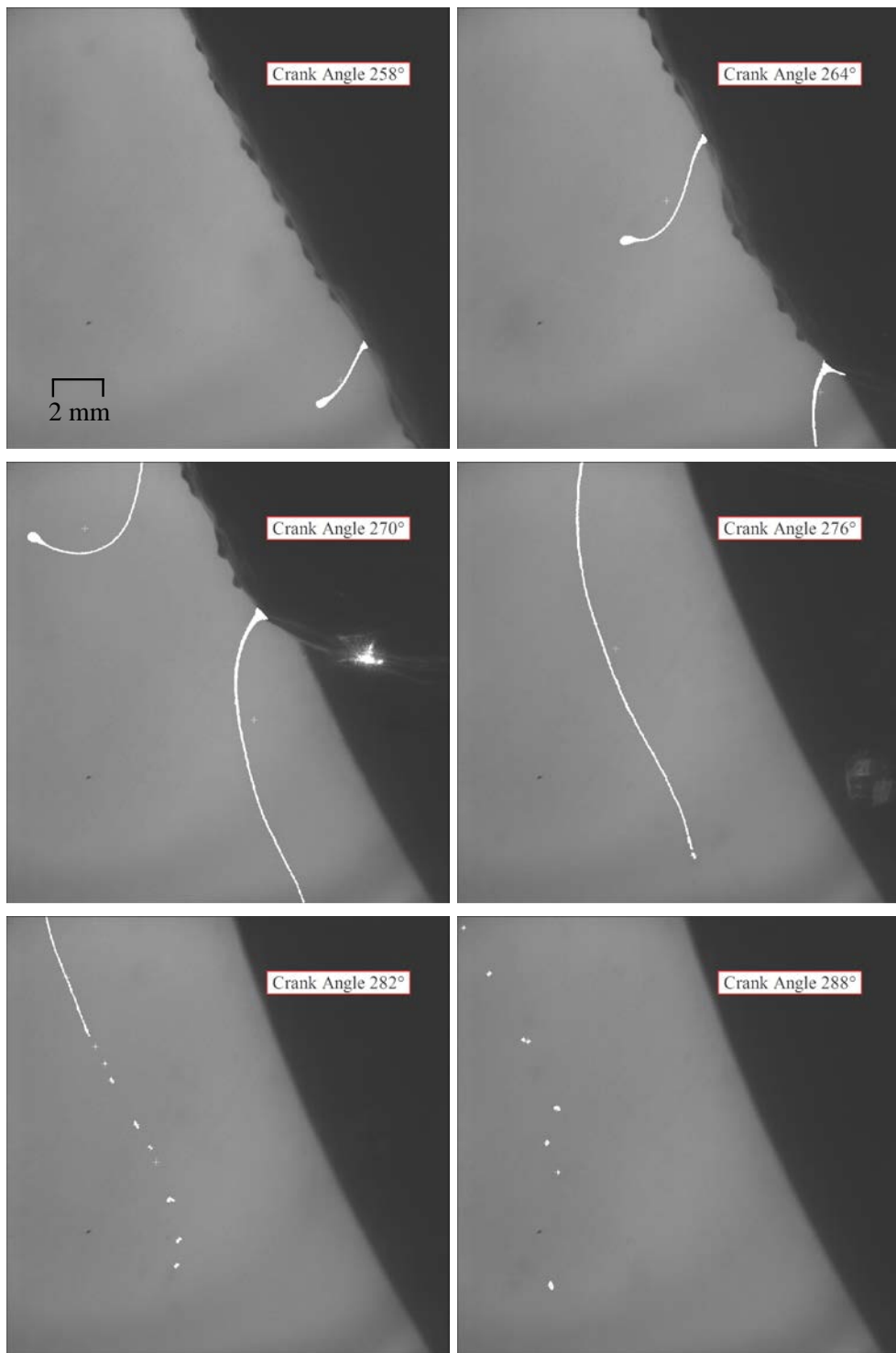
Figure 6.22 Crankshaft oil ligament generation and breakup at 1000 rpm

The major axis length of the oil ligament generated from the leading edge of the crankshaft at 1000 rpm is plotted in Figure 6.23. In an identical manner to that discussed in Section 4.3.4, the oil ligament is generated as the oil surface tension and viscosity act to resist the centripetal acceleration of the crankshaft. The oil film changes shape to maximise the surface tension force. Oil drops formed in the crankshaft oil film are stretched out into ligaments. Consequently the diameter of the large oil drop at the head of the oil ligament corresponds to the drop diameters formed in the crankshaft oil film. Figure 6.23 shows a 400 μm oil drop generated at the head of an 80 μm thick oil ligament, the ligament length increases with the crank angle. Once the ligament, generated at the front of the crankshaft, is drawn 5 mm away from the crankshaft surface the ligaments starts to curve. The curvature of the ligament is caused by the acceleration of the crankshaft and the high velocity flow generated tangentially to the crankshaft surface.
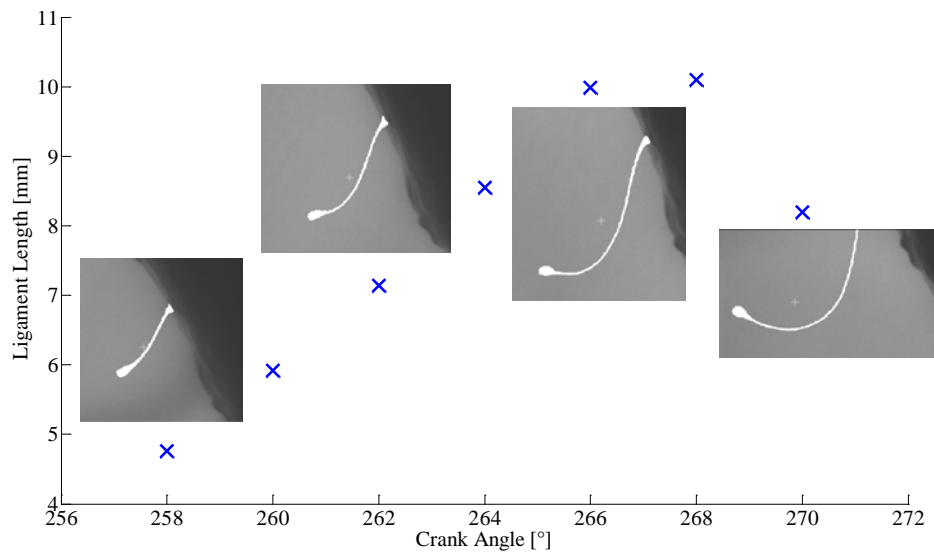
Figure 6.23 Crankshaft oil ligament generation at 1000 rpm

A ligament generated further down the crankshaft surface at 1000 rpm, shown in Figure 6.22, was traced through to final breakup and drop generation. The final drop diameters are plotted in Figure 6.24 and the breakup of the $a_L = 30$ μm ligament is shown in Figure 6.25. The surface tension of the oil is not sufficient to support the full ligament length, therefore Rayleigh type breakup occurs. Breakup of the ligament generates primary drops separated by a series of smaller satellite drops as identified in Figure 6.25. We can see in Figure 6.24 that initially the drop number

increases with crank angle. Further increase of the crank angle reveals that the drop diameters vary, this is caused by the surface tension of the oil adjusting the drop geometry to create a stable shape. It should also be noted that some of the drops will leave the image region and new drops will enter. If the Weber number of the drops in the flow tangential to the crankshaft is too high further drop breakup will occur. The Weber numbers of the oil drops are calculated in Section 6.8.2, following presentation of the PIV measurements and CFD calculations. These results are required to quantify the flow velocity around the crankshaft.
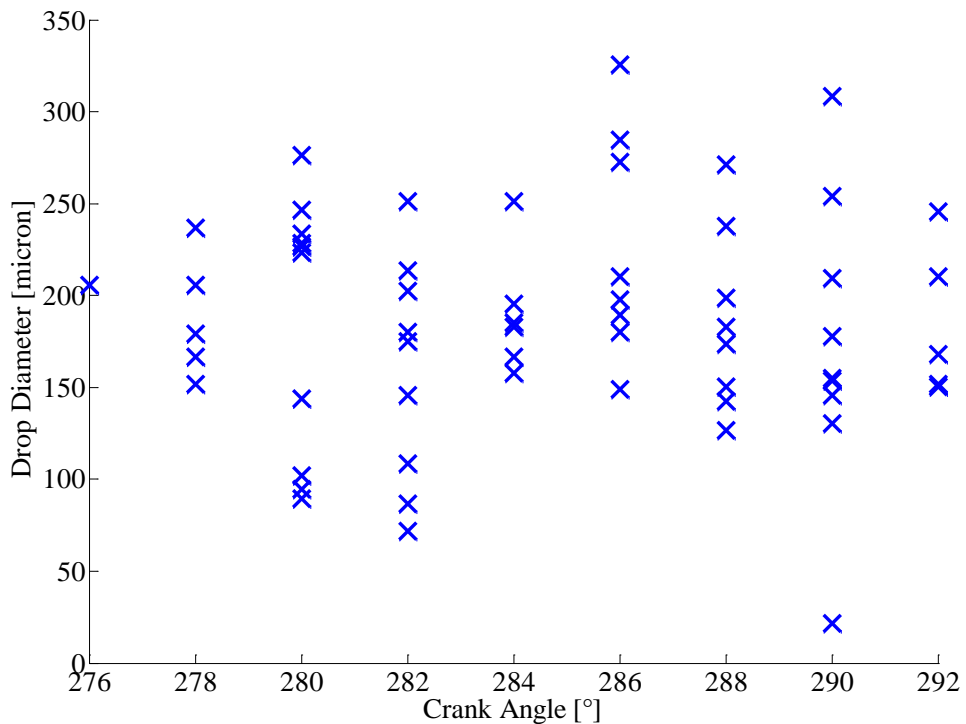
Figure 6.24 Final drop diameters from a 60 μm oil ligament generated at 1000 rpm
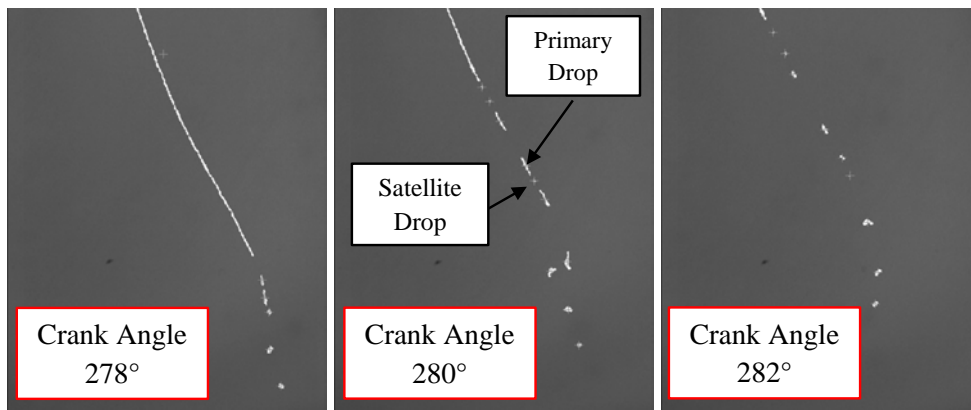
Figure 6.25 Crankshaft oil ligament breakup at 1000 rpm
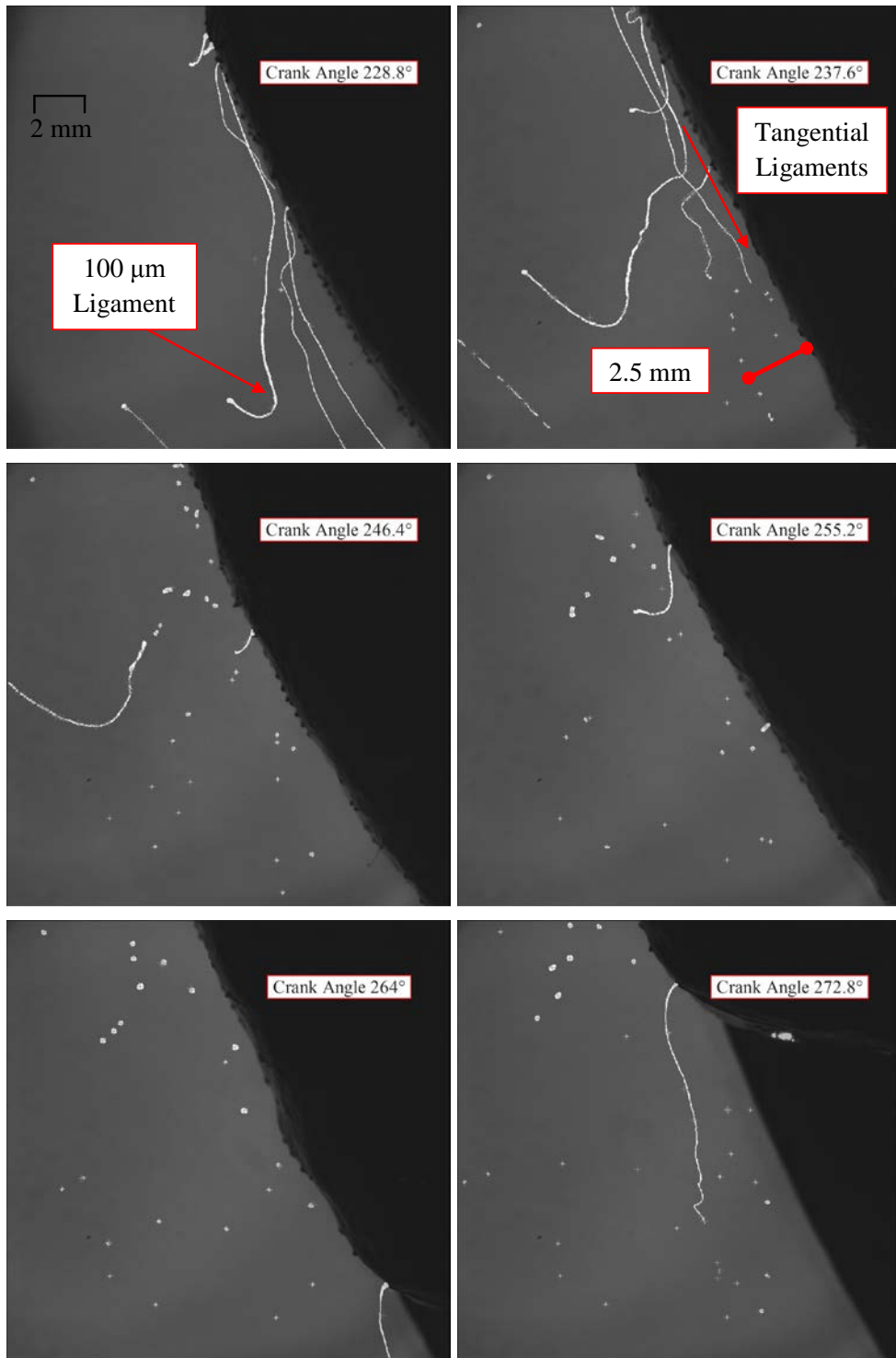
Figure 6.26 Crankshaft oil ligament generation and breakup at 2200 rpm

The final drop generation is controlled by the oil ligament geometry which itself is strongly affected by the crankshaft angular velocity. At 2200 rpm, the highest engine speed tested, multiple oil ligaments were generated from the crankshaft oil film, these ligaments were thinner and consequently broke up into smaller primary and satellite oil drops. Crankshaft oil ligament generation and breakup at 2200 rpm is displayed in Figure 6.26. At 2200 rpm the high angular velocity of the crankshaft forced the oil film into small drops $d_p \approx 200$ μm, which were then drawn into thinner 30 - 60 μm ligaments. The final drop diameters generated from the ligaments in Figure 6.26 are plotted in Figure 6.27.
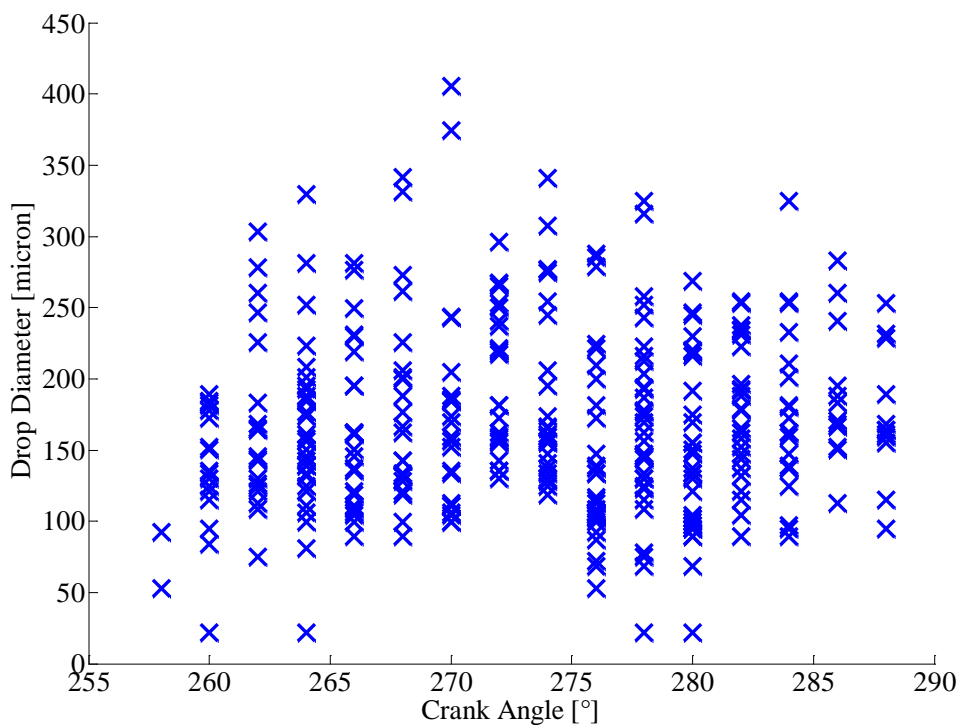
Figure 6.27 Final drop diameters from 30 - 60 μm oil ligaments generated at 2200 rpm

Most of the ligaments were drawn tangentially to the crankshaft edge until breakup occurred. Some larger $a_L = 50$ μm oil ligaments were drawn away from the crankshaft edge and exhibited a curved profile similar to that witnessed at lower engine speeds in Figure 6.22 and Figure 6.23. At the higher engines speeds the majority of the oil drops were smaller in diameter and they were generated closer to the crankshaft. Additionally, at 2200 rpm oil ligaments originated over more of the crankshaft circumference not just at the leading and trailing edges of the crankshaft.

Chapter 2 discussed existing investigations of rotary and crankshaft oil atomisation. Commonly the disk Bond number Bo_D, shown in Equation (2.23), is employed as a dimensionless number to characterise the ratio of surface tension forces to the acceleration forces of a rotating component.

Rotating Disk Bond Number

$$Bo_D = \frac{\rho_l a_c D^2}{4\sigma}$$

(6.5)

For this investigation the final drop diameters have been normalised against the crankshaft diameter (D) and plotted against the disc Bond number in Figure 6.28. The results from this experimental investigation show good agreement with the measurements taken by Begg, Sercey, Miche and Heikal (2010) who investigated oil atomisation from a gasoline crankshaft.
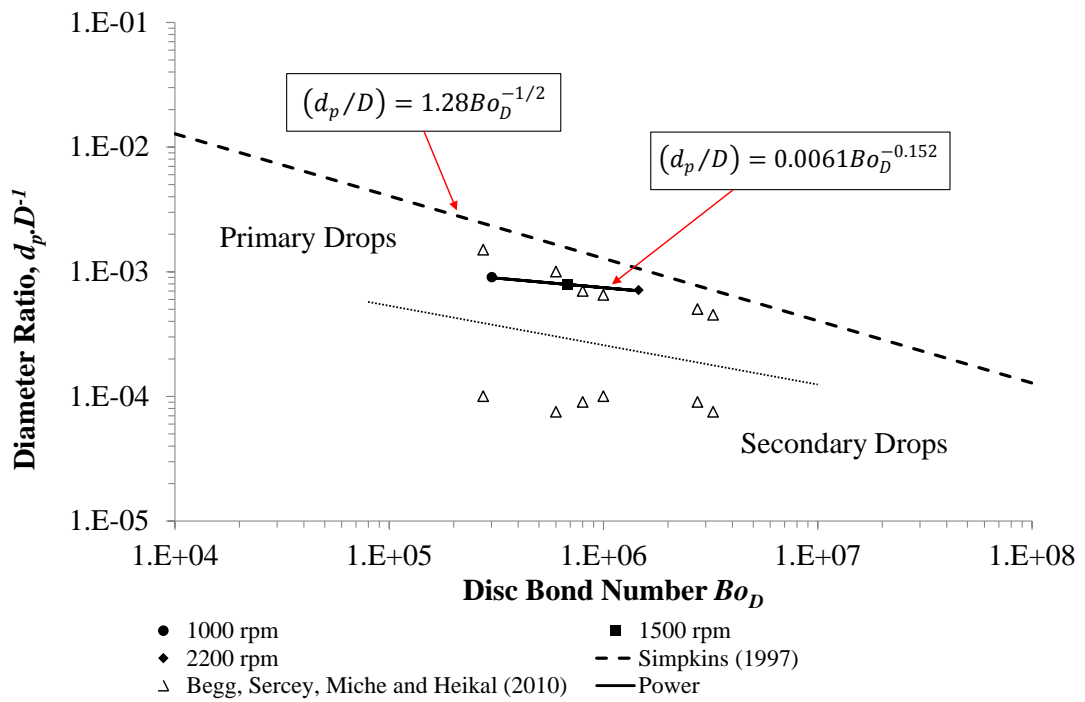
Figure 6.28 Predicting crankshaft oil ligament breakup

Rotary atomisers are utilised to generate a controlled monodisperse aerosol, Lefebvre (1989) shows ligaments formed along the circumference of a rotating disk in a repeatable pattern. The experimental results presented in this chapter, particularly at high engine speeds, have shown that the rough cast surface of a heavy duty engine

crankshaft generates ligaments in a more complex, less predictable pattern over the crankshaft circumference. Despite the less uniform ligament generation, Figure 6.28 shows that the primary drop diameters generated by crankshaft ligament generation can be predicted mathematically.

6.5.3 High Speed Analysis of Crankshaft Oil Atomisation Discussion

The experimental images presented in this section characterise the crankshaft oil atomisation process, and quantify the size of the primary and satellite oil drops that are generated. Valuable information has been gained on how the oil ligaments are formed over the surface of the crankshaft and how the oil film is atomised. The next stage of this experimental investigation focused on the transport of the oil drops generated by the crankshaft. The atomised oil drops are carried through the crankcase and contribute to the crankcase emissions. High Speed Digital Particle Image Velocimetry and Computation Fluids Dynamics modelling were employed to evaluate the flow structure around the crankshaft, and therefore quantify the aerodynamic Weber number of oil drops generated by ligament breakup.

6.6 Mathematical Analysis of Crankcase Flow

Initially assuming that there is no slip at the boundary of the rotating crankshaft, the flow velocity close to the crankshaft is equal to the tangential velocity component of the crankshaft at a given angular velocity. An annotated diagram of the crankshaft and the equations required to calculate the tangential velocity components are displayed in Figure 6.29, where ω is the crankshaft angular velocity, r is the specific radius of the crankshaft and v is the tangential velocity component of the crankshaft. The specific regions of interest are over the full periphery of the crankshaft edge, including in front of and behind the crankshaft. The speed and velocity of the flow in these regions is of interest as it effects primary ligament breakup and drop transport. The tangential velocity components at 2200 rpm in the regions of interest are displayed in Figure 6.29. Moving radially outwards from the crankshaft edge the flow will asymptotically approach the free stream flow velocity in the crankcase. Calculating the thickness of this boundary layer is complex and is the subject of

significant research, Schlichting (1968) provides a comprehensive discussion on this topic.
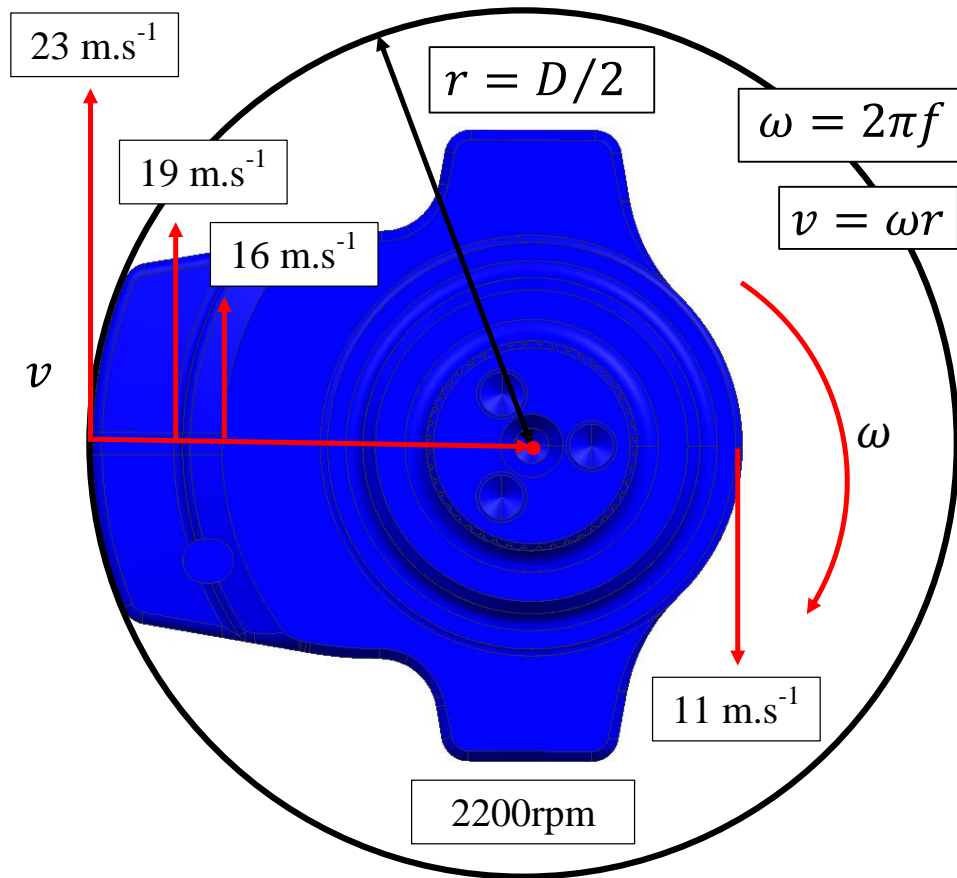
Figure 6.29 1104C-44 crankshaft tangential velocity components at 2200 rpm (Hibbeler, 2004)

Additionally, viscous drag over the surface of the crankshaft generates a swirling flow axially towards the disk as illustrated in Figure 6.30. White (1974) highlighted that the flow motion over the disc surface is a genuine three-dimensional motion. As highlighted in Section 6.4.6, the PIV technique does not lend itself to large three-dimensional out of plane motion. Despite the three-dimensional flow structure the additional spatial resolution achieved by PIV compared to point measurements is extremely beneficial and provides valuable novel information. Out of plane motion was investigated by carefully choosing the laser sheet position and examining multiple image planes along the crankshaft axis, as displayed in Table 6.5.
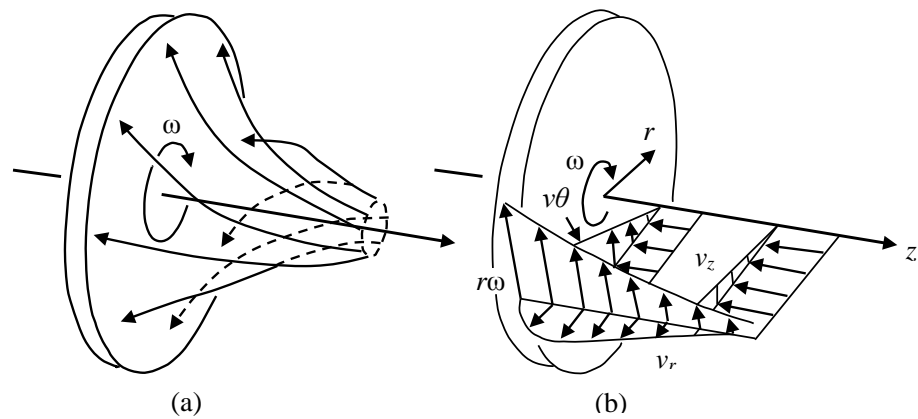
Figure 6.30 Laminar flow near a rotating disk (a) streamlines (b) velocity components. Adapted from White (1974)

The rotation of a disc near a solid wall is analogous to the crankshaft rotating within the confines of the crankcase. Boedewadt (1940) mathematically calculated the three velocity components in the boundary layer of a disc rotating near a solid wall, the resulting velocity distributions are displayed in Figure 6.31 against the dimensionless coordinate ζ, where z is the Cartesian coordinate along the axis of the rotating component and v_r is the radial velocity component.

$$\zeta = z \sqrt{\frac{\omega}{v_r}}$$
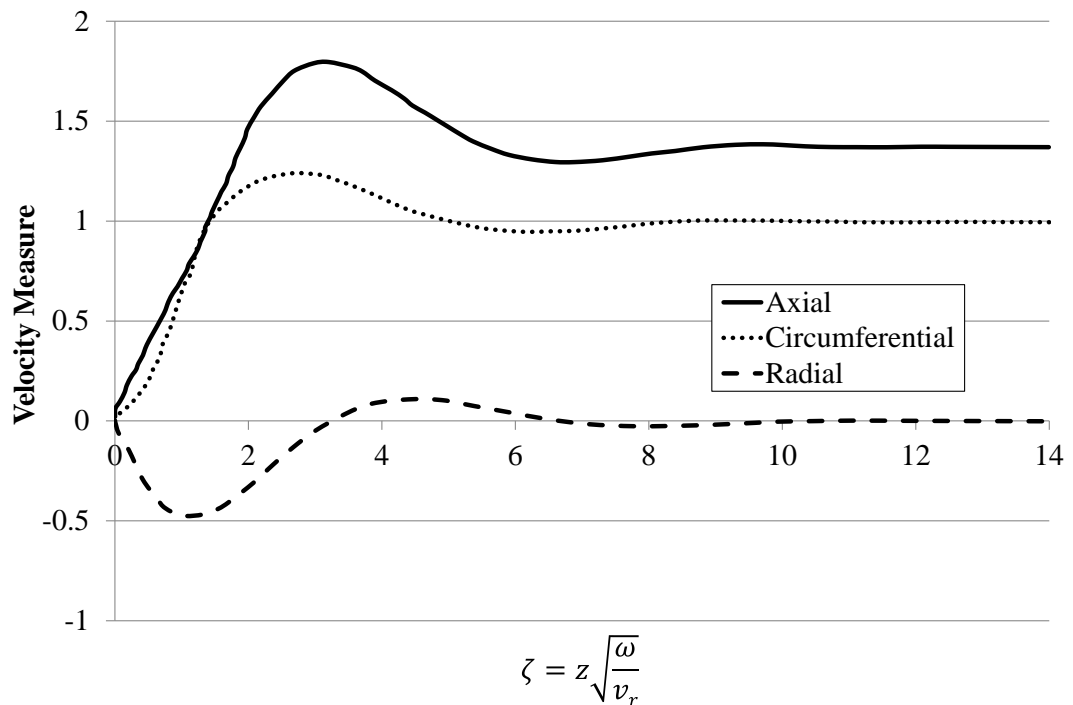
Figure 6.31 Velocity distribution in the boundary layer of a disc rotating near a solid wall. Adpated from Boedewadt (1940) referenced in Schlichting (1979)

6.7 CFD Analysis of Crankshaft Flow

A single phase computational fluid dynamic model was developed in Star CCM+ Version 7.02.011 to enhance the understanding of the fundamental aspects of the crankshaft flow. The flow domain comprised of a single crankshaft web and a 15 mm section of the big end bearing shell. The section of the crankshaft and the flow domain are displayed in Figure 6.32. A single mass flow inlet at the top of the flow domain replicated the olive oil jet displayed in Figure 6.9.
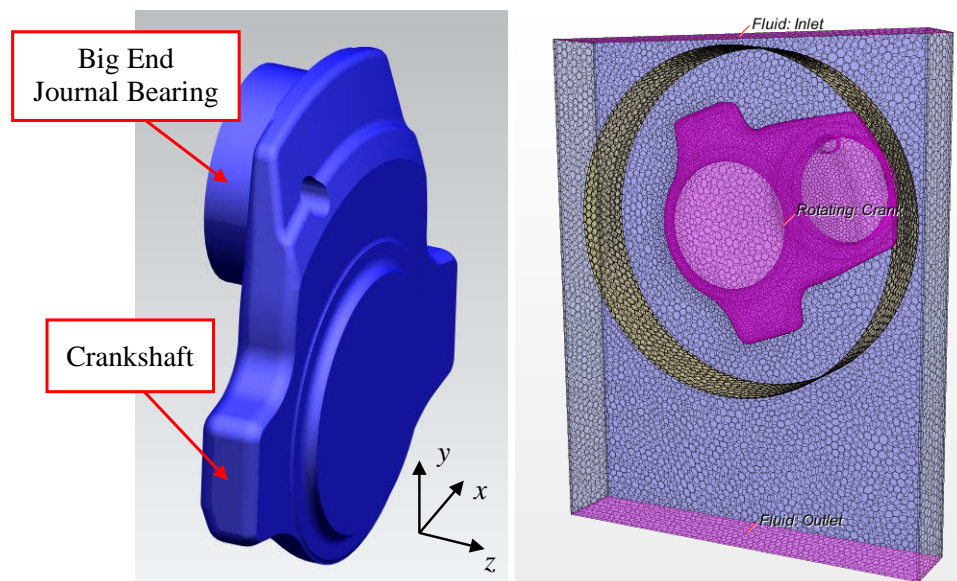
Figure 6.32 Rotating crankshaft (a) model (b) CFD fluid domain

A simple pressure outlet at the bottom flow domain replicated the large volume sump in the bottom of the engine. The large walls in the x – y plane were symmetry planes representating an infinitely long crankcase domain in the axial direction of the crankshaft. A polyhedral mesh containing 81000 cells with a base cell size of 5 mm was applied to the flow domain. The cell size was selected to ensure there were no distorted or heavily skewed cells over the flow domain, and to achieve a compromise between the accuracy of the solution and the processing time.

An implicit unsteady segregated turbulent gas flow model with constant density was selected. With little knowledge of the turbulence levels present in the crankshaft flow, the widely acknowledged and validated K-Epsilon turbulence model was selected. Further details of the performance of this turbulence model can be found in

Versteeg and Malalasekera (2007). Rigid body rotation of the crankshaft about a central axis replicated the crankshaft motion on the motored engine. At each engine speed the implicit solver was set to increment 1° CA for each time step with 20 inner iterations. The model ran for 4 complete rotations to stabilise the flow domain, and ensure satisfactory convergence of the momentum and energy had been achieved.

6.7.1 Crankcase Flow CFD Results

The flow around the crankshaft was modelled at speeds of 1000, 1500 and 2200 rpm. A vector plot of the flow including the tangential velocity components within the boundary layer of the crankshaft is displayed in Figure 6.33. There is excellent agreement between the tangential velocity components and the vector magnitudes in the CFD results. We can also see that slip in the boundary layer close to the crankshaft surface, the flow velocity reduces until the flow reaches the very low free stream velocity in the outer fluid domain.
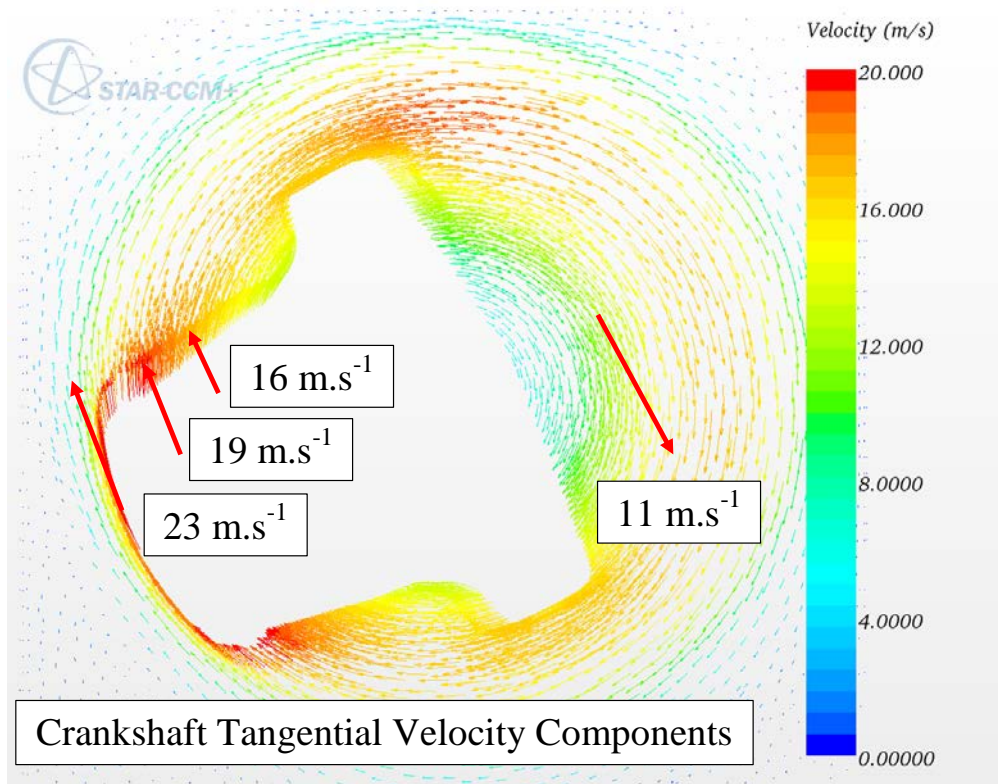
Figure 6.33 Crankshaft CFD at 2200 rpm including crankshaft tangential velocity components

The boundary layer at the outer edge of the crankshaft in Figure 6.33 is 10 mm thick. Oil ligament generation in this region was significant but from the model we can see that the velocity of the flow quickly drops as the ligament moves out radially from the crankshaft centre. At the other tested engine speeds there was continued good agreement between the CFD velocities and the tangential velocity components. Consequently the overall vector magnitude reduced with engine speed.
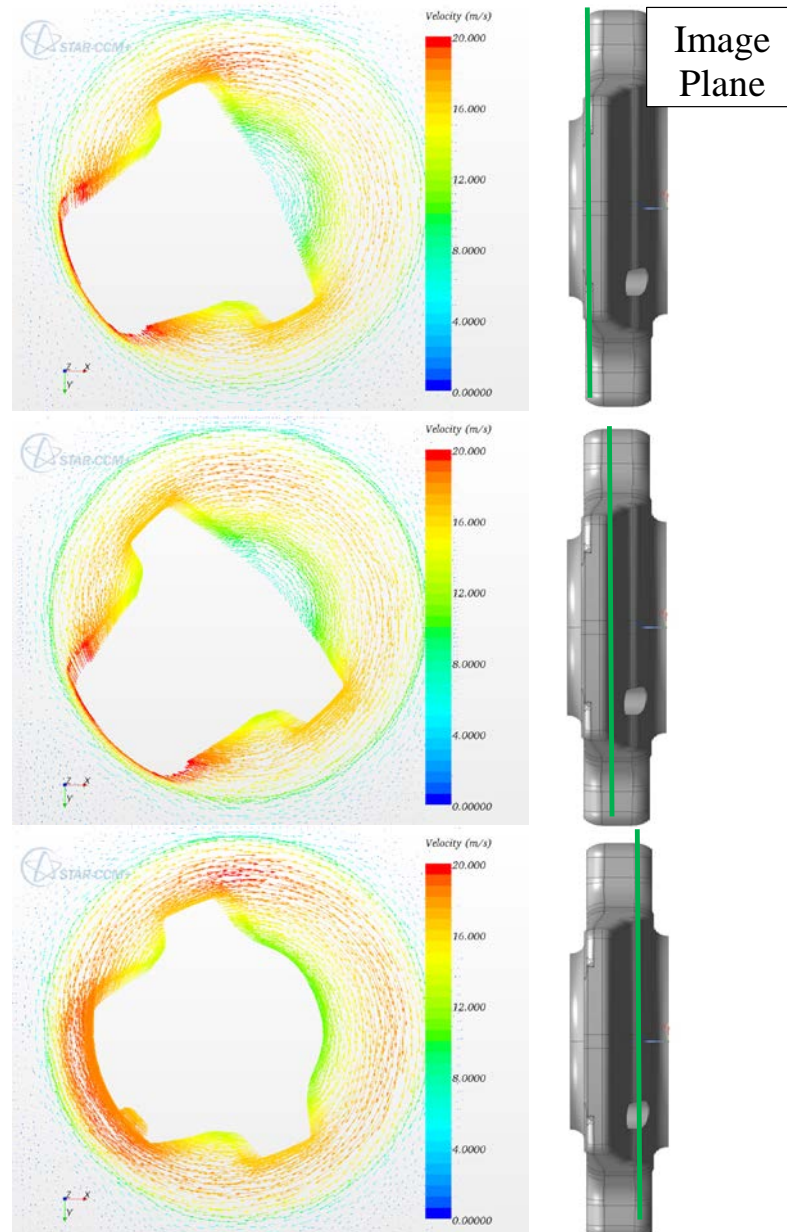
Figure 6.34 Crankshaft CFD at 2200 rpm for three axial planes over the crankshaft surface

To examine all the velocity components and the three-dimensional nature of the flow that was highlighted in Section 6.6, the velocity vectors were examined in three planes over the crankshaft surface as denoted in Table 6.5. The resulting vector fields at 2200 rpm are displayed in Figure 6.34. Examining the three planes again shows excellent correlation of the tangential velocity components calculated in Section 6.6 and the CFD results within the boundary layer close to the crankshaft surface.

From the results summarised in Figure 6.31, radial and axial velocity components caused by viscous pumping over the crankshaft surface were expected. In Figure 6.35 small magnitude $1 - 2$ m.s^{-1} radial velocity components were present between the crankshaft and the left side of the flow domain wall as the crankshaft approached. The radial and axial velocities were examined further using streamline plots, a representative plot at 1000 rpm is displayed in Figure 6.36. At 1000 rpm radial velocity components peaking at 1.3 m.s^{-1}, were present around the leading edge of the crankshaft lobe, with decreasing radial velocity over the crankshaft circumference. The streamline plot in Figure 6.36 shows that although the velocities are low a complex flow structure is present between the crankshaft circumference, the wall of the flow domain and the outlet.
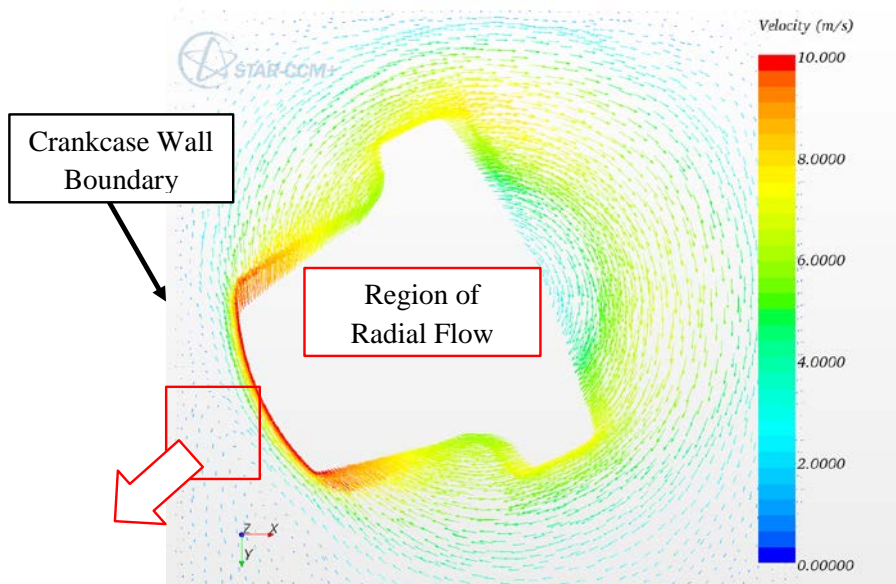
Figure 6.35 Crankshaft CFD at 1000 rpm highlighting small radial velocity components

Radial Velocity (m/s)

-1.5447   -0.98112   -0.41759   0.14594   0.70947   1.2730
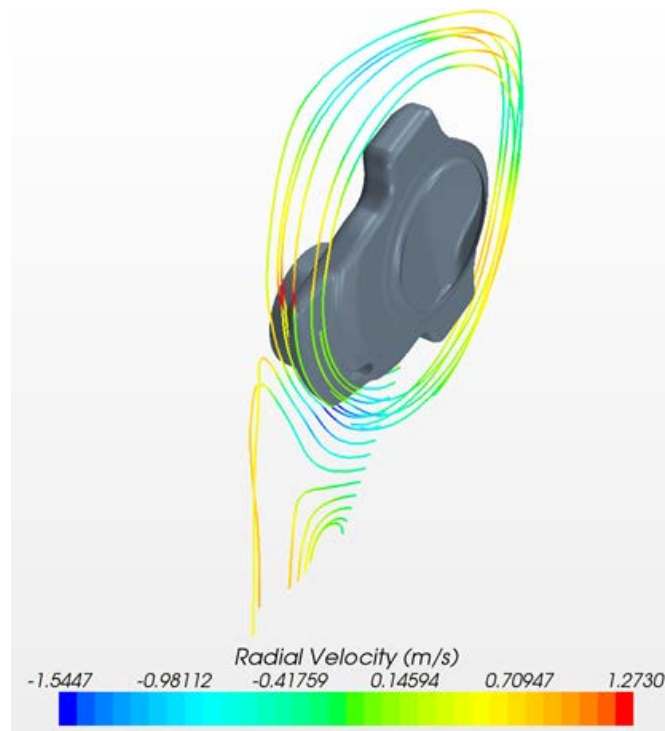
Figure 6.36 CFD streamlines of crankshaft radial flow at 1000 rpm

6.7.2 Crankshaft CFD Discussion

Computation Fluid Dynamics was utilised to enhance the understanding of the crankshaft flow. Correlation of the CFD model with the simple tangential velocity components in the boundary layer near the crankshaft surface, showed good agreement. Comprehensive work by Edelbauer (2007), Edelbauer, Kratochwill, Brenn and Tatschl (2009), Edelbauer, Diemath, Kratochwill and Brenn (2010) provides a thorough mathematical and computational model of crankcase flow. It should be noted that the authors acknowledge the complexity of modelling crankcase flows, and thus, a fully validated solution was not achieved.

Full computation model validation requires identical boundary conditions between the computational model and the experimental setup. Modelling the full crankcase architecture was beyond the objective of this computational study. A simple CFD model was developed to enhance the understanding of crankshaft oil ligament breakup and drop generation. The model has indicated the magnitude of the tangential, radial and axial velocity components that are expected within the boundary layer close to the crankshaft surface. The thorough experimental

investigation described in the next section was required, as it provided novel measurement and quantification of the crankcase flow velocities present in a real motored engine.

6.8 HSDPIV Analysis of Crankcase Flow

Vector fields were generated for all the test conditions described in Table 6.4 and Table 6.5, to provide a thorough measurement of the crankshaft flow at various engine speeds over the crankshaft surface. The valuable information gained from this analysis is discussed and critical vector fields are displayed. As concluded from the oil ligament generation in Section 6.5 and the mathematical analysis in Section 6.6, the main flow regions that affect crankshaft oil aerosol generation were at the periphery of the crankshaft.

HSDPIV vector fields at 1500 rpm and 2200 rpm are displayed in Figure 6.37 and Figure 6.38. Vector fields in front of the crankshaft and whilst the crankshaft passes through the field of view are displayed.

Initially ahead of the crankshaft there is a smooth uniform flow field moving vertical upwards. The flow well ahead of the crankshaft is stable with minimal velocity fluctuations. As expected and witnessed in all the vector fields in Figure 6.37, the velocity magnitudes are higher at elevated engine speeds. When the crankshaft enters the image it pushes the flow ahead of the crankshaft, and the flow close to the crankshaft edge is pushed tangentially with the crankshaft motion. The flow over the crankshaft periphery is forced radially outwards. The large tangential velocity components that were expected within the boundary layer close to the crankshaft edge were not captured until the crankshaft had rotated further through the field of view. At the trailing edge of the crankshaft and behind the crankshaft lobe the vector fields show high tangential velocity components following the crankshaft rotation.
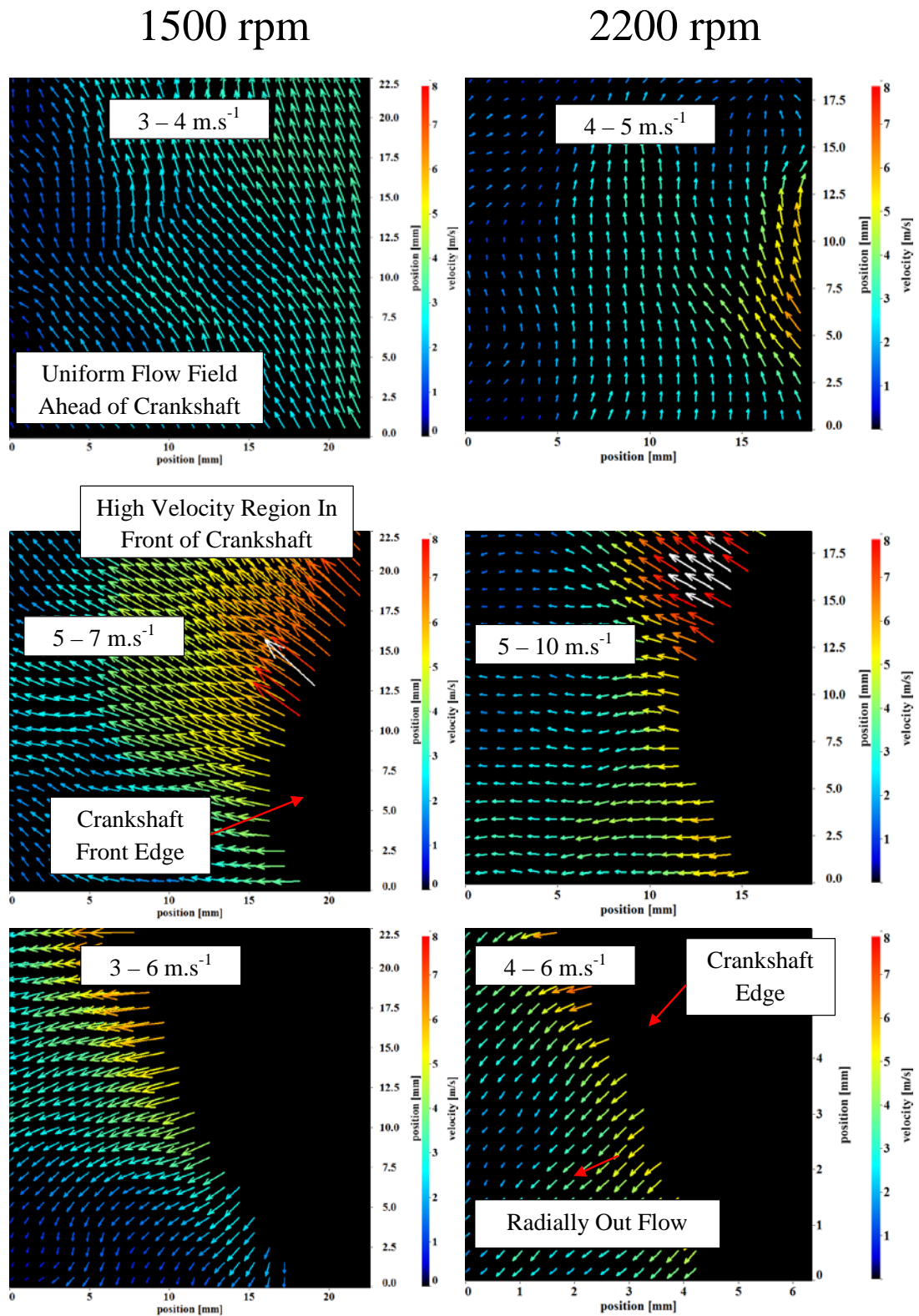
Figure 6.37 HSDPIV vector plots at 1500 rpm and 2200 rpm at various crank angle positions
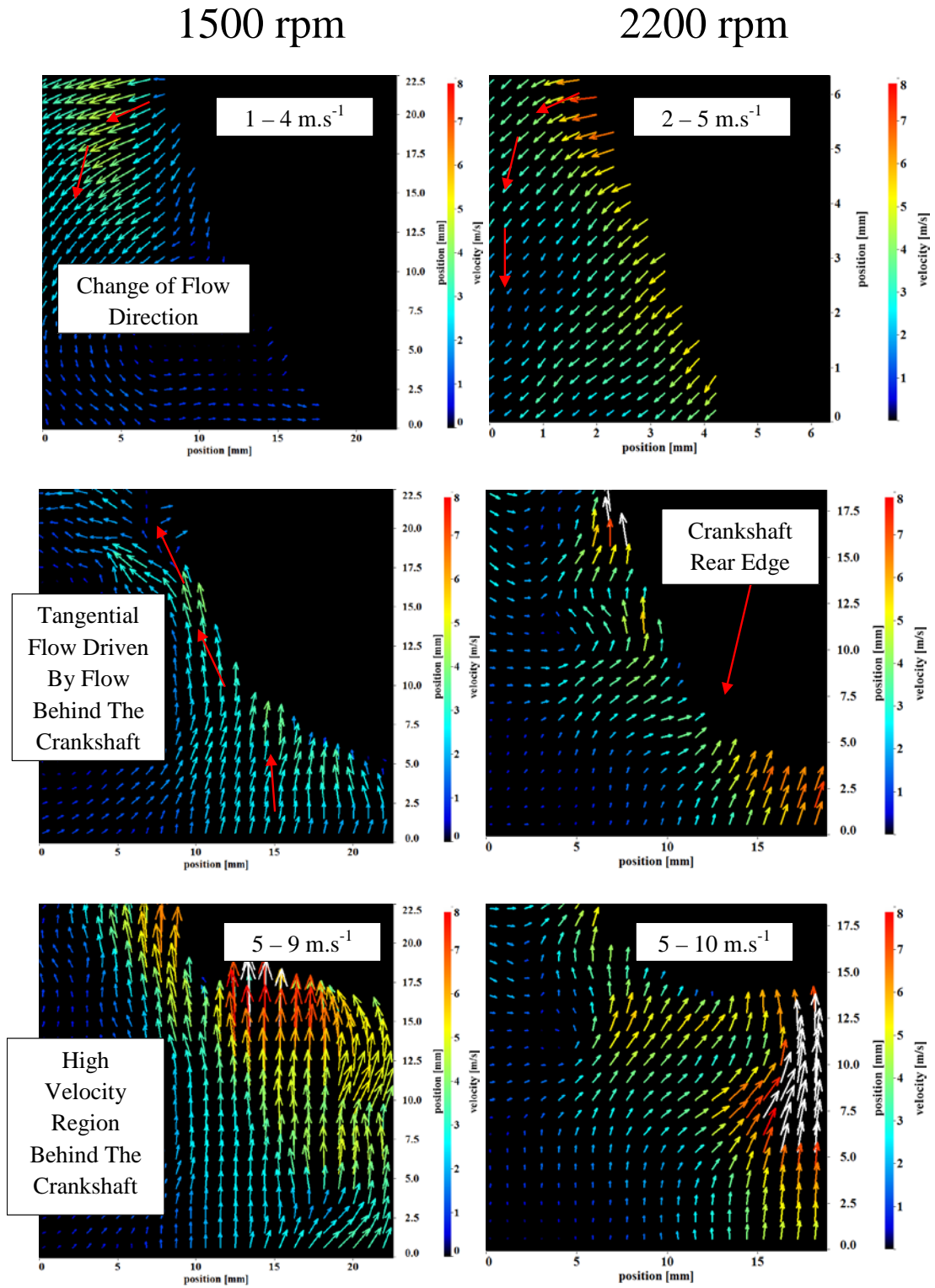
1500 rpm   2200 rpm

Figure 6.38 PIV vector plots at 1500 rpm and 2200 rpm at various crank angle positions
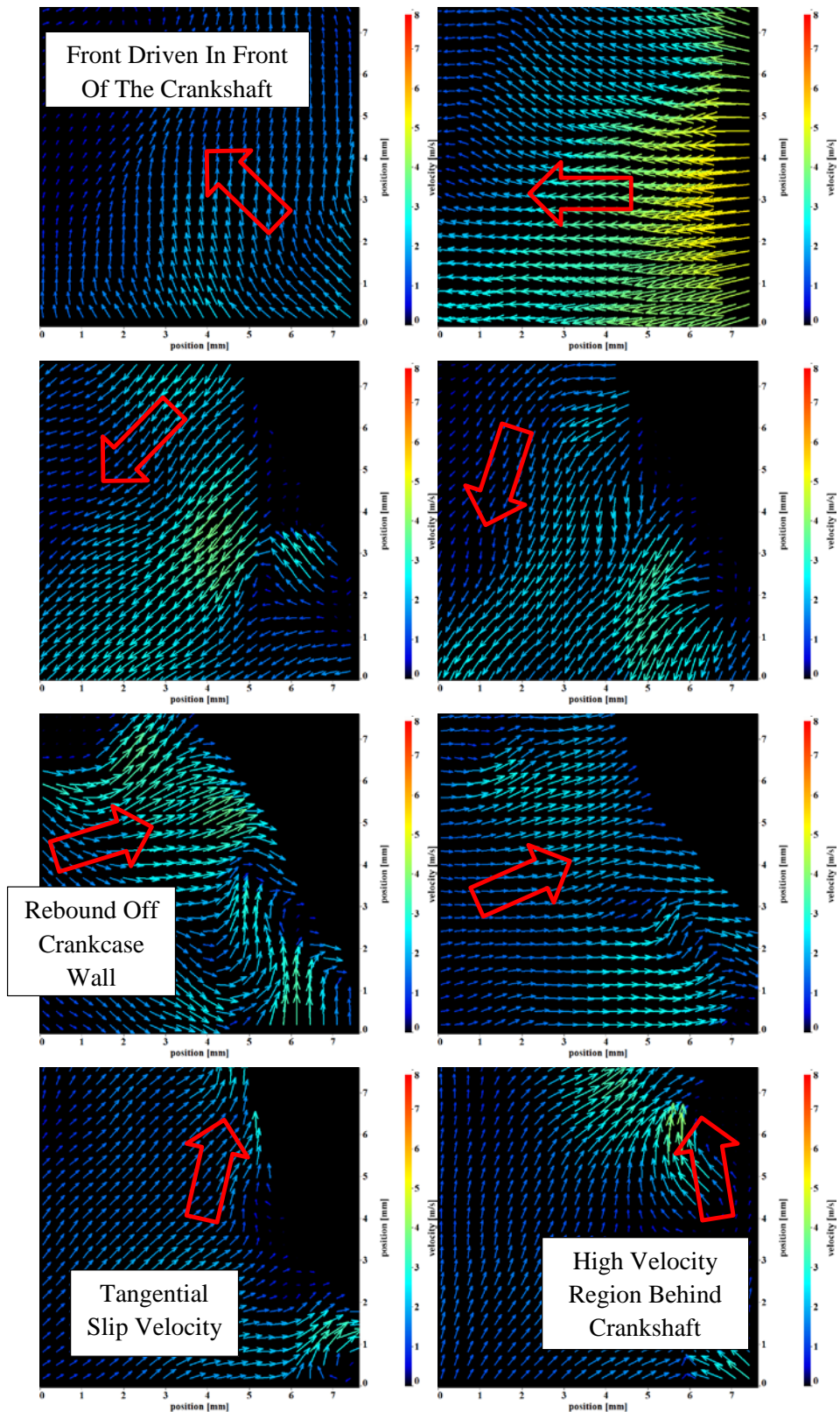
Figure 6.39 Small scale PIV flow at 1500 rpm over the crankshaft event

Images in Figure 6.39 display vector fields of the crankshaft flow over a smaller 8 mm x 8 mm image region at 2200 rpm. The same flow patterns as those witnessed over a larger image region were evident, however, the radial velocity components generated following the crankshaft approach are more apparent. The flow moves radially outwards from the leading edge of the crankshaft. As the crankshaft progressed through the image region the radial flow appears to rebound and move radially inwards towards the boundary layer close to the crankshaft edge. Tangential velocity components were again present towards the trailing edge of the crankshaft and behind the crankshaft lobe.

Within a boundary layer 1 mm from the crankshaft edge the vector fields were not uniform due to loss of seeding particles consequently making it hard to resolve the flow field in this region. From the modelling in the Section 6.7 it was expected that the flow in this region was composed of high tangential velocity components matching the velocity of the crankshaft. The boundary layers thickness in this region on the CFD model was much thicker at 10 mm. It is hypothesised that the small 2 mm boundary layer thickness and the lack of strong tangential velocity components in the PIV was caused by particles moving out of the interrogation region.

The flow away from the crankshaft edge was also examined in detail. Once the crankshaft passed through the image region a high velocity region remained behind the crankshaft. Figure 6.40 shows the boundary layer present behind the crankshaft that splits a high velocity flow region generated by the tangential velocity of the crankshaft and the low velocity free stream flow in the surrounding crankcase. The boundary layer was clearly present both behind and ahead of the crankshaft lobe for 90° CA of the crankshaft rotation. 180° CA after the crankshaft passed through the image region the boundary layer was less apparent as the difference between the crankshaft flow and the free stream velocities was smaller. The clear presence of the boundary layer was captured in both the PIV and CFD results at all engine speeds, however, the PIV results showed lower velocity magnitudes than predicted by the CFD.
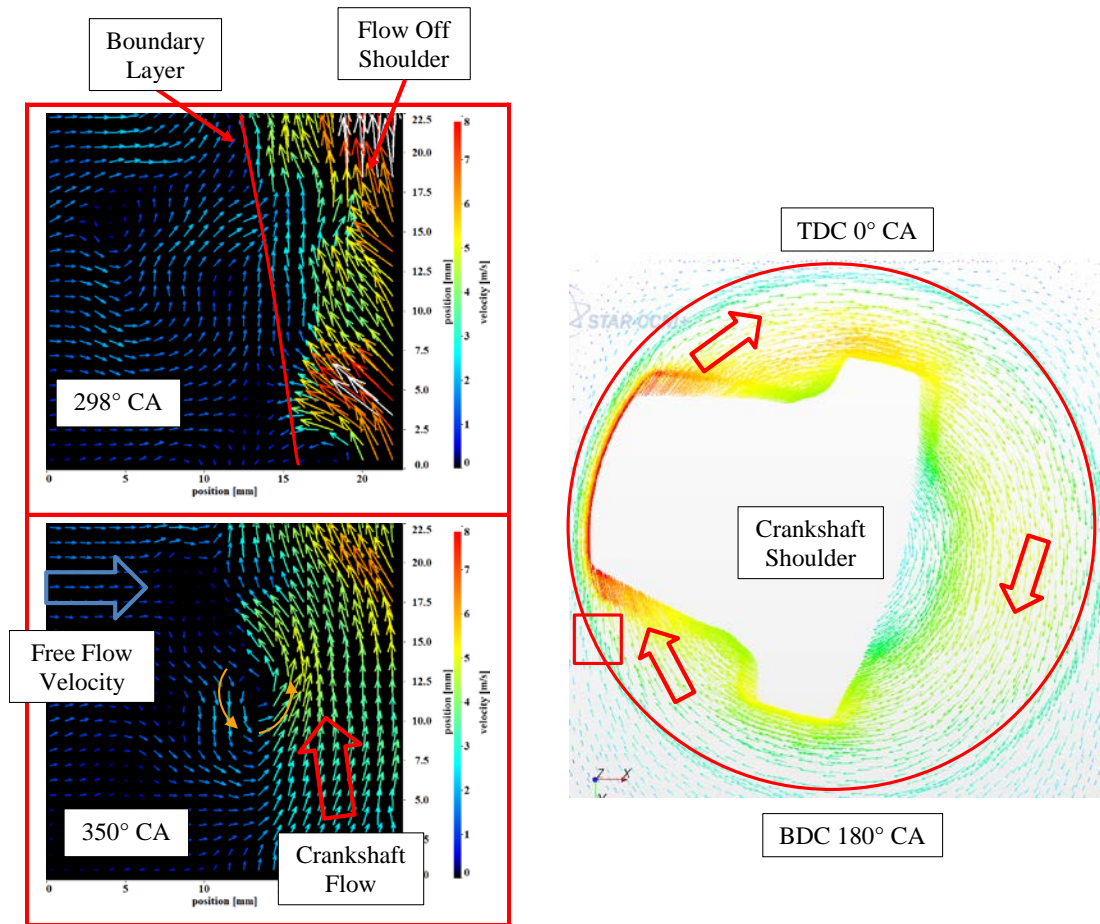
Figure 6.40 Crankshaft flow following the crankshaft at 1500 rpm

6.8.1 HSDPIV Discussion

The HSDPIV investigation of the flow around the crankshaft has captured some of the complex flow structure present. The combination of experimental and computational data has quantified the range of flow velocities expected around the crankshaft, from the periphery of the crankshaft where ligament atomisation occurs, to 180° CA after the crankshaft has passed through the image region. The Weber numbers of the drops generated are calculated using the measured and calculated flow velocities in Section 6.8.2.

Difficulties in maintaining an appropriate frame separation over the boundary layer closer to the crankshaft edge prevented capture of a vector field close to the edge of the crankshaft. The experimental investigation has produced valuable novel results

illustrating the complex flow around a crankshaft and the interaction between the flow and the crankcase walls.

6.8.2 Oil Drop Transport

Ligament generation and atomisation is discussed in Section 6.5, drops d_p = 10 - 450 μm were generated by the crankshaft. Considering crankshaft speeds of 1500 and 2200 rpm, the range of measured and calculated velocities present around the crankshaft ranged from $4 – 23$ m.s^{-1}. A series of high resolution images around the crankshaft are displayed in Figure 6.41, they illustrate that when oil is constantly supplied to the crankshaft the oil atomisation is significant and a large number concentration of drops are generated. The images displayed in Figure 6.41 correlated well with the results collected in Section 4.6 where the large number concentration of oil drops generated by the crankshaft were transported up into the rocker cover.
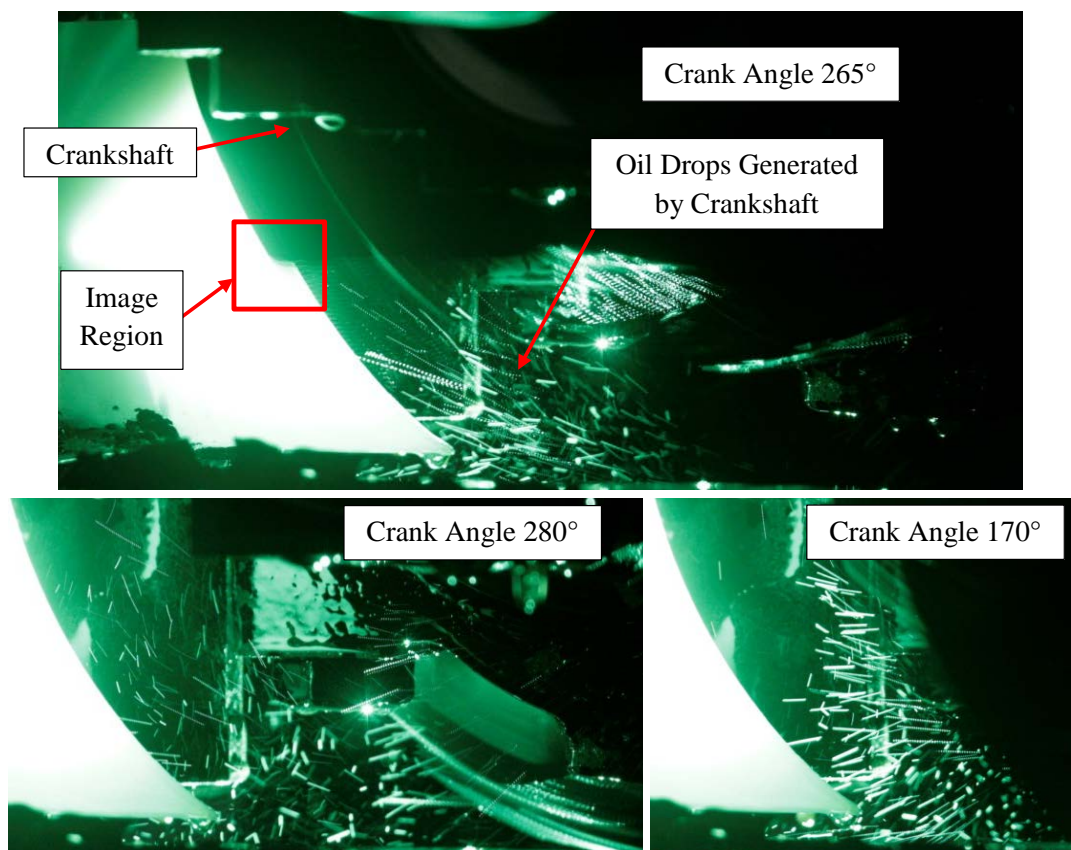
Figure 6.41 High resolution images of 1104C-44 crankshaft oil atomisation

High speed images were collected of the oil drops transported around the crankshaft using the previous imaging setup shown in Figure 6.6. The diffraction limited spot size of the imaging setup used to captured the oil drops was 10 μm, any drops smaller than this would appear to be 10 μm in the high speed images. The diameter of the oil drops generated at 1500 rpm, which were present in the image region from 273° CA through to the crankshaft approach again at 218° CA, are plotted in Figure 6.42.
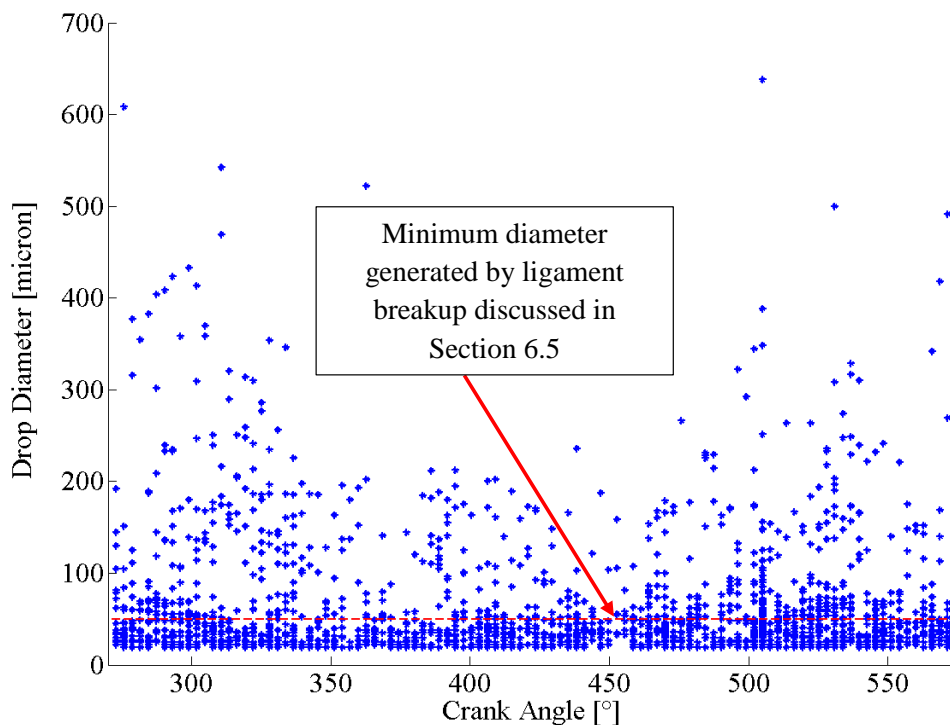
Figure 6.42 Oil drops generated around the crankshaft at 1500 rpm

From studying the images and Figure 6.42, it is clear that a range of oil drop diameters are present around the crankshaft. Drops ranging from $d_p = 10 - 700$ μm were captured, this shows good agreement with the results in Section 6.5. It is expected that smaller satellite drops are generated by ligament breakup but their diameters could not be resolved below 10 μm.

Smaller $d_p < 50$ μm oil drops were present in much higher numbers in Figure 6.42 compared to the results in Section 6.5. As oil was only supplied to the crankshaft journal bearings an additional oil atomisation source is not likely. The generation of additional small drops can be attributed to two main factors. Firstly oil ligament

generation occurs throughout the crankshaft rotation not just around the image region, as shown in Figure 6.41. The small oil drops will be more stable and therefore transported in the high velocity flow boundary around the crankshaft. Secondly secondary atomisation of large oil drops by the high velocity crankshaft flow may generate small drops.

Secondary oil drop breakup was examined further to explain the occurrence of the smaller $d_p < 50$ μm oil drops. Considering crankshaft speeds of 1500 and 2200 rpm, the range of measured and calculated velocities present around the crankshaft ranged from $4 - 23$ m.s^{-1}. In an identical manner to that presented in Section 4.3.2, Equation (2.11) was used to calculate the critical aerodynamic Weber number for drop breakup to occur in a low Reynolds number flow. The Reynolds number and drop drag coefficient were calculated using Equation (2.13) and the approximations listed in Appendix C Table C-1.1. Again it is important to remember that the Reynolds number was calculated using the air density and dynamic viscosity at 70°C, ρ_a and η_a respectively. The aerodynamic Weber number was calculated using Equation (2.9).

Once the drop drag coefficient and therefore critical aerodynamic Weber number were known, the aerodynamic Weber number was calculated for the range of measured oil drop diameters and crankshaft flow velocities, the results are displayed in Table 6.6

Table 6.6 Aerodynamic Weber numbers of crankshaft atomised oil drops

d_p [μm]	Drop Velocity, U_R [m.s^{-1}]	$We_{Aero,Crit}$	We_{Aero}	Air Flow Re
50	4	1.85	0.03	9.76
50	23	5.43	0.86	56.14
450	4	6.28	0.23	87.87
450	23	**7.64**	**7.70**	505.23
700	4	6.81	0.36	136.68
700	23	7.76	11.97	785.91

The aerodynamic Weber number was only sufficient for secondary breakup of $d_p > 450\,\mu\text{m}$ oil drops travelling within the boundary layer at the crankshaft periphery at 2200 rpm. Secondary breakup of large drops in high velocity flow boundary around the crankshaft is a potential cause of the additional number of oil drops $d_p < 50\,\mu\text{m}$.

The images analysed for the plot in Figure 6.42 also showed good agreement with the HSDPIV data presented earlier in Section 6.8, as the oil drops acted as seeding tracing the crankcase flow. The notable similarities between the drop motion and the HSDPIV were as follows; drops were pushed tangentially ahead of the crankshaft as it approached the image region, there was significant inwards radial motion of the oil drops $180°$ CA after the crankshaft event, the bulk of the flow following the crankshaft passing through the image region was vertically upwards.

6.9 Control of Crankshaft Oil Atomisation

The characterisation of crankshaft oil atomisation presented in this chapter has provided valuable information to modellers and engineers. What is critical to engine manufactures is how this fundamental physical information can be utilised to regulate crankcase oil aerosol emissions. The primary breakup of oil ligaments and their transport in the complex three-dimensional flow around the crankshaft, generated a substantial number of oil drops as witnessed in Chapter 4 and throughout this chapter. High speed images in Section 6.5 showed that the drop breakup occurred a repeatable distance away from the crankshaft surface. Recognising the impaction behaviour of oil drops as discussed in Section 4.4.2, an initial investigation was conducted into the performance of an oil shield. The oil shield was designed to force coalescence of the crankshaft oil ligaments before atomisation. The initial investigation presented below explores the validity of an oil shield to directly reduce crankcase oil aerosol emissions.

6.9.1   Crankshaft Oil Shield

The precise details of the design are owned by IPSD, and thus, remain confidential. The oil shield was positioned a fixed distance from the crankshaft periphery as shown in Figure 6.43and Figure 6.44.
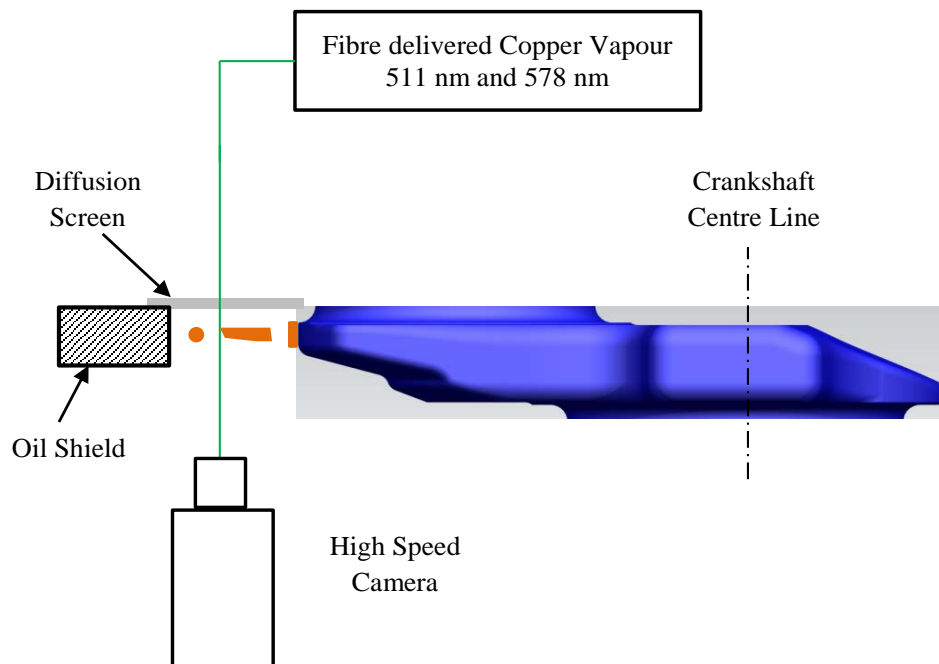
Figure 6.43 Optical schematic for crankshaft imaging
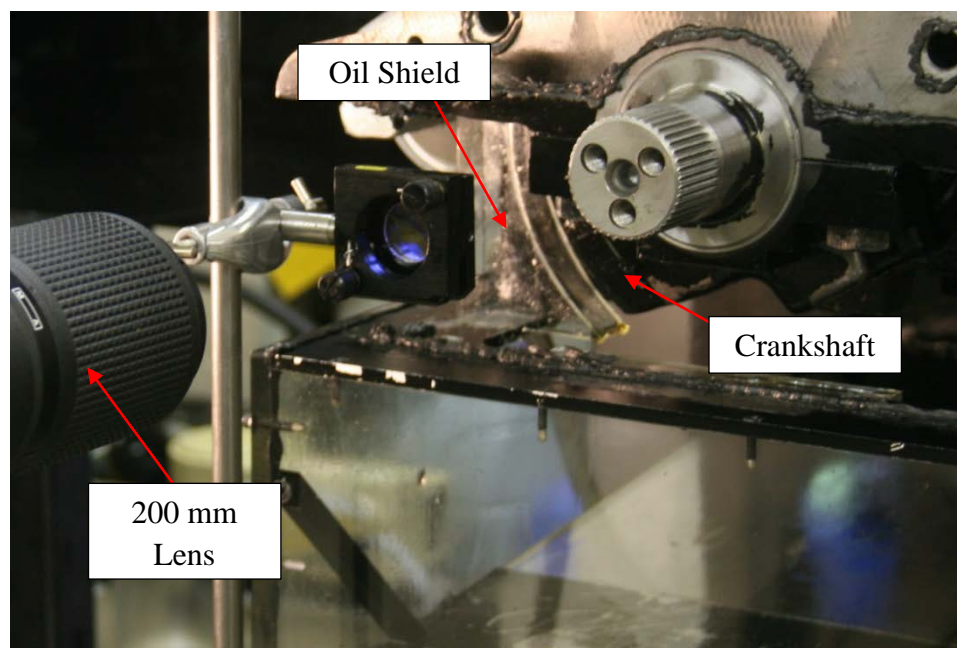
Figure 6.44 Crankshaft imaging setup

Spacing between the crankshaft and the oil shield was selected to ensure that the high tangential velocity of the crankshaft did not atomise any oil present on the oil shield. Conversely, the shield spacing was chosen to ensure that the oil ligaments would impact onto the surface and coalesce before ligament breakup occurred. The process of drop coalescence is displayed in Figure 4.40.

Although ligament breakup and oil atomisation will occur over the whole crankshaft rotation, the oil shield was positioned in the image region used throughout the experimental investigation listed in this chapter. Additionally, drops generated on this left side of the crankcase are closest to the camshaft channel and therefore have the shortest flow path to reach the pushrod galleries and subsequently be transported out of the crankcase. Consequently drop removal in this region of the crankcase should have a notable effect on the crankcase oil aerosol emissions.

An identical experimental setup to that described in Section 6.3 was employed, however, production oil pressures were used to replicate the oil films present on the crankshaft in a fired engine. Again an oil temperature of 80°C was used for all tests. An oil film was generated on the oil shield using a simple oil feed taken from the camshaft channel journal bearing, which was previously blocked.

A copper vapour laser $\lambda = 511$ and 578 nm was used to illumination the oil, a schematic and image of the optical setup used to image around the oil shield are displayed in Figure 6.43 and Figure 6.44.

6.9.2   Crankshaft Oil Shield Results

Crankshaft oil atomisation and the behaviour of the oil shield have been analysed using sequenced high speed images captured at 3000 fps. The crankshaft event at 1800 rpm is displayed in Figure 6.45. When comparing these images to those collected in Section 6.5, it is clear that the larger amount of oil on the crankshaft edge is forced into a series of complex oil ligaments, sheets and drops. Oil ligaments moved radially outwards from the leading edge of the crankshaft. Further down the crankshaft edge in Figure 6.45, $a_L = 85$ μm ligaments are drawn tangentially over the crankshaft surface due to the high flow velocity in the crankshaft boundary layer. The oil shield was positioned a sufficient distance from the crankshaft for the ligaments to coalescence into the 3 mm oil film coating the oil shield.
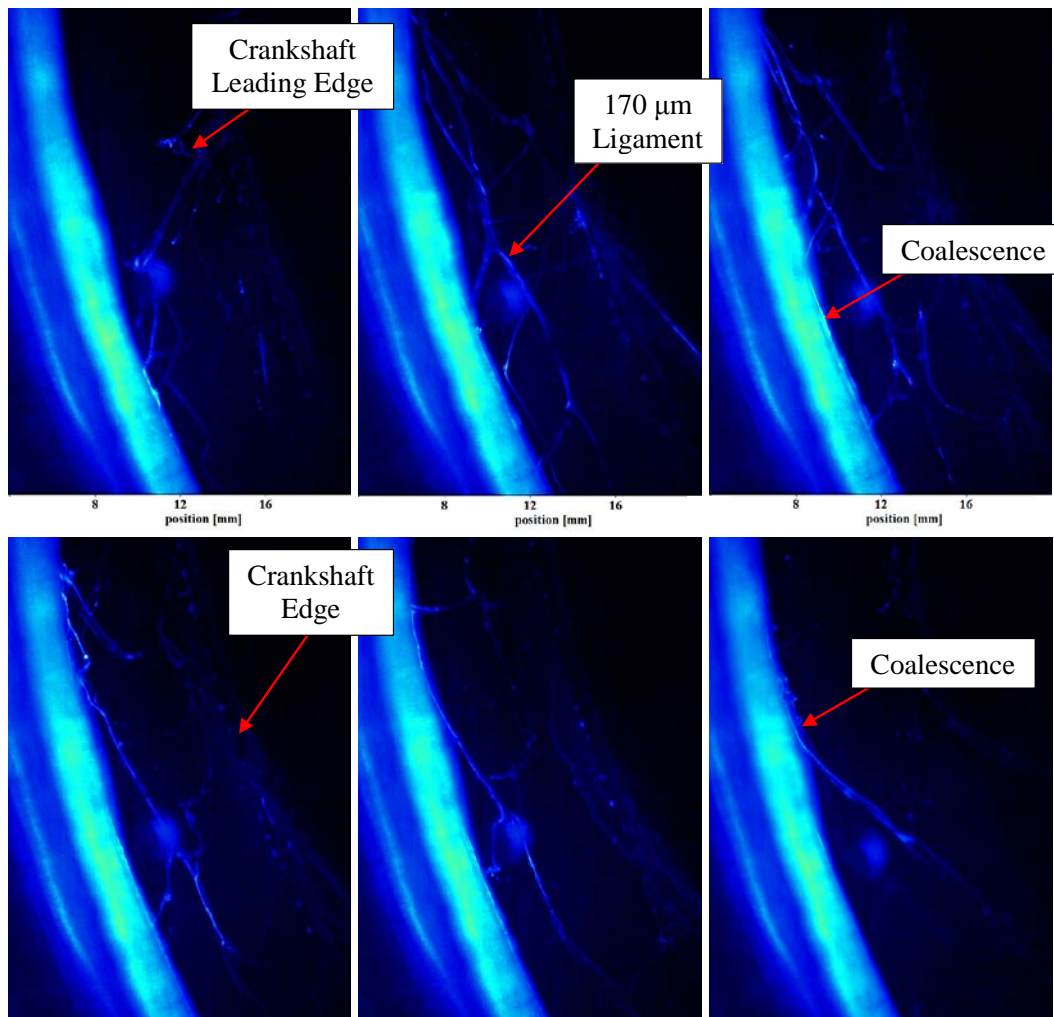
Figure 6.45 Crankshaft oil atomisation control at 1800 rpm

Another crankshaft event is displayed in Figure 6.46, where a large "spider" volume of oil was generated in front of the crankshaft before the crankshaft event. During the crankshaft event the oil ligaments and sheets coagulated with the oil thrown ahead of the crankshaft. The large volume of oil contained twisted ligaments and sheets similar to those witnessed in Section 4.5.1, when imaging in the rocker cover. Breakup of these ligaments and sheets is complex and generates a range of drop diameters with high angular velocity. The total oil volume coagulated and after 11 ms or 120° CA the surface tension and viscosity of the oil was sufficient for the oil volume to coalesce into the oil film. The results in this chapter and Chapter 4 show that without the oil shield a large number and size range of oils drop would have been generated.
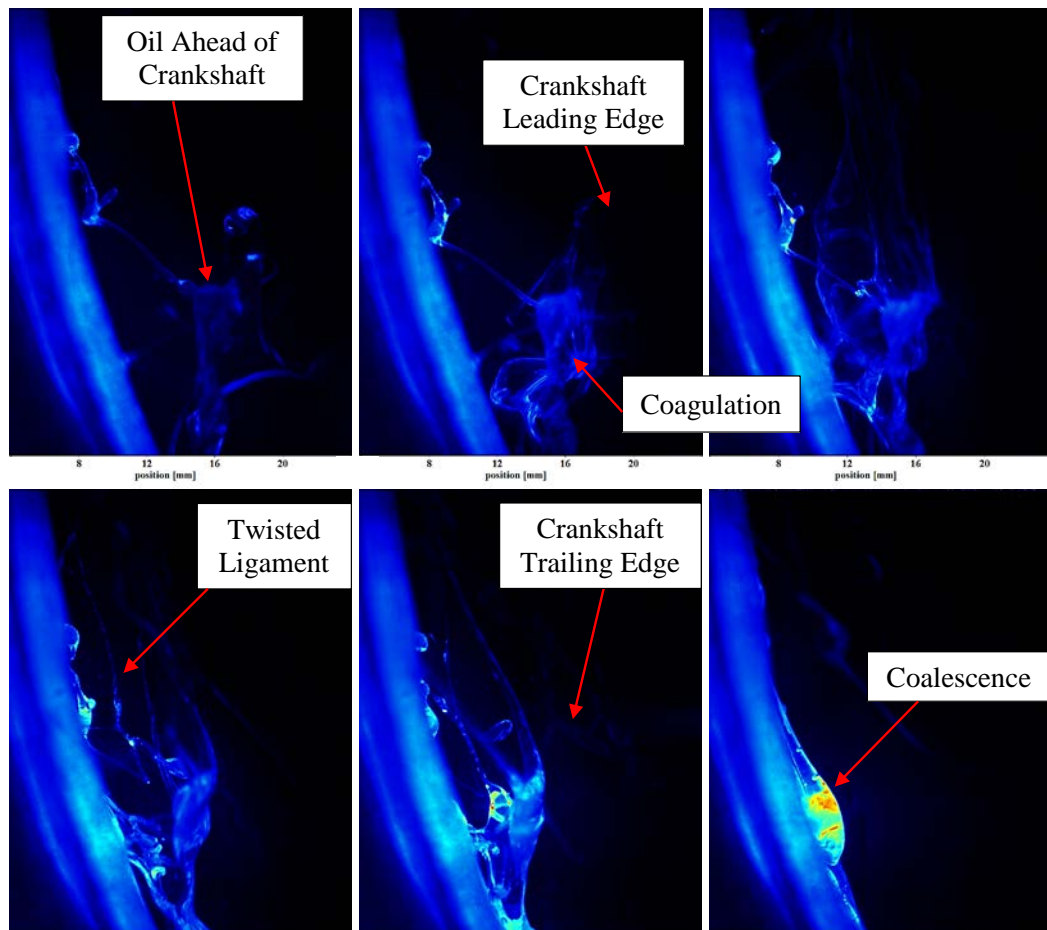
Figure 6.46 Crankshaft oil atomisation control at 1800 rpm
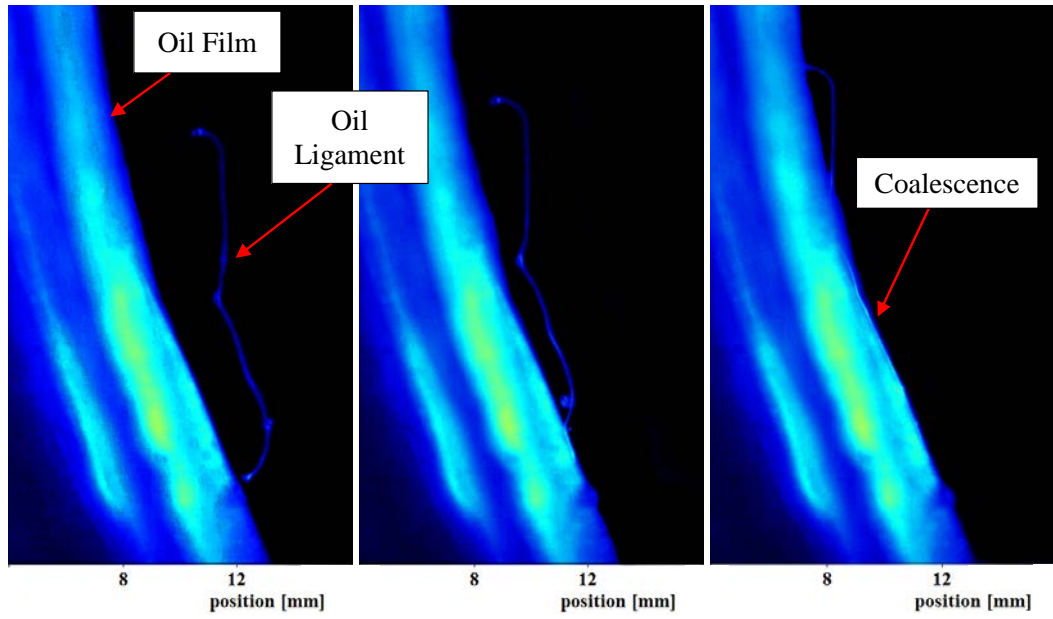
Figure 6.47 Oil ligament generation and coalescence 30° CA ahead of the crankshaft at 1800 rpm
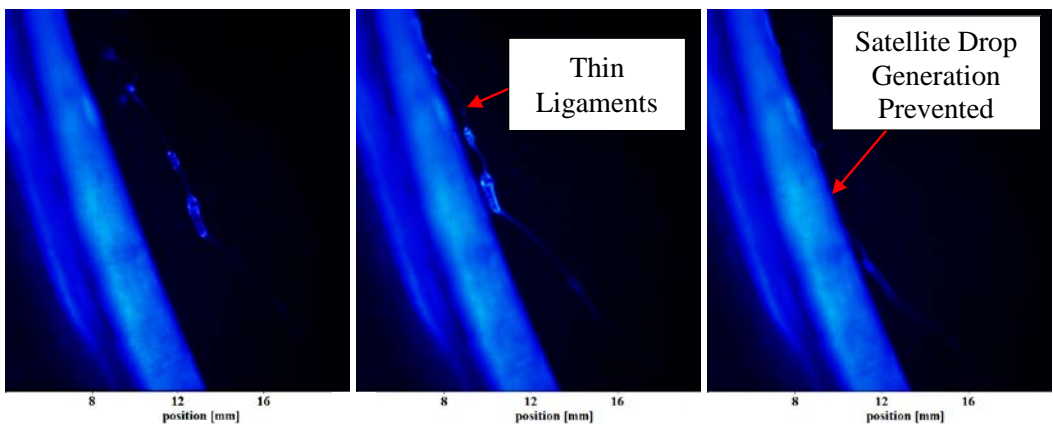
Figure 6.48 Oil ligament generation and coalescence 30° CA ahead of the crankshaft at 1800 rpm
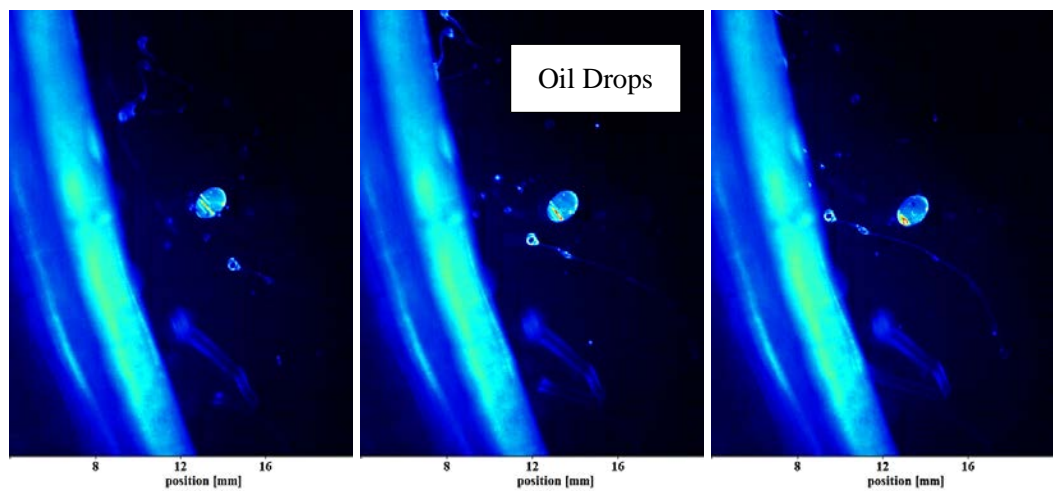
Figure 6.49 Oil drops 30° CA ahead of the crankshaft at 1800 rpm

Critical to the events witnessed in Figure 6.46 was the presence of a large bulk of oil before the crankshaft passed into view. This oil distribution was not examined in Section 6.5. Images in Figure 6.47, Figure 6.48 and Figure 6.49 display the ligaments and oil drops thrown ahead of the crankshaft. The atomisation of oil at additional points throughout the crankshaft rotation helps to explain the presence of drops $d_p < 50$ μm in Figure 6.42. The sequence of images in Figure 6.47, Figure 6.48 and Figure 6.49 were collected 30° CA before the crankshaft event when oil drops and ligaments where consistently present.

In Figure 6.47 a $a_L = 84$ μm oil ligament is thrown ahead of the crankshaft, it is likely that the ligament originated from the shoulder of the crankshaft. The 12 mm long ligament moved radially outwards through the image and once it impacted onto the oil film was removed from the crankcase flow in 1 ms.

Again in Figure 6.48 a thin $a_L = 28$ μm ligament joins multiple oil drops with an approximate width of 450 μm. Previous experimental data has shown that the breakup of thin oil ligaments connecting large volumes of oil would have been eminent if the oil shield was not present. Breakup of the thin connecting oil ligaments would have generated small satellite oil drops.

The oil distribution in Figure 6.49 is very different despite the crank angle still being 30° CA before the crankshaft event. The oil drops have already been generated, presumably from ligament breakup, as this is occurring throughout the crankshaft rotation. Despite atomisation having occurred, the drops exhibited the characteristic motion and moved radially outwards in the crankshaft flow. The shield continued to perform well, as the oil drops impacted on the oil film and were removed from the crankcase aerosol.

The oil distribution was captured at a series of different crank angle positions in Figure 6.50 and Figure 6.51. These images illustrate the complex and variable behaviour of the oil ligaments, and highlight that with production oil film levels the crankshaft oil atomisation process is amplified. The ligament generation and breakup process remains, but it is exaggerated as more ligaments and drops are generated, not only during the crankshaft event, but throughout the crankshaft rotation. The oil was

also thrown as thin sheets from the crankshaft. The sheets were difficult to resolve in the high speed images, but they illustrated the effect of increasing the oil volume. Figure 6.50 captures the oil ligaments and sheets drawn behind the crankshaft. Although the oil ligament geometry was varied, the oil sheets and ligaments consistently coagulated with each other and coalesced into the oil film on the oil shield.
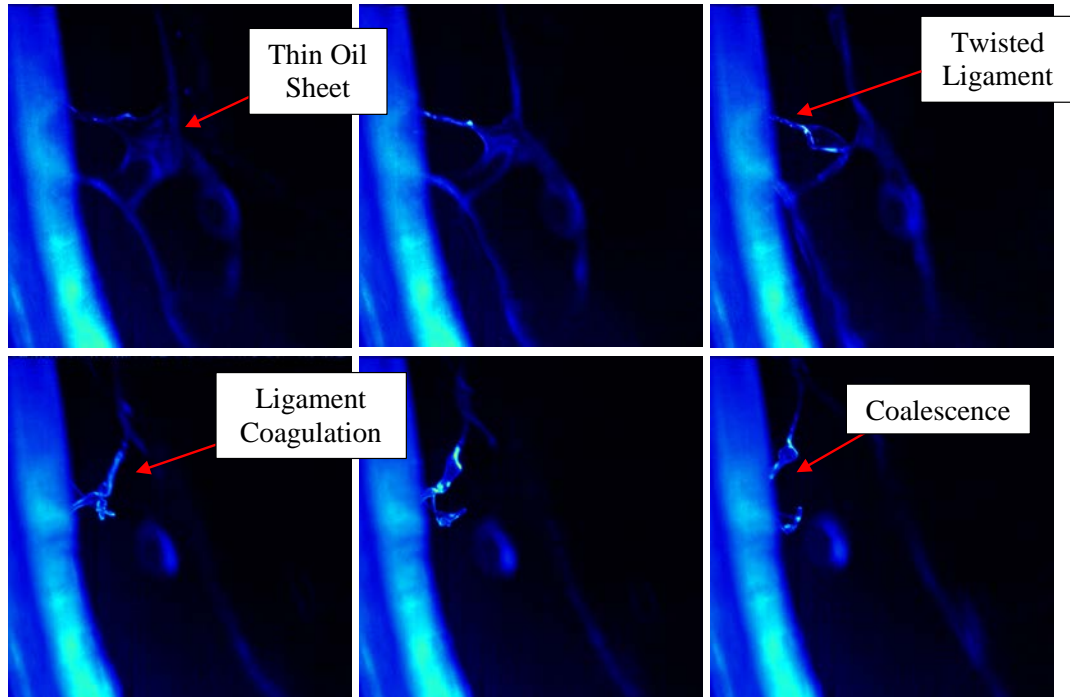
Figure 6.50 Oil ligament coagulation 3° CA after crankshaft event at 1800 rpm
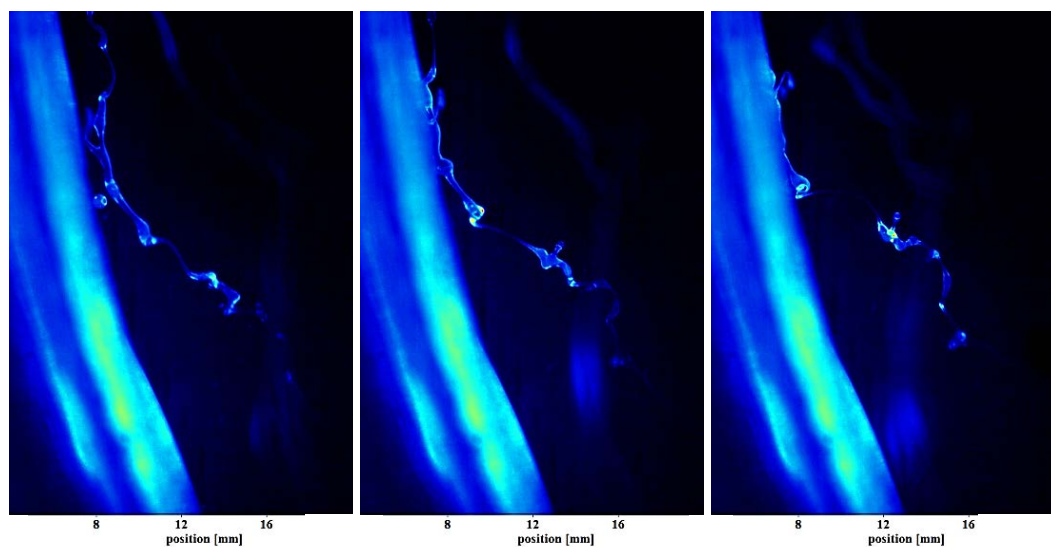
Figure 6.51 Oil ligament generation and coalescence 90° CA after the crankshaft event at 1800 rpm

Figure 6.51 shows generation of oil ligaments and drops after the crankshaft event, the oil shield continues to fulfil its purpose and remove them from the crankcase flow. The large $a_L = 175$ μm oil ligament was generated 90° CA after the crankshaft passed through the image region, i.e. at TDC. From examining the high speed images prior to the crankshaft event, it is clear that this thicker oil ligament was generated by a large volume of oil being thrown off the crankshaft surface not the edge of the crankshaft. The oil volume coagulates into the thick ligament displayed in Figure 6.51.

6.9.3 Crankshaft Oil Atomisation Discussion

A large number of high speed images have been presented illustrating not only the oil ligament and drop generation at 1800 rpm, but also the success of an oil shield to minimise and prevent the generation of oil drops from the crankshaft. With the higher oil volume present on the crankshaft the oil atomisation was significant, occurring not just at the crankshaft edge but throughout the crankshaft rotation. The amplified crankshaft oil atomisation witnessed reinforces the requirement for direct control of this significant contributor to oil aerosol generation.

In this initial investigation no ejection or atomisation from the oil film on the oil shield was witnessed. The oil shield performed excellently at the tested conditions, oil ligaments generated by the crankshaft throughout the crankshaft rotation were consistently removed from the crankcase flow.

6.10 Concluding Remarks

A range of powerful optical and computational diagnostics techniques have been successfully employed to collect a wealth of experimental and computation data. The intensive data analysis has characterised crankshaft oil atomisation, which was highlighted as a significant contributor to crankcase oil aerosol generation. The knowledge and understanding gained from achieving the experimental objectives, has highlighted the potential for controlling and reducing the crankshaft oil aerosol generation at source. This initial investigation has illustrated the huge potential of an oil shield to control crankcase oil aerosol emissions. The data collected provides a solid foundation for further experimental validation.

CHAPTER 7

CONCLUSIONS AND RECOMMENDATIONS FOR FURTHER WORK

7.1   Research Summary

The work presented in this thesis has addressed the requirement for a better understanding of crankcase oil aerosol generation. The specific objectives of this experimental research are outlined in Section 1.7, as a consequence of achieving these objectives a series of valuable conclusions have been drawn, they are listed in the next section.

Visualisation of the oil aerosol generation and oil distribution within the crankcase of a motored engine, at a range of representative engine conditions, has provided novel and extremely valuable information. Major contributors to crankcase oil aerosol generation have been identified throughout the entire crankcase volume. Data has helped to identify simple but effective design rules to provide better management of oil aerosol generation and oil drainage.

A thorough particle sampling study, on both a fired and motored engine crankcase, has delivered valuable insight into the generation and behaviour of the complex submicron emissions. The isolated contribution of the lubricating oil to this emission size range has been quantified. The breadth of the results obtained illustrate the complex thermal processes generating the submicron oil aerosol emissions. The conclusions drawn offer direction to future research, as they illustrate that more control of this problematic emission species can be achieved within the crankcase itself provided the temperature, pressure and condensation sites are controlled.

The compilation of multiple experimental investigations showed that a reduction in crankcase oil aerosol emissions can be achieved by reducing crankshaft oil atomisation. Detailed characterisation of the oil aerosol generation and transport on an optically accessed motored engine demonstrated that an oil shield around the crankshaft has excellent potential to control crankcase emissions. This hypothesis was supported by experimental testing, fulfilling the desired objective of providing recommendations to control crankcase oil aerosol emissions at source.

Finally, images capturing crankcase oil atomisation and distribution have been used to access the feasibility of using computation fluid dynamics to predict oil

atomisation. A two-dimensional, volume of fluid, computational fluid dynamics model was able to predict rocker oil distribution and oil ligament breakup.

7.2 Conclusions

The experimental results have identified the major regions and mechanisms of crankcase oil aerosol generation. The results have been analysed with a view to regulating aerosol generation directly. The following conclusions can be confidently made from the experimental investigation:

1. Optical investigation of a motored engine has highlighted that changes can be made to internal combustion engine crankcase design to reduce crankcase oil aerosol emissions.

2. The main mechanism of oil drop generation was from the atomisation of oil films on rotating components, most notably the crankshaft. Crankshaft atomisation was dependent on the oil film thickness and the engine speed. Rayleigh type oil ligament necking and breakup was the most significant mechanism of primary oil breakup and drop generation.

3. Crankcase oil aerosol generation was strongly affected by the oil temperature, since the surface tension and viscosity of the oil reduces with increasing temperature. Optical data showed significant oil drop generation at low oil temperatures, increasing the oil temperature to 80°C generated more oil drops with a lower mean drop diameter.

4. Careful attention should be paid to the throat of the crankcase, namely the smallest cross-section of the crankcase. For the motored engine studied, the throat of the crankcase is above the camshaft at the bottom of the pushrod gallery. This region constrains both the oil drainage from the top of the engine and the blow-by transport through the crankcase, and should be the focal point of any changes to the crankcase ventilation and oil drainage.

5. Extensive images collected around the crankcase show that conditions can be generated where the drop Weber number and Stokes number is sufficient to remove oil drops from the blow-by. Controlling this behavior is a valuable method of directly reducing oil aerosol within the crankcase.

6. Oil film generation and atomisation at the following locations contributed to crankcase oil aerosol generation and impeded oil drainage: oil leaking from the crankshaft and camshaft journal bearings was atomised, oil draining down the pushrod gallery onto the camshaft was atomised and oil delivered to the rockers was atomised by the rocker acceleration.

7. Submicron oil particles were generated in both the motored and fired engines. Varying the engine load, and therefore blow-by rate, crankcase pressure and temperature, caused a shift from the nucleation mode to the accumulation mode. The shift indicates different modes of vapour condensation generating submicron oil particles. This experimental conclusion indicates that there is potential to force condensation at certain locations within the crankcase by controlling the vapour pressure, temperature and size and number of condensation sites.

8. Submicron oil emissions increase with engine speed, even at low engine speeds of 360 rpm and 900 rpm. The increased emission is caused by higher oil temperatures and drop generation at elevated engine speeds.

9. Further evidence of the effect of engine speed and oil temperature on crankcase emissions was recorded by comparing the submicron crankcase emissions from the motored engine at fixed engine conditions, but with sump oil temperatures of 60°C and 85°C. A 25°C increase in sump oil temperature caused a 300% increase in the total number of submicron crankcase oil emissions.

10. At 900 rpm the motored engine submicron crankcase oil aerosol emissions were 35% of the maximum oil exposure limits as specified by the oil manufacturers. Noting initially that the oil temperature and blow-by rate were low at 80°C and 40 litres.min^{-1} respectively. Secondly, that particles larger than 1 μm were not included. Crankcase emissions will continue to be a significant problem for engine manufacturers.

11. A detailed analysis of crankshaft ligament breakup captured satellite and primary oil drops $d_p = 10 - 450$ μm. The flow velocity around the crankshaft ranged from $4 - 23$ m.s^{-1}. The oil drop generation occured within a repeatable distance of the crankshaft. When a simple curved oil shield covered in an oil film was positioned a fixed distance from the crankshaft lobe, oil ligament breakup and drop

generation was minimised. No secondary atomisation from the oil film on the oil shield was witnessed.

A graphical illustration of the main sources of crankcase emissions including typical drop size ranges and contributions is displayed in Figure 7.1. The figure represents the knowledge gained largely from this research, but it also draws conclusions from other investigations of crankcase oil aerosol emissions.

Sources of Crankcase Oil Aerosol Particle Number and Particle Mass

Rockers 1 – 100 μm
Minimal Atomisation
Poor Oil drainage

Turbocharger 1 – 20 μm
Lotus (2009)
Mass and Number Contribution

Camshaft 1 μm – 1 mm
Mass and Number Contribution

Piston Rings 1 – 80 μm
Dyson (2010)
Significant Number Contribution

Crankshaft 1 μm – 1 mm
Significant Mass and Number contribution

Timing Gears Mass and Number Contribution

Large Speed Dependency – More force therefore more atomisation

Oil Temperature Dependency – Lower viscosity and surface tension therefore more atomisation

Figure 7.1 Sources of crankcase oil aerosol generation

7.3   Recommendations to Reduce Crankcase Emissions

Based on the conclusions made for this body of work, a series of recommendations to reduce crankcase oil aerosol generation have been made, including design rules. Other areas worthy of further, more fundamental, investigation are listed in the next section.

Analysis of the results has revealed the following design rules to regulate crankcase oil aerosol generation and improve oil return to the sump:

- Directly lubricate components and avoid splash lubrication. If splash lubrication is necessary i.e for the piston cooling jets and cylinder liner, quantify the amount of lubrication required and direct the lubrication to the specific region.
- Avoid pooling of oil and minimise oil drainage and delivery onto flat surfaces where the oil will not flow down into the sump.
- Prevent oil drainage on to rotating and dynamic components.
- Maximise the cross sectional area through which the blow-by and oil drainage must pass.

The oil supply to the rockers is an excellent example of controlling crankcase emissions at source utilising the simple design rules. The rocker design investigated in this body of research, supplies oil to a flat surface at the top of the rocker above the valve stem. The oil on the rocker is atomised into a large range of oil drops, contributing little to the lubrication but adding to the crankcase emissions and impeding oil drainage. Conversely, in the current rocker design oil is supplied directly to the top of the valve stem where it is required for lubrication. This focused design improves the valve lubrication and reduces crankcase oil atomisation, an excellent example of controlling crankcase emissions at source.

Conclusions have consistently pointed towards the crankshaft and camshaft as regions of substantial crankcase oil aerosol generation. The Rayleigh type ligament breakup has been characterised in detail. Drops generated by crankshaft oil atomisation contribute directly to fine and coarse crankcase particulate emissions and they contribute to submicron crankcase emissions by providing sites for evaporation and condensation.

Control of crankshaft oil atomisation should focus on reducing the number concentration of oil drops and also generating a specific size of oil drop. Utilising the crankshaft as a controlled atomiser to generate a specific oil drop size has several benefits:

- Improved cylinder liner lubrication.

- Improved impaction separator efficiency as the crankshaft oil aerosol is monodispersed.

- Potential for forced condensation of oil vapour onto oil drops generated by crankshaft atomisation.

Both control and reduction of crankshaft oil atomisation should focus on:

Oil shields to prevent oil ligament breakup

The first approach is to use an oil shield to prevent primary ligament breakup and drop generation, this method is discussed in detail in Chapter 6. Further work is required to validate the performance, however, initial results show that the simple design prevents oil ligament breakup with no atomisation from the oil film on the shield.

Oil Film Generation

Oil film generation on the crankshaft is inevitable, the feasibility of controlling the oil film thickness and position should be explored. Investigations should focus on the bearing cap and crankshaft designs, including surface roughness and oleophobic coatings. If the oil film thickness and location can be controlled then the ligament thickness and final drop diameter can be controlled.

A fundamental crankshaft rig with excellent optical access has been designed and manufactured. The validity of these proposed recommendations can be assessed on this rig.

7.4 Recommendations for Further Work

The wealth of novel information gained following this experimental research has indicated several areas that can be exploited to regulate and control crankcase oil aerosol emissions, with minimal impact on engine performance. The two key fundamental areas requiring further investigation are:

Oil impaction and Coalescence

Oil drop removal was investigated in detail by Long *et al* (2009) supplementary to this Bai and Gosman (1995) characterised fuel drop impact regimes. A beneficial area of further work is to focus on the optimum oil film thickness, Weber and Stokes numbers required to remove the range of oil aerosol quantified in this thesis from the crankcase flow.

With detailed knowledge of how to remove oil drops using coalescence and coagulation, the hypothesis of integrating impaction separators into the engine crankcase should be investigated. On the 1104C-44 engine examined in this study, there is potential merit in installing an impaction separator into the pushrod galley section of the engine. This would prevent the large mass of oil drops generated by the crankshaft, camshaft and turbocharger oil drain from leaving the bottom of the engine, therefore dramatically reducing crankcase oil aerosol emissions. As the source of lubrication is not altered any dependence on an oil aerosol in the bottom of the engine for lubrication will not be affected.

Oil evaporation and condensation

Trends in engine design are pushing oil temperature towards their limits, with oil temperature in excess of 125°C, the knowledge gained from this research is vital. Reducing the global crankcase oil temperature is not possible, however, focusing on the critical atomisation sites and oil drainage is a realistic approach to controlling submicron crankcase oil atomisation within the crankcase.

Hot oil is a characteristic of modern internal combustion engines. Designers are constantly searching for methods to manage ever increasing thermal demands. The lubricating oil circuit is critical to transferring heat away from vital engine

components, most notably the pistons. As such it is not feasible to address the problem of submicron crankcase oil emissions by simply advising lower oil temperatures. Control of submicron crankcase oil emissions should focus firstly on acknowledging the regions of high oil temperature and therefore oil evaporation. The predominant regions of oil evaporation within an internal combustion engine crankcase are:

- Piston rings and cylinder liner
- Underside of the piston
- Crankshaft and camshaft journal bearings
- Turbocharger oil return

Oil vapour will be generated at these locations when the appropriate oil temperature and pressure are achieved. Further work should focus on this initial oil vapour generation and then the condensation of the oil vapour. Understanding the temperatures and pressures throughout the crankcase and its ventilation system, and the presence of nucleation and condensation sites will assist in controlling the generation of submicron oil particles. This novel but complex approach has the potential to avoid fouling of intake components and reduce the crankcase filtration requirement.

REFERENCES

ABDUL-KHALEK, I.S., KITTELSON, D.B., GRASKOW, B.R., WIE, Q. AND BREAR, F. 1998 Diesel Exhaust Particle Size: Measurement Issues and Trends. SAE Technical Paper 980525.

ACU Automotive Council UK, UK engine manufacturing statistics [online]. Available at: http://www.automotivecouncil.co.uk/automotive-industry-in-the-uk/uk-industry-factbook/ [Accessed 10/02/12].

ADRIAN, R.J. 1984 Scattering Particle Characteristics and Their Effect on Pulsed Laser Measurements of Fluid Flow: Sepckle Velocimetry vs. Paricle Image Velocimetry. *Applied Optics* Vol **23-11**, pp 1690-1691.

AITKEN, J. 1897 On some nuclei of cloudy condensation. *Trans. Royal Soc.* XXXIX.

ANDERSON, H. R. 2000. Differential Epidemiology of Ambient Aerosols. Phil. Trans. R. Soc. Lond. A. **358**: 2771- 2785.

AUDETTE III, W.E. AND WONG, V.W. 1999 A Model For Estimating Oil Vaporization From The Cylinder Liner As A Contributing Mechanism to Engine Oil Consumption. SAE Technical Paper 1999-01-1520.

AVERGARD, P. AND LINDSTROM, F. 2003. Modelling of Crankcase Gas Behaviour in a Heavy-Duty Diesel Engine. Master Thesis Department of Automatic Control, Lund Institute of Technology, January 2003.

AVL List GmbH 2006 Multiphase Flow FIRE Version 8 User Guide. Graz Austria.

AVL List GmbH 2008a CFD Solver v2008, FIRETM version 2008 Manual, Graz, June, Austria.

AVL List GmbH 2008b CFD Workflow Manager v2008, FIRETM version 2008 Manual, Graz, June, Austria.

BAGLEY, S. T., BAUMGARD, K. J. GRATZ, L. G. JOHNSON, J. H. AND LEDDY, D. G. 1996 Characterization of fuel and aftertreatment device effects on diesel emissions. Health Effects Institute (HEI), Research Report No. 76.

BAI, C., GOSMAN, A.D. 1995 Development of Methodology for Spray Impingement Simulation. SAE Technical Paper 950283.

BARAN, B. AND CHENG, W.K. 2007 Assessing the Windage Tray Blockage Effect on Aeration in the Oil Sump. SAE Technical Paper 2007-01-4109.

BAUMGARTEN, C. 2006 Mixture formation in internal combustion engines. Springer ISSN-1860-4846.

BECKER, R. AND DORING, W. 1954 Kinetic Treatment Of The Nucleation In Supersaturated Vapors. National Advisory Committee For Aeronautics Technical Memorandum 1374. Washington September 1954.

BEGG, S., de SERCEY, G., MICHE, N. AND HEIKAL, M. 2010 High-speed video observation and phase Doppler anemometry measurements of oil break-up in a model engine crankcase. *ILASS-Europe, 3rd Annual Conference on Liquid Atomization and Spray Systems, Brno, Czech Republic.*

BODEWADT, U.T. 1940 Die Drehstromung uber festem Grund. ZAMM *20*, **241 – 253**.

BOND, W.N. 1927 *Phil. Mag.* Vol **4,** (7) pp 889-898.

BOND, W.N. AND NEWTON, D.A. 1927 *Phil. Mag.* Vol **5,** (7) pp 794-800. *Environ Sci. Technol.* Vol. **38**, pp 2551-2556.

BOWEN, I.G., DAVIES, G.P. 1951 Report ICT 28 Shell Research Ltd., London 1951.

BRAUER, H. 1971 Grundlagen der Einphasen- und Mehrphasenströmugen, Sauerländer Verlag, Frankfurt am Main, Germany.

BURNS, J.R., RAMSHAW, C. AND JACHUCK, R.J.J. 2003 *Chemical Engineering Science* **58**, 2245.

BURTSCHER,H. 2005 Physical characterization of particulate emissions from diesel engine: a review *J.Aerosol Sci.* Vol. **36**, No. 7 896-932.

CAMBUSTION 2010 Cambustion DMS500 operating principle [online]. Available at: .http://www.cambustion.co.uk/instruments/dms500/principleoperation. [Accessed 7/04/10].

CAMERON, A. 1964 *Principles of Lubrication*. Longmans.

CANDY, J. AND GUERBE, L. 2009 Blow-by Gases Coalescing Separation: Performances on Passenger car Engines. SAE Technical Paper 2009-01-0869.

CATERPILLAR 2000 Electric Power Application and Installation Guide - Crankcase Ventilation. Caterpillar Inc., Peoria, IL, USA.

CENGEL, Y. AND BOLES, M.A. 2002 Thermodynamics an Engineering Approach. McGraw Hill.

CHIN, J.S., DURRETT, R. AND LEFEBVRE, A.H. 1984 The Interdependence of Spray Characteristics and Evaporation History of Fuel Sprays. *ASME J.Eng. Gas Turbines Power*, *Vol*. **106**, 639-644.

CHO, Y. AND TIAN, T. 2004 Modeling Engine Oil Vaporization and Transport of the Oil Vapor in the Piston Ring Pack of Internal Combustion Engines. SAE Technical Paper 2004-01-2912.

CLARK, N., MCKAIN, D., BARNETT, R., WAYNE, S., GAUTAM, M., THOMPSON, G. AND LYONS, D. 2006a Evaluation of crankcase emissions abatement device. Center for Alternative Fuels Engines & Emissions, West Virginia University report to New Condensator, Inc.

CLARK, N.N., TATLI, E., BARNETT, R., SCOTT, W. AND MCKAIN, D.L. 2006b Characterization and abatement of diesel crankcase emissions. SAE Technical Paper 2006-01-3372.

COLLINGS, N., REAVELL, K.S., HANDS, T., TATE, J. 2003 Roadside Aerosol Measurements with a Fast Particulate Spectrometer JSAE Paper 20035407.

DEKATI 2010 Dekati Electrical Low Pressure Impactor operating principle [online]. Available at: http://dekati.com/cms/elpi. [Accessed 7/04/10].

DIESELNET 2010 Crankcase ventilation [online]. Available at: http://www.dieselnet.com/ tech/engine_crank.html [Accessed 7/04/2010].

DIRECTIVE 2002 1970L0220 – 31/10/2002 by Consleg.

DOLLMEYER, T. A., VITTORIO, D.A., GRANA, T.A., KATZENMEYER, J.R. AND CHARLTON, S.J. 2007 Meeting the US 2007 heavy-duty diesel emission standards - designing for the customer SAE Technical Paper 2007-01-4170.

DONALDSON 2008 Spiralce ^{TM} Crankcase Filtration Technology for Open (OCV) and Closed (CCV) Systems Brochure No. F111118 (9/08).

DYSON, C., PRIEST, M. AND LEE, P.M. 2010 Oil Misting in the Piston Assembly of Automotive Engine and the Effect on Tribological Performance. STLE Annual Meeting Engine and Drivetrain III 20th May 2010.

EBNER, H.W., JASCHEK, A.O. 1998 The Importance of Blow-by Measurements, Measuring Equipment Required and Implementation SAE Technical Paper 981081.

EDELBAUER, W. 2007 Numerical Simulation of the Lubricating Oil and Air Flows in the Crankcase of an Internal Combustion Engine. PhD Thesis Graz University of Technology.

EDELBAUER, W., DIEMATH, A., KRATOCHWILL, H. AND BRENN, G. 2010 Simulation of the ventilation losses in the crankcase of an internal combustion engine. *Progress in Computational Fluid Dynamics,* Vol. **10**, No. 1.

EDELBAUER, W., KRATOCHWILL, H., BRENN, G. AND TATSCHL, R. 2009 Simulation of the oil droplet laden air flow in the crankcase of an internal combustion engine. *Progress in Computational Fluid Dynamics,* Vol. **9**, No. 1.

FARMER, L.E., 2004. Final Report on Testing Performed For NCI On the Condensator On a MY1996 Dodge RAM 2500 Truck With the 12-valve, 5.9L

Cummins Turbo Diesel Engine. Automotive Testing and Development Services, Inc., Ontario, CA, USA.

FRIEDLANDER, S.K. 1977 *Smoke, Dust and Haze*. New York: John Wiley and Sons.

GANGOPADHYAY, A. 2000 Development of a Piston Ring-Cylinder Bore Wear Model" SAE Technical Paper 2000-01-1788.

GELBARD, F. AND SEINFELD, J.H. 1979 Theory and Application to Aerosol Formation and Growth. *Journal of Colloid and Interface Science*, Vol. **68**, No. 2, February 1979.

GIECHASKIEL, B., CARRIERO, M., MARTINI, G., KRASENBRINK, A. AND SCHEDER, D. 2009 Calibration and Validation of Various Commercial Particle Number Measurement Systems SAE Technical Paper 2009-01-1115.

GIECHASKIEL, B., CARRIERO, M., MARTINI, G., KRASENBRINK, A., SCHEDER, D. 2009 Calibration and Validation of Various Commercial Particle Number Measurement Systems. SAE Technical Paper 200-01-1115.

GIFFEN,E. AND MURASZEW, A. 1953 The Atomisation of Liquid Fuels John Wiley and Sons, New York.

GIVENS, W. A., BUCK, W. H., JACKSON, A., KALDOR, A., HERTZBERG, A., MOEHRMANN, W., *et al*. 2003 Lube formulation effects on transfer of elements to exhaust after-treatment system components. SAE Technical Paper 2003-01-3109.

GOHAR, R. AND RAHNEJAT, H. 2008 *Fundamental od Tribology*. Imperial College Press.

GONZALEZ, R.C., WOODS, R.E. 2001 *Digital Image Processing Second Edition* Prentice Hall ISBN 0-201-18075-8.

GONZALEZ, R.C., WOODS, R.E., EDDINS, S.L. 2004 Digital Image Processing Using MATLAB Edition Prentice Hall ISBN 0-13-008519-7.

GORDON, D.G. 1959 Mechanism and Speed of Breakup of Drops. *J.Appl.Phys.,* Vol. **30**, No.11, 1759-1761.

GPO 2012 Environmental Protection Agency Part 1065 Engine Testing Procedures [online]. Available at: http://www.gpo.gov/fdsys/. [Accessed 10/02/12].

GRAVE, B. 1967 Die Flüssigkeits Ablösung an Rotierende Zersatäuber Scheiben, Master Thesis at TU Berlin Fachbereich Verfahrenstechnik, Germany.

GRAY,C., IRVING, M. AND LOCKE, C. 2004 Comparison of the Turbo/Intercooler Glassware Test (Using Din 51535) to a fired Heavy Duty Diesel Engine Test. SAE Technical Paper 2004-01-1957.

GROENEWEG,M., BARBER, G.C. AND HREIHEIT, T. 1992 Vapor Delivered Lubrication of Diesel Engines – Uncooled Single Cylinder Engine Test. SAE Technical Paper 922351.

HAISCH, C. AND NIESSNER, R. 2002 Light and Sound – Photoacoustic Spectroscopy. Spectroscopy Europe.

HARPER, E.Y., GRUBE, G.W. AND CHANG, I.D. 1972 *J.Fluid Mech.* **52**: 565-591.

HARRIS, S.J., MARICQ,M.M. 2002 The role of fragmentation in defining the signature size distribution of diesel soot *J.Aerosol Sci.* Vol. **33**, 935-942.

HECKEL, S. P., STEFFEN, B. P. AND FEDOROWICZ, J. 2006 Characterization of Diesel Engine Crankcase Blowby. Proceedings of the 2006 AFS 19th Annual Conference, Rosemont, IL, USA, May 9-11, 2006.

HEGE, H. 1964 Flüssigkeitsauflösung durch schleuderscheiben. *Chem.ing.Tech.,* Germany, Vol. **36**, No. 1, pp.52-59.

HEYWOOD, J.B. 1988 *Internal Combustion Engine Fundamentals*. McGraw-Hill International Editors.

HIBBLER, R.C. 2004 *Engineering Mechanics Dynamics*. Pearson Prentice Hall.

HINDS, W.C. 1999 Aerosol Technology, Properties, Behaviour, and Measurement of Airborune Particles. John Wiley & Sons.

HINZE, J.O., 1955 Fundamentals of the Hydrodynamic Mechanism of Splitting in Dispersion Processes. *AIChE J,* Vol. **1**, No. **3**, 289-295.

HUNTER, G 1997 Formation and characterization of particles: Report of the 1996 HEI Workshop, Particle formation in Combustion, HEI Commun. 5, 6-7.

IARC 2012. International Agency for Research on Cancer: Diesel Engine Exhuast Carcinogenic. Press Release N° 213 12 June 2012.

IPSD 2007a 1100 Series 1104C-44 Specification Sheet.

IPSD 2007b 1100 Series 1104C-44TA Specification Sheet.

IPSD 2008a Service Manual, Publication Number RENR9401.

IPSD 2008b 1100 Series 1104D-E44TA Specification Sheet.

JAROSZCZYK, T. *et al.*. 2006. New developments in diesel engine crankcase emission reduction - requirements, design and performance, Journal of KONES Powertrain and Transport, **13**(2), 155-167.

KIM, J.Y., KOTCHMAR, D., ROSS, M., WHITE, L., WICHERS, L. AND WILSON, W. 2006 Provisional Assessment of Recent Studies on Health Effects of Particulate Matter Exposure. National Centre for Environmental Assessment, Office of Research and Development, U.S. Environmental Protection Agency. EPA/600/R-06/063.

KISSNER,G AND RUPPEL, S. 2009 Highly Efficient Oil Separation Systems for Crankcase Ventilation. SAE Paper 2009-01-0974.

KITTELSON, D., WATTS, W. AND JOHNSON, J. 2002 Diesel Aerosol Sampling Methodology – CRC E-43. Technical summary and conclusions report. University of Minnesota Department of Mechanical Engineering.

KITTELSON,D.B. 1998 Engines and Nanoparticles: A review *J.Aerosol Sci.* Vol. **29**, No. 5/6 575-588.

KLUSENER,O. 1933 The injection Process in Compressorless Diesel Engines *VDI Z.,* Vol. **77**, No. 7.

KULKARNI, P., BARON, P.A. AND WILLEKE,K. 2011 *Aerosol Measurement Principles, Techniques and Application.* Wiley.

LA VISION 2011 Product-Manual FlowMaster Item-Number(s): 1105011-4.

LANE, W.R., 1951 Shatter of Drops in Streams of Air, *Ind. Eng. Chem Vol.* **43**, No. 6, pp 1312-1317.

LANGMUIR, I. AND BLODGETT, K. 1946 A Mathematical Investigation of Water Droplet Trajectories. A.A.F Tech. Rep. 5418, Air Material Command, Wright Patterson Air Force Base.

LEFEBVRE, A.H. 1989 Atomisation and Sprays. New York: Taylor & Francis.

LIN, S.P. 2003 Breakup of Liquid Sheets and Jets. Cambridge University Press.

LONG, E.J., HARGRAVE, G.K., PAGE, V.J., SABRAZAT, N., WAGSTAFF, S. 2009 The separation of oil particles from a two-phase flow using an inertial impaction device. Turbulence, Heat and Mass Transfer 6, 2009.

MAASSEN,F., KOCH, F. AND PISCHINGER, F. 1998 Connecting Rod Bearing Operation with Aerated Lube Oil. SAE Technical Paper 981404.

MANZ, D.L., COWART, J.S. AND CHENG, W.K. 2004 High-speed Video Observation of Engine Oil Aeration. SAE Technical Paper 2004-01-2913.

MARICQ, M.M. 2007 Chemical characterization of particulate emissions from diesel engines: A review. *Journal of Aerosol Science* **38**, 1079-1118.

MARTYR, A.J. AND PLINT, M.A. 2007 Engine Testing Oxford: Elsevier 2007.

MATAR, O.K., SISOEV, G.M. AND LAWRENCE, C.J. 2008 *Chemical Engineering Science* Vol **63**, 225-2232.

MECA (MANUFACTURERS OF EMISSION CONTROLS ASSOCIATION) 2007 Emission Control Technologies for Diesel-Powered Vehicles. Technical Report.

MEHRHARDT, E. 1978 Zerstäubung von Flüssigkeiten mit rotierenden Scheiben. Flüssigkeitsauflosung, Tropfengröben und Tropfengröbenverteilungen, PhD Thesis at TU Berlin Fachbereich 10 – Verfahrenstechnik, Germany, September.

MELLOR, R. 1969 Ph.D. thesis, University of Sheffield.

MIAN, M.A. 1997 Design and Analysis of Engine Lubrication Systems. SAE Technical Paper 970637.

MUNSON,.B.R., YOUNG, D.F. AND OKIISHI, T.H. 2002 Fundamentals of Fluid Mechanics. John Wiley & Sons, Inc.

NEMOTO, S., KAWATA, K., KURIBAYASHI, T., AKIYAMA,K., KAWAI, H. AND MURAKAWA, H. 1997 A study of engine oil aeration. JSAE Review **18** pp 271-276.

OKADA, S., KWEON, C.B., STETTER, J. C., FOSTER, D. E., SHAFER, M. M., CHRISTENSEN, C. G., *et al*. 2003 Measurement of trace metal composition in diesel engine particulate and its potential for determining oil consumption. SAE Technical Paper 2003-01-0076.

PARDUE, B. A. 2004 Fundamentals of Crankcase Ventilation Open and Closed Systems. Short Course, 9th World Filtration Congress, New Orleans, 19-24, 2004.

PAYRI, F., GALINDO, J., CLIMENT, H. AND GUARDIOLA, C. 2005. Measurement of the oil consumption of an automotive turbocharger. Experimental Techniques, **29**(5), 25-27.

PHEN,R.V., RICHARDSON, D. AND BORMAN, G. 1993 Measurements of Cylinder Liner Oil Film Thickness in a Motored Diesel Engine. SAE Technical Paper 932789.

PICKERING, C.J.D. AND HALLIWELL, N.A. 1984 Laser Speckle Photography and Particle Image Velocimetry: Photographic Film Noise. *Applied Optics*. Vol **23-17**, pp 2961-2969.

POPE III, C. A., THUN, M. J., NAMBOODIRI, M. M., DOCKERY, D. W., EVANS, J. S., SPEIZER, F. E. AND HEATH, JR. C. W. 1995 Particulate air pollution as a predictor of mortality in a prospective study of U.S. adults. *Am. J. Respir.Crit. Care Med.* **151**, 669-674.

PRANDTL, L. 1944 *Guide to the Theory of Flow*, 2nd ed., Braunschweig, 1944 p. 173.

PRICE, P., STONE, R., COLLIER, T., DAVIES, M. AND SCHEER, V. 2006 Dynamic Particulate Measurements from a DISI Vehicle: A Comparison of DMS500, ELPI, CPC and PASS. SAE Technical Paper, 2006-01-1077.

PULKRABEK,W.W. 2001 Engineering Fundamentals of the Internal Combustion Engine. 2nd. New York: Pearson Prentice-Hall.

PULKRABEK,W.W. 2001 Engineering Fundamentals of the Internal Combustion Engine. New York: Pearson Prentice-Hall.

RAFFEL, M., WILLERT, C., WERELEY, S. AND KOMPENHANS, J. 2001 *Particle Image Velocimetry A Practical Guide*. Springer.

REAVELL, K.S., HANDS, T. AND COLLINGS, N. 2002a Determination of Real Time Particulate Size Spectra and Emission Parameters with a Differential Mobility Spectrometer. 6th International ETH Conference on Nanoparticle Measurement.

REAVELL,K., HANDS, T. AND COLLINGS, N. 2002b A Fast Response Particulate Spectrometer for Combustion Aerosols. SAE Technical Paper 2002-01-2714.

ROSS. S. 1950 Variation With Temperature Of Surface Tension Of Lubricating Oils. National Advisory Committee For Aeronautics Technical Note 2030 February 1950.

RTI, 2003 Environmental Technology Verification Report Mobile Source Emission Control Devices Donaldson Company, Inc. Series 6000 Diesel Oxidation Catalyst Muffler and Spiracle Closed Crankcase Filtration System. Research Triangle

Institute, Research Triangle Park, NC, USA; EPA Cooperative Agreement No. CR829434-01-1.

RTI, 2005. Environmental Technology Verification Report Test Report of Mobile Source Emission Control Devices Cummins Emission Solutions & Cummins Filtration Diesel Oxidation Catalyst and Closed Crankcase Ventilation System.

RTI, 2007. Environmental Technology Verification Report Mobile Source Emission Control Devices Cummins Emission Solutions & Cummins Filtration Closed Crankcase Ventilation System (201350N Precious Metal Diesel Oxidation Catalyst Plus Coalescer Breather CV5061200 and Crankcase Depression Regulator Valve 395587500). Research Triangle Institute, Research Triangle Park, NC, USA; EPA Cooperative Agreement No. CR831911-01-1, June 2007.

RUBINO, L., PHILLIPS, P.R. AND TWIGG, M.V. 2005 Measurements of Ultrafine Particle Number Emissions from a Light-Duty Diesel Engine Using SMPS, DMS, ELPI and EEPS. SAE Technical Paper 2005-24-015.

SARTOR, J.D AND ABBOTT, C.E. 1990 Momentum slip correction factor for small particles in nine common gases. *J.Aerosol Sci*. 21: 161-168.

SATOH,K., KAWAI, T., ISHIKAWA, M. AND MATSUOKA, T. 2000 Development of Method for Predicting Efficiency of Oil Mist Separators. SAE Technical Paper 2000-01-1234.

SCHELLHASE, T., SAUTER, H. AND RUPPEL, S. 200 Assembled Camshaft with Integrated Oil Mist Separation. SAE Technical Paper 2007-01-0260.

SCHILLING, A. 1968 *Motor Oils and Engine Lubrication*. Scientific Publications.

SCHINDLER, W. *et al*. 2004 A Photoacoustic Sensor System for Time Resolved Quantification of Diesel Soot Emissions. SAE Technical Paper 2004-01-0968.

SCHLICHTING, H. 1979 Boundary-Layer Theory. 7th *ed.,* New York: McGraw-Hill.

SCHMEICHEL, S.D., SCHMIDT, F.W., IMES, J.A. AND DUSHEK, R.A. 2007 Apparatus for emissions control systems, and methods. US Patent 7,278,259.

SEINFELD, J.H. AND PANDIS, S.N. 2006 Atmospheric Chemistry and Physics, From Air Pollution to Climate Change Wiley-Interscience Publication.

SHELL 1998 Rimula X (SAE 15W40) thermal properties – Shell Global Solutions (UK) For 1998/Euro 2 on highway exhaust emissions standards.

SHINJO, J. AND UMEMURA, A. 2010 Simulation of liquid jet primary breakup: Dynamics of ligament and droplet formation *International Journal of Multiphase Flow* **36** pp 513-532.

SHINJO, J., MATSUYAMA, S., MIZOBUCHI, Y., OGAWA, S., UMEMURA, A., 2009. A numerical study on ligament disintegration mechanism by propagative capillary waves. Atomization, 36–43.

SIMPKINS, P.G. 1997 *Aerosol Science and Tech* **26**:1, 51-54.

SISOEV, G.M., MATAR, O. AND LAWRENCE, C.J. 2003 Modelling of film flow over a spinning disk *J Chem Technol Biotechnol journal of engineering physics* Vol. **78**, 151-155.

SKF, 2006 Valve Stem Seals. SKF Sealing Solutions GmbH, Leverkusen-Opladen, Germany, Publication 6244 EN.

SPURNY, K.R 1997 Advances in aerosol filtration. Boca Raton, FL; London: Lewis Publishers.

STERNOWSKY, S., SCHULTE, G., GUARDANI, R. AND NASCIMENTO, C.A.O. 2002 Experimental study and neural network modelling of the ligament disintegration in rotary atomization. *Atomization and Sprays.* Vol **12** pp 107-121.

STOKES, G.G. 1901 *Scientific Papers*. University Press Cambridge.

STONE, H.A., 1994 Dynamics of drop deformation and breakup in viscous fluids. *Annu. Rev. Fluid Mech.*, 65–102.

STONE, H.A., BENTLEY, B.J., LEAL, L.G., 1986 An experimental study of transient effects in the breakup of viscous drops. *J Fluid Mech.*, Vol **173** pp 131–158.

STONE, H.A., LEAL, L.G., 1989a Relaxation and breakup of an initially extended drop in an otherwise quiescent fluid. *J Fluid Mech.*, Vol **198** pp 399–427.

STONE, H.A., LEAL, L.G., 1989b The influence of initial deformation on drop breakup in subcritical time-dependent flows at low Reynolds numbers. *J. Fluid Mech.*, Vol **206** pp 223–263.

STUCKE,P., NOBIS, M. AND SCHMIDT, M. 2009 3D-CFD Flow Structures in Journal Bearings. SAE Technical Paper 2009-01-2688.

TAKAHASHI, K., KIKUCHI, T., OKADA, N., KIMURA, Y. AND KATAOKA, T. 2008 Method for Prediction of Engine Oil Aeration Rate. SAE Technical Paper 2008-01-1361.

TATLI, E. AND CLARK, N.N. 2008 Crankcase Particulate Emissions from Diesel Engines. SAE Technical Paper 2008-01-1751.

TAYLOR, G.I., 1934 The function of Emulsion in Definable Field Flow *Proc. R. Soc. London Sr. A,* Vol. **146** pp 501-523.

TAYLOR, R.I, MAINWARING, R. AND MORTIER, R.M. 2005 Engine lubricant trends since 1990. *Proc. ImechE Vol **219** Part J: J.Engineering Tribology J04204.*

THIROUARD, B. 2001 Characterization and Modeling of the Fundamental Aspects of Oil transport in the Piston-Ring Pack of Internal Combustion Engines. Ph.D. Thesis, Department of Mechanical Engineering, MIT.

TIAN, T. 1997 Modeling the performance of the Piston Ring-Pack in Internal Combustion Engines. Ph.D. Thesis, Department of Mechanical Engineering, MIT.

TIAN, T. 2002 Dynamic behaviours of piston rings and their practical impact. Part 1:ring flutter and ring collapse and their effects on gas flow and oil transport. *Proc. Instn Mech. Engrs*, Vol. **216**, *Part J, Journal of Engineering Tribology*, pp. 209-228.

TIAN, T., WONG, V. W. AND HEYWOOD, J. B. 1998 Modelling the Dynamics and Lubrication of Three Piece Oil Control Rings in Internal Combustion Engines. SAE Technical paper 982657.

TSI 2003 Aerosol Diluter 3302A Instruction Manual P/N 1933786, Revision B.

TSI 2005 Scanning Mobility Particle Sizer^{TM} Spectrometers. Instruction Manual P/N 2980347.

TSI 2010 Aerodynamic Particle Sizer specification sheets [online]. Available at: http://www.tsi.com/uploadedFiles/Product_Information/Literature/Spec_Sheets/3 321.pdf [Accessed 7/04/2010].

TSI 2012 Aerosol Statistics Lognormal Distributions Application Note PR-001 [online]. Available at: http://www.tsi.com/uploadedFiles/Product_Information /Literature/Application_Notes/PR-001-RevA_Aerosol-Statistics-AppNote.pdf [Accessed 20/01/2012].

UMEMURA, A., 2007a. Self-destabilizing mechanism of circular liquid jet (first report: capillary waves associated with liquid jet destabilization). *J. Jpn. Soc.Aeronaut. Space Sci.,* 216–223.

UMEMURA, A., 2007b. Self-destabilizing mechanism of circular liquid jet (second report: proposal of breakup feedback loop model). *J. Jpn. Soc. Aeronaut. Space Sci.*, 224–231.

UMEMURA, A., 2007c. Self-destabilizing mechanism of circular liquid jet (third report: model simulation of liquid jet disintegration process). *J. Jpn. Soc. Aeronaut Space Sci.,* 359–366.

UMEMURA, A., WAKASHIMA, Y., 2002 Atomization regimes of a round liquid jet with near-critical mixing surface at high pressure. *Proc. Combust. Inst.*, 633–640.

USUI, M., MURAYAMA, K., OOGAKE, K. AND YOSHIDA, H. 2008 Study of Oil Flow Surrounding Piston Rings and Visualization Observation. SAE Technical Paper 2008-01-0795.

VERSTEEG, H.K. AND MALALASEKERA, W. 2007 An Introduction to Computational Fluid Dynamics The Finite Volume Method. Second Edition Pearson Prentice Hall.

VIRTANEN, A.K.K., RISTIMAKI, J.M., VAARASLAHTI, K.M. AND KESKINEN, J. 2004 Effect of Engine Load on Diesel Soot Particles.

VOKAC, A. AND TIAN, T. 2004 An experimental Study of Oil Transport on the Piston Third Land and the Effects of Piston Ring Designs. SAE Technical Paper 2004-01-1934.

WEISSTEIN, E.W. 2010 Torus from MathWorld A Wolfram Web Resource [online]. http://mathworld.wolfram.com/Torus.html [Accessed 24/03/2010].

WHITBY, K.T. AND CANTRELL, B. 1976 Fine particles. Proc. Int. Confe. Environmental Sensing and Assessment, Las Vegas, NV, Institue of Electrical and Electronic Engineers.

WHITE, F.M. 1974 1995 Viscous Fluid Flow. New York: McGraw-Hill.

YILMAZ, E., TIAN, T., WONG, V. W. AND HEYWOOD, J. B 2004 The Contribution of Different Oil Consumption Sources to Total Oil Consumption in a Spark Ignition Engine. SAE Technical Paper 2004-01-2909.

YILMAZ, E., TIAN, T., WONG, V. W. AND HEYWOOD, J. B. 2002 An Experimental and Theoretical Study of the Contribution of Oil Evaporation to Oil Consumption. SAE Technical paper 2002-01-2684.

ZIELINSKA, B., CAMPBELL, D., LAWSON, D.R., IRESON, R.G., WEAVER, C.S., HESTERBERG, T.W., LARSON, T., DAVEY, M. AND LIU, S.L.J. 2008 Detailed Characterization and Profiles of Crankcase Diesel Particulate Matter Exhaust Emissions Using Speciated Organics. *Environ Sci. Technol.* **42**, 566-5666.

APPENDIX A

A-1 IPSD 1104C-44 Engine Specification (IPSD, 2007a)

Table A-1.1 IPSD 1104C-44 engine specification (IPSD, 2007a)

IPSD 1104C-44	
Cylinder No.	4 in-line
Bore and Stroke	105 mm x 127 mm
Displacement	4.4 litres
Aspiration	Natural
Valve Actuation	Pushrod and rocker
Valve No.	8
Cycle	4 Stroke
Combustion System	Direct Injection
Compression Ratio	19.3:1
Rotation	Anti-clock wise viewed on fly wheel
Cooling System	Pressurised water
Dimensions	Length 663 mm Width 470 mm Height 812 mm
Dry Weight	357 kg
Power Output	64.0 kW @ 2400 rpm
Peak Torque	308 Nm @ 1200 rpm
Emissions Compliance	EC Stage 2 and USA EPA Tier 2 off-highway

A-2 IPSD 1104C-44 Lubrication Circuit Description (IPSD, 2008a)
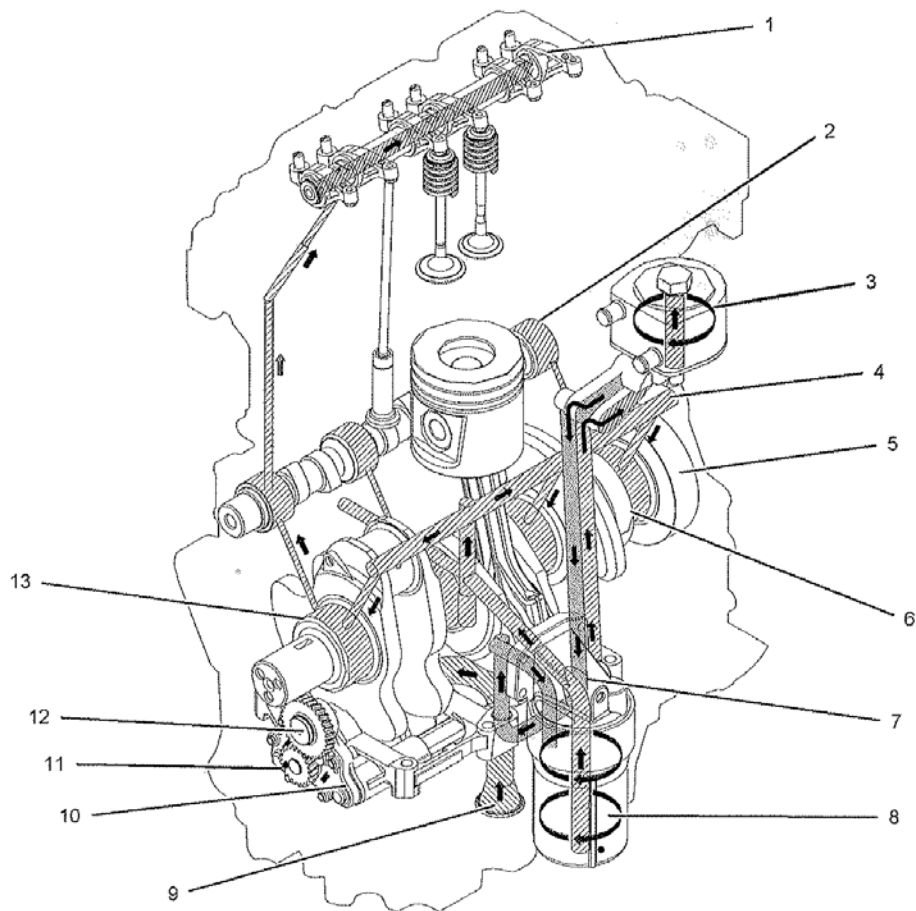
Figure A-2.1 IPSD 1104C-44 lubrication system (IPSD, 2008a)

Lubricating oil from the oil pan flows through a strainer and pipe (9) to the suction side of the engine oil pump (10). Pressure for the lubrication system is supplied by the oil pump. The crankshaft gear (13) drives a lower idler gear (12). The lower idler gear drives the oil pump gear (11). The pump has an inner rotor and an outer rotor. The axis of rotation of the rotors are off-centre relative to each other. There is an interference fit between the inner rotor and the drive shaft.

The inner rotor has five lobes which mesh with the six lobes of the outer rotor. When the pump rotates, the distance increases between the lobes of the outer rotor and the lobes of the inner rotor in order to create suction. When the distance decreases between the lobes, pressure is created.

The lubricating oil flows from the outlet side of the oil pump (10) through a passage to the oil filter head (7). The oil then flow from the oil filter head through a passage to a plate type oil cooler for the 1104 engine (or a modine oil cooler (3) for the 1103 engine). The oil cooler is located on the left side of the cylinder block.

From the oil cooler, the oil returns through a passage to the oil filter head. The oil then flows through a bypass valve that permits the lubrication system to function if the oil filter becomes blocked. Under normal conditions, the oil then flows to the oil filter (8).

The oil flows from the oil filter through a passage that is drilled across the cylinder block to the oil gallery (4). The oil gallery is drilled through the total length of the left side of the cylinder block. If the oil filter is on the right side of the engine, the oil flows through a passage that is drilled across the cylinder block to the pressure gallery.

Lubricating oil from the oil gallery flows through high pressure passages to the main bearing of the crankshaft (5). Then, the oil flows through the passages in the crankshaft to the connecting rod bearing journals (6). The pistons and the cylinder bores are lubricated by the splash of oil and the oil mist.

Lubricating oil from the main bearings flows through passages in the cylinder block to the journals of the camshaft. Then, the oil flows from the second journal of the camshaft (2) at a reduced pressure to the cylinder head. The oil then flows through the centre of the rocker shaft (1) to the rocker arm levers. The valve stems, the valve springs and the valve lifters are lubricated by the splash and the oil mist.

The hub of the idler gear is lubricated by the oil from the oil gallery. The timing gears are lubricated by the splash from the oil.

An external line from the cylinder block supplies oil to the turbocharger. The oil then flows through a return line to the oil pan.

Engines have piston cooling jets that are supplied with oil from the oil gallery. The piston cooling jets spray lubricating oil on the underside of the pistons in order to cool the pistons.
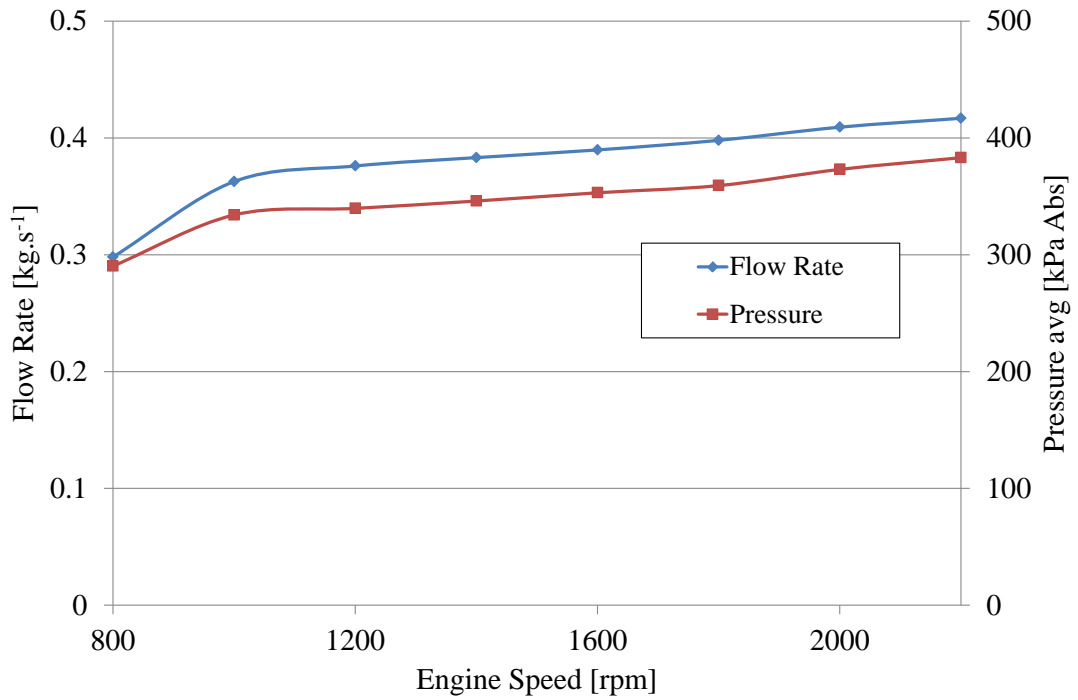
Figure A-2.2 Oil rail pressure and flow rate SAE 15W-40 oil 60°C oil temperature
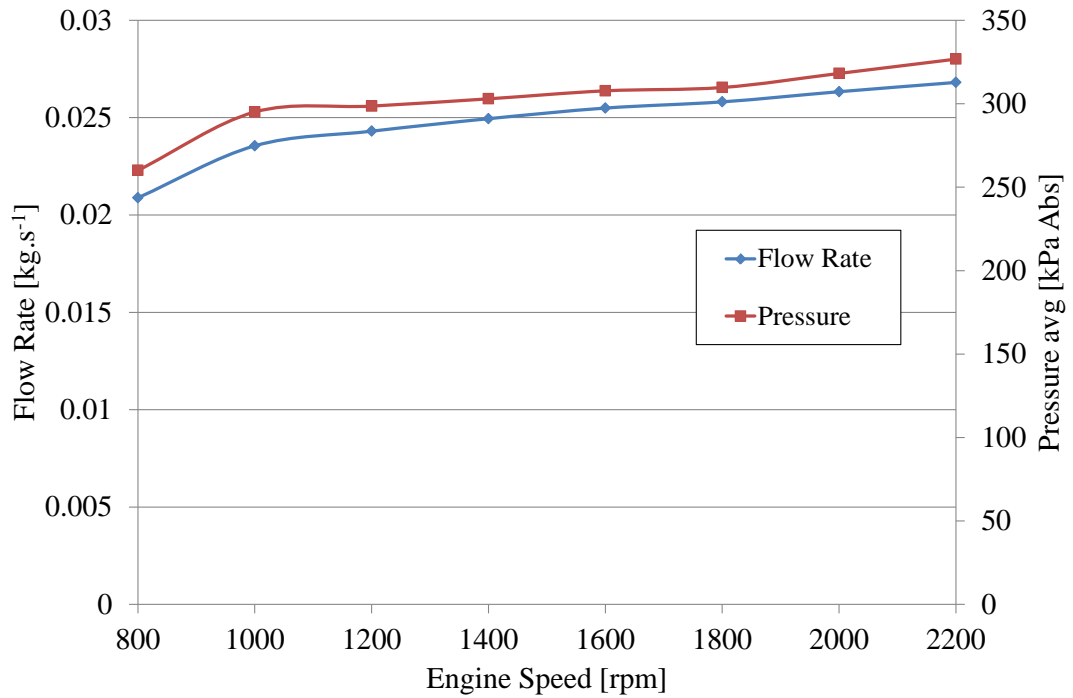
Figure A-2.3 Rocker shaft oil pressure and flow rate SAE 15W-40 oil 60°C oil temperature

A-3 IPSD 1104C-44TA Engine Specification (IPSD, 2007b)

Table A-3.1 IPSD 1104C-44TA engine specification (IPSD, 2007b)

IPSD 1104C-44TA	
Cylinder No.	4 in-line
Bore and Stroke	105 mm x 127 mm
Displacement	4.4 litres
Aspiration	Turbocharged
Valve Actuation	Pushrod and rocker
Valve No.	8
Cycle	4 Stroke
Combustion System	Direct Injection
Compression Ratio	18.2:1
Rotation	Anti-clock wise viewed on fly wheel
Cooling System	Pressurised water
Dimensions	Length 663 mm Width 620 mm Height 810 mm
Dry Weight	306 kg
Power Output	97.0 kW @ 2400 rpm
Peak Torque	500 Nm @ 1200 rpm
Emissions Compliance	EC Stage 2 and USA EPA Tier 2 off-highway
Fuel Type	Low Sulphur Diesel

A-4 IPSD 1104C-44 Crankshaft Main Bearing side Flow

Equations below taken from Gohar and Rahnejat (2008). Please refer to nomenclature for definitions. The results are displayed in Table A-4.1.

Table A-4.1 Narrow bearing side flow calculations Gohar and Rahnejat (2008)

Narrow Bearing Side Leakage	$Q_s = (\pi R N L c) 2 \epsilon$	(A.1)
Side Flow Factor	$Q_s^* = Q_s (\pi R N L c) 2 \epsilon$	(A.2)
Narrow Bearing Side Flow Factor	$Q_s^* = 2 \epsilon$	(A.3)
Total Pump Axial Flow	$Q_a = \left(\dfrac{d_c h_f^3 p_0}{12 \eta_l L} \right) Q_a^*$	(A.4)
Side Flow Axial Flow Factor	$Q_a^* \approx 1.2 + 11 \dfrac{d_c}{L}$	(A.5)
Total Side Flow	$Q_P = Q_a + Q_s$	(A.6)

Crankshaft main bearing side flow assumptions:

1. SAE 15W-40 oil at 80°C. The dynamic viscosity value can be found in Appendix B Table B-1.1.
2. Crankshaft speed was constant at 1800 rpm
3. The main crankshaft bearing only had a feed hole, i.e there was no output in the journal bearing to feed to camshaft. Two of the five main crankshaft journal bearing were arranged in this manner, analysis of this geometry provides the maximum oil leakage from the crankshaft main bearing.

4. Oil flow in the cross drillings in the crankshaft feeding the connecting rod big end bearings was not considered.

Table A-4.2 Total bearing side flow for a single main crankshaft journal bearing on the 1104C-44

|	
Eccentricity Ratio, ε	0.8
Radial Bearing Clearance, c [m]	0.000117
Oil Film Thickness, h_f [m]	0.0001
Bearing Radius, R [m]	0.039560
Bearing Speed, N [rev.s^{-1}]	30
Bearing Length, L [m]	0.0316
Oil Supply Hole Diameter, d_c [m]	0.008
Oil Suppy Pressure, p_0 [kPaA]	353.822
SAE 15W-40 Dynamic Viscosity, η_l [kg.m^{-1}.s^{-1}]	0.0205
SAE 15W-40 Density, ρ_l [kg.m^{-3}]	849.742
Results	
Narrow Bearing Side Leakage, Q_s [m^3.s^{-1}]	0.0000221
Pump Axial Flow, Q_a [m^3.s^{-1}]	0.0000006
Total Side Flow, Q_p [m^3.s^{-1}]	0.0000227
Total Side Flow, m$_p$ [g.s^{-1}]	19.25

A-5 1104C-44 Crankshaft Surface Profile
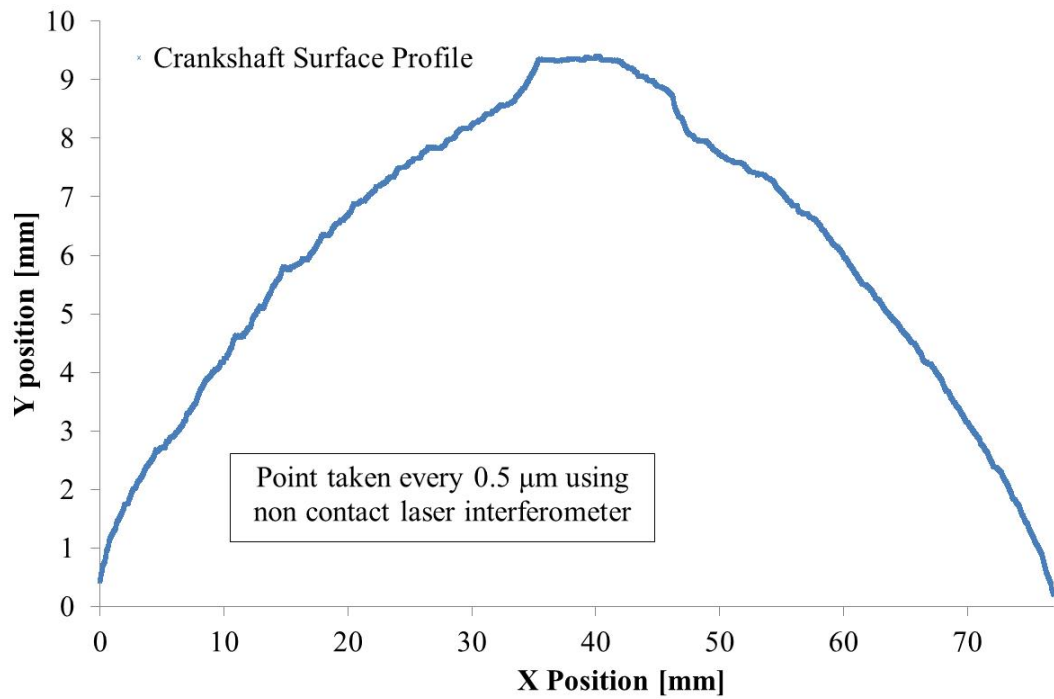
Figure A-5.1 1104C-44 dry crankshaft lobe circumference surface profile

APPENDIX B

B-1 SAE 15W-40 Engine Oil Properties

(Obtained from Shell Global Solutions (UK))

Table B-1.1 Shell Rimula X SAE 15W-40 oil properties

| T [°C]	Thermal Conductivity [W.m^{-1}.°C^{-1}]	Density [kg.m^{-3}]	Kinematic Viscosity [m^2.s^{-1}]	Dynamic Viscosity [kg.m^{-1}.s^{-1}]	Specific Heat Capacity [J.kg^{-1}.°C^{-1}]	Prandtl Number
0	0.13062	899.29	1.21E-03	1.09E+00	1779.25132	13263.2
10	0.13081	893.097	5.74E-04	5.12E-01	1821.29557	6434.48
20	0.13101	886.903	3.01E-04	2.67E-01	1863.65438	3449.52
30	0.13121	880.71	1.71E-04	1.51E-01	1906.33284	2009.21
40	0.13142	874.516	1.05E-04	9.16E-02	1949.33615	1255.35
50	0.13162	868.323	6.78E-05	5.89E-02	1992.6694	830.165
55	0.13173	865.226	5.70E-05	4.81E-02	2014.5042	705.018
60	0.13183	862.129	4.62E-05	3.98E-02	2036.33876	588.615
70	0.13205	855.935	3.28E-05	2.81E-02	2080.34911	409.93
80	0.13226	849.742	2.41E-05	2.05E-02	2124.70641	317.172
85	0.13237	846.645	2.12E-05	1.77E-02	2147.06147	276.193
90	0.13248	843.548	1.83E-05	1.55E-02	2169.41653	241.657
100	0.1327	837.355	1.43E-05	1.20E-02	2214.48549	193.713
110	0.13293	831.161	1.18E-05	9.48E-03	2260.1051	162.845
120	0.13316	824.968	9.28E-06	7.66E-03	2305.72471	130.759
130	0.13339	818.774	7.87E-06	6.30E-03	2352.10002	112.818
140	0.13363	812.58	6.47E-06	5.25E-03	2389.47533	94.249
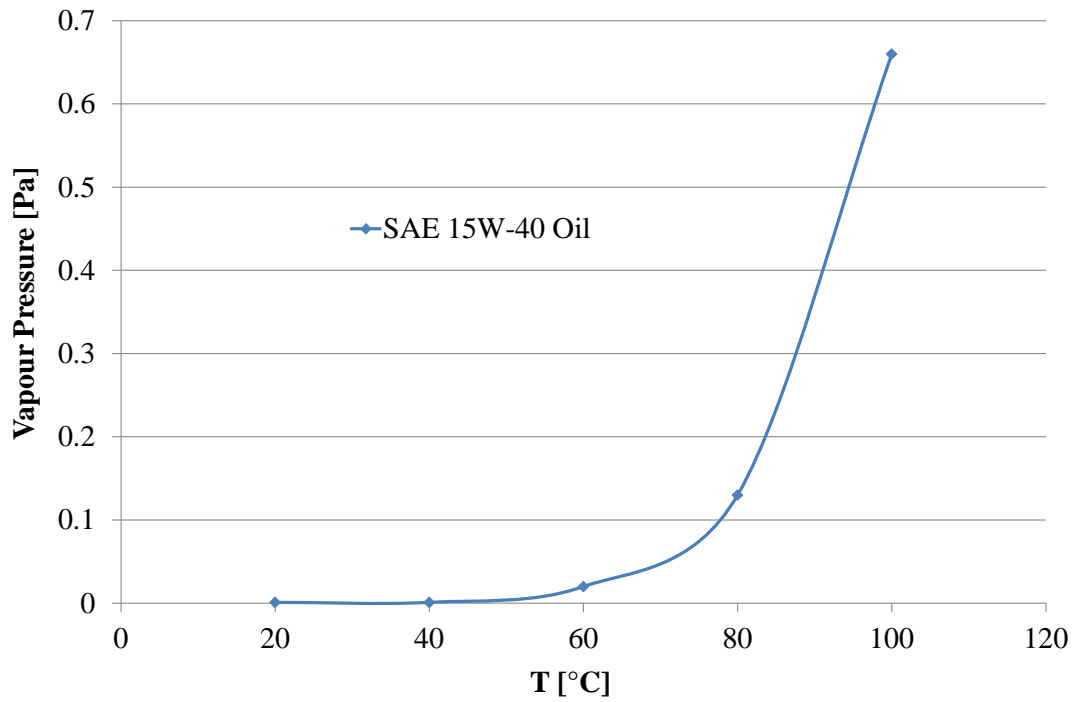
Figure B-1.1 SAE 15W-40 saturation vapour pressure courtesy of Shell-UK
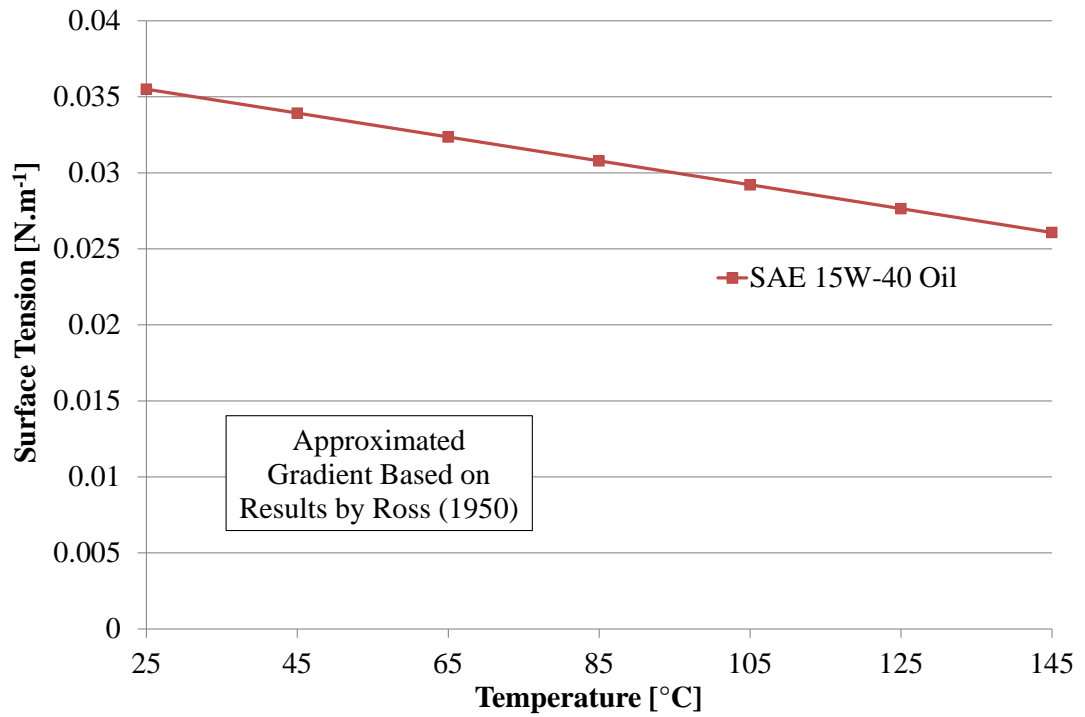

Figure B-1.2 SAE 15W-40 surface tension. Calculated with reference to Ross (1950).

B-2 SAE 15W-40 and SAE 5W-30 Oil Comparison

Table B-2.2 Oil properties (a) SAE 15W-40 (Shell, 2010) Intertek Testing Services (UK) Ltd (b) SAE 5W-30 (Comma, 2009) and Intertek Testing Services (UK) Ltd

Test	Unit	Typical	Typical
Oil Type	SAE	15W-40	5W-30
Viscosity @ 40 °C	$m^2 \cdot s^{-1}$	1.18×10^{-5}	5.8×10^{-5}
Viscosity @ 100 °C	$m^2 \cdot s^{-1}$	1.55×10^{-5}	1.04×10^{-5}
Viscosity Index		139	165
Density @ 15 °C	$kg.m^{-3}$	883	853
Flash Point	°C	227	200
Surface Tension ASTM D971 (Mod)	$N.m^{-1}$	0.0355	0.0326
Noack Volatility ASTM D5800 B	$\% \ m.m^{-1}$	11.3	12.0

APPENDIX C

C-1 Drop Drag Coefficient

The drop drag coefficient is dependent on the particle Reynolds number, for low Reynolds number flows viscous forces dominate, but for high Reynolds numbers inertia becomes significant. Lefebvre (1989) and Kulkarni, Baron and Willeke (2011) present a range of approximations to calculate the drop drag coefficient, as shown in Table E-1.

Table C-1.1 Drop drag coefficient calculations taken from Lefebvre (1989) and Kulkarni, Baron and Willeke (2011)

C_D for Low Reynolds Numbers < 0.1	$$C_D = \frac{24}{Re}$$	(C.1)
C_D for Reynolds Numbers < 1000 (Prandtl, 1944)	$$C_D = \frac{24}{Re} + 1$$	(C.2)
C_D (Langmuir and Blodgett, 1946)	$$C_D \frac{24}{Re} = 1 + 0.197Re^{0.63} + 2.6 \times 10^{-4}Re^{1.38}$$	(C.3)
C_D (Mellor, 1969)	$$C_D = \frac{1}{Re}[23 + (1 + 16Re^{0.33})^{0.5}]$$	(C.4)
C_D (Sartor and Abbott, 1975) $0.1 \leq Re \geq 5$	$$C_D = \frac{24}{Re}(1 + 0.0196Re)$$	(C.5)
C_D (Friedlander, 1977) $5 \leq Re \geq 1000$	$$C_D = \frac{24}{Re}\left(1 + 0.0158Re^{2/3}\right)$$	(C.6)

APPENDIX D

D-1 Example MATLAB Image Processing Code

```matlab
%Rocker Oil Distribution Example MATLAB Image Processing Code Ben
Johnson
%14/05/12

%Clear information in figures from previous programs
close all;
clear all;

%Define Necessary values
img_no = 1;
Drop_number = 0;
Drop_number_matrix= zeros(1,3);
pos=NaN(1,3);

%Select files to open
cd('C:\Users\mmbtj2\Personal Documents - Not Backed Up\My
PhD\RESULTS\Perkins Motored Engine\Imaging\rocker\test012\');
Filename='test012_C001H001S000100';
Struct = strcat('%0',num2str(4),'.0f');
FileExt = '.jpg';
StartNum =121;
EndNum = 121;
FileCount = EndNum-StartNum+1;
TempFileNum = StartNum;

%Main image processing for loop
for img_number=1:5:FileCount;

% Read Images
TempImage = strcat(Filename,sprintf(Struct,TempFileNum),FileExt);
I=imread(TempImage);

Drop_number = 0;

%Window Image
I = I(292:835,259:795);
figure,imshow(I);
f =I;

%Threshold image
T2 = 0.2;
BW = im2bw(f,T2);
figure,imshow(~BW);

%Fill in holes
BW_filled = imfill(~BW,'holes');
figure,imshow(BW_filled);

%Filter image
J = medfilt2(BW_filled, [5 5]);
```

```matlab
figure,imshow(J);

%Find droplets using bwLabel connected components function
[L,NUM] = bwlabeln(J,8);
figure, imshow(L)

%Store drop data using regionprpos function
STATS = regionprops(L,'all');

%Plot data on droplets
for m = 1 : size(STATS,1)
    for n = 1 :size(STATS,2)
            %Drop criteria
            if ([STATS(m).Eccentricity] <0.9) & ([STATS(m).Area] >
2) &([STATS(m).Area] < 5000)
            %Drop_number = Drop_number +1;
            droplet_data(m,n)= (STATS(m).Area);
            n2 = n + 1;
            droplet_data(m,n2)= STATS(m).Centroid(1,1);
            n3 = n2 + 1;
            droplet_data(m,n3)= STATS(m).Centroid(1,2);
            Drop_number = Drop_number +1;
            Drop_number_matrix(Drop_number,1) = Drop_number;
            Drop_number_matrix(Drop_number,2) =
STATS(m).Eccentricity;
            Drop_number_matrix(Drop_number,3) =
STATS(m).EquivDiameter *0.069;
            % Clear values for next drop
            clear X
            clear Y
            clear Z
            clear n2;
            clear n3;
            end
    end

end

%Plot Drop data
figure(img_number), imshow(J);
hold on;
plot(droplet_data(:,2),droplet_data(:,3),'r+');
    for m = 1 : size(STATS,1)
        if ([STATS(m).Eccentricity] <0.9) & ([STATS(m).Area] > 2)
&([STATS(m).Area] < 5000)
                radius = ((STATS(m).Area)/pi)^0.5;
                rectangle('Position', [STATS(m).Centroid(1,1)-
radius,STATS(m).Centroid(1,2) - radius, 2*radius, 2*radius],
'Curvature',[1,1], 'edgecolor','b','linewidth',1.5);
        end
    end

%Increment image number
img_no = img_no +1

clear stats;
```

```matlab
%Increment file name
TempFileNum=TempFileNum+5;
end

%Plot Drop Data
figure
xt = Drop_number_matrix(:,1);
yeccn = Drop_number_matrix(:,2);
yequdia = Drop_number_matrix(:,3);
[AX,H1,H2] = plotyy(xt,yequdia, xt, yeccn ,'plot')
set(get(AX(1),'Ylabel'),'String','Drop Diameter [mm]','FontSize',
24,'FontName', 'Times New Roman')
set(get(AX(2),'Ylabel'),'String','Drop Eccentricity','FontSize',
24,'FontName', 'Times New Roman')
xlabel('Drop Number','FontSize', 24,'FontName', 'Times New Roman')

axis(AX(1),[1 61 0 4]);
axis(AX(2),[1 61 0 1]);

set(AX(1),'FontSize', 24,'FontName', 'Times New Roman');
set(AX(2),'FontSize', 24,'FontName', 'Times New Roman');
set(H1,'LineStyle','-', 'LineWidth',2)
set(H2,'LineStyle',':', 'LineWidth',2)
```

APPENDIX E

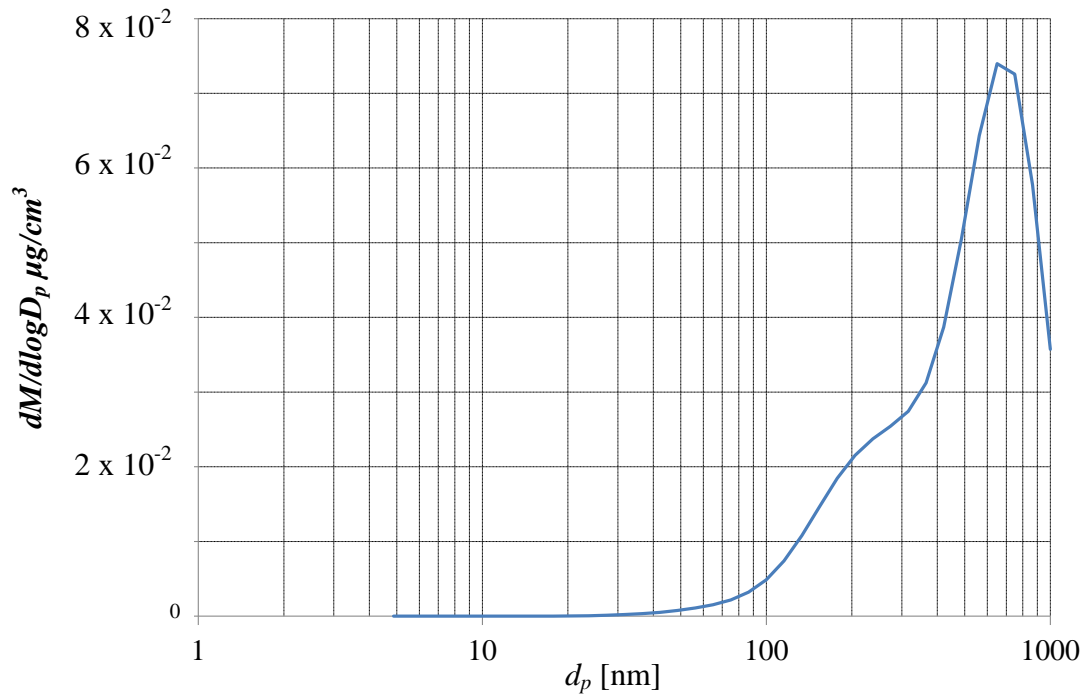## E-1 Particle Sampling Mass Concentration Size Distribution

Figure E-1.1 Total fired engine DMS500 submicron mass concentration at 900 rpm 75% load sampling from the rocker cover